Doctoral Thesis

Investigation of Efficient Organic Solar Cells through Optimized Morphology Control and Understanding of Mechanisms

Tanya Kumari

Department of Energy Engineering

(Energy Engineering)

Graduate School of UNIST

2019

Investigation of Efficient Organic Solar Cells through Optimized Morphology Control and Understanding of Mechanisms

Tanya Kumari

Department of Energy Engineering
(Energy Engineering)

Graduate School of UNIST

Investigation of Efficient Organic Solar cells through Optimized Morphology Control and Understanding of Mechanisms

A thesis/dissertation
submitted to the Graduate School of UNIST
in partial fulfillment of the
requirements for the degree of
Doctor of Philosophy

Tanya Kumari

12. 10. 2018 of submission

Approved by

Advisor

Changduk Yang

Investigation of Efficient Organic Solar cells through Optimized Morphology Control and Understanding of Mechanisms

Tanya Kumari

This certifies that the thesis/dissertation of Tanya Kumari is approved.

12/10/2018

Advisor: Changduk Yang

Hyesung Park: Thesis Committee Member #1

Kwanyong Seo: Thesis Committee Member #2

Sung You Hong: Thesis Committee Member #3

Seok Ju Kang: Thesis Committee Member #4

Abstract

In the global search for clean-energy harvesting technology, organic solar cells (OSCs) have gain considerable attention for their ability to form highly efficient, large-area flexible solar panels by low-cost solution processing techniques. In the solution-processible method, organic donor polymers/small molecules are intimately blended with fullerene/non-fullerene acceptors to form bulk-heterojunction (BHJ). This device architecture has produced the most efficient OSCs with >12% power conversion efficiency (PCE) to date. To further enhance the performance of OSCs, apart from the materials design, proper understanding and subsequent tuning of four important factors during device fabrication are of great importance. These four factors are; morphology control of donor (D) and acceptor (A), broadening of absorption window of active layer components, selection of the proper solvent for smooth film formation of the active layer, and strengthening of the built-in electric field for faster charge carriers' separation and transport. Thus in this dissertation, a series of studies have been carried out to deeply understand the governing mechanism of each of the four phenomena in order to achieve highly efficient OSCs.

In my 1st study, to improve the BHJ nanomorphology of the small molecule donor, DTGe(FBTTh$_2$)$_2$:fullerene composite, various macromolecular additives are chosen to thoroughly investigate the crystallinity, crystal orientation, and D:A phase separations for proper charge separation and transport. Each additive played a unique role in tuning BHJ morphology thereby improving the device performance.

If we wish to obtain higher PCE then we must design the OSCs which can absorb the entire visible spectrum. Since most of the organic semiconductors have a narrow bandgap, organic solar cells made up of one donor and one acceptor is unable to harness wider window of the solar spectrum. Therefore, in the 2nd study, small molecule donor, DR3TSBDT as a third component having complementary absorption with the PTB7-Th:PC$_{71}$BM binary blend is introduced to form ternary solar cells with >12% PCE.

Currently, most of the highly efficient OSCs are fabricated using toxic halogenated solvents which is not desirable for large-scale production. With non-halogenated solvents, the solubility of donor/acceptor material is relatively poor and so is the film formation. Therefore, it is difficult to choose a proper non-halogenated solvent with desirable solubility to fabricate highly efficient OSCs. In my 3rd study, Hansen solubility parameter (HSP) and other material-solvent interaction parameters such as relative energy difference (RED), Florry-Huggins interaction parameter (χ) were employed to investigate the active layer's material-solvent interaction as well as to predict the morphology of the formed film using the given materials and the solvent.

Interestingly during this study, well defined bimolecular cubic crystals of PTB7-Th:$PC_{71}BM$ with proper p-n junction were obtained in mesitylene solvent which insisted upon the fact that the physical properties of a material applied from two different solvents can exceed the variation in the properties of the two different materials applied from the same solvent.

Light absorption in organic donors generates strongly bound excitons which can separate efficiently in presence of sufficient driving force. However due to the higher binding energy of organic materials and low driving force at the D:A interface, exciton dissociation and charge separation is not very efficient. Therefore, generating strong internal electric field locally by means of permanently polarized material can help in solving this issue and high photocurrent with low voltage loss can be achieved at the same time. In my last work, ferroelectric polymers are incorporated in the already optimized binary host matrix as additives generated a strong electric field in the local surrounding which further enhanced the device efficiency. Ferroelectric nature of the polymer additives was confirmed using P-E hysteresis curve which revealed that these material possess very high remnant polarization value (without ant treatment like thermal annealing or poling) being beneficial for faster charge dissociation and transport at the respective device electrode.

Table of Contents

List of Figures

List of Tables

Glossary of Symbols and Abbreviations

A	:	Area
α	:	Absorption coefficient; slope of J_{SC} vs. light intensity
Å	:	Angstrom
AM	:	Air mass
AC	:	Alternating current
AFM	:	Atomic force microscopy
BHJ	:	Bulk heterojunction
β	:	Slope of V_{OC} vs. light intensity
c	:	Speed of light (299,792,458 m/s)
CT	:	Charge transfer
CV	:	Cyclic voltammetry
CCLs	:	Coherence lengths
D/A	:	Donor/acceptor
DC	:	Direct current
$d_{(h,k,l)}$	:	Stacking length of (hkl) plane
e	:	Elementary charge (1.6×10^{-19} C)
ε	:	Relative permittivity
ε_0	:	Relative permittivity of free space
EQE	:	External quantum efficiency
FF	:	Fill factor
GIWAXS	:	Grazing incidence wide angle X-ray scattering
γ	:	Surface energy
h	:	Planck's constant (6.626×10^{-34} J·s)
HOMO	:	Highest occupied molecular orbital
HR-TEM	:	High resolution-transmission electron microscopy
HSP	:	Hansen solubility parameter
J	:	Current density
J_0	:	Reverse saturation current density
J_{ph}	:	Photocurrent density
J–V	:	Current density–voltage
J_{SC}	:	Short-circuit current density

k	:	Boltzmann constant (8.617×10^{-5} eV/K)
LUMO	:	Lowest unoccupied molecular orbital
λ	:	Wavelength
MALDI-TOF	:	Matrix Assisted Laser Desorption/Ionization- Time-of-Flight Mass Spectrometer
η	:	Efficiency
NMR	:	*Nuclear magnetic resonance*
OSC	:	Organic solar cell
PCE	:	Power conversion efficiency
PPM	:	Parts Per million
P	:	Polarization
RED	:	Relative energy difference
RPM	:	Revolutions per minute
RT	:	Room temperature
R_P	:	Parallel (or shunt) resistance
R_S	:	Series resistance
SCLC	:	Space charge limited current
SEM	:	Scanning electron microscopy
SMDs	:	Small molecular donors
T	:	Temperature
τ	:	Lifetime
TEM	:	Transmission electron microscopy
UV	:	Ultraviolet
μ	:	Mobility
V	:	Voltage
V_{OC}	:	Open-circuit voltage
ω	:	Frequency
χ	:	Florry-Huggins Interaction Parameter

List of Chemicals and Materials

BDT	:	4,8-bis(alkyloxy)benzo[1,2-*b*:4,5-*b*']dithiophene
CB	:	Chlorobenzene
$CDCl_3$	:	deuterochloroform
CF	:	Chloroform
DIW	:	Deionized water
DIO	:	Diiodooctane
DTGe	:	dithieno[3,2-*b*:2′,3′-*d*]germole
DTGe($FBTTh_2$)$_2$	:	7, 7'-(4,4-bis(2-ethylhexyl)-4H-germolo[3,2-*b*:4,5-*b*']dithiophene-2,6-diyl) bis(6-fluoro-4-(5'-hexyl-[2,2'-bithiophen]-5-yl)benzo[*c*][1,2,5]thiadiazole)
G18	:	Poly(vinylidene fluoride)–grafted–poly(*tert*-butyl acrylate)
G44	:	Poly(vinylidene fluoride-trifluoroethylene)–grafted–poly(*tert*-butyl acrylate)
IPA	:	Isopropyl alcohol
ITO	:	Indium tin oxide
MeOH	:	Methanol
MES	:	Mesitylene
OXY	:	O-Xylene
$PC_{71}BM$	:	[6,6]-phenyl C71 butyric acid methyl ester
$PC_{61}BM$	:	[6,6]-phenyl C61 butyric acid methyl ester
PDMS	:	Polydimethylsiloxane
PEDOT:PSS	:	Poly(3,4,-ethylene dioxythiophene):poly(styrenesulfonate)
PMMA	:	Poly(methyl methacrylate)
PTB7-Th	:	Poly(4,8-bis(5-(2-ethylhexyl)thiophen-2-yl)benzo[1,2-*b*;4,5-*b*']dithiophene-2,6-diyl-alt-(4-(2-ethylhexyl)-3-fluorothieno[3,4-*b*]thiophene-)-2-carboxylate-2-6-diyl)
PS	:	Polystyrene
PVDF	:	Poly(vinylidene fluoride)
P(VDF-TrFE)	:	Poly(vinylidene fluoride-trifluoroethylene)
TOL	:	Toluene

Chapter 1. Objectives and Introduction of the Study

1.1 Objectives and Structure of the Dissertation

The efficiency limitation of the organic solar cells (OSCs) is a very important issue. With an aim to improve the power conversion efficiency (PCE), I present few inspired ideas of optimizing and improving the efficiency of thin film OSCs with various experimental results and deep characterization analysis within this thesis. This thesis mainly focuses on four research areas for the development of organic solar cells: a) morphology control for proper charge dissociation and transport, b) an effective method for harnessing entire visible spectrum, c) importance of material-solvent interaction in choosing proper nontoxic solvent for efficient device fabrication, and d) generation of extra built-in electric field to separate excitons and prevent recombination loss upon incorporating ferroelectric material with permanent polarization.

- Chapter 1 presents a brief introduction of solar cells followed by basic characteristics of solar cells. Then the rapidly emerging and most focused area of solar cells, i.e. organic solar cell and ternary organic solar cells are discussed.
- Chapter 2 discusses the basic properties of material used in the various study during my PhD. course followed by the detailed fabrication steps used for fabricating various kinds of binary and ternary devices during my PhD. course. At the end all the characterization techniques used to study various optical, electrical and morphological properties are briefly discussed.
- Chapter 3 details my study on the morphology control of bulk heterojunction film for proper charge separation and transport. Additives play a major role in controlling the crystallinity of donor (D) and acceptor (A) therefore, by introducing macromolecular additives, morphology of DTGe(FBTTh$_2$)$_2$:PC$_{71}$BM is controlled to obtain better performance.
- Chapter 4 is on an effective design for obtaining a higher PCE upon extending absorption window through ternary approach. Because of the intrinsic limited absorption window of organic donor materials, the PCE of binary blend OSCs is lower than inorganic solar cells. To overcome this issue, Small molecule donor, DR3TSBDT as a third component having the complementary absorption and proper band alignment with PTB7-Th:PC$_{71}$BM is chosen to fabricate ternary solar cell with > 12% PCE. EDAX elemental mapping shown that the two donors are well dispersed in the active layer and GIWAXs measurement indicated that the ternary blend have mixed edge-on face-on orientation of donors' crystal which are beneficial for 3-D charge transport.
- Chapter 5 discusses the role of material-solvent interaction in defining the nanostructure of active layer components in a ternary system. By means of Hansen solubility parameters (HSP) relative energy difference (RED), and Florry-Huggins interaction parameter (χ), interaction between various solvents with active layer components is deeply studied. Well defined cubic crystals were

obtained in mesitylene solvent which insists on the fact that physical properties of a material dissolved in two different solvents can surpass the variation of the two different materials dissolved in a same solvent.

- Chapter 6 includes my work on strengthening the internal built-in electric field for faster charge dissociation and lower recombination in OSCs. For this, poly(vinylidene fluoride (PVDF), poly(vinylidene fluoride-trifluoroethylene) P(VDF-TrFE), and their grafted co-/ter polymer, poly(vinylidene fluoride)–grafted–poly(tert-butyl acrylate) (PVDF–g–PtBA, G18), and poly(vinylidene fluoride-trifluoroethylene)–grafted–poly(tert-butyl acrylate) (P(VDF-TrFE)–g–PtBA, G44) with high dielectric constant and remnant polarization are selected to use as an ferroelectric additive in already optimized PTB7-Th:$PC_{71}BM$ based binary solar cells to surpass its highest efficiency. These additives with high dipole moments created permanently polarized smaller domains without any poling through strong external bias to generate local internal field in the surrounding for better charge separation and transport.

For achieving these ideas, some of the essential modern techniques and methods were employed during the entire duration of my Ph.D. course. All the necessary experimental processes, data analysis, theoretical and mathematical calculation, and relevant discussions with essential characterization techniques are all included in this dissertation. Moreover, this dissertation is also expected to propose some inspirations for overcoming current limitations in increasing PCE of OSCs and give a brief outlook for future work.

1.2 Introduction

Energy is needed for the existence of humankind. This energy is continuously produced through discovery and advancement of technologies that have evolved over time. Nowadays, the modern sources of energy implemented in our day to day life are the results of years of deep research, development and finally, commercialization of the verified techniques. To solve and minimize today's energy crisis and associated environmental concern, exploiting renewable energy resources such as solar energy have become indispensable. Amongst various exhaustible/inexhaustible sources of energy, solar energy has always attracted a lot of interests. The energy provided by the Sun in the form of light is something natural as clearly shown in photosynthesis. The idea to convert sunlight into a usable form of energy is the base concept of the solar cell. The solar cell is an optoelectronic device able to convert light into electric current, both the direct Sun light and also artificial or ambient light. However, the term light referred here is the electromagnetic spectrum radiated by the Sun onto the Earth's surface. The Sun emits electromagnetic waves all over the range of frequencies while only a fraction of this radiation reaches the surface of the Earth. The air mass coefficient (AM) is an index used to determine the effective electromagnetic radiation emitted by the Sun at the sea level.[1] The AM1.5 spectrum represents the maximum amount of energy

available for a solar cell to be converted in electrical current. According to the AM1.5 spectrum, the maximum emitted electromagnetic spectrum peak lies in the visible region, therefore an efficient solar cell must be able to convert the whole part of the spectrum to maximize the yield of photo generated current. Undeniably, OSCs is going to play a very significant roles in our day to day life. Due to the rapid progress in its efficiency in the last 3 years, it is very rational to believe that its bloom is forthcoming. Recently, bulk heterojunction (BHJ) OSCs has achieved a very high PCE over 12%.[2] Comparing to the inorganic ones, organic solar cells are environmentally friendly, having the advantages of low-cost production, easy processability, and flexibility. In addition to these unexampled properties, OSCs have been widely applied in various fields, such as telecommunication, water pumping, commercial building or residential home systems, space power supply, photovoltaic (PV) power plants, public system power supply, automobiles, military uses and other digital consumption as well.[3]

1.2.1 *Organic Solar Cells*

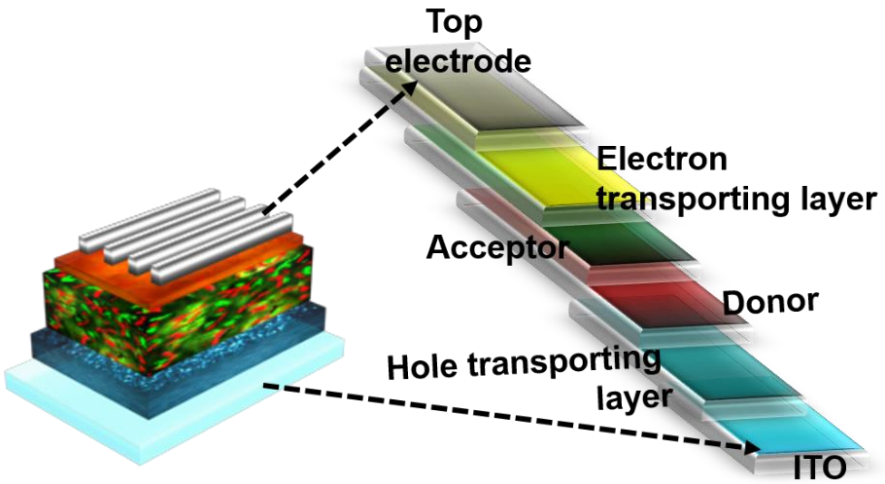

Figure 1.1. Device architecture of conventional organic solar cells (OSCs).

OSCs are made by fabricating thin films made of organic materials dissolvent in non-polar solvents with thickness in the nanometer range. It was first introduced at Kodak Research Laboratories by Dr. Ching W. Tang in 1986.[4] The main motive behind the introduction of organic material was to find a replacement for the expensive silicon solar cells and to use low cost solution processible techniques. Interestingly, OSCs can be fabricated on light weighted, flexible substrates and so they are ideal candidates for wearable and portable systems. As shown in Figure 1.1, OSCs basically comprise the following layers: bottom electrode, hole transport layer, photoactive layer (consisting of donor (D) and acceptor (A) components), electron transport layer, and the top electrode. In general, a solar cell absorbs light, generate excitons which get separated at the D:A interface and the created electrons and holes collected by the respective electrodes

delivering electrical power. The basic difference between the working mechanism of organic and inorganic solar cells is that in the latter case, immediate generation of free charge carries upon the light absorption takes places while in the former case, the light absorption is followed by the creation of excitons with a typical binding energy of 0.3-0.5 eV due to coulomb-interaction. This coulombic interaction needs to overcome in the presence of the built-in electric field to get separated as free charge carriers.[4-5]

1.2.2 *Ternary Organic Solar Cells*

Several appreciable and potential efforts have been carried out recently in the binary BHJ architecture to lower the bandgap of organic photoactive materials for harvesting a larger portion of the solar spectrum, but, the light absorption in OSCs remain insufficient due to the intrinsic limited absorption window.[6] The first advance strategy to solve this issue is the use of tandem solar cell. This device architecture combines two or more individual active layer blends stacked vertically and separated using HTL and ETL as interlayer (for forming proper ohmic contact). As compared to the single-junction OSCs, solar cells in tandem configuration can overcome Shockley-Queisser limit not only by extending light absorption window but also reducing thermalization loss by harvesting high and low energy photons in the separated active layer blends with complementary absorption range.[7] The Shockley–Queisser limit is designated to the maximum achievable theoretical efficiency of a solar cell that can be harnessed from p-n junction to generate power from the device. However, due to the several drawbacks such as complexity of device fabrication including controlling metal or PEDOT:PSS based robust intermediate layer as well as the optimization of the active layers thicknesses, it is so far less popular than single BHJ OSCs. Another significant strategy is to use of ternary solar cells by providing complementary absorption spectra in single bulk heterojunction (BHJ) solar cells by using multiple-donor/acceptor components with entire coverage of the solar radiation spectrum. This not only have the advantage of simplicity in fabrication conditions as used in single BHJ OSCs but also in amplified photon harvesting by selecting multiple donors/acceptors organic materials with complementary absorption as used in tandem architecture.[8] Recently, ternary solar cells involving as either two polymer donors/one acceptor, one polymer donor/two acceptors, one small molecule donor/two acceptors, one polymer donor/one small molecule donor/one acceptor, or two small molecule donor/one acceptor are considered as one of the promising candidate for obtaining higher performance than theoretical Shockley-Queisser limit (Figure 1.2). Figure 1.2a shows the number of reported literature each year in last ten years. As it can be seen due to several advantages of ternary solar cell, it is continuously being explored all around the world. Figure 1.2b is a contour plot of reported efficiencies as a function of the bandgap of two donors.

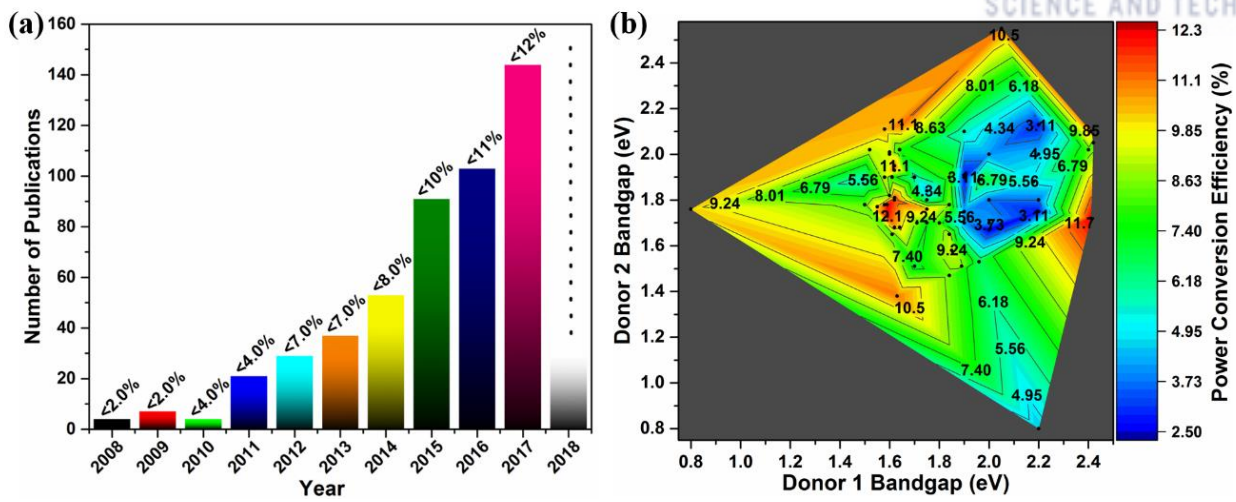

Figure 1.2. (a) Number of publications and power conversion efficiencies (PCEs) of the ternary reported in each year screened using web of science. (b) PCEs of ternary solar cells as a function of donors band gaps from the reported literatures.

Since all the device fabrication techniques for increasing the performance of single BHJ solar cells can be also effectively used in ternary solar cells, tuning the performance in ternary blend is much easier and approachable. The key parameters, short-circuit current (J_{SC}), open-circuit voltage (V_{OC}) and, fill factor (FF), can be individually or simultaneously increased to their maximum values by designing and selecting materials with complementary absorption for controlling the morphology by means of additives and through optimizing the donor or acceptor blending ratios or the overall concentration. The ternary solar cells contain three components in the active layer: the dominating D:A host system and the third component, which can be a polymer, a dye (sensitizer), a small molecule, or a nanoparticle. Therefore, on the basis of function of the third component, ternary solar cells can be broadly categorized into three types: two donors/one acceptor (D1/D2/A), donor/nonvolatile additive/acceptor (D/NA/A), and one donor/two acceptors (D/A2/A1).

Apart from ability to enhanced light absorption, devices based on additional component in the binary blend also exhibit several advantages. These advantages can be broadly categorized into either tuning blend morphology (such as phase separation, polymer crystallization, domain purity, alloy formation, etc.) or facilitating charge transport mechanism through the additional component.[6b, 9] Selection of the appropriate material by selecting proper band gaps as well as the molecular compatibility of active material components are the key factors in order to simultaneously or individually optimizing various photovoltaic parameters, V_{OC}, J_{SC} and FF to their maximum values for enhanced photovoltaic performance.

1.3 The Physics of Organic Solar Cells

1.3.1 *Binary Organic Solar Cells*

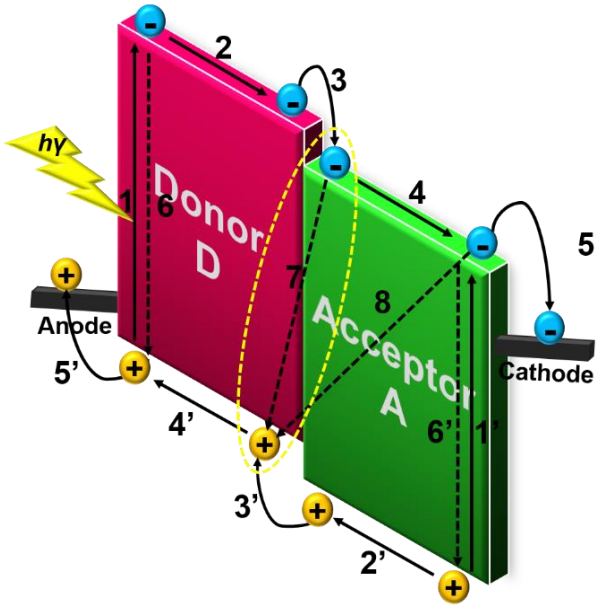

Figure 1.3. Working mechanism of organic solar cells.

The working principle of BHJ OSCs are illustrated with the help of diagram (Figure 1.3). At first, photons are absorbed to generate excitons in D and A, respectively (1 & 1′) then the generated excitons diffuses for dissociation at the D/A interface (2 & 2′). The charge-transfer (CT) states are generated and gets dissociated into free charge carriers (electrons and holes) through charge transfer process (3 & 3′) and finally charge carriers are transported through D or A (4 & 4′) and then collected by the respective electrodes (5 & 5′). Simultaneously in between these charge transfer and transport processes, various recombination processes takes place which prevent the device to achieve its maximum PCE. Like the generated excitons get recombined intra-molecularly (6 & 6′) or the separated charge carriers at the interface may recombine with each other (7, geminate recombination) before dissociation. Secondly, prior to collection by the respective electrodes (5 & 5′), the separated charge carriers from D and A domains may collide with each other and get recombined (8) which is known as bimolecular recombination or non-geminate recombination.

1.3.2 *Ternary Organic Solar Cells*

The morphology and charge transport mechanism in ternary blends are highly dependent on the location of the third component and therefore has been classified into four models (Figure 1.4): (1) the third component with suitable energy level alignment embedded/located in the dominating donor/acceptor phase to facilitate

cascade like charge transfer; (2) the third component is present at the donor/acceptor interface favoring energy transfer; (3) the third component forms an individual separate charge transport channel with the dominating donor/acceptor to form parallel linkage. (4) The third component and dominating donor/acceptor are electronically coupled into a new charge transfer state to form alloy. In the real ternary blending, sometimes the one model is insufficient to explain the charge transport dynamics as well as morphology of the blended material.[8a, 8b, 10]

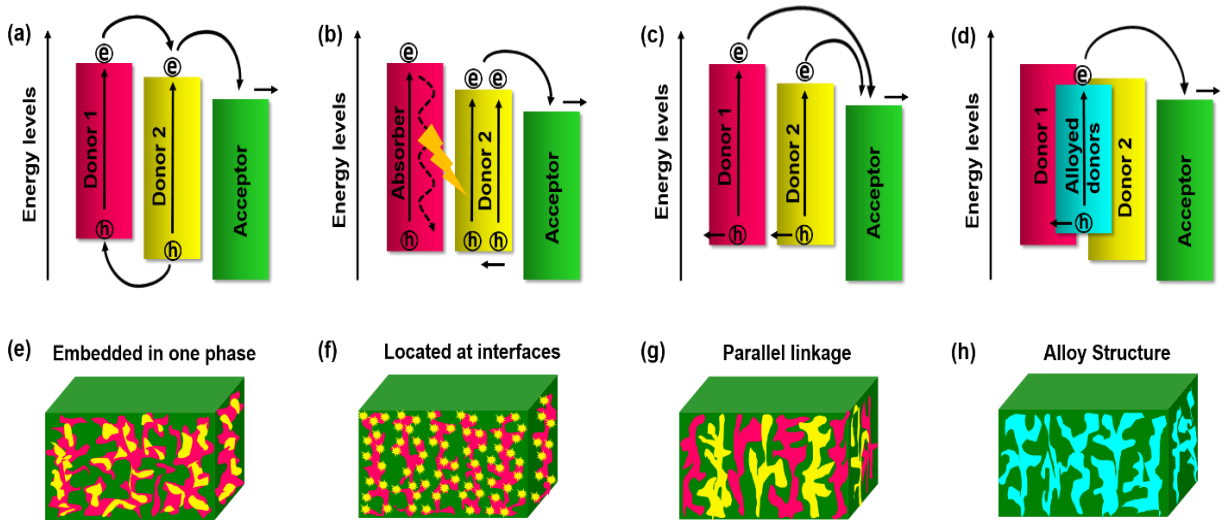

Figure 1.4. Schematic of the working mechanisms and material's localization in ternary solar cells. The arrows indicate the possible charge carrier transfer and transport pathway. (a),(e) The charge transfer mechanism. (b),(f) The energy transfer mechanism. (c) The parallel like mechanism. (d) The alloy model.

Cascade Charge Transfer

For cascade charge transfer mechanism, the location of the third component in the ternary active layer is very important as the additional component functions as a cascade for the charge transport. Mostly for the charge transfer, the lowest unoccupied molecular orbital (LUMO) and the highest occupied molecular orbital (HOMO) energy levels of the third component molecule are located between those of the dominating D and A to form the cascade like energy level alignment. To investigate charge transfer mechanism, photoluminescence (PL) measurement is a convenient tool. For example, if charge transfer occurs between two donors then with different doping ratios, the PL intensity of one would be quenched without increase in PL intensity for the other.

Energy Transfer

Another important working mechanism with multiple donor/acceptor components based ternary OSCs is energy transfer. Förster resonance energy transfer (FRET) is the main working phenomena in the energy

transfer model which enhances the light harvesting and separation. An essential criteria for occurrence of FRET in the ternary blend is the overlapping between the emission spectra of one component and the absorption spectra of the other component. For example, in the multiple-donor system, the exciton energy can be transferred from a large bandgap donor material to a low bandgap donor material. To characterize this model, steady state and transient PL measurements are very useful techniques for determining the occurrence of an energy-transfer process in the given ternary system. In general, if energy transfer occurs between two donors with different bandgap and similar quantum yields, the emission (PL) intensity is increased for the relatively low bandgap donor while for the other donor, emission (PL) intensity is decreased.

Parallel Linkage

For the parallel-linkage mechanism in two donors and one acceptor (D1/D2/A) ternary OSCs, the excitons that are generated in individual domains of two donors would separately diffuse to their respective D/A interface and then get dissociated into electrons and holes as free charge carriers. Thus, the second donor material forms its own independent charge-transport network with the acceptor in addition to the dominating D:A system. In general, for the ternary OSCs with parallel linkage model, the J_{SC} value is almost equal to the sum of the two single D1:A and D2:A cells. The V_{OC} values are in between the observed value for the individual D1:A and D2:A cells, which are much distinct from the charge transfer or energy transfer model in the ternary OSCs.

Alloy Model

The alloy model in ternary solar cell is most popular model to date. In this two electronically similar materials of the ternary blend (i.e. either two acceptors or two donors) form an electronic alloy. And based on the average composition of the two donors/acceptors material, same frontier orbital (HOMO and LUMO) energies are thus formed. Therefore the additional component and the dominating donor/acceptor gets electronically coupled into a new charge transfer state. Hence, for achieving high PCE in ternary OSCs with alloy model, good miscibility and structural/morphological compatibility of the donors/acceptors is required.

1.4 Importance of Morphology in Solar Cell Performance

In OSCs, photon generated excitons which are coulombically bound electron-hole pairs does not readily generate into free charge carriers free electron hole pairs. Instead, they diffuses towards the D-A interface for dissociation. However, the diffusion length of generated excitons are in the range of 10-20 nm prior to recombination. Hence, it less is essential to have phase separation for donor and acceptor entities in the range of 10-20 nm for successful exciton dissociation.[11] OSCs consist of blends of donor and acceptor casted from organic solvents into thin films gets spontaneously phase separate into small domains. The

evolved nanomorphology of the active layer has a very dramatic influence on the OSCs' device performance.[2c, 12] In solution processing, the drying of the solvent significantly impacts the final organization of the blend components in the photoactive layer. Moreover, casting from a single solvent often produces a non-ideal morphology with either excessive or insufficient phase separation between the blend components as well as lack of crystallinity, thereby reducing the device efficiency.

Since a very long time, several additives such as diiodooctane (DIO), chloronaphthalene (CN), diphenyl ether (DPE) etc.[13] have been employed to control the nanomorphology and improve the crystallinity. Since all the device parameters such as J_{SC}, V_{OC}, and FF in the solar cells are sensitive to the morphology of active layer components. Fine control over morphological features enabled by such solvent additives is a very crucial step for optimizing the device performance. Therefore, investigation of additives to control the morphology of blends contain several amorphous and pure crystalline phases is very crucial for the optimization of photovoltaic devices.

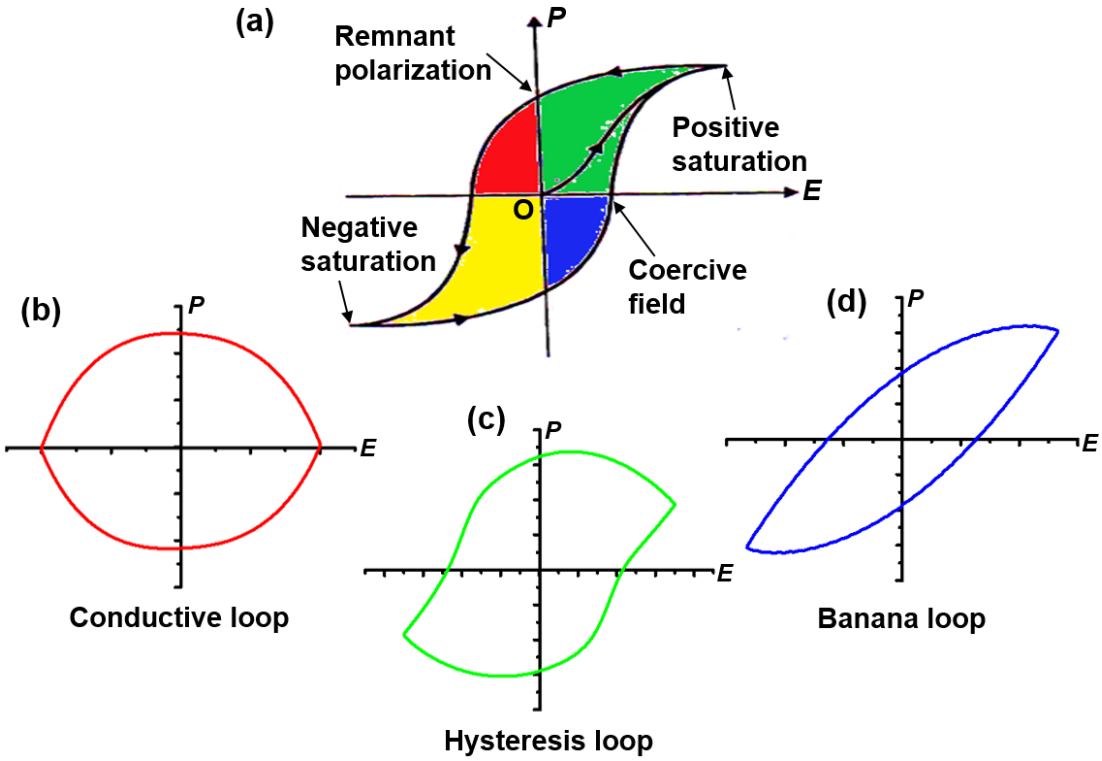

Figure 1.5. Hysteresis loop. (a) Characteristics of hysteresis loop. (b), (c), and (d) Types of P-E loops observed in different materials.

1.5 Ferroelectricity and its Application in Organic Solar Cells

Ferroelectricity is a material characteristics of possessing electric polarization upon application of an external electric field. In ferroelectrics materials, the reversal of the spontaneous polarization by applying

a strong electric field in the opposite direction.[14] Therefore, the polarization is not only dependent on the currently applied electric field but also on its history, producing a hysteresis loop as shown in Figure 1.5a. Positive saturation means material got polarized by alignment of domains in one direction which is reversed upon reversal of electric field direction leading to negative saturation. When driving electric field drops to zero, the ferroelectric material retains a considerable degree of polarization called remnant polarization. This is useful for generating internal electric field in organic photovoltaic devices to separate electrons and holes locally thus, preventing recombination. Coercive field is the minimum amount of electric field which must be applied to a ferroelectric material to make the polarization return to zero.

The shape of the hysteresis loop of ferroelectric material shows the ability of material to display ferroelectricity.[14a, 15] For example, the round shape of P-E loop (see Figure 1.5b) means the material has high electrical conductivity. Figure 1.5c shows the hysteresis loop for a truly ferroelectric material while the banana loop in Figure 1.5d is due to larger leakage currents or a lossy dielectric.[15c] In a ferroelectric material, the internal electric dipoles are coupled to the lattice structure of the material, thus changes in the lattice structure will change the dipoles' strength. The larger is the strength of dipoles, larger is the ability of a material to generate internal electric field which is advantageous for charge separation in OSCs.[16]

1.6 References

1. (a) Gueymard, C. A.; Myers, D.; Emery, K., Proposed reference irradiance spectra for solar energy systems testing. *Sol. Energy* **2002,** *73* (6), 443-467; (b) Laue, E. G., The measurement of solar spectral irradiance at different terrestrial elevations. *Sol. Energy* **1970,** *13* (1), 43-57.

2. (a) Jiang, W.; Yu, R.; Liu, Z.; Peng, R.; Mi, D.; Hong, L.; Wei, Q.; Hou, J.; Kuang, Y.; Ge, Z., Ternary Nonfullerene Polymer Solar Cells with 12.16% Efficiency by Introducing One Acceptor with Cascading Energy Level and Complementary Absorption. *Adv. Mater.* **2018,** *30* (1), 1703005-n/a; (b) Xu, X.; Yu, T.; Bi, Z.; Ma, W.; Li, Y.; Peng, Q., Realizing Over 13% Efficiency in Green-Solvent-Processed Nonfullerene Organic Solar Cells Enabled by 1,3,4-Thiadiazole-Based Wide-Bandgap Copolymers. *Adv. Mater.* **2018,** *30* (3), 1703973-n/a; (c) Zhao, W.; Li, S.; Yao, H.; Zhang, S.; Zhang, Y.; Yang, B.; Hou, J., Molecular Optimization Enables over 13% Efficiency in Organic Solar Cells. *J. Am. Chem. Soc.* **2017,** *139* (21), 7148-7151.

3. (a) Kylberg, W.; de Castro, F. A.; Chabrecek, P.; Sonderegger, U.; Chu, B. T.-T.; Nüesch, F.; Hany, R., Woven Electrodes for Flexible Organic Photovoltaic Cells. *Adv. Mater.* **2011,** *23* (8), 1015-1019; (b) Lien, S.-Y.; Hsu, C.-H.; Ou, Y.-C., Innovation and fabrication of 5.5 generation image-patterned translucent photovoltaic module by using laser scribing technology. *Prog. Photovolt: Res. Appl.* **2013,** *21* (3), 374-378;

(c) Lipomi, D. J.; Tee, B. C.-K.; Vosgueritchian, M.; Bao, Z., Stretchable Organic Solar Cells. *Adv. Mater.* **2011,** *23* (15), 1771-1775; (d) Søndergaard, R.; Hösel, M.; Angmo, D.; Larsen-Olsen, T. T.; Krebs, F. C., Roll-to-roll fabrication of polymer solar cells. *Mater. Today* **2012,** *15* (1), 36-49; (e) Yoon, J.-H.; Song, J.; Lee, S.-J., Practical application of building integrated photovoltaic (BIPV) system using transparent amorphous silicon thin-film PV module. *Sol. Energy* **2011,** *85* (5), 723-733.

4. Tang, C. W., Two-layer organic photovoltaic cell. *Appl. Phys. Lett.* **1986,** *48* (2), 183-185.

5. (a) Lee, J. M.; Lim, J.; Lee, N.; Park, H. I.; Lee, K. E.; Jeon, T.; Nam, S. A.; Kim, J.; Shin, J.; Kim, S. O., Synergistic Concurrent Enhancement of Charge Generation, Dissociation, and Transport in Organic Solar Cells with Plasmonic Metal–Carbon Nanotube Hybrids. *Adv. Mater.* **2015,** *27* (9), 1519-1525; (b) Servaites, J. D.; Savoie, B. M.; Brink, J. B.; Marks, T. J.; Ratner, M. A., Modeling geminate pair dissociation in organic solar cells: high power conversion efficiencies achieved with moderate optical bandgaps. *Energy Environ. Sci.* **2012,** *5* (8), 8343-8350; (c) Zhang, S.; Zuo, L.; Chen, J.; Zhang, Z.; Mai, J.; Lau, T.-K.; Lu, X.; Shi, M.; Chen, H., Improved photon-to-electron response of ternary blend organic solar cells with a low band gap polymer sensitizer and interfacial modification. *J. Mater. Chem. A* **2016,** *4* (5), 1702-1707.

6. (a) An, Q.; Zhang, F.; Sun, Q.; Wang, J.; Li, L.; Zhang, J.; Tang, W.; Deng, Z., Efficient small molecular ternary solar cells by synergistically optimized photon harvesting and phase separation. *J. Mater. Chem. A* **2015,** *3* (32), 16653-16662; (b) Xiao, L.; Gao, K.; Zhang, Y.; Chen, X.; Hou, L.; Cao, Y.; Peng, X., A complementary absorption small molecule for efficient ternary organic solar cells. *J. Mater. Chem. A* **2016,** *4* (14), 5288-5293; (c) Yang, L.; Yan, L.; You, W., Organic Solar Cells beyond One Pair of Donor–Acceptor: Ternary Blends and More. *J. Phys. Chem. Lett.* **2013,** *4* (11), 1802-1810.

7. (a) Ameri, T.; Dennler, G.; Lungenschmied, C.; Brabec, C. J., Organic tandem solar cells: A review. *Energy Environ. Sci.* **2009,** *2* (4), 347-363; (b) Shockley, W.; Queisser, H. J., Detailed Balance Limit of Efficiency of p-n Junction Solar Cells. *J. Appl. Phys.* **1961,** *32* (3), 510-519; (c) You, J.; Dou, L.; Yoshimura, K.; Kato, T.; Ohya, K.; Moriarty, T.; Emery, K.; Chen, C.-C.; Gao, J.; Li, G.; Yang, Y., A polymer tandem solar cell with 10.6% power conversion efficiency. *Nature Commun.* **2013,** *4*, 1446.

8. (a) An, Q.; Zhang, F.; Zhang, J.; Tang, W.; Deng, Z.; Hu, B., Versatile ternary organic solar cells: a critical review. *Energy Environ. Sci.* **2016,** *9* (2), 281-322; (b) Lu, L.; Kelly, M. A.; You, W.; Yu, L., Status and prospects for ternary organic photovoltaics. *Nat. Photon.* **2015,** *9* (8), 491-500; (c) Savoie, B. M.; Dunaisky, S.; Marks, T. J.; Ratner, M. A., The Scope and Limitations of Ternary Blend Organic Photovoltaics. *Adv. Energy Mater.* **2015,** *5* (3), n/a-n/a.

9. (a) An, Q.; Zhang, F.; Li, L.; Wang, J.; Sun, Q.; Zhang, J.; Tang, W.; Deng, Z., Simultaneous Improvement in Short Circuit Current, Open Circuit Voltage, and Fill Factor of Polymer Solar Cells through Ternary Strategy. *ACS Appl. Mater. Interfaces* **2015,** *7* (6), 3691-3698; (b) Farahat, M. E.; Patra, D.; Lee,

C.-H.; Chu, C.-W., Synergistic Effects of Morphological Control and Complementary Absorption in Efficient All-Small-Molecule Ternary-Blend Solar Cells. *ACS Appl. Mater. Interfaces* **2015,** *7* (40), 22542-22550; (c) Scharber, M. C.; Mühlbacher, D.; Koppe, M.; Denk, P.; Waldauf, C.; Heeger, A. J.; Brabec, C. J., Design Rules for Donors in Bulk-Heterojunction Solar Cells—Towards 10 % Energy-Conversion Efficiency. *Adv. Mater.* **2006,** *18* (6), 789-794; (d) Zhang, J.; Zhang, Y.; Fang, J.; Lu, K.; Wang, Z.; Ma, W.; Wei, Z., Conjugated Polymer–Small Molecule Alloy Leads to High Efficient Ternary Organic Solar Cells. *J. Am. Chem. Soc.* **2015,** *137* (25), 8176-8183.

10. Tayebeh, A.; Parisa, K.; Jie, M.; J., B. C., Organic Ternary Solar Cells: A Review. *Adv. Mater.* **2013,** *25* (31), 4245-4266.

11. (a) Lunt, R. R.; Giebink, N. C.; Belak, A. A.; Benziger, J. B.; Forrest, S. R., Exciton diffusion lengths of organic semiconductor thin films measured by spectrally resolved photoluminescence quenching. *J. Appl. Phys.* **2009,** *105* (5), 053711; (b) Mikhnenko, O. V.; Azimi, H.; Scharber, M.; Morana, M.; Blom, P. W. M.; Loi, M. A., Exciton diffusion length in narrow bandgap polymers. *Energy Environ. Sci.* **2012,** *5* (5), 6960-6965.

12. (a) Friedel, B.; McNeill, C. R.; Greenham, N. C., Influence of Alkyl Side-Chain Length on the Performance of Poly(3-alkylthiophene)/Polyfluorene All-Polymer Solar Cells. *Chem. Mater.* **2010,** *22* (11), 3389-3398; (b) Guo, X.; Baumgarten, M.; Müllen, K., Designing π-conjugated polymers for organic electronics. *Prog. Polym. Sci.* **2013,** *38* (12), 1832-1908; (c) Liu, S.; You, P.; Li, J.; Li, J.; Lee, C.-S.; Ong, B. S.; Surya, C.; Yan, F., Enhanced efficiency of polymer solar cells by adding a high-mobility conjugated polymer. *Energy Environ. Sci.* **2015,** *8* (5), 1463-1470; (d) Liu, Y.; Zhao, J.; Li, Z.; Mu, C.; Ma, W.; Hu, H.; Jiang, K.; Lin, H.; Ade, H.; Yan, H., Aggregation and morphology control enables multiple cases of high-efficiency polymer solar cells. *Nat. Commun.* **2014,** *5*.

13. (a) Graham, K. R.; Mei, J.; Stalder, R.; Shim, J. W.; Cheun, H.; Steffy, F.; So, F.; Kippelen, B.; Reynolds, J. R., Polydimethylsiloxane as a Macromolecular Additive for Enhanced Performance of Molecular Bulk Heterojunction Organic Solar Cells. *ACS Appl. Mater. Interfaces* **2011,** *3* (4), 1210-1215; (b) Huang, Y.; Wen, W.; Mukherjee, S.; Ade, H.; Kramer, E. J.; Bazan, G. C., High-Molecular-Weight Insulating Polymers Can Improve the Performance of Molecular Solar Cells. *Adv. Mater.* **2014,** *26* (24), 4168-4172; (c) Moulé, A. J.; Meerholz, K., Controlling Morphology in Polymer–Fullerene Mixtures. *Adv. Mater.* **2008,** *20* (2), 240-245; (d) Perez, L. A.; Rogers, J. T.; Brady, M. A.; Sun, Y.; Welch, G. C.; Schmidt, K.; Toney, M. F.; Jinnai, H.; Heeger, A. J.; Chabinyc, M. L.; Bazan, G. C.; Kramer, E. J., The Role of Solvent Additive Processing in High Performance Small Molecule Solar Cells. *Chem. Mater.* **2014,** *26* (22), 6531-6541; (e) Yao, Y.; Hou, J.; Xu, Z.; Li, G.; Yang, Y., Effects of Solvent Mixtures on the Nanoscale Phase Separation in Polymer Solar Cells. *Adv. Funct. Mater.* **2008,** *18* (12), 1783-1789.

14. (a) Chen, X.; Han, X.; Shen, Q.-D., PVDF-Based Ferroelectric Polymers in Modern Flexible Electronics. *Adv. Electron. Mater.* **2017,** *3* (5), 1600460; (b) Li, Q.; Wang, Q., Ferroelectric Polymers and Their Energy-Related Applications. *Macromol. Chem. Phys.* **2016,** *217* (11), 1228-1244.

15. (a) Scott, J. F., Ferroelectrics go bananas. *J. Phys. Condens. Matter* **2008,** *20* (2), 021001; (b) Xu, B.; Paillard, C.; Dkhil, B.; Bellaiche, L., Pinched hysteresis loop in defect-free ferroelectric materials. *Phys. Rev. B* **2016,** *94* (14), 140101; (c) Zhu, L.; Wang, Q., Novel Ferroelectric Polymers for High Energy Density and Low Loss Dielectrics. *Macromolecules* **2012,** *45* (7), 2937-2954.

16. (a) Liu, F.; Wang, W.; Wang, L.; Yang, G., Ferroelectric-semiconductor photovoltaics: Non-PN junction solar cells. *Appl. Phys. Lett.* **2014,** *104* (10), 103907; (b) Nalwa, K. S.; Carr, J. A.; Mahadevapuram, R. C.; Kodali, H. K.; Bose, S.; Chen, Y.; Petrich, J. W.; Ganapathysubramanian, B.; Chaudhary, S., Enhanced charge separation in organic photovoltaic films doped with ferroelectric dipoles. *Energy Environ. Sci.* **2012,** *5* (5), 7042-7049; (c) Yuan, Y.; Reece, T. J.; Sharma, P.; Poddar, S.; Ducharme, S.; Gruverman, A.; Yang, Y.; Huang, J., Efficiency enhancement in organic solar cells with ferroelectric polymers. *Nat. Mater.* **2011,** *10*, 296; (d) Yuan, Y.; Xiao, Z.; Yang, B.; Huang, J., Arising applications of ferroelectric materials in photovoltaic devices. *J. Mater. Chem. A* **2014,** *2* (17), 6027-6041.

Chapter 2. Materials, Fabrication, and Characterization Methods

This chapter first introduces the materials used in the fabrication of organic solar cells (OSCs) along with their brief introduction which makes them suitable for their corresponding applications. Subsequently the fabrication procedure of organic photovoltaic devices that were used in my research with the required essential preparation steps are discussed in great detail. At the end the typical characterization methods used in characterization of devices as well as the analysis of thin films for optical and morphological properties are also discussed.

2.1 Materials

In this section, all the photo-active materials (donors-acceptors), polymer additives, hole transporting materials, substrates used for fabricating organic solar cells in various studies during my entire Ph.D. course are described briefly.

2.1.1 *Substrate*

Indium doped Tin oxide (ITO) coated glass substrate is commonly used for the fabrication of solar cells. ITO was purchased from Delta technologies limited. The size of the substrate is 15×15×1.1mm with 5mm non ITO part (Figure 2.1). The sheet resistance of ITO coated part is 10-12 ohms.

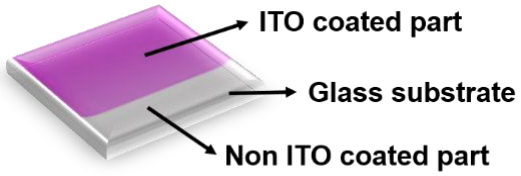

Figure 2.1. ITO coated glass substrate.

2.1.2 *PEDOT:PSS*

Poly-3,4-ethylenedioxythiophene (PEDOT) is transparent and an intrinsically conducting polymer. PEDOT [poly (3,4-ethylenedioxythiophene)] is a conjugated polymeric cation. PSS [poly(styrenesulfonate)] is based on sulfonated polystyrene. Part of sulfonyl groups are deprotonated and acts as an anion.[1] The work function of the PEDOT PSS is 5.1ev, so it can form good ohmic contact with the polymers and thus act as good hole transporting layer in optoelectronic devices. A common type PEDOT:PSS called CLEVIOS P AI4083 received from Heraeus Clevios is used throughout my work.

2.1.3 *Macromolecular Additives*

a. *Insulating Macromolecular Additives*

Various solvent additives, such as 1,8-diiodooctane (DIO), 1,8-octanedithiol (OT), nitrobenzene (NB), 3-methylthiophene, 3-hexylthiophene (3HT), oleic acid (OA), N-methyl pyrrolidone (NMP), and 1-chloronaphthalene (CN), have been widely used in increasing the PCE of OSCs.[2] The crucial factors for choosing a desirable additive are selective solubility towards one blend component and a low volatility. Recently instead of liquid additives, typical insulating polymers as macromolecular additives have begun to improve the performance of BHJ OSCs without fulfilling the above requirements. Insulating polymer additives (see Figure 2.2, top) used in the study are described below:

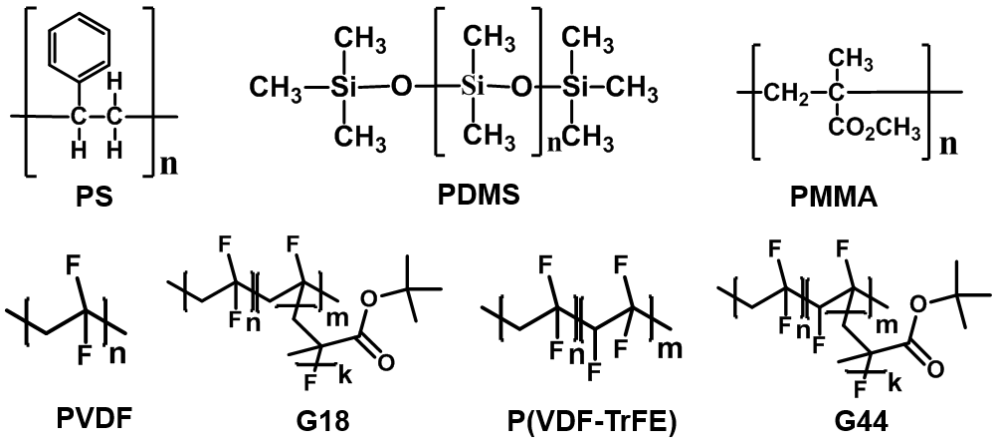

Figure 2.2. Chemical structure of polymer additives used in various studies.

Polystyrene

Polystyrene, (PS) is a hydrophobic polymer synthesized from the monomer styrene. It is soluble in common organic solvent like acetone, chloroform, and chlorobenzene. PS (M.W. 2,000,000) purchased from Alfa-Aesar was used as additive.

Poly(methyl methacrylate) (PMMA)

PMMA also known as acrylic or acrylic glass is transparent type of polymer material obtained via polymerization of monomer called methyl methacrylate. PMMA (Avg. MW ~ 996,000) was purchased from Sigma-Aldrich for the study.

Polydimethylsiloxane (PDMS)

PDMS is an optically clear, non-flammable polymeric organosilicon compound. Polydimethylsiloxane, trimethylsiloxy terminated (M.W. 117,000) was obtained from Alfa-Aesar for use as an additive.

b. *Ferroelectric Insulating Macromolecular Additives*

Ferroelectric insulating materials have the capability of spontaneous electric polarization that can be reversed by the applying electric field externally in the opposite direction. Various organic materials such as polyvinylidene difluoride (PVDF), PVDF-tetrafluoroethylene (P(VDF-TrFE)) and their grafted polymers belong to the class of ferroelectric polymers which have relatively high dielectric constant and possesses net polarization w/o poling (applying strong electric field to induce a net dipole moment).[3] PVDF-based ferroelectric polymers as additives (see Figure 2.2, bottom) used in my study are described below:

Polyvinylidene difluoride (PVDF)

PVDF is a non-reactive fluoropolymer synthesized using the polymerization of vinylidene difluoride. PVDF is a ferroelectric polymer and exhibits efficient electric polarization properties after poling. PVDF (KF1100) with polydispersity index (PDI) = 2.94 and molecular weight, Mn = 168.8 kDa, was purchased from Kureha.

PVDF-tetrafluoroethylene (P(VDF-TrFE))

P(VDF-TrFE) is a copolymer of PVF with tetrafluoroethylene. P(VDF-TrFE) has shown better ferroelectric/piezoelectric response by improving the crystallinity of the material. P(VDF-TrFE) with VDF(n):TrFE(m) = 75:25, were purchased from Kureha having PDI = 3.06, Mn = 85.0 kDa.

To further improve the ferroelectric response of the PVDF and P(VDF-TrFE), grafting with *tert*-butyl acrylate (*t*-BA) using Atom Transfer Radical Polymerization (ATRP) method.

PVDF-*g*-PtBA (G18)

G18 was obtained with molecular weight, M_n = 102 kDa, and PDI = 2.55. F-H decoupled ^{1}H NMR (400MHz, $(CD_3)_2CO$), δ (ppm): 2.9 to 3.2 (br, $–CF_2CH_2CF_2CH_2–$), 2.3 to 2.5 (br, $−CF_2CH_2CH_2CF_2–$), 1.5 ~ 2.0 (-$C(COO)H_2$-CH_2-), 0.8 ~ 1.4 (-$C(COO)H_2$-CH_2-) and 1.4 to 1.65 (br, 9H, $−C(CH_3)_3$).

P(VDF-TrFE)-*g*-PtBA (G44)

G44 was obtained with molecular weight, Mn = 174 kDa, and PDI = 2.53. F-H decoupled ^{1}H NMR (400MHz, $(CD_3)_2CO$), δ (ppm): 5.3 ~ 5.7 (br, -$CFHCF_2$-), 2.7 ~ 3.2 (br, -$CF_2CH_2CF_2CH_2$-), 2.2 ~ 2.7 (br, -$CF_2CH_2CH_2CF_2$-), 1.5 ~ 2.0 (-$C(COO)H_2$-CH_2-), 0.8 ~ 1.4 (-$C(COO)H_2$-CH_2-) and 1.4 to 1.6 (br, $−OC(CH_3)_3$).

2.1.4 *Photo-active Material*

The delocalization of electrons along the backbone of the π-conjugated polymer or small molecule exhibits the semiconducting properties making them a promising candidate for low-cost solution-processed photovoltaic technology. Chemical structures of photo-active materials (donors and acceptors) used in various studies during my Ph.D. course are provided in Figure 2.3.

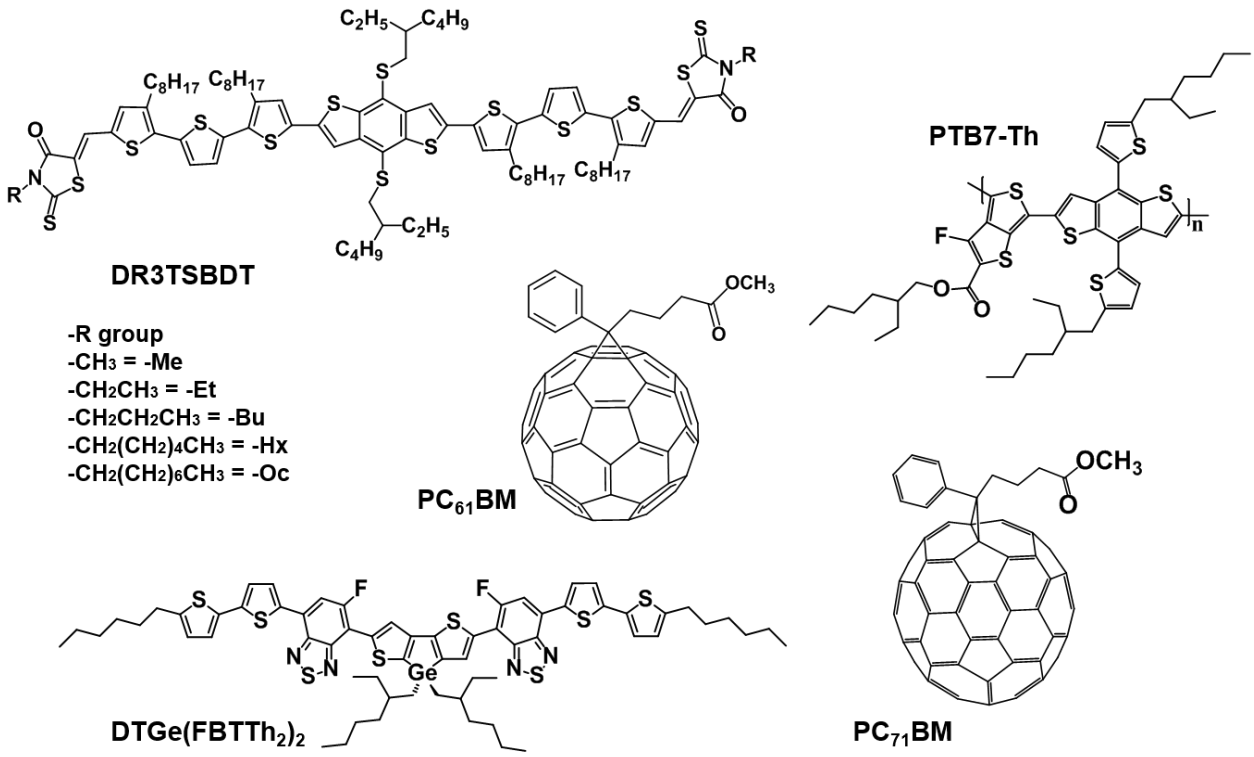

Figure 2.3. Chemical structures of photo-active materials.

a. *Small Molecule Donors*

Conjugated Small molecules donors (SMDs) can exhibit good miscibility with broad absorption spectra. Moreover, SMDs can enhance the light absorption ability in ternary OSCs by providing complementary absorption to harvest broad spectrum window in visible region. Therefore, together with the advantages of well-defined structure and high purity with no batch-to-batch variation, SMDs have attracted more and more attention for use in SMDs based OSCs. In my study various small molecule donors (SMDs) containing benzo[1,2-*b*:4,5-*b*']dithiophene (BDT) unit, and dithieno[3,2-*b*:2′,3′-*d*]germole (DTGe) unit have been used to fabricate small molecule based binary solar cell or ternary solar cells with SMDs as the third component. Although various small molecule donors, such as DTGe(FBTTh$_2$)$_2$, DTSi(FBTTh$_2$)$_2$, DTGe(FBTTh$_2$Cy)$_2$, DTSi(FBTTh$_2$Cy)$_2$,, DR3TSBDT with different alkyl chain (-methyl, -ethyl, -butyl, -hexyl, -octyl) have been investigated during my study,[4] in this thesis, I will particularly focus on

DTGe(FBTTh$_2$)$_2$, and DR3TSBDT with different alkyl chain (as shown in Figure 2.3) based OSC devices.[4b, 4c, 5] All the BDT based SMDs have been synthesized in our lab according to reported literatures and characterizations are as follows:

- SMD-Me: Isolated yield = 66%. ^{1}H NMR ($CDCl_3$, 400 MHz, 298 K) δ ppm 7.73 (s, 2H), 7.60 (s, 2H), 7.19 (br, 4H), 7.10 (br, 4H), 3.50 (m, 6H), 2.99 (br, 4H), 2.93-2.76 (br, 8H), 1.73-1.67 (m, 8H), 1.54-1.20 (m, 58H), 0.92-0.83 (m, 24H). ^{13}C NMR ($CDCl_3$, 100 MHz, 298 K) δ ppm 192.21, 167.48, 144.56, 141.53, 141.10, 141.09, 140.99, 140.95, 140.89, 139.47, 137.50, 137.26, 135.49, 135.14, 134.79, 130.82, 128.50, 127.13, 126.09, 124.75, 122.51, 120.46, 119.32, 39.97, 32.24, 31.96, 31.92, 31.36, 30.41, 30.24, 29.78, 29.68, 29.51, 29.38, 29.34, 28.87, 25.59, 23.05, 22.72, 14.20, 14.15, 10.89. MALDI-TOF MS (m/z) 1734.870 (M^+). Anal.calc. for $C_{92}H_{120}N_2O_2S_{14}$: C, 63.69; H, 6.97; N, 1.61; S, 25.88; Found: C, 63.54; H, 7.01; N, 1.61; S, 25.69.
- SMD-Bu: Isolated yield = 71%. ^{1}H NMR ($CDCl_3$, 400 MHz, 298 K) δ ppm 7.73 (s, 2H), 7.60 (s, 2H), 7.19 (br, 4H), 7.10 (br, 4H), 4.12-4.07 (m, 4H), 2.99 (br, 4H), 2.93-2.76 (br, 8H), 1.73-1.67 (m, 8H), 1.54-1.20 (m, 66H), 0.92-0.83 (m, 30H). ^{13}C NMR ($CDCl_3$, 100 MHz, 298 K) δ ppm 192.21, 167.48, 144.56, 141.53, 141.10, 141.09, 140.99, 140.95, 140.89, 139.47, 137.50, 137.26, 135.49, 135.14, 134.79, 130.82, 128.50, 127.13, 126.09, 124.75, 122.51, 120.46, 119.32, 44.62, 40.34, 39.97, 32.24, 31.96, 31.92, 30.43, 30.25, 29.77, 29.66, 29.56, 29.50, 29.37, 29.34, 29.08, 28.87, 25.59, 23.05, 22.74, 22.71, 20.11, 14.20, 14.16, 13.72, 10.90. MALDI-TOF MS (m/z) 1817.743 (M^+). Anal.calc. for $C_{98}H_{132}N_2O_2S_{14}$: C, 64.71; H, 7.31; N, 1.54; S, 24.68; Found: C, 64.66; H, 7.32; N, 1.51; S, 24.71.
- SMD-Hx: Isolated yield = 85%. ^{1}H NMR ($CDCl_3$, 400 MHz, 298 K) δ ppm 7.75 (s, 2H), 7.68 (s, 2H), 7.22 (br, 4H), 7.18 (br, 4H), 4.11-4.07 (m, 4H), 2.99 (br, 4H), 2.93-2.76 (br, 8H), 1.73-1.67 (m, 8H), 1.54-1.20 (m, 74H), 0.92-0.83 (m, 30H). ^{13}C NMR ($CDCl_3$, 100 MHz, 298 K) δ ppm 192.21, 167.48, 144.56, 141.53, 141.10, 141.09, 140.99, 140.95, 140.89, 139.47, 137.50, 137.26, 135.49, 135.14, 134.79, 130.82, 128.50, 127.13, 126.09, 124.75, 122.51, 120.46, 119.32, 44.87, 40.34, 39.98, 32.24, 31.94, 31.90, 31.36, 30.46, 29.72, 29.53, 29.47, 29.34, 29.31, 28.87, 26.96, 26.48, 25.58, 23.04, 22.71, 22.53, 14.19, 14.14, 14.03, 10.89. MALDI-TOF MS (m/z) 1875.072 (M^+). Anal.calc. for $C_{102}H_{140}N_2O_2S_{14}$: C, 65.33; H, 7.53; N, 1.49; S, 23.94; Found: C, 65.32; H, 7.44; N, 1.48; S, 23.75.
- SMD-Oc: Isolated yield = 80%. Isolated yield = 80%. ^{1}H NMR ($CDCl_3$, 400 MHz, 298 K) δ ppm 7.70 (s, 2H), 7.61 (s, 2H), 7.19 (br, 4H), 7.11 (br, 4H), 4.10-4.06 (m, 4H), 2.99 (br, 4H), 2.93-2.76 (br, 8H), 1.73-1.67 (m, 8H), 1.54-1.20 (m, 82H), 0.92-0.83 (m, 30H). ^{13}C NMR ($CDCl_3$, 100 MHz, 298 K) δ ppm 192.17, 167.43, 144.54, 141.53, 141.10, 141.09, 140.99, 140.95, 140.89, 139.47, 137.50, 137.26, 135.49, 135.14, 134.79, 130.82, 128.50, 127.13, 126.09, 124.75, 122.51, 120.46,

119.32, 44.85, 40.33, 39.97, 32.24, 31.97, 31.93, 31.81, 30.42, 30.24, 29.90, 29.79, 29.68, 29.64, 29.57, 29.51, 29.38, 29.35, 29.18, 29.16, 28.87, 26.99, 26.83, 25.59, 23.06, 22.74, 22.72, 22.66, 14.21, 14.16, 14.12, 10.90. MALDI-TOF MS (m/z) 1931.145 (M^+). Anal.calc. for $C_{106}H_{148}N_2O_2S_{14}$: C, 65.92; H, 7.72; N, 1.45; S, 23.24; Found: C, 65.85; H, 7.66; N, 1.50; S, 23.27.

b. *Polymer Donors*

In organic solar cells, donor material is the main component actively responsible for absorption of photons to generate charge carriers. Currently, polymer donors are extensively used in solar cell to reach maximum efficiency. Therefore, the development and deep investigation of polymer donor materials is one of the crucial factor to elevate PCEs of fullerene or non-fullerene OSCs. In my PhD. course I have studied several polymer such as P3HT, PBDB-T, PTB7, PTB7-Th, DPPTT-OD, and random 2D-2A quarterpolymers based on DPP2T-TT and BDT-QTT.[4b, 5-6] Among them, most actively investigated polymer is PTB7-Th (Figure X), which I have used in host matrix for study of several kinds of ternary solar cells. PTB7-Th, poly[4,8-bis(5-(2-ethylhexyl)thiophen-2-yl)benzo[1,2-*b*;4,5-*b*']dithiophene-2,6-diyl-alt-(4-(2-ethylhexyl)-3-fluorothieno[3,4-*b*]thiophene-)-2-carboxylate-2-6-diyl)] is a low bandgap polymer (E_g = 1.58 eV) known to exhibit very reproducible efficiency of 10%. P3HT, DPPTT-OD, random 2D-2A quarterpolymers based on DPP2T-TT and BDT-QTT, PTB7, PBDB-T have been synthesized in our lab, PTB7-Th was purchased from 1-material.

c. *Acceptors*

Similar to polymer donors, acceptors also play a major role in in elevating solar cell performance. $PC_{61}BM$ and $PC_{71}BM$ as shown in Figure X are fullerene electron acceptors commonly used in the most efficient OSC devices. These two materials have been purchased from Ossila. Apart from these, non-fullerene polymer acceptor, poly((*N*,*N*'-bis(2-octyldodecyl)-naphthalene-1,4,5,8-bis(dicarboximide)-2,6-diyl)-*alt*-5,5'-(2,2'-bithiophene)) also known as N2200 synthesized in our lab have also been investigated in my study.[4a] However, I will discuss fullerene derivatives, for fabricating various kind of OSC devices such as binary small molecule based solar cells, ternary solar cells, non-halogenated solvent processed solar cells, ferroelectric additive based solar cell etc.

2.2 Device Fabrication

2.2.1 *Cleaning of Substrate*

Cleaning of substrates was done normal ambience and is same for all the study based on fabrication of OSC devices. ITO coated glass substrates were cleaned using ultra-sonic bath in four sequential steps. First, the substrates were cleaned using liquid detergent for 15 minutes, followed by thoroughly washing with de-

ionized water and sonicating in it for 15minutes. Next, it was sonicated in acetone and finally in iso-propyl alcohol for 15 minutes each. The substrates were then dried overnight in oven at 70°C. Before, deposition of PEDOT:PSS, cleaned ITO substrate were either given UV-ozone treatment for 20 minutes or plasma cleaning for 5 minute. This makes the ITO surface hydrophilic for uniform deposition of PEDOT:PSS.

2.2.2 *Spin Coating*

Spin coating is the most crucial process for the preparation of OSCs. This is the main technique employed for the deposition of hole transporting layer (HTL), active layer and electron transporting layer (ETL). In my study, for device fabrication, I used spin coating method two times using static and dynamic dispensing method as shown in Figure 2.4. In former case, the deposition of solution on the substrate was the first step. Importantly, at this step the chuck of spin coater stays at stand still position and the solution is dispensed to spread all over the surface. Thereafter, at desired speed, material is spin coated. In later case, that is dynamic dispensing, the substrate is already rotating at desired speed and the solution is dispensed on the rotating substrate to get the desired film. The detailed spin coating process for HTL and active layer is mentioned below:

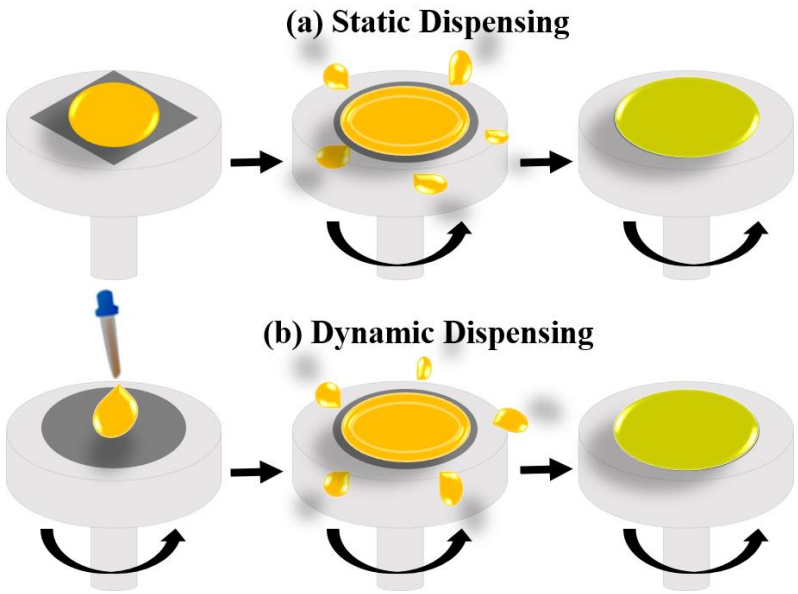

Figure 2.4. Illustration of static and dynamic spin coating method.

- PEDOT:PSS deposition as HTL using static dispensing

  Throughout my study, I used convention device architecture as mention in chapter 1. Thus, after UV-ozone/ a thin PEDOT:PSS (Baytron P VP AI 4083, H. C. Starck) , filtered using a 0.45 μm PVDF

syringe filter was deposited over ITO surface at 4000 rpm. After sequentially annealed at 140 ˚C for 20 minutes, the substrates were transferred to the nitrogen filled glove box.

- Active layer deposition using dynamic dispensing

  In active layer deposition case, 20-25 μl of active layer solution was dynamically dispensed on the rotating substrate for 30-40 seconds to get the desired thickness. In each study, the concentration of active layer solution and the speed of rotation is varied to get the optimum device condition.

2.2.3 *Preparation of Active Layer Solution*

Preparation of active layer solution for each study are different therefore, for each chapter, 2, 3, 4, and 5 experimental section regarding solution preparation will be discussed here.

(a) Solution preparation for study of morphology control in chapter 3

For preparation of active layer solution, 12 mg of DTGe(FBTTh$_2$)$_2$ and 8 mg of PCBM ($PC_{61}BM$/$PC_{71}BM$) in 6:4 ratio was mixed in 570 µl of chlorobenzene. The solution was heated at 70 ˚C for 3 hours under minimal stirring. In each polymer additive case (0.5, 1, 2, and 3) w/w % of the total active layer concentration while in DIO case (0.2, 0.4, and 1) v/v % of the solvent volume was used in the preparation of additive based active layer solution. 20 μl of the active layer solution with or without additive was added on already spinning PEDOT:PSS coated ITOs at 1000 rpm for 30 seconds. The films were dried for 10 minutes in petri dish and then dried over hot plate at 60 ˚C for 10 minutes to remove extra solvents prior to Al deposition.[4c]

(b) Solution preparation for study of ternary solar cell in chapter 4

For the preparation of the active layer solution, 14 mg of donor (PTB7-Th or DR3TSBDT) and 21 mg of $PC_{71}BM$ (1:1.5 ratio) were dissolved in 1 ml of chlorobenzene. The solutions were heated overnight at 60 °C under minimal stirring. Later, 3.0 vol.% of DIO was added to the solutions and stirred well for homogeneity. For ternary blending, the two solutions were mixed according to the different weight ratios of the two donors and heated at 60 °C for 1 h under minimal stirring in the glove box. The active layer was then spin coated to yield a ~140–150 nm thick film as shown in Figure 2.5. Films were dried in vacuum for 30 min prior to top electrode deposition.[5]

For extensive study of ternary solar cells using SMDs molecule with different terminal alkyl chain, the fabrication of SMDs:$PC_{71}BM$ based binary OSCs, the active layer was prepared by the donor and acceptor ratio of 1:1.5 wt./wt. with donor concentration of 14 mg ml^{-1} in CB solution and the ratio of 1:0.8 wt./wt. with total blend concentration of 18 mg ml^{-1} in chloroform (CF). Note that in the CF-processed cases, the films were thermal annealed at 100 °C for 10 min, followed by solvent vapor annealing (SVA) in CF for 1 min. Thereafter, perylene diimides functionalized with

amino N-oxide (PDINO) as an electron transporting layer (ETL in methanol, 0.75 mg ml^{-1}) was applied on the top of active layers at 3000 RPM for 40 s prior to deposition of Al as cathode.[4b]

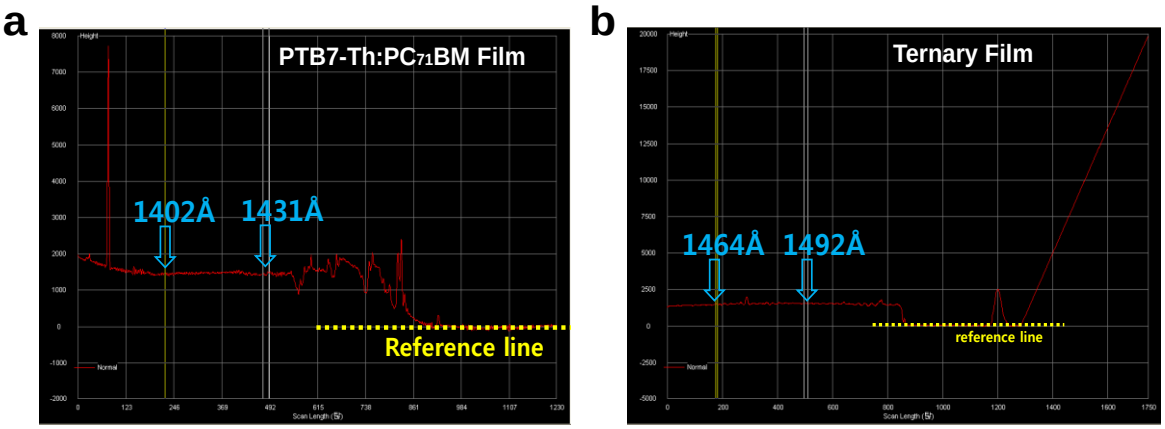

Figure 2.5. Thickness of optimized films in the range of 140-150 nm. a) PTB7-Th:$PC_{71}BM$ binary film. b) Ternary film.

(c) Solution preparation for study of material-solvent interaction in chapter 5

For preparation of active layer solution, 10.5 mg mL^{-1} of PTB7-Th and 21 mg mL^{-1} of $PC_{71}BM$ was dissolved in 1 mL of the each solvent (toluene, o-xylene, mesitylene). The solutions were heated at 60 °C for overnight under minimal stirring. Later, various vol.% of NMP was added to the solutions (according to the type of solvent used; see Table 1 and S3) and stirred well for uniformity. For ternary blending, DR3TSBDT was mixed in the solutions according to the 75:25 weight ratio of the two donors (PTB7-Th:DR3TSBDT such that the overall donor concentration is 14 mg mL^{-1}) and heated at 60 °C for 3h under minimal stirring in the glove box. The active layer was then spin coated to give ~170–180 nm, ~140–150 nm, and ~30–40 nm thick film in case of toluene, o-xylene, and mesitylene respectively. It should be noted that that in case of mesitylene, the given film thickness does not include the thickness of cubic-like crystals present throughout the film. Films were dried in vacuum for 50-60 prior to cathode deposition.[6b]

(d) Solution preparation for study of ferroelectric property and electric field generation in chapter 6

For the preparation of the active layer solution in a nitrogen filled glovebox, PTB7-Th:$PC_{71}BM$ (1:1.5 w/w) was dissolved in o-xylene with a total active layer concentration of 35 mg ml^{-1} and stirred at 60 °C for overnight. All the four additives in a concentrated concentration was dissolved in NMP and stirred at 60 °C for overnight. Different additives was added next day to the active layer solution at different wt% concentration with respect to the total active layer concentration in order to optimize the device performance. Similarly NMP in different v% is used for device optimization and finally all the additives based solutions were further kept on stirring at 60 °C for 2 hrs to ensure homogeneous mixing prior to

spin coating. The active layer w/o each additive was then spin-coated to yield varied thickness of ≈167–216 nm to individually optimize the performance in each case. Films were dried in vacuum for 30 min prior to deposition of Al as cathode.

2.2.4 *Evaporation of Cathode*

In evaporation process the substrates were loaded on a shadow mask and placed inside a vacuum chamber, in which the source material to be deposited is placed. Then a high vacuum by creating a pressure $<3 \times 10^{-6}$ Torr is applied to make the chamber suitable for evaporation. After applying suitable current and voltage, source material is heated to a point where it starts evaporating and the molecules were freely evaporated in the vacuum and condensed on the substrate. In my study, Al was used as cathode to fabricate all kinds of OSCs devices. 80-100 nm thick Al cathode was thermally evaporated on top of the organic layer (see Figure 2.6) using a shadow mask (device area: 0.13 cm^2) under a pressure of $<3 \times 10^{-6}$ (or $< 9 \times 10^{-7}$) Torr.

Figure 2.6. Image of fully fabricated organic solar cells used in various studies with device area: 0.13 cm^2.

2.3 Characterization Methods

Characterization using suitable technique is very important for thorough investigation of any kind of research work. In this section, the methods and the investigation techniques used in the development of the experiments of all kinds of study during Ph.D. course is described. In particular, in the first part the electrical characterization of solar cells that are produced during the research work is discussed. The second part regards the preparation of the thin film and other samples along with the appropriate morphological characterization techniques.

2.3.1 *Characterization of Devices*

Current density-voltage (*J-V*) measurements for the photovoltaic devices were obtained using a Keithley 2365A source measure unit. Measurements were done under simulated sunlight (AM 1.5G) with an

intensity of 100 mW cm^{-2} in a nitrogen filled glove box. Prior to device measurement, the irradiance was calibrated using a standard silicon photodiode. External quantum efficiency (EQE) measurements were done using QEX7 quantum efficiency measurement system (PV Measurements, Inc.) in an ambient atmosphere. For mobility measurements, the hole- and electron-only devices were fabricated using a device architecture of ITO/PEDOT:PSS/active layer/Au and ITO/Al/active layer/Al, respectively. The hole (μh) and electron (μe) mobilities were measured using the SCLC method, which is described by the Mott–Gurney square law as:[7]

$J_{SCLC} = (9/8)\varepsilon_0\varepsilon_r\mu((V^2)/(L^3))$

where J_{SCLC} is the current density, ε_0 is the dielectric constant of free space, ε_r is the relative permittivity of the transport medium (assumed to be 3), μ is the hole (μ_h) or electron (μ_e) mobility, V is the applied voltage across the device, and L is the thickness of the active layer.

Impedance Spectroscopy measurement were carried out using a potentiostat (Versa STAT 3, AMETEK) in the frequency range of 0.1 Hz to 1 MHz at room temperature in air. Illumination measurement were performed at the irradiation intensity of one sun (AM 1.5G, 100 mW cm^{-2}), under open-circuit conditions. For the dark condition, measurement was carried out without open circuit voltage condition.[8]

The polarization–electric field (P–E) hysteresis measurement were carried out using a ferroelectric test system (TF2000E analyzer, Aixacct, Germany) by applying the triangular waveform of the voltage with 1Hz. The dielectric constants of the pure additive films were measured at room temperature by an impedance analyzer (Agilent) over the frequency range of 10^3 to 10^6 Hz.

2.3.2 *Characterization of Thin Films*

All the characterizations otherwise mentioned were performed in ambient atmospheric condition and the optimized device fabrication processing condition were used to prepare thin films. Glass substrate was used to fabricate samples for the absorption, optical microscopy, and thickness measurement while for all other characterizations, samples were fabricated on a silicon substrate.

UV-Vis spectra were obtained using a UV-1800 (SHIMADZU) spectrophotometer and the absorption coefficient was obtained using the following equation:[5]

$\alpha = 2.303*(A/l)$

where, α is the absorption coefficient of the material, A is the absorbance, and l is the thickness of the thin film (in cm). PL spectra were obtained using a Varian Cary Eclipse fluorescence spectrometer. The DSC data were obtained from DSC Q200 TA Instrument, U.S.A. The heating rate was 5 °C min^{-1}. Static contact angles of water and glycerol were measured using Phoenix 300 (SEO) for the surface energy measurement using Young's equation. For EDAX, a Hitachi SU 8220 Cold FE-SEM was used. To achieve sufficient X-ray excitation, the FE-SEM was operated at an acceleration voltage of 10 kV. Note that only a relative

concentration distribution of elements can be obtained from the resulting elemental mapping over the mapped area. Optical microscopy images were acquired using an inverted metallurgical microscope (Alpha300S, WlTec). Optical florescence microscopy images were taken with Olympus motorized inverted microscope IX81, and imaging was done using blue, green, and red light. AFM investigations were performed using a multimode V microscope (Veeco, USA) in the tapping mode with a nanoscope controller using Si tips (Bruker) at a resonance frequency of 300 kHz. HR-TEM analysis was performed using a JEOL USA JEM-2100F (Cs corrector) transmission electron microscope equipped with an EDAX at an acceleration voltage of 200 kV. The specimen for HR-TEM measurement was prepared by spin coating the blend solution on a PEDOT:PSS-coated silicon substrate and floating the film on de-ionized water surface. The film was then transferred to lacey carbon grids (HC200-Cu). GIWAXS characterization was carried out at the PLS-II 9A U-SAXS beam line of the Pohang Accelerator Laboratory in Korea. The scattering signal was recorded using a 2-D CCD detector (Rayonix SX165). The X-ray light had an energy of 11.24 keV (λ = 1.103 Å). The incidence angle of X-rays was adjusted to 0.13–0.145° to maximize the signal to background ratio. The detector was located at a distance of approximately 232 mm from the sample centre. The raw data were processed and analysed using Igor-Pro software package. The thickness of the binary, ternary and pure material films were measured using a stylus profilometer (P6, KLA Tencor).[4-6]

2.4 References

1. (a) Groenendaal, L.; Jonas, F.; Freitag, D.; Pielartzik, H.; Reynolds, J. R., Poly(3,4-ethylenedioxythiophene) and Its Derivatives: Past, Present, and Future. *Adv. Mater.* **2000,** *12* (7), 481-494; (b) Kirchmeyer, S.; Reuter, K., Scientific importance, properties and growing applications of poly(3,4-ethylenedioxythiophene). *J. Mater. Chem.* **2005,** *15* (21), 2077-2088.

2. (a) Lee, J. K.; Ma, W. L.; Brabec, C. J.; Yuen, J.; Moon, J. S.; Kim, J. Y.; Lee, K.; Bazan, G. C.; Heeger, A. J., Processing Additives for Improved Efficiency from Bulk Heterojunction Solar Cells. *J. Am. Chem. Soc.* **2008,** *130* (11), 3619-3623; (b) Liao, H.-C.; Ho, C.-C.; Chang, C.-Y.; Jao, M.-H.; Darling, S. B.; Su, W.-F., Additives for morphology control in high-efficiency organic solar cells. *Mater. Today* **2013,** *16* (9), 326-336; (c) McDowell, C.; Abdelsamie, M.; Toney, M. F.; Bazan, G. C., Solvent Additives: Key Morphology-Directing Agents for Solution-Processed Organic Solar Cells. *Adv. Mater.* **2018,** *30* (33), 1707114.

3. (a) Chen, X.; Han, X.; Shen, Q.-D., PVDF-Based Ferroelectric Polymers in Modern Flexible Electronics. *Adv. Electron. Mater.* **2017,** *3* (5), 1600460; (b) Li, Q.; Wang, Q., Ferroelectric Polymers and Their Energy-Related Applications. *Macromol. Chem. Phys.* **2016,** *217* (11), 1228-1244; (c) Yuan, Y.; Xiao, Z.; Yang,

B.; Huang, J., Arising applications of ferroelectric materials in photovoltaic devices. *J. Mater. Chem. A* **2014,** *2* (17), 6027-6041.

4. (a) Han, D.; Kumari, T.; Jung, S.; An, Y.; Yang, C., A Comparative Investigation of Cyclohexyl-End-Capped Versus Hexyl-End-Capped Small-Molecule Donors on Small Donor/Polymer Acceptor Junction Solar Cells. *Sol. RRL* **2018,** *2* (5), 1800009; (b) Kumari, T.; Lee, S. M.; Lee, K. C.; Cho, Y.; Yang, C., Harmonious Compatibility Dominates Influence of Side-Chain Engineering on Morphology and Performance of Ternary Solar Cells. *Adv. Energy Mater.* **2018,** *8* (22), 1800616; (c) Kumari, T.; Moon, M.; Kang, S.-H.; Yang, C., Improved efficiency of DTGe(FBTTh2)2-based solar cells by using macromolecular additives: How macromolecular additives versus small additives influence nanoscale morphology and photovoltaic performance. *Nano Energy* **2016,** *24*, 56-62.

5. Kumari, T.; Lee, S. M.; Kang, S.-H.; Chen, S.; Yang, C., Ternary solar cells with a mixed face-on and edge-on orientation enable an unprecedented efficiency of 12.1%. *Energy Environ. Sci.* **2017,** *10* (1), 258-265.

6. (a) Kang, S.-H.; Kumari, T.; Lee, S. M.; Jeong, M.; Yang, C., Densely Packed Random Quarterpolymers Containing Two Donor and Two Acceptor Units: Controlling Absorption Ability and Molecular Interaction to Enable Enhanced Polymer Photovoltaic Devices. *Adv. Energy Mater.* **2017,** *7* (15), 1700349; (b) Kumari, T.; Lee, S. M.; Yang, C., Cubic-Like Bimolecular Crystal Evolution and over 12% Efficiency in Halogen-Free Ternary Solar Cells. *Adv. Funct. Mater.* **2018,** *28* (19), 1707278.

7. (a) Goh, C.; Kline, R. J.; McGehee, M. D.; Kadnikova, E. N.; Fréchet, J. M. J., Molecular-weight-dependent mobilities in regioregular poly(3-hexyl-thiophene) diodes. *Appl. Phys. Lett.* **2005,** *86* (12), 122110; (b) Kline, R. J.; McGehee, M. D.; Kadnikova, E. N.; Liu, J.; Fréchet, J. M. J., Controlling the Field-Effect Mobility of Regioregular Polythiophene by Changing the Molecular Weight. *Adv. Mater.* **2003,** *15* (18), 1519-1522; (c) Schilinsky, P.; Waldauf, C.; Brabec, C. J., Recombination and loss analysis in polythiophene based bulk heterojunction photodetectors. *Appl. Phys. Lett.* **2002,** *81* (20), 3885-3887; (d) Seki, K., Overall current-voltage characteristics of space charge controlled currents for thin films by a single carrier species. *J. Appl. Phys.* **2014,** *116* (6), 063716.

8. (a) Kyaw, A. K. K.; Wang, D. H.; Gupta, V.; Leong, W. L.; Ke, L.; Bazan, G. C.; Heeger, A. J., Intensity Dependence of Current–Voltage Characteristics and Recombination in High-Efficiency Solution-Processed Small-Molecule Solar Cells. *ACS Nano* **2013,** *7* (5), 4569-4577; (b) Riedel, I.; Parisi, J.; Dyakonov, V.; Lutsen, L.; Vanderzande, D.; Hummelen, J. C., Effect of Temperature and Illumination on the Electrical Characteristics of Polymer–Fullerene Bulk-Heterojunction Solar Cells. *Adv. Funct. Mater.* **2004,** *14* (1), 38-44.

Chapter 3. Morphology Control using Macromolecular Additives

Controlling the morphology of the donor:acceptor (D:A) blends to find an optimal materials combination with proper interface has proven to improve the efficiency of OSCs. Additives have been known to fine tune the morphology of active layer material. In order to address the question of how macromolecular additive processing in recent years, sparsely used, affects structural organization and photovoltaic performance, various macromolecular additives (PS, PDMS, and PMMA) vis-à-vis small DIO additive are applied to a model bulk-heterojunction (BHJ) system based on DTGe(FBTTh$_2$)$_2$. These additives have been shown to exhibit a strong influence on film morphology as a function of additives type, with significant changes in packing orientation, film roughness, and feature size observed, leading to improved power-conversion efficiency (PCE).

Chapter 3 is reproduced in part with permission of "Improved Efficiency of DTGe(FBTTh$_2$)$_2$-Based Solar Cells by Using Macromolecular Additives: How Macromolecular Additives Versus Small Additives Influence Nanoscale Morphology and Photovoltaic Performance" from Kumari T. *et al*. *Nano Energy*, **2016**, 24, 56–62.

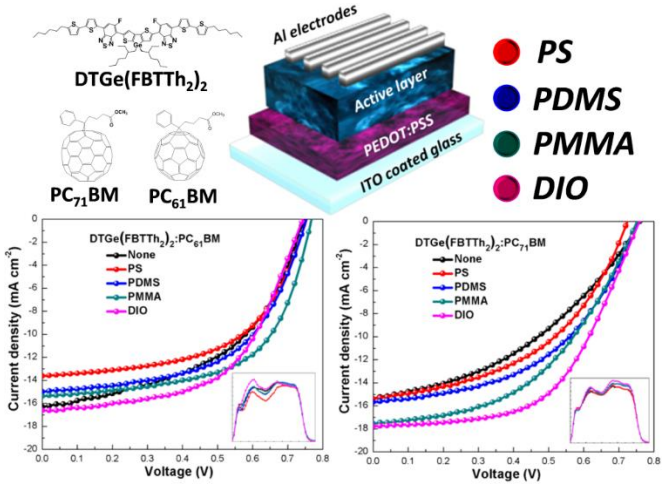

3.1 Introduction

It is the future hope that organic thin-film solar cells (OSCs) can be better than traditional inorganic photovoltaic devices in terms of material, and that there will be the possibility to develop large area, light, and flexible energy conversion sources through being simple, cost effective and environmentally friendly technologies.[1] In order to separate the strongly bound Frenkel excitons in organic thin films, the donor-acceptor (D-A) concept referred to as bulk-heterojunction (BHJ) OSCs comprised of electron-rich and electron-deficient components was proposed,[2] which has become one of the most successful device

structures developed in the field to date. Based on the short diffusion distance of excitons in organic materials, BHJ OSCs with optimized morphology can present a much larger interfacial D/A contacting area, which thus allows the collection and dissociation of a larger number of excitons and hence improved power-conversion efficiency (PCE). Therefore, the two-phase morphology of BHJ OSCs plays a critical role in influencing device performance.[1a, 1b, 3]

For a high PCE, aside from state-of-the-art π-conjugated semiconductor development, many largely empirical methods have been employed to create nanoscale bicontinuous morphology of D/A phases, including post-production annealing,[4] solvent annealing,[3e, 5] and the introduction of processing additives.[6] Among these approaches, processing additives provide the simplest and most effective means for optimizing a BHJ device's morphology and significantly enhancing PCEs.

In recent years, a variety of additives, such as 1,8-octanedithiol (OT), 1,8-diiodooctane (DIO), 1,6-diiodohexane (DIH), nitrobenzene (NB), 3-methylthiophene, 3-hexylthiophene (3HT), oleic acid (OA), N-methyl pyrrolidone (NMP), and 1-chloronaphthalene (CN), have been demonstrated to improve PCE of BHJ systems.[7] However, exactly how additives improve OSC performance is still under debate.[7a, 8] The primary requirements postulated are selective solubility towards one blend component and a low volatility. Curiously, recent studies have begun to demonstrate that the use of typical insulating polymers as macromolecular additives without fulfilling the requirements above can improve the performance of BHJ OSCs.[9] Yet, direct evidence for this is lacking and the mechanism responsible for the evolution of the morphology as well as the function of processing macromolecular additives is still not clear.

In the quest to build a comprehensive understanding of this very important topic, in the present work, the effects of adding various macromolecular additives (e.g., polystyrene (PS), polydimethylsiloxane (PDMS), and poly(methyl methacrylate) (PMMA)) have been investigated on optical properties, nanostructural order, and device performance of a model small-molecule BHJ system based on 7, 7'-(4,4-bis(2-ethylhexyl)-4H-germolo[3,2-b:4,5-b']dithiophene-2,6-diyl) bis(6-fluoro-4-(5'-hexyl-[2,2'-bithiophen]-5-yl)benzo[*c*][1,2,5]thiadiazole), DTGe(FBTTh$_2$)$_2$ (see Figure 3.1). Upon adding 1% (w/w) PMMA to the BHJ active layer, a PCE as high as 7.07% is achieved, and based on the current literature, appears to be the highest performing system available that functions best with the addition of macromolecular additives. It is also demonstrated that the PCE of BHJ OSCs from DTGe(FBTTh$_2$)$_2$:PC$_{71}$BM blends can be improved from 4.71% to 7.55% – a relative increase of 60% – after incorporating DIO. Not only do the results from this study will aid in understanding the mechanisms underlying the impact of macromolecular additive processing, but they will also be key in leading to future studies that will elucidate the driving forces behind and exact points of interaction of macromolecular additives.

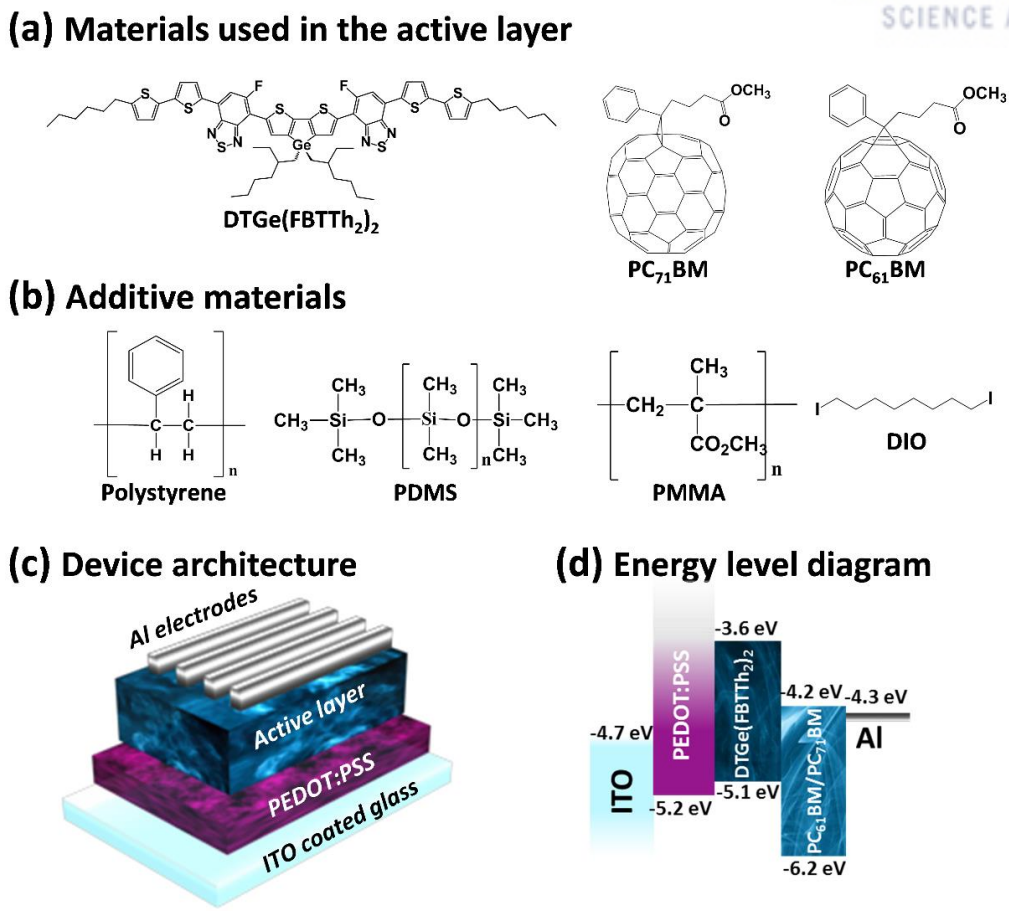

Figure 3.1. (a) Molecular structures of active layer components. (b) Various additives and (c) Device architecture used in the study. (d) Energy-level diagram of the components.

3.2 Results and Discussion

3.2.1 *Device Characteristics*

The synthesis and energy levels (HOMO and LUMO) of DTGe(FBTTh$_2$)$_2$ has been previously reported by us (see Figure 3.1 d).[10] In addition, at that time, it was verified that DIO affords the largest PCE enhancement for a DTGe(FBTTh$_2$)$_2$:PC$_{71}$BM-bsaed system (from 4.12% to 6.4%).[10] Therefore, examination took place alongside both cases via DIO and employing PC$_{61}$BM, respectively, which would facilitate not only better understanding the mechanism for improvement but also for identifying what the differences induced by small and macromolecular additives are.

First, the characteristics of the devices that were prepared by casting DTGe(FBTTh$_2$)$_2$:PC$_{61}$BM from chlorobenzene following our group previously reported optimized fabrication process (a 6:4 (w/w) D/A blend ratio and an annealing step at 80 ˚C) were examined. Single-junction BHJ OSCs performances were

evaluated with the regular structure of indium tin oxide (ITO)/poly(3,4-ethylenedioxythiophene): poly(styrenesulfonate) (PEDOT:PSS)/ DTGe(FBTTh$_2$)$_2$:PCBM derivative/Al. Device fabrication details are provided in the device fabrication section of chapter 2. We varied the concentration of macromolecular additives from 0.5 to 3% (w/w) and DIO from 0.2 to 1% (v/v). The optimized concentration was 1% (w/w) for each macromolecular additive and 0.2% (v/v) for DIO. The representative device current density/voltage (*J-V*) characteristics (simulated AM 1.5 G irradiation at 100 mW cm^{-2}) are shown in Figure 3.2 a, b and the parameters listed in Table 3.1 (see Supporting figures of section 3.5 at the end of this chapter for all testing data, Figure 3.7, 3.8 and Table 3.2, 3.3). The corresponding external quantum efficiency (EQE) curves for the best performing cells in each case are also provided (Figure 3.2 c, d), clearly showing EQE as a function of the additive types in the devices. In the case of DTGe(FBTTh$_2$)$_2$:PC$_{61}$BM without using any additives, the best PCE of 6.03% was obtained with a J_{SC} of 16.3 mA cm^{-2}, an open-circuit voltage (V_{OC}) of 0.746 V, and a fill factor (FF) of 50%.

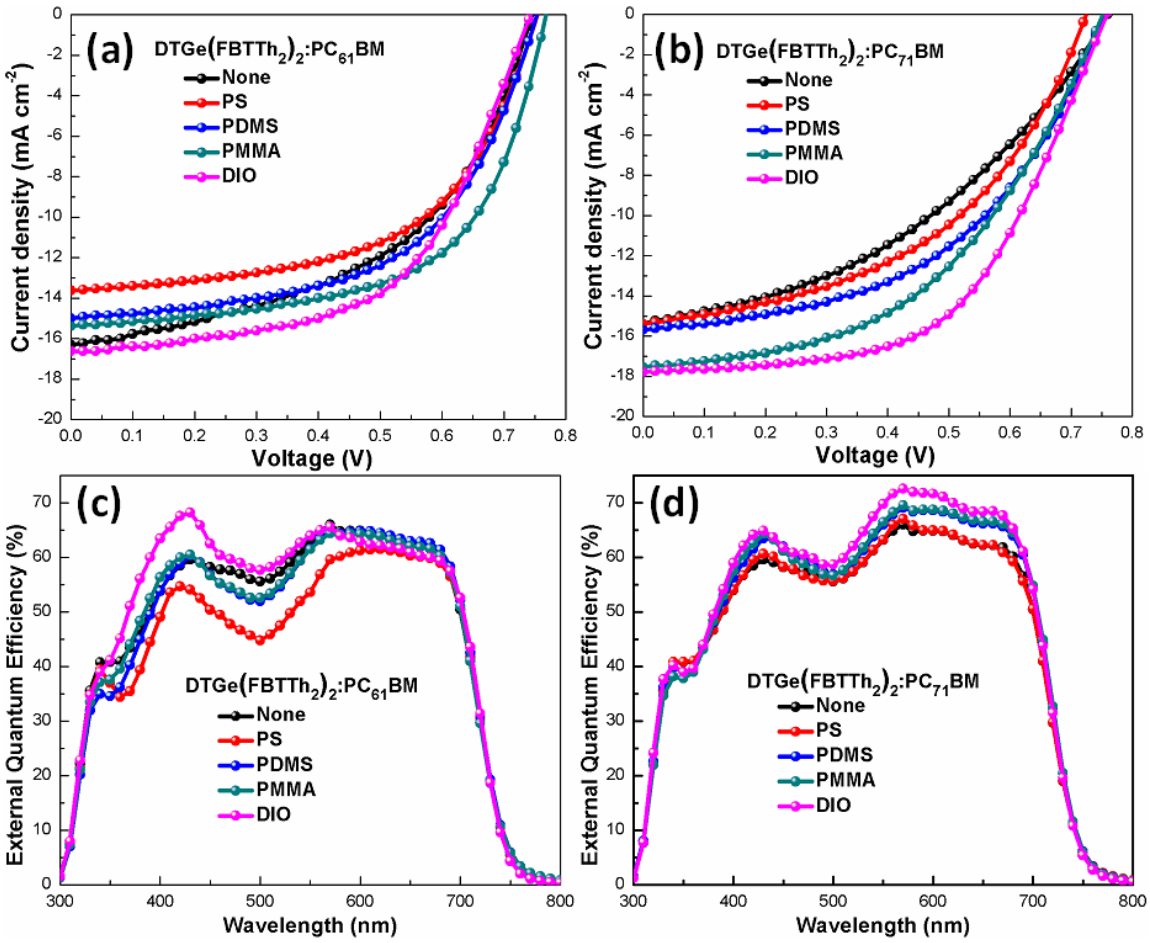

Figure 3.2. (a, b) Representative *J-V* curves under AM 1.5 G irradiation at 100 mW cm^{-2} and (c, d) corresponding EQE spectra of BHJ devices processed without and with additives.

As documented by others, the use of additives on DTGe($FBTTh_2$)$_2$:$PC_{61}BM$ films enhanced overall PCE, except with the PS additive. In particular, the PMMA additive proved the most effective in DTGe($FBTTh_2$)$_2$:$PC_{61}BM$ blends and resulted in PCE of up to 7.07%, even better than the DIO case, mainly attributed to the notably increased FF. Interestingly, this was the largest improvement and highest PCE achieved through the addition of macromolecular additives.

Given our observation of the efficient OSCs performance by adding additives, consideration was then turned to devices using $PC_{71}BM$. Although a similar trend was observed regarding PCE improvement being a function of adding all additives, the PCE values for DTGe($FBTTh_2$)$_2$:$PC_{71}BM$ films with macromolecular additives were lower than those of the corresponding devices using $PC_{61}BM$. This is in contrast to many other works where replacing $PC_{61}BM$ with $PC_{71}BM$ generally gives rise to improved performance.[11]

Table 3.1. Photovoltaic parameters of optimized OSCs without and with additives [a].

Active layer	Additive (w/v %)	J_{SC} (mA cm^{-2})	V_{OC} (V)	FF	PCE (%)
DTGe($FBTTh_2$)$_2$:$PC_{61}BM$	None	16.5 (16.3)	0.759 (0.746)	0.48 (0.50)	5.95 (6.03)
DTGe($FBTTh_2$)$_2$:$PC_{61}BM$	1% PS	15.4 (13.6)	0.736 (0.754)	0.50 (0.56)	5.62 (5.75)
DTGe($FBTTh_2$)$_2$:$PC_{61}BM$	1% PDMS	14.1 (15.0)	0.753 (0.753)	0.58 (0.56)	6.16 (6.30)
DTGe($FBTTh_2$)$_2$:$PC_{61}BM$	1% PMMA	15.0 (15.4)	0.767 (0.768)	0.59 (0.60)	6.83 (7.07)
DTGe($FBTTh_2$)$_2$:$PC_{61}BM$	0.2% DIO	17.4 (16.6)	0.737 (0.743)	0.53 (0.56)	6.80 (6.93)
DTGe($FBTTh_2$)$_2$:$PC_{71}BM$	None	15.5 (15.4)	0.741 (0.760)	0.40 (0.40)	4.60 (4.71)
DTGe($FBTTh_2$)$_2$:$PC_{71}BM$	1% PS	15.2 (15.4)	0.718 (0.724)	0.46 (0.47)	5.02 (5.25)
DTGe($FBTTh_2$)$_2$:$PC_{71}BM$	1% PDMS	16.4 (15.7)	0.747 (0.753)	0.45 (0.49)	5.63 (5.78)
DTGe($FBTTh_2$)$_2$:$PC_{71}BM$	1% PMMA	17.5 (17.5)	0.757 (0.752)	0.47 (0.48)	6.27 (6.30)
DTGe($FBTTh_2$)$_2$:$PC_{71}BM$	0.2% DIO	17.8 (17.8)	0.746 (0.759)	0.54 (0.56)	7.23 (7.55)

[a] The data shown are the average values obtained from 10 devices with standard deviation. The data in parentheses are the highest values.

Another interesting aspect of additive processing in DTGe($FBTTh_2$)$_2$:$PC_{71}BM$ is that DTGe($FBTTh_2$)$_2$:$PC_{71}BM$ devices containing 0.2% (v/v) DIO, a small amount, showed the best PCE of up

to 7.55%, which is beyond the hitherto reported highest PCE of the DTGe(FBTTh$_2$)$_2$-based OSCs even using an optical spacer.[10] Among the macromolecular additives studied, both PC$_{61}$BM- and PC$_{71}$BM-based devices processed with PMMA showed the largest extent of performance improvement, respectively.

3.2.2 Optical Properties and Film Morphologies

To shed light on the origin of the enhanced performance of the OSCs processed with additives, the change in the optical properties and microstructure of optimized BHJ blend films upon addition of the additives through a combination of absorption spectra, atomic force microscopy (AFM), grazing incidence wide-angle X-ray scattering (GIWAXS), and high resolution transmission electron microscopy (HR-TEM) was investigated.

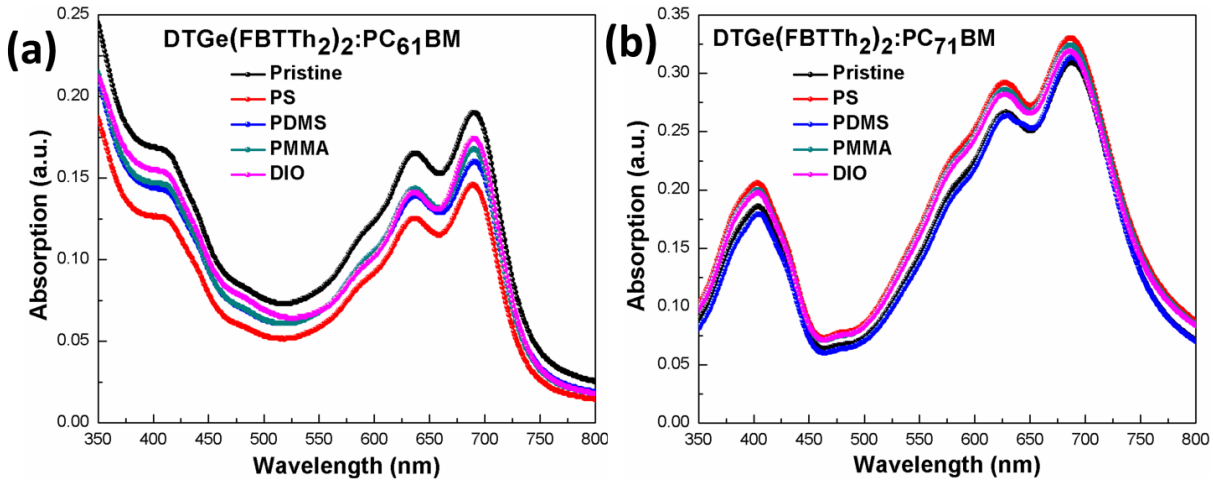

Figure 3.3. UV-Vis absorption spectra of DTGe(FBTTh$_2$)$_2$:PCBM films with and without additives.

Absorbance measurements of both DTGe(FBTTh$_2$)$_2$:PC$_{61}$BM and DTGe(FBTTh$_2$)$_2$:PC$_{71}$BM show a very broad absorbance spanning the entire visible region up to ~750 nm as shown in Figure 3.3. Despite no significant variation in position of peaks being observed, changes in absorbance intensity was seen when the films were processed with additives. This provided supporting evidence for additive-dependent morphology of D/A phases in both PC$_{61}$BM- and PC$_{71}$BM-based devices.

Figure 3.4 (a~j) shows the q_z (out-of-plane) and q_{xy} (in-plane) GIWAXS profiles for the best OSCs processed with or without additives. The corresponding line cuts and lattice parameters are presented in section 3.5 (Figure 3.9 and Table 3.4).

For both the non-additive treated DTGe(FBTTh$_2$)$_2$:PC$_{61}$BM and DTGe(FBTTh$_2$)$_2$:PC$_{71}$BM, first diffraction (001) peaks were observed in the q_z direction at d(001) = 23.99 Å and 25.73 Å respectively, while the diffraction peaks (previously indicated as (141))[12] arising from the π-π stacking along q_z were very weak

and therefore could be ignored. For the BHJ films processed with macromolecular additives, there was no significant change in packing orientations when compared with pristine films. This indicates that both films with and without macromolecular additives are similarly semi-crystalline, adopting edge-on packing relative to the substrates.

On the other hand, together with the presence of intensified peaks around 1.35 $Å^{-1}$ assigned to PCBM derivatives, both the $PC_{61}BM$- and $PC_{71}BM$-based samples with DIO not only exhibited more intense and sharper (001) peaks along q_z, but also a strong π-π stacking peak near the q_z plane was clearly observed and this suggested improved microstructural ordering with either the co-existence of face-on and edge-on orientations or the tilted orientation.

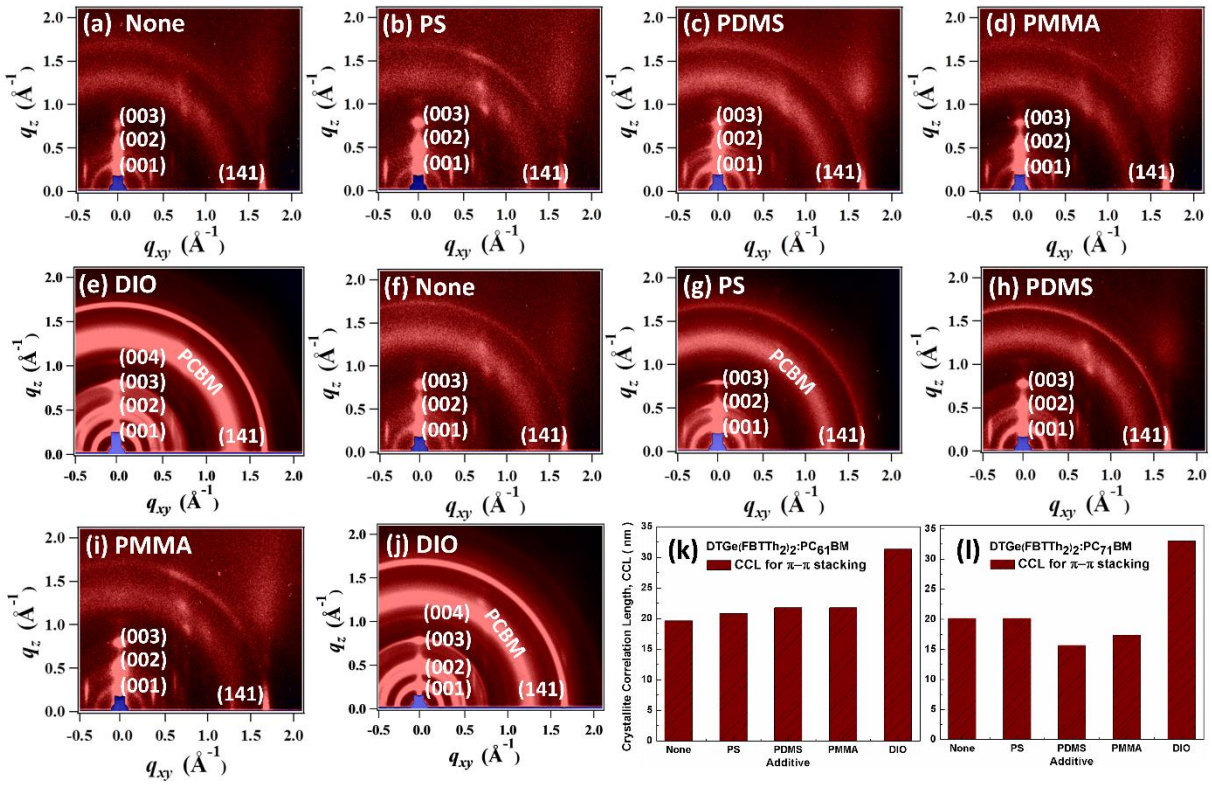

Figure 3.4. GIWAXS patterns and π-π CCLs for the best OSCs processed with or without additives. (a~e) DTGe(FBTTh$_2$)$_2$:$PC_{61}BM$ and (f~ j) DTGe(FBTTh$_2$)$_2$:$PC_{71}BM$ GIWAXS images, (k) and (l) π-π CCL values respectively.

One may conclude that the introduction of DIO enhances the crystallinity of both the edge-on and face-on DTGe(FBTTh$_2$)$_2$ lamellae, with reduced edge-on crystallites and an increased population of face-on ones. This is most likely attributed to the superior PCEs in the devices with DIO, since the face-on geometry is postulated to be the preferred orientation in BHJs because the average charge transport direction is

commensurate with device geometry.[13] It should be noted that a closer look at the line-cut profiles along q_{xy} reveals another interesting feature in the PMMA-treated DTGe(FBTTh$_2$)$_2$:PC$_{61}$BM - a splitting of the π-π stacking (141) is observed, which indicates there is a double population of π-π stacking distances. This is identification of one of the specific points of interaction between PMMA and DTGe(FBTTh$_2$)$_2$ and reasonably attributed to the high PCE obtained from DTGe(FBTTh$_2$)$_2$:PC$_{61}$BM devices with PMMA.

We also calculated crystallite correlation length (CCL) of π-π stacking lattice planes along q_{xy} by using Debye Scherrer's equation,[14] where Gaussian fitting is used to obtain full widths at half-maximum (FWHM) values (Figure 3.4 k, l). All DTGe(FBTTh$_2$)$_2$:PC$_{61}$BM films with macromolecular additives had nearly similar CCL values in the range of 20±4 nm, while a larger CCL (32±1nm) was observed when using the DIO additive. Note that the calculated CCL for PMMA-treated DTGe(FBTTh$_2$)$_2$:PC$_{61}$BM would be somewhat smaller than the real value because of the existence of π-π stacking peak splitting, as mentioned earlier. In the cases of DTGe(FBTTh$_2$)$_2$:PC$_{71}$BM, similar variation trends were found. These results confirm that BHJ films processed with DIO as a small additive versus macromolecular additives have larger π-π CCL values, likely because of increased π-π interactions dominating film formation. This would therefore allow DTGe(FBTTh$_2$)$_2$ molecules to pack with a longer-range order and is in solid agreement with what is observed in the GIWAXS profiles of DIO treated films.[15]

This matched well with the present study's AFM observations (Figure 3.5); the root mean square (RMS) roughness (R_q) values do not vary significantly by using different macromolecular additives, while DIO results in larger surface roughness compared to the corresponding non-additive treated films. As a point of interest, in a close up of the phase images (section 3.5, Figure 3.10), the films proceeded with macromolecular additives, especially those containing PDMS, and have a pronounced nano-fibril formation relative to the DIO systems. Such nano-fibrillar features have been previously reported for other small molecule-based BHJ systems processed with PDMS.[9b]

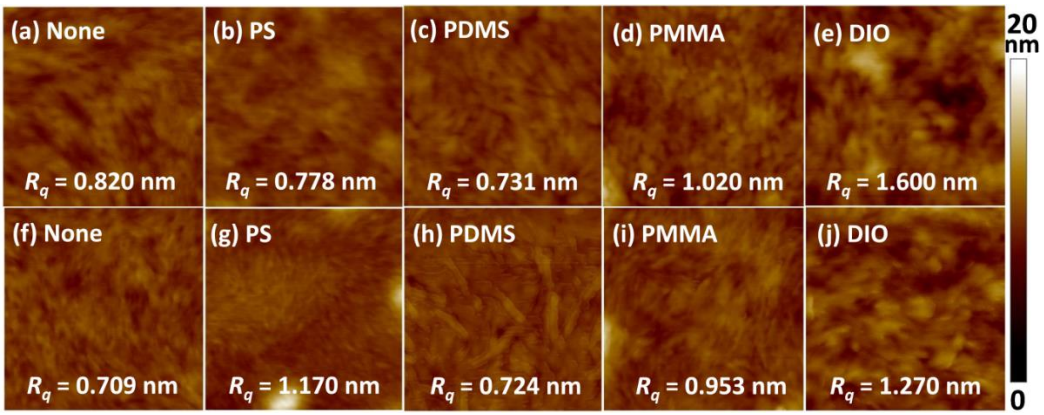

Figure 3.5. Morphology analysis of the best OSCs processed with or without additives by AFM (1×1 μm). (Top: a~e) DTGe(FBTTh$_2$)$_2$:PC$_{61}$BM and (Bottom: f~j) DTGe(FBTTh$_2$)$_2$:PC$_{71}$BM.

Next, HR-TEM was measured to monitor the morphological features of the blend films more directly. Consistent with the AFM morphology, in HR-TEM images (Figure 3.6), the pristine films without additives do not show obvious contrast that would emanate from largely homogenous morphology, while in the additive-treated samples, wire-like structures with nanoscale phase separation are evident from the contrast deviation.

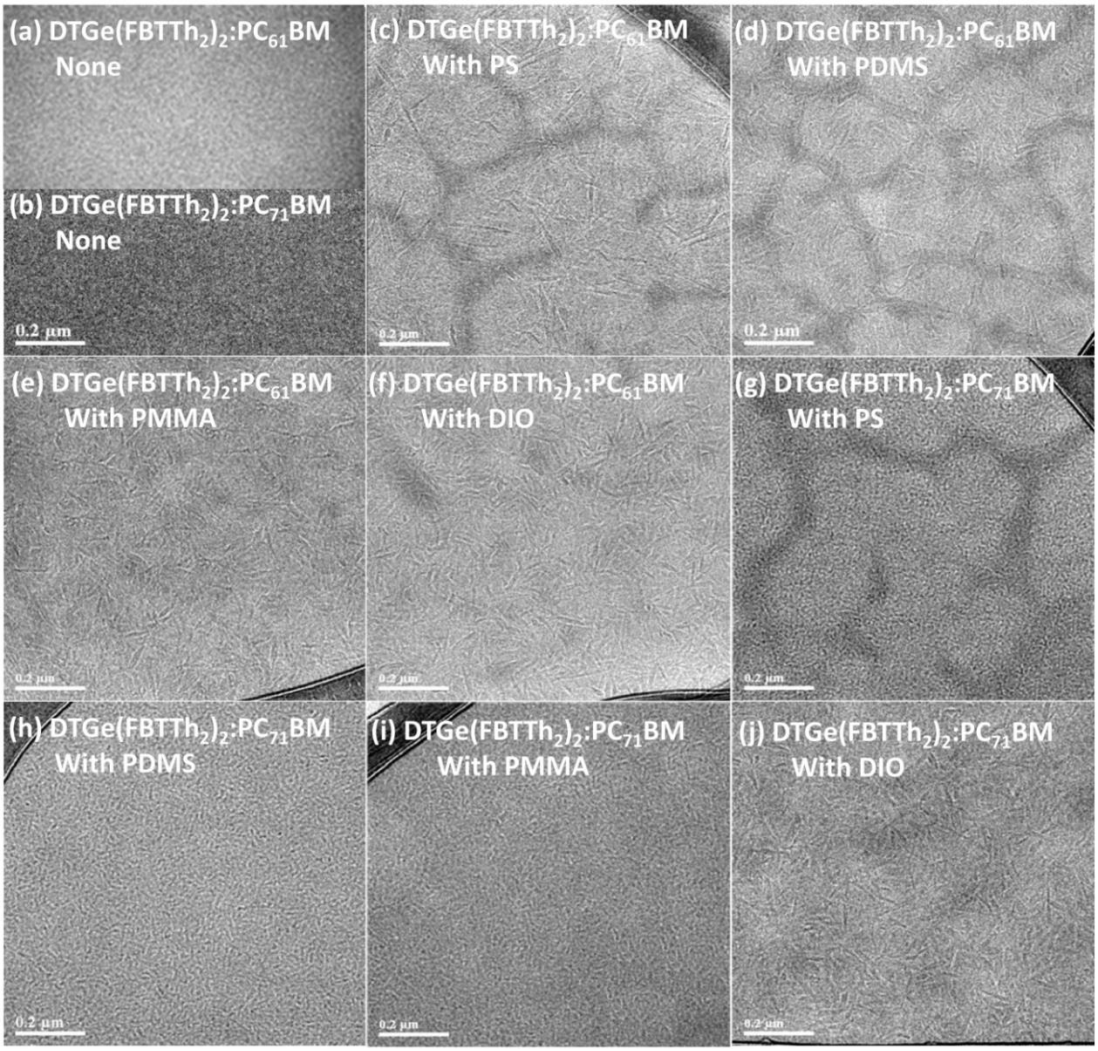

Figure 3.6. Morphology analysis of the best OSCs processed with or without additives by HR-TEM (Scale bar is 0.2 μm). (Top: a,c~f) DTGe(FBTTh$_2$)$_2$:PC$_{61}$BM and (Bottom: b,g~j) DTGe(FBTTh$_2$)$_2$:PC$_{71}$BM.

Compared with the TEM images of films with macromolecular additives, the wire-like structures are more vivid with DIO. These results correlate well with the morphology trends induced by macromolecular additives versus DIO observed with AFM and GIWAXS. Note that there is subtle difference in a closer

look of the TEM images between $PC_{61}BM$- and $PC_{71}BM$-based blend films proceeded with macromolecular additives, while both $PC_{61}BM$- and $PC_{71}BM$-based films with DIO have similar features. In addition, the observed better crystallinity of DTGe(FBTTh$_2$)$_2$:$PC_{61}BM$ films compared to the corresponding $PC_{71}BM$-based analogues is one important reason that can contribute to the enhanced FF values, though this cannot be solely the result of the changes seen in BHJ OSCs. It is worth highlighting that similar crystalline domain sizes (length = 30±10 nm, width = 10±3 nm) are observed in films with PMMA (Figure 3.6 e) or DIO (Figure 3.6 f,j), being beneficial for exciton separation and charge transport.[16] This is likely the cause of the higher PCEs in the PMMA- and DIO-treated devices.

Even though all results described here are associated with molecular packing/crystallinity and cannot provide solid microscopic clues towards understanding the largely improved PCEs by adding PMMA, it is still believed that favorable morphology, as in the DIO case, comes about with assistance from the addition of the optimized content of PMMA, and therefore, the OSCs with either PMMA or DIO outperform those of other additives. Another possible reason is that friendly active materials-PMMA interactions may lead to a beneficial effect on several key device metrics.

3.3 Conclusion

In summary, the work presented here has systematically examined the effect of macromolecular additives (PS, PDMS, and PMMA) versus the most widely-used small DIO additive on the morphology and photovoltaic property of a model BHJ system based on DTGe(FBTTh$_2$)$_2$. Based on optimizing the amount of additives included, PCEs can improve as a result of fine-tuning the blended film nanoscale morphology. Of particular significance is that the introduction of PMMA in DTGe(FBTTh$_2$)$_2$:$PC_{61}BM$ blends can bring over 17% improvement in PCE (from 6.03% to 7.07%), even greater performance than in the case of DIO. Furthermore, it was possible to attain PCEs of up to 7.55% in DIO-treated DTGe(FBTTh$_2$)$_2$:$PC_{71}BM$ films, far beyond the current known levels for DTGe(FBTTh$_2$)$_2$-based OSCs. With a combination of device characterization and morphological studies, and despite the obvious differences in morphology as a function of macromolecular additives versus DIO, PMMA has been demonstrated to be well-suited for BHJ OSCs as a new macromolecular additive and gives rise to the enhanced PCEs. Ultimately, PMMA utility may be applicable to other systems, and new materials with even higher performance might be discovered in the near future.

3.4 References

1. (a) Günes, S.; Neugebauer, H.; Sariciftci, N. S., Conjugated Polymer-Based Organic Solar Cells. *Chem. Rev.* **2007,** *107* (4), 1324-1338; (b) Thompson, B. C.; Fréchet, J. M. J., Polymer–Fullerene Composite Solar Cells. *Angew. Chem. Int. Ed.* **2008,** *47* (1), 58-77; (c) Dennler, G.; Scharber, M. C.; Brabec, C. J., Polymer-Fullerene Bulk-Heterojunction Solar Cells. *Adv. Mater.* **2009,** *21* (13), 1323-1338; (d) Kim, Y.; Yeom, H. R.; Kim, J. Y.; Yang, C., High-efficiency polymer solar cells with a cost-effective quinoxaline polymer through nanoscale morphology control induced by practical processing additives. *Energy Environ. Sci.* **2013,** *6* (6), 1909-1916; (e) Mishra, A.; Bäuerle, P., Small Molecule Organic Semiconductors on the Move: Promises for Future Solar Energy Technology. *Angew. Chem. Int. Ed.* **2012,** *51* (9), 2020-2067; (f) Dou, L.; Gao, J.; Richard, E.; You, J.; Chen, C.-C.; Cha, K. C.; He, Y.; Li, G.; Yang, Y., Systematic Investigation of Benzodithiophene- and Diketopyrrolopyrrole-Based Low-Bandgap Polymers Designed for Single Junction and Tandem Polymer Solar Cells. *J. Am. Chem. Soc.* **2012,** *134* (24), 10071-10079; (g) Cabanetos, C.; El Labban, A.; Bartelt, J. A.; Douglas, J. D.; Mateker, W. R.; Fréchet, J. M. J.; McGehee, M. D.; Beaujuge, P. M., Linear Side Chains in Benzo[1,2-b:4,5-b′]dithiophene–Thieno[3,4-c]pyrrole-4,6-dione Polymers Direct Self-Assembly and Solar Cell Performance. *J. Am. Chem. Soc.* **2013,** *135* (12), 4656-4659.

2. Tang, C. W., Two-layer organic photovoltaic cell. *Appl. Phys. Lett.* **1986,** *48* (2), 183-185.

3. (a) Peet, J.; Kim, J. Y.; Coates, N. E.; Ma, W. L.; Moses, D.; Heeger, A. J.; Bazan, G. C., Efficiency enhancement in low-bandgap polymer solar cells by processing with alkane dithiols. *Nat. Mater.* **2007,** *6* (7), 497-500; (b) Bijleveld, J. C.; Zoombelt, A. P.; Mathijssen, S. G. J.; Wienk, M. M.; Turbiez, M.; de Leeuw, D. M.; Janssen, R. A. J., Poly(diketopyrrolopyrrole−terthiophene) for Ambipolar Logic and Photovoltaics. *J. Am. Chem. Soc.* **2009,** *131* (46), 16616-16617; (c) Boudreault, P.-L. T.; Najari, A.; Leclerc, M., Processable Low-Bandgap Polymers for Photovoltaic Applications. *Chem. Mater.* **2011,** *23* (3), 456-469; (d) Lim, K.-G.; Park, J.-M.; Mangold, H.; Laquai, F.; Choi, T.-L.; Lee, T.-W., Bimolecular Crystals with an Intercalated Structure Improve Poly(p-phenylenevinylene)-Based Organic Photovoltaic Cells. *ChemSusChem* **2015,** *8* (2), 337-344; (e) Jo, J.; Na, S.-I.; Kim, S.-S.; Lee, T.-W.; Chung, Y.; Kang, S.-J.; Vak, D.; Kim, D.-Y., Three-Dimensional Bulk Heterojunction Morphology for Achieving High Internal Quantum Efficiency in Polymer Solar Cells. *Adv. Funct. Mater.* **2009,** *19* (15), 2398-2406.

4. (a) Wang, T.; Pearson, A. J.; Lidzey, D. G.; Jones, R. A. L., Evolution of Structure, Optoelectronic Properties, and Device Performance of Polythiophene:Fullerene Solar Cells During Thermal Annealing. *Adv. Funct. Mater.* **2011,** *21* (8), 1383-1390; (b) Loser, S.; Bruns, C. J.; Miyauchi, H.; Ortiz, R. P.; Facchetti, A.; Stupp, S. I.; Marks, T. J., A Naphthodithiophene-Diketopyrrolopyrrole Donor Molecule for Efficient Solution-Processed Solar Cells. *J. Am. Chem. Soc.* **2011,** *133* (21), 8142-8145.

5. Li, G.; Yao, Y.; Yang, H.; Shrotriya, V.; Yang, G.; Yang, Y., "Solvent Annealing" Effect in Polymer Solar Cells Based on Poly(3-hexylthiophene) and Methanofullerenes. *Adv. Funct. Mater.* **2007,** *17* (10), 1636-1644.

6. Hoven, C. V.; Dang, X.-D.; Coffin, R. C.; Peet, J.; Nguyen, T.-Q.; Bazan, G. C., Improved Performance of Polymer Bulk Heterojunction Solar Cells Through the Reduction of Phase Separation via Solvent Additives. *Adv. Mater.* **2010,** *22* (8), E63-E66.

7. (a) Rogers, J. T.; Schmidt, K.; Toney, M. F.; Kramer, E. J.; Bazan, G. C., Structural Order in Bulk Heterojunction Films Prepared with Solvent Additives. *Adv. Mater.* **2011,** *23* (20), 2284-2288; (b) Yao, Y.; Hou, J.; Xu, Z.; Li, G.; Yang, Y., Effects of Solvent Mixtures on the Nanoscale Phase Separation in Polymer Solar Cells. *Adv. Funct. Mater.* **2008,** *18* (12), 1783-1789; (c) Su, M.-S.; Kuo, C.-Y.; Yuan, M.-C.; Jeng, U. S.; Su, C.-J.; Wei, K.-H., Improving Device Efficiency of Polymer/Fullerene Bulk Heterojunction Solar Cells Through Enhanced Crystallinity and Reduced Grain Boundaries Induced by Solvent Additives. *Adv. Mater.* **2011,** *23* (29), 3315-3319; (d) Moulé, A. J.; Meerholz, K., Controlling Morphology in Polymer–Fullerene Mixtures. *Adv. Mater.* **2008,** *20* (2), 240-245; (e) Chang, Y.-M.; Wang, L., Efficient Poly(3-hexylthiophene)-Based Bulk Heterojunction Solar Cells Fabricated by an Annealing-Free Approach. *J. Phys. Chem. C* **2008,** *112* (45), 17716-17720; (f) Sun, Y.; Cui, C.; Wang, H.; Li, Y., Efficiency Enhancement of Polymer Solar Cells Based on Poly(3-hexylthiophene)/Indene-C70 Bisadduct via Methylthiophene Additive. *Adv. Energy Mater.* **2011,** *1* (6), 1058-1061; (g) Woo, C. H.; Beaujuge, P. M.; Holcombe, T. W.; Lee, O. P.; Fréchet, J. M. J., Incorporation of Furan into Low Band-Gap Polymers for Efficient Solar Cells. *J. Am. Chem. Soc.* **2010,** *132* (44), 15547-15549.

8. Peet, J.; Cho, N. S.; Lee, S. K.; Bazan, G. C., Transition from Solution to the Solid State in Polymer Solar Cells Cast from Mixed Solvents. *Macromolecules* **2008,** *41* (22), 8655-8659.

9. (a) Huang, Y.; Wen, W.; Mukherjee, S.; Ade, H.; Kramer, E. J.; Bazan, G. C., High-Molecular-Weight Insulating Polymers Can Improve the Performance of Molecular Solar Cells. *Adv. Mater.* **2014,** *26* (24), 4168-4172; (b) Graham, K. R.; Mei, J.; Stalder, R.; Shim, J. W.; Cheun, H.; Steffy, F.; So, F.; Kippelen, B.; Reynolds, J. R., Polydimethylsiloxane as a Macromolecular Additive for Enhanced Performance of Molecular Bulk Heterojunction Organic Solar Cells. *ACS Appl. Mater. Interfaces* **2011,** *3* (4), 1210-1215.

10. Moon, M.; Walker, B.; Lee, J.; Park, S. Y.; Ahn, H.; Kim, T.; Lee, T. H.; Heo, J.; Seo, J. H.; Shin, T. J.; Kim, J. Y.; Yang, C., Dithienogermole-Containing Small-Molecule Solar Cells with 7.3% Efficiency: In-Depth Study on the Effects of Heteroatom Substitution of Si with Ge. *Adv. Energy Mater.* **2015,** *5* (9), doi: 10.1002/aenm.201402044.

11. (a) Zhang, F.; Zhuo, Z.; Zhang, J.; Wang, X.; Xu, X.; Wang, Z.; Xin, Y.; Wang, J.; Wang, J.; Tang, W.; Xu, Z.; Wang, Y., Influence of PC60BM or PC70BM as electron acceptor on the performance of polymer solar cells. *Sol. Energ. Mat. Sol. Cells* **2012,** *97* (0), 71-77; (b) He, Y.; Li, Y., Fullerene derivative acceptors

for high performance polymer solar cells. *Phys. Chem. Chem. Phys.* **2011,** *13* (6), 1970-1983; (c) Huang, Y.-C.; Tsao, C.-S.; Chuang, C.-M.; Lee, C.-H.; Hsu, F.-H.; Cha, H.-C.; Chen, C.-Y.; Lin, T.-H.; Su, C.-J.; Jeng, U. S.; Su, W.-F., Small- and Wide-Angle X-ray Scattering Characterization of Bulk Heterojunction Polymer Solar Cells with Different Fullerene Derivatives. *J. Phys. Chem. C* **2012,** *116* (18), 10238-10244.

12. Love, J. A.; Proctor, C. M.; Liu, J.; Takacs, C. J.; Sharenko, A.; van der Poll, T. S.; Heeger, A. J.; Bazan, G. C.; Nguyen, T.-Q., Film Morphology of High Efficiency Solution-Processed Small-Molecule Solar Cells. *Adv. Funct. Mater.* **2013,** *23* (40), 5019-5026.

13. (a) Hammond, M. R.; Kline, R. J.; Herzing, A. A.; Richter, L. J.; Germack, D. S.; Ro, H.-W.; Soles, C. L.; Fischer, D. A.; Xu, T.; Yu, L.; Toney, M. F.; DeLongchamp, D. M., Molecular Order in High-Efficiency Polymer/Fullerene Bulk Heterojunction Solar Cells. *ACS Nano* **2011,** *5* (10), 8248-8257; (b) Gomez, E. D.; Barteau, K. P.; Wang, H.; Toney, M. F.; Loo, Y.-L., Correlating the scattered intensities of P3HT and PCBM to the current densities of polymer solar cells. *Chem. Commun.* **2011,** *47* (1), 436-438.

14. Langford, J. I.; Wilson, A. J. C., Scherrer after sixty years: A survey and some new results in the determination of crystallite size. *J. Appl. Cryst.* **1978,** *11* (2), 102-113.

15. (a) Perez, L. A.; Rogers, J. T.; Brady, M. A.; Sun, Y.; Welch, G. C.; Schmidt, K.; Toney, M. F.; Jinnai, H.; Heeger, A. J.; Chabinyc, M. L.; Bazan, G. C.; Kramer, E. J., The Role of Solvent Additive Processing in High Performance Small Molecule Solar Cells. *Chem. Mater.* **2014,** *26* (22), 6531-6541; (b) Chen, M. S.; Niskala, J. R.; Unruh, D. A.; Chu, C. K.; Lee, O. P.; Fréchet, J. M. J., Control of Polymer-Packing Orientation in Thin Films through Synthetic Tailoring of Backbone Coplanarity. *Chem. Mater.* **2013,** *25* (20), 4088-4096.

16. (a) Wang, C.; Yu, S.; Chen, W.; Sun, C., Highly Efficient Light-Trapping Structure Design Inspired By Natural Evolution. *Sci. Rep.* **2013,** *3*, doi: 10.1038/srep01025; (b) Lin, J. D. A.; Mikhnenko, O. V.; Chen, J.; Masri, Z.; Ruseckas, A.; Mikhailovsky, A.; Raab, R. P.; Liu, J.; Blom, P. W. M.; Loi, M. A.; Garcia-Cervera, C. J.; Samuel, I. D. W.; Nguyen, T.-Q., Systematic study of exciton diffusion length in organic semiconductors by six experimental methods. *Mater. Horiz.* **2014,** *1* (2), 280-285; (c) Mikhnenko, O. V.; Azimi, H.; Scharber, M.; Morana, M.; Blom, P. W. M.; Loi, M. A., Exciton diffusion length in narrow bandgap polymers. *Energy Environ. Sci.* **2012,** *5* (5), 6960-6965; (d) Peumans, P.; Yakimov, A.; Forrest, S. R., Small molecular weight organic thin-film photodetectors and solar cells. *J. Appl. Phys.* **2003,** *93* (7), 3693-3723; (e) Lunt, R. R.; Giebink, N. C.; Belak, A. A.; Benziger, J. B.; Forrest, S. R., Exciton diffusion lengths of organic semiconductor thin films measured by spectrally resolved photoluminescence quenching. *J. Appl. Phys.* **2009,** *105* (5), 053711.

3.5 Supporting Figures

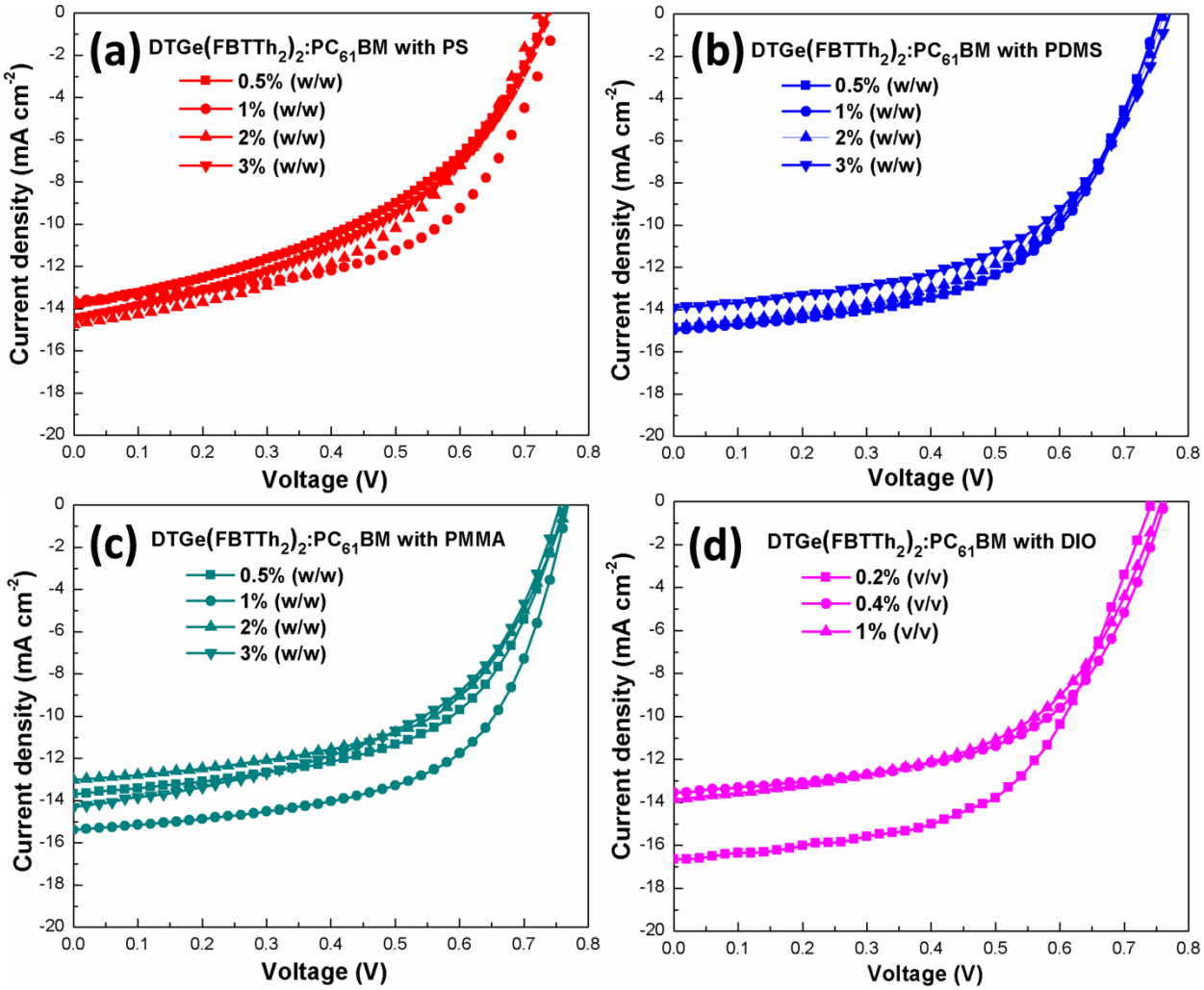

Figure 3.7. *J-V* characterization plots for DTGe(FBTTh$_2$)$_2$:PC$_{61}$BM films with different concentration of each additive. (a) PS, (b) PDMS, (c) PMMA, and (d) DIO as additives under 100 mW cm^{-2} simulated solar radiation.

Table 3.2. Photovoltaic parameters of OSCs with and without additives at different concentration.

Active layer	Additive (w/v %)	J_{SC} (mA cm^{-2})	V_{OC} (V)	*FF*	PCE (%)
DTGe(FBTTh$_2$)$_2$:PC$_{61}$BM	0.5% PS	13.8	0.763	0.44	4.51
DTGe(FBTTh$_2$)$_2$:PC$_{61}$BM	1% PS	13.6	0.754	0.56	5.75
DTGe(FBTTh$_2$)$_2$:PC$_{61}$BM	2% PS	14.5	0.722	0.48	5.10
DTGe(FBTTh$_2$)$_2$:PC$_{61}$BM	3% PS	13.0	0.738	0.44	4.73
DTGe(FBTTh$_2$)$_2$:PC$_{61}$BM	0.5% PDMS	14.8	0.760	0.55	6.26
DTGe(FBTTh$_2$)$_2$:PC$_{61}$BM	1% PDMS	15.0	0.753	0.56	6.30
DTGe(FBTTh$_2$)$_2$:PC$_{61}$BM	2% PDMS	14.8	0.763	0.53	6.03
DTGe(FBTTh$_2$)$_2$:PC$_{61}$BM	3% PDMS	13.9	0.771	0.53	5.74
DTGe(FBTTh$_2$)$_2$:PC$_{61}$BM	0.5% PMMA	13.7	0.764	0.57	5.91
DTGe(FBTTh$_2$)$_2$:PC$_{61}$BM	1% PMMA	15.4	0.768	0.60	7.07
DTGe(FBTTh$_2$)$_2$:PC$_{61}$BM	2% PMMA	13.0	0.768	0.56	5.60
DTGe(FBTTh$_2$)$_2$:PC$_{61}$BM	3% PMMA	14.3	0.757	0.50	5.45
DTGe(FBTTh$_2$)$_2$:PC$_{61}$BM	0.2% DIO	16.6	0.743	0.56	6.93
DTGe(FBTTh$_2$)$_2$:PC$_{61}$BM	0.4% DIO	13.5	0.763	0.57	5.87
DTGe(FBTTh$_2$)$_2$:PC$_{61}$BM	1% DIO	13.8	0.757	0.54	5.64

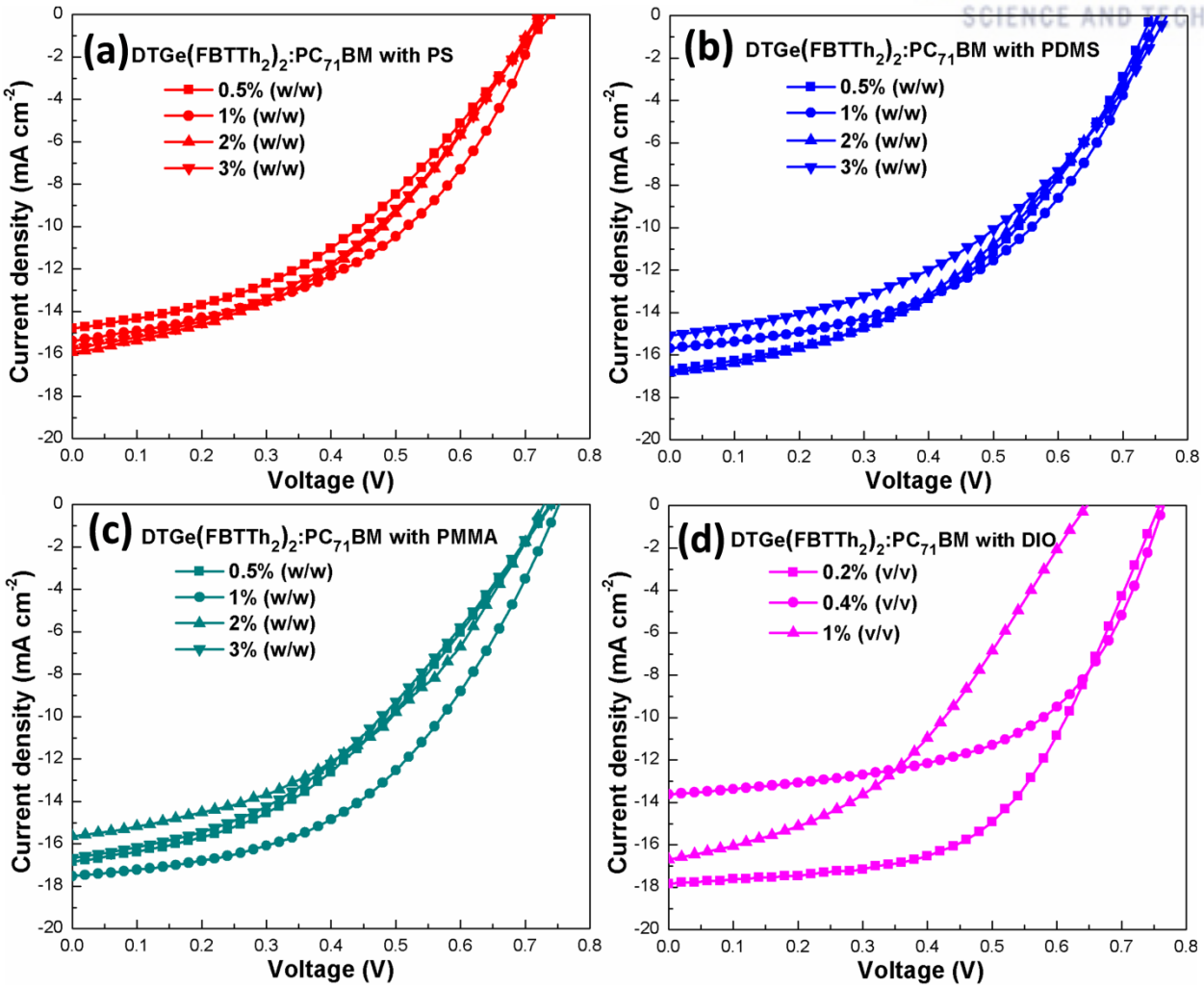

Figure 3.8. *J-V* characterization plots for DTGe(FBTTh$_2$)$_2$:PC$_{71}$BM films with different concentration of each additive. (a) PS, (b) PDMS, (c) PMMA, and (d) DIO as additives under 100 mW cm^{-2} simulated solar radiation.

Table 3.3. Photovoltaic parameters of OSCs with and without additives at different concentration.

Active layer	Additive (w/v %)	J_{SC} (mA cm^{-2})	V_{OC} (V)	*FF*	PCE (%)
DTGe(FBTTh$_2$)$_2$:PC$_{71}$BM	0.5% PS	14.8	0.741	0.41	4.46
DTGe(FBTTh$_2$)$_2$:PC$_{71}$BM	1% PS	15.4	0.724	0.47	5.25
DTGe(FBTTh$_2$)$_2$:PC$_{71}$BM	2% PS	15.9	0.721	0.42	4.85
DTGe(FBTTh$_2$)$_2$:PC$_{71}$BM	3% PS	15.8	0.724	0.42	4.77
DTGe(FBTTh$_2$)$_2$:PC$_{71}$BM	0.5% PDMS	16.8	0.745	0.45	5.60
DTGe(FBTTh$_2$)$_2$:PC$_{71}$BM	1% PDMS	15.7	0.753	0.49	5.78
DTGe(FBTTh$_2$)$_2$:PC$_{71}$BM	2% PDMS	16.9	0.756	0.43	5.45
DTGe(FBTTh$_2$)$_2$:PC$_{71}$BM	3% PDMS	15.1	0.768	0.44	5.05
DTGe(FBTTh$_2$)$_2$:PC$_{71}$BM	0.5% PMMA	16.8	0.740	0.41	5.08
DTGe(FBTTh$_2$)$_2$:PC$_{71}$BM	1% PMMA	17.5	0.752	0.48	6.30
DTGe(FBTTh$_2$)$_2$:PC$_{71}$BM	2% PMMA	15.6	0.729	0.44	5.04
DTGe(FBTTh$_2$)$_2$:PC$_{71}$BM	3% PMMA	16.7	0.739	0.40	4.92
DTGe(FBTTh$_2$)$_2$:PC$_{71}$BM	0.2% DIO	17.8	0.759	0.56	7.55
DTGe(FBTTh$_2$)$_2$:PC$_{71}$BM	0.4% DIO	13.6	0.765	0.56	5.82
DTGe(FBTTh$_2$)$_2$:PC$_{71}$BM	1% DIO	16.7	0.647	0.41	4.42

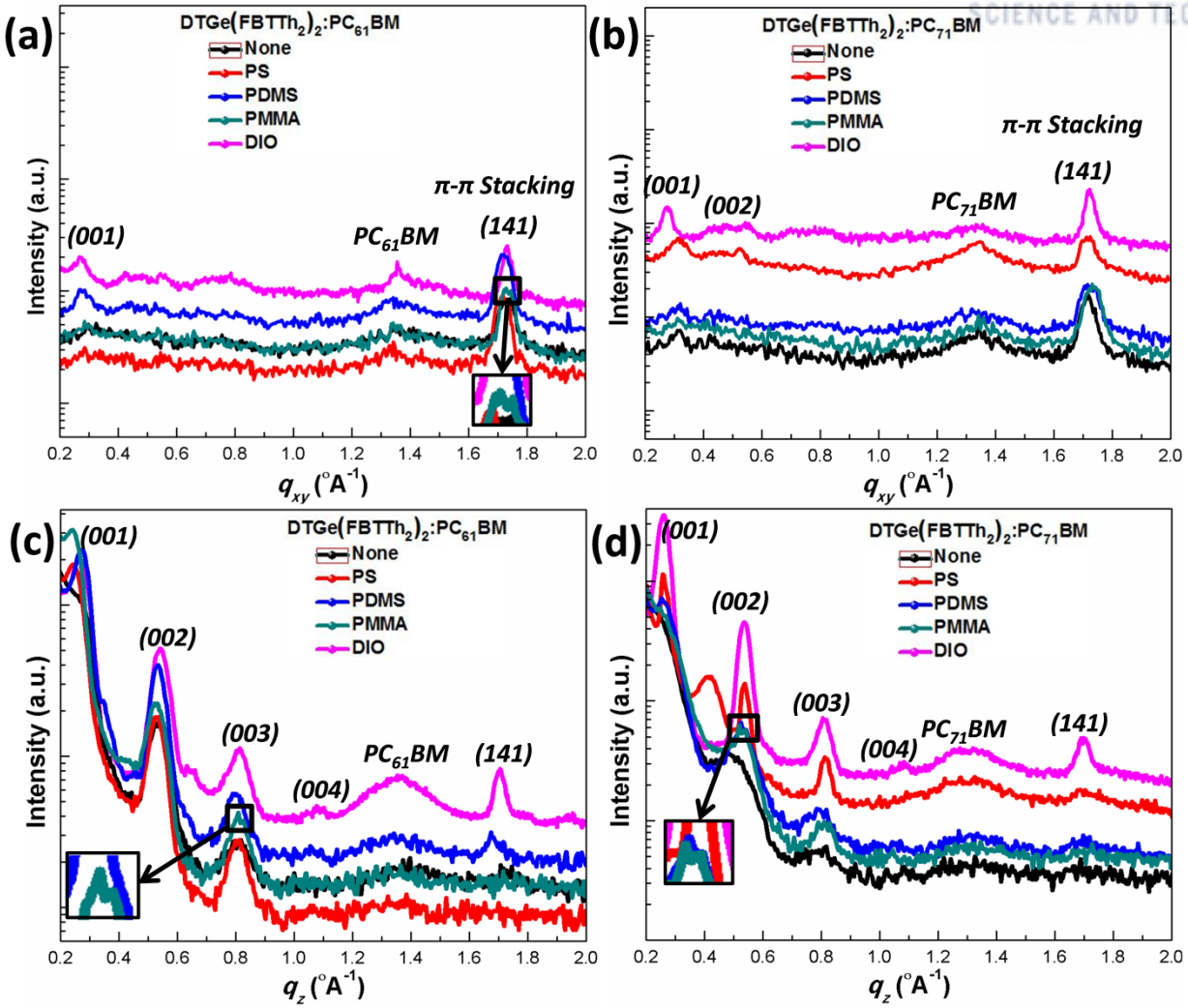

Figure 3.9. Line cuts obtained from GIWAXS data; (a), (b) in plane and (c), (d) out of plane profiles for DTGe(FBTTh$_2$)$_2$:PC$_{61}$BM and DTGe(FBTTh$_2$)$_2$:PC$_{71}$BM films without and with additives, respectively. Insets: zoom in views for peak splitting in case of PMMA additive.

Table 3.4. Lattice parameters for both DTGe(FBTTh$_2$)$_2$:PC$_{61}$BM and DTGe(FBTTh$_2$)$_2$:PC$_{71}$BM- based BHJ systems.

Active layer	Additive (w/v %)	Unit cell long axis (001) (Å^{-1})	d_{001} (Å)	π-π stacking cell axis (141) (Å^{-1})	d_{141} (Å)
DTGe(FBTTh$_2$)$_2$:PC$_{61}$BM	None	0.2618	23.99	1.732	3.627
DTGe(FBTTh$_2$)$_2$:PC$_{61}$BM	1% PS	0.2393	26.26	1.717	3.660
DTGe(FBTTh$_2$)$_2$:PC$_{61}$BM	1% PDMS	0.2770	22.68	1.720	3.652
DTGe(FBTTh$_2$)$_2$:PC$_{61}$BM	1% PMMA	0.2428	25.88	1.734	3.624
DTGe(FBTTh$_2$)$_2$:PC$_{61}$BM	0.2% DIO	0.2632	23.87	1.732	3.628
DTGe(FBTTh$_2$)$_2$:PC$_{71}$BM	None	0.2442	25.73	1.717	3.659
DTGe(FBTTh$_2$)$_2$:PC$_{71}$BM	1% PS	0.2606	24.11	1.717	3.659
DTGe(FBTTh$_2$)$_2$:PC$_{71}$BM	1% PDMS	0.2534	24.80	1.722	3.649
DTGe(FBTTh$_2$)$_2$:PC$_{71}$BM	1% PMMA	0.2463	25.51	1.733	3.625
DTGe(FBTTh$_2$)$_2$:PC$_{71}$BM	0.2% DIO	0.2589	24.27	1.723	3.646

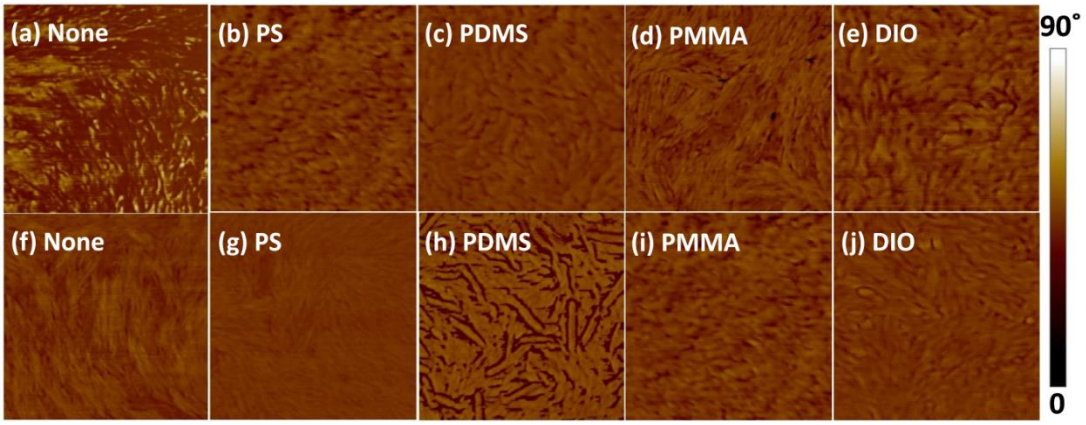

Figure 3.10. Morphology analysis of the best OSCs processed with or without additives by AFM phase images (1×1 μm). (Top: a~e) DTGe(FBTTh$_2$)$_2$:PC$_{61}$BM and (Bottom: f~j) DTGe(FBTTh$_2$)$_2$:PC$_{71}$BM.

Chapter 4. Ternary Solar Cells an approach to achieve Unprecedented Efficiency

Ternary blend organic solar cells (OSCs) comprising multiple donor or acceptor materials in an active layer have been emerged as promising alternatives to enhance photovoltaic parameters for spectrally broad light harvesting while retaining the simplicity of a single step for processing the active layer as compared with traditional binary or tandem OSCs. Recent ternary structures of conjugated polymers have achieved around 10% power conversion efficiencies (PCEs), showing the great potential of ternary systems. Herein, we report ternary OSCs fabricated by incorporating DR3TSBDT as an additional donor into PTB7-Th:$PC_{71}BM$ host matrix at different weight ratios, exhibiting the record-PCE of >12.0% in the highly optimized conditions. Through a series of characterizations, we identified that our ternary OSCs have the mixed face-on and edge-on orientations, reaching much improved PCEs unlike common high-performing OSCs that preferentially favor face-on orientated host systems. Additionally, the high PCE in this ternary structure results from not only broadening the photon absorption range, but also facilitating charge transporting characteristics with reduced recombination through a combination of cascade energy levels in the optimized condition. Secondly, detailed investigation of the effect of side-chain engineering of the third component on the blend morphology and performance of ternary organic solar cells (OSCs) has also been investigated. In this study, we measured the performance of ternary OSCs in a given PTB7-Th:$PC_{71}BM$ host set by introducing various small molecule donors (SMDs) with different terminal side-chain lengths. As expected, the performance of binary OSCs with SMDs depended greatly on the side-chain length. In contrast, we observed that all SMD-based ternary OSCs exhibited almost identical and high power-conversion efficiencies of 12.0%–12.2%. This minor performance variation was attributed to good molecular compatibility between the two donor components, as evidenced by in-depth electrical and morphological investigations. Our results highlight that the alloy-like structure formed due to the high compatibility of the donor molecules had a more significant effect on the overall performance than the side-chain length, offering a new guideline for pairing donor components for achieving high-performance ternary OSCs.

4.1 Complementary Absorption & Suitable Energy Level Alignments for Enhanced Electrical and Morphological Features

Chapter 4.1 is reproduced in part with permission of "Ternary Solar Cells with a Mixed Face-On and Edge-On Enable an Unprecedented Efficiency of 12.1%." from Kumari T. *et al. Energy Environ. Sci.* 2017, **10**, 258 with permission from the Royal Society of Chemistry.

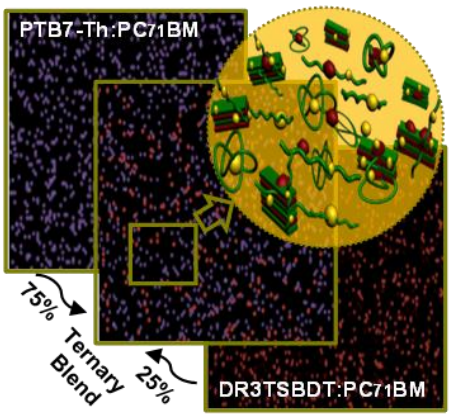

4.1.1 Introduction

An in-depth understanding of the operating mechanism of binary blend organic solar cells (OSCs), consisting of a polymeric donor and a fullerene acceptor, has enabled several research efforts aimed at increasing the power conversion efficiencies (PCEs) of OSCs.[1] An optimization process involving a synergistic combination of active materials design,[1b, 2] nanoscale morphology control,[3] and device engineering[4] resulted in a significant breakthrough of over 10% PCEs for single-junction binary OSCs.[1c, 1d, 5] In a promising approach for further increasing the PCEs, tandem OSCs–in which two (or more) sub-cells absorbing light in different regions of the solar spectrum are connected in either series or parallel–have been studied.[6] The impressive progress in the field of tandem OSCs has laid a solid foundation for improving the PCEs by ~40–50%,[7] demonstrating their immense potential for a practically realizable OSC technology. Nonetheless, there are several drawbacks in using tandem architectures, such as the complex fabrication process and high production cost, which limits their practical application.[6a, 8]

Ternary blend OSCs comprising two donors and one acceptor (or one donor and two acceptors) are emerging as a fascinating alternative to overcome the challenges encountered during spectrally broad light harvesting using multi-junction OSC processing while retaining the simplicity of a single-step processing of the active layer.[5b, 9] Despite some successful examples of ternary OSCs achieved by carefully selecting multiple components,[3a, 10] the current PCEs generally continue to be

far less than the state-of-the-art binary and tandem systems. This is because the third component within the host binary systems can act as a recombination centre or a morphological trap rather than a control agent to extend the absorption of the solar spectrum, since unfavourable interactions between the third component and host blend are inevitable.[11] Therefore, the molecular compatibility of the active materials used in ternary OSCs is believed to be critical in achieving high PCEs.[1c, 5b, 12] We speculate that in a vast pool of available active materials, the use of an archetype of high-performance poly(4,8-bis(5-(2-ethylhexyl)thiophen-2-yl)benzo[1,2-*b*;4,5-*b*']dithiophene-2,6-diyl-alt-(4-(2-ethylhexyl)-3-fluorothieno[3,4-*b*]thiophene-)-2-carboxylate-2-6-diyl)) (PTB7-Th):[6,6]-phenyl-C_{71}-butyric acid methyl ester ($PC_{71}BM$) binary host can pave a shortcut for discovering ideal ternary systems. In addition to its appropriate energy level alignment and high-crystalline characteristics, a benzo[1,2-*b*;4,5-*b*']dithiophene (BDT)-based small molecule, namely DR3TSBDT, is intuitively expected to have good compatibility with PTB7-Th because of the molecular similarity in their backbones, which is based on identical BDT units.

Given this background, a ternary OSC was designed and fabricated by incorporating DR3TSBDT as the additional donor into the PTB7-Th:$PC_{71}BM$ host matrix. The ternary system demonstrated an unprecedented PCE of 12.1% under optimal conditions. Unlike common high-performance OSCs that favour face-on orientation, our ternary OSCs have a mixed orientation, which is a combination of face-on and edge-on orientations, thus enabling much higher PCEs compared to the preferentially face-on orientated host system. Our in-depth study reveals that the exceptionally high PCE results from not only improving the photon absorption range but also facilitating charge transport while reducing recombination. This is achieved through a combination of cascade energy levels and optimized morphology.

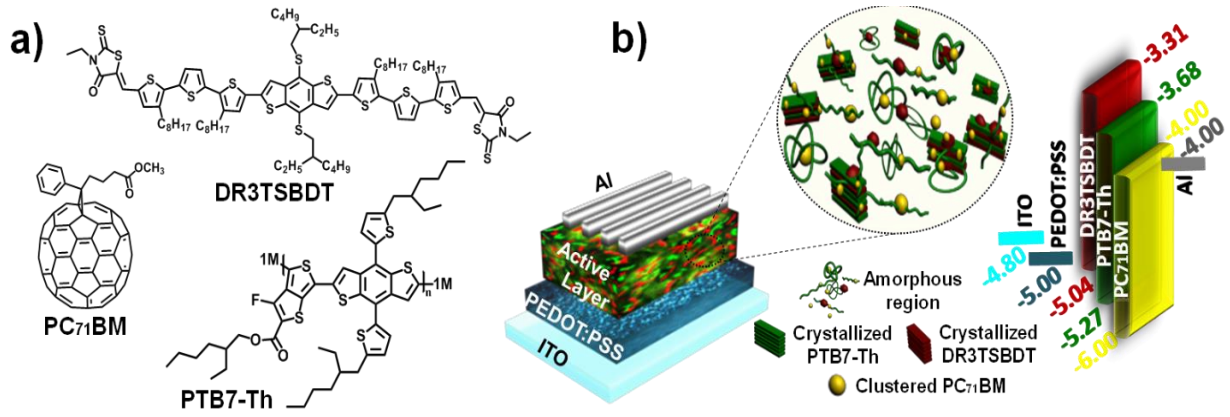

Figure 4.1.1. a) Chemical structures of PTB7-Th, DR3TSBDT, and $PC_{71}BM$. b) Device architecture with illustration of the active layer morphology in ternary OSCs and Energy level diagram.

4.1.2 Results and Discussion

4.1.2.1 *Structure and Optical Properties*

The chemical structures of PTB7-Th, DR3TSBDT, and $PC_{71}BM$, as well as the device architecture and corresponding energy levels, are given in Figure 4.1.1 a and b. We first carried out a detailed spectroscopy study to understand the changes in chlorobenzene (CB) solution and in solid chlorobenzene based thin film following the incorporation of the third component. The two donor components exhibit complementary absorption spectra (Figure 4.1.2a). The maximum absorption for the PTB7-Th film is at 706 nm and that of the DR3TSBDT film is centred at 586 nm. As the DR3TSBDT content in PTB7-Th increased, the absorption intensity gradually increased in the region of 400–600 nm, while the absorption at around 700 nm decreased. Note that the maximum absorption of PTB7-Th is red-shifted following the incorporation of DR3TSBDT.

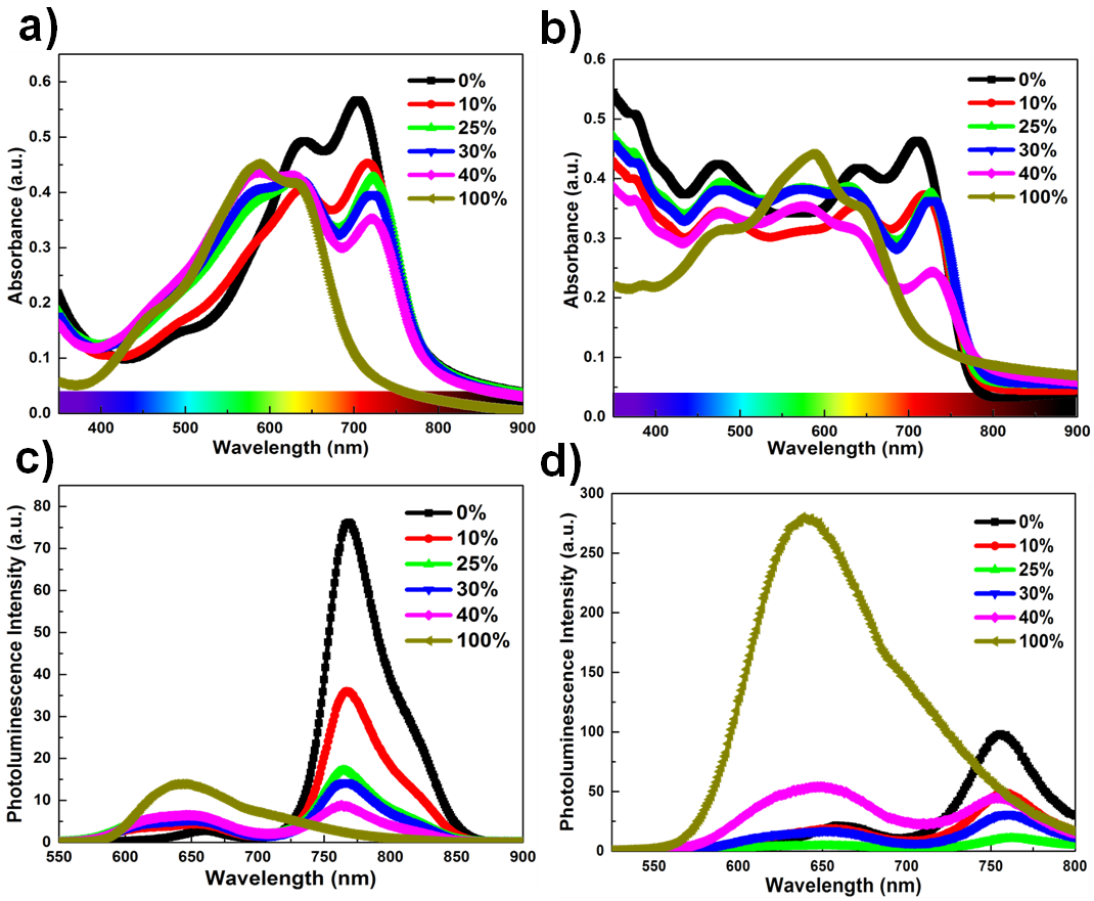

Figure 4.1.2. a) Absorption spectra of two donors' blend films. b) Absorption spectra of ternary blend films. c) Photoluminescence spectra (PL) of two donors' binary blend. d) Photoluminescence spectra (PL) of two donors' ternary blend with $PC_{71}BM$ in chlorobenzene solution (excitation at ~500 nm).

Figure 4.1.2b shows the effect of incorporating various concentrations of DR3TSBDT into the PTB7-Th:$PC_{71}BM$ host at a certain blending ratio (1:1.5 wt./wt.). As for the absorption spectra of the two donor mixtures (Figure 4.1.2a), it is seen that incorporating DR3TSBDT to form ternary blends leads to a small red-shift in the low-energy absorption band, implying an increased molecular ordering in PTB7-Th, which is induced by the favourable interaction with DR3TSBDT. Therefore, we expect that an optimal amount of DR3TSBDT will facilitate the crystallization of PTB7-Th in ternary OSCs. In addition, the ternary films formed using 10–30 wt.% DR3TSBDT provide a relatively high absorption intensity over a broad wavelength range of 300 to 800 nm (Figure 4.1.2b). Figure 4.1.2c and d show the photoluminescence (PL) spectra of each neat donor, two-donor binary blend, and ternary blend solutions under excitation at ~500 nm. PTB7-Th exhibits a rather structured emission with a maximum at 760 nm and DR3TSBDT shows a broad emission peak from 580 to 800 nm, which overlaps with the absorption spectrum of PTB7-Th. A gradual increase in the emission intensity of DR3TSBDT was observed, while the emission intensity of PTB7-Th decreased with increasing DR3TSBDT loading ratios, reflecting the existence of Förster energy transfer between DR3TSBDT and PTB7-Th.[9a, 9d, 10b, 10e] Interestingly, the quenching of the emission was more efficient in ternary films with 25 wt.% DR3TSBDT than in other ternary blends, implying the feasibility of a relatively optimized charge transfer pathway at the two donors/acceptor interface.

4.1.2.2 *Photovoltaic Performance*

The photovoltaic performance of OSCs fabricated using different DR3TSBDT concentrations was evaluated using a conventional architecture of indium-tin oxide (ITO)/poly(3,4-ethylenedioxythiophene):poly(styrene sulfonate) (PEDOT:PSS)/active layer/Al under simulated AM 1.5G irradiation (100 mW cm^{-2}). The overall donor to $PC_{71}BM$ ratio in the active layer was fixed at 1:1.5 wt./wt. 1,8-Diiodooctane (DIO, 3.0 vol.%) was used as a processing additive. This paper presents a discussion on the representative ternary blend systems (0, 10, 25, 30, 40, and 100 wt.% DR3TSBDT loading ratios). Additional details of ternary blends examined in this study are included in supporting figures of 4.1.5 section (Figure 4.1.10 and 4.1.11), and detailed in the device fabrication section of chapter 2. The current density–voltage (*J*–*V*) characteristics of OSCs are shown in Figure 4.1.3a and the corresponding device parameters are summarized in Table 4.1.1. Using highly optimized conditions for PTB7-Th:$PC_{71}BM$ binary OSCs, a maximum PCE of 10.10% was obtained, with a short-circuit current density (J_{SC}) of 19.43±0.30 mA cm^{-2}, an open-circuit voltage (V_{OC}) of 0.785±0.004 V, and a fill factor (FF) of 64.90±0.40%. The PCE value reported in this study is comparable with that of the previous best OSCs based on PTB7-Th:$PC_{71}BM$.[9d, 13] Upon the addition of 25 wt.% DR3TSBDT into the host system, J_{SC} increases continuously together with

a moderate enhancement in FF (up to 70.44%), whereas a marginal decrease in V_{OC} was observed in the range of 0.794–0.772 V. Meanwhile, at DR3TSBDT loadings higher than 30 wt.%, a large drop in J_{SC} was observed. Therefore, ternary OSCs with a 25 wt.% DR3TSBDT content exhibited the best photovoltaic performance with a J_{SC} of 22.63±0.67 mA cm^{-2}, a V_{OC} of 0.765±0.007 V, and a FF of 68.5±1.9%, in an unprecedented PCE of 12.1% (average PCE = 11.78±0.34%).

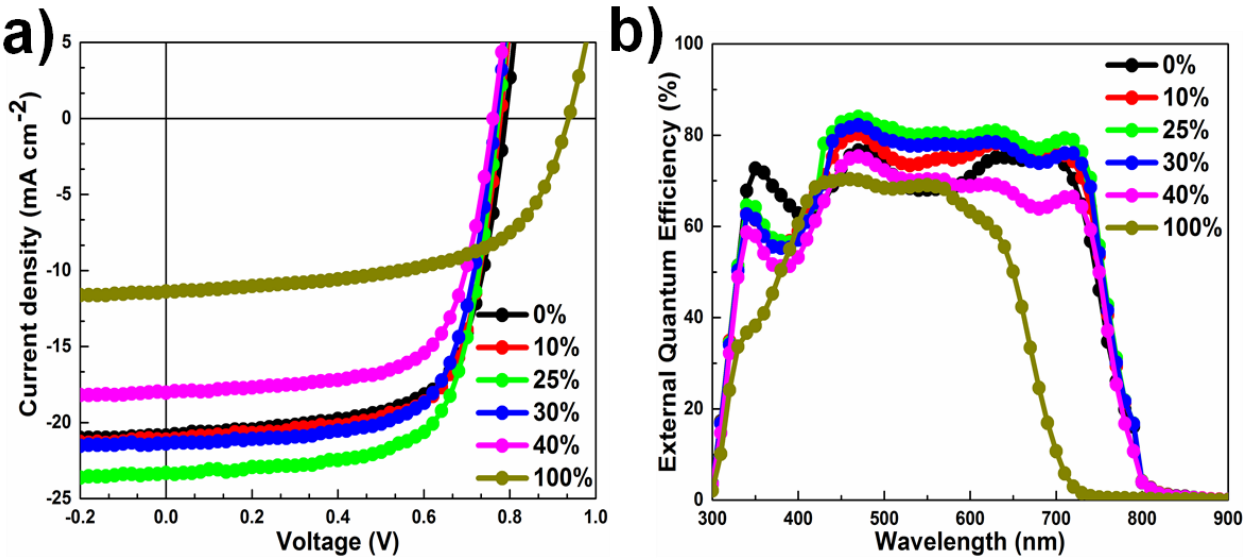

Figure 4.1.3. a) *J-V* characteristics of OSCs under AM 1.5G irradiation at 100 mWcm^{-2}. b) The corresponding EQE curves.

One of our best cells was sent to an independent solar cell calibration laboratory (Nano Convergence Practical Application Center, South Korea) for certification, confirming a PCE of 11.76%, with V_{OC} = 0.756 V, J_{SC} = 23.76 mA cm^{-2}, FF = 65.5%, (see Figure 4.1.12 of section 4.1.5). To the best of our knowledge, this value is among the highest certified PCE reported during that period for any type of OSCs. Evidence of hysteresis less *J–V* characteristic curve for one of the best device is also provided (see Figure 4.1.13 of section 4.1.5). Additionally, we observed that V_{OC} is composition-dependent in the blend systems studied, rather than being determined by the difference between $PC_{71}BM$ LUMO and the lowest-available donor HOMO level. The observed behaviour in V_{OC} suggests the formation of an alloy-like model induced by the compatible donors.[1a, 1c, 14] External quantum efficiency (EQE) spectra revealed an excellent photocurrent response over the absorption range 300–800 nm (Figure 4.1.3b). For all devices, the shapes of the EQE plots are similar to the corresponding absorption spectra, indicating that the absorption over the entire wavelength range contributes to the photocurrent generation.

Table 4.1.1. Photovoltaic parameters and charge transport properties of OSCs with different DR3TSBDT loading ratios.

DR3TSBDT ratios	J_{SC} (mA cm^{-2})[a]	V_{OC} (V)[a]	FF (%)[a]	PCE (%)[a]	μ_h (cm^2 V^{-1}s^{-1})[b]	μ_e (cm^2 V^{-1}s^{-1})[b]	μ_h/μ_e[b]
0%	19.43 (19.70)	0.785 (0.789)	64.90 (65.30)	9.87 (10.10)	1.578×10^{-4}	1.066×10^{-4}	1.478
10%	20.72 (21.69)	0.772 (0.782)	67.83 (69.90)	10.79 (11.30)	1.683×10^{-4}	1.134×10^{-4}	1.483
25%	22.63 (23.31)	0.765 (0.772)	68.51 (70.44)	11.78 (12.10)	2.200×10^{-4}	1.268×10^{-4}	1.735
30%	19.90 (21.38)	0.762 (0.770)	67.78 (69.30)	10.97 (11.30)	2.119×10^{-4}	1.176×10^{-4}	1.801
40%	17.37 (18.00)	0.756 (0.766)	67.60 (69.10)	8.88 (9.26)	2.020×10^{-4}	1.048×10^{-4}	1.927
100%	12.92 (13.41)	0.897 (0.902)	54.80 (56.72)	4.99 (5.52)	0.208×10^{-4}	0.159×10^{-4}	1.309

[a]The average values obtained from at least 16 devices with standard deviation. The data in parentheses are the highest values. [b]The average values obtained from at least 4 devices with standard deviation.

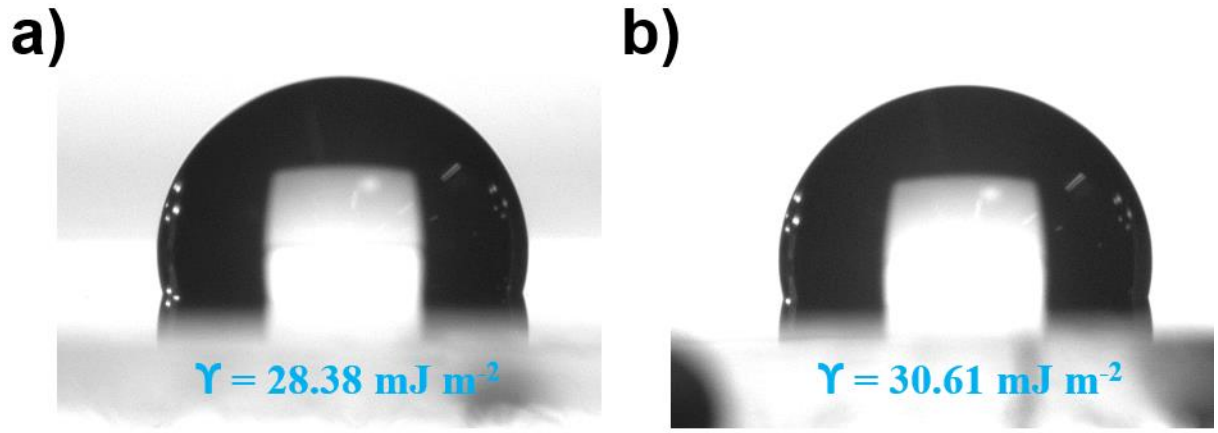

Figure 4.1.4. Surface energy measurement. Photographs of the drop of water on the surface of a) DR3TSBDT and b) PTB7-Th:$PC_{71}BM$ films on a glass substrate.

From differential scanning calorimetry (DSC) data as shown in supporting Figure 4.1.14 of section 4.1.5, the heating curve of the pristine DR3TSBDT shows a clearly endothermic transition (i.e., melting peak), confirming its relatively high crystallinity. In contrast, no such thermally induced transition occurs during the heating cycle of both the pristine PTB7-Th and all the blend systems of

PTB7-Th:DR3TSBDT, suggesting a lack of pure DR3TSBDT domains in the blends.[1c, 15] The similar surface energies of 28.4 and 30.6 mJ m^{-2} for DR3TSBDT and PTB7-Th:$PC_{71}BM$ host blend, respectively, calculated using Young's equation[16] provide additional proof of the good miscibility in ternary systems (see Figure 4.1.4). This is further evidenced from energy dispersive X-ray analysis (EDAX) and optical microscopy. The EDAX elemental mapping indicates that the nitrogen signals from DR3TSBDT are well-spread and are adjacent to the fluoride peaks of PTB7-Th in the ternary blends (see Figure 4.1.5). Each ternary film appears to be uniformly blended, at least at the scale shown in the optical microscopy, lacking any gross aggregation (see supporting Figure 4.1.15 of section 4.1.5).

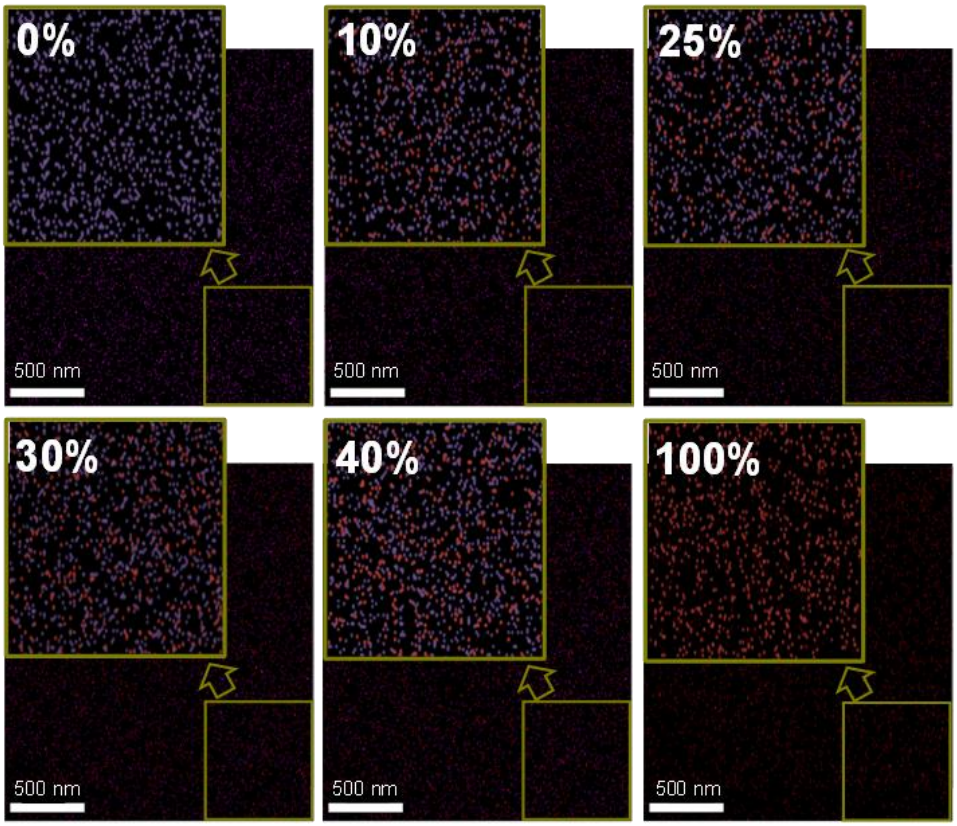

Figure 4.1.5. Energy dispersive X- ray elemental mapping; the fluorine (purple dots) and nitrogen (red dots) indicate PTB7-Th and DR3TSBDT, respectively and the inset is the corresponding zoomed images.

4.1.2.3 *Carrier Transport and Recombination Dynamics*

To understand the working mechanism and the different photovoltaic performances in the tested OSCs, we characterized the charge transport property and recombination dynamics. The charge carrier mobilities of the hole- and electron-only devices were estimated using space-charge limited

curve (SCLC)[17] as detailed in the characterization methods section of chapter 2 (Table 4.1.1 and see supporting Figure 4.1.16 of section 4.1.5). With the electron mobilities being relatively constant for all ternary cases, the hole mobilities are sensitive to the DR3TSBDT loading ratios. All blends investigated in this study exhibited highly balanced charge-transport properties (hole/electron mobility ratios of 1.30–1.92). In addition, it was found that both the hole and electron mobilities gradually increased at low DR3TSBDT loadings (0–25 wt.%), while a further increase in the DR3TSBDT content caused a decrease in the mobilities. Thus, the ternary OSCs with 25 wt.% DR3TSBDT showed a superior mobility level compared to the other samples, implying better percolation pathways for the charge carriers. This is due to the optimized DR3TSBDT:$PC_{71}BM$, especially low FF.

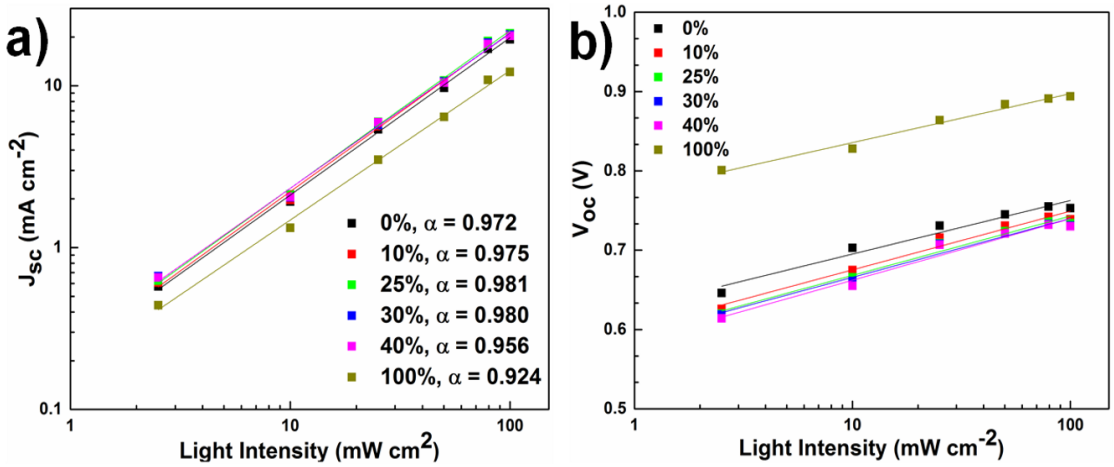

Figure 4.1.6. a) Dependence of current density (J_{SC}) and b) V_{OC} on light intensity of OSCs.

To further investigate recombination dynamics, light intensity dependence on J_{SC} and V_{OC} is measured. The device with 25 wt.% DR3TSBDT exhibited the weakest bimolecular recombination with an α value of 0.98 (see Figure 4.1.6a), which partially explains the highest J_{SC} and mobility levels observed. Figure 4.1.6b shows a plot of V_{OC} as a function of the logarithm of light intensity. For all cases, a strong dependence of V_{OC} on light intensity with a slope larger than 2 kT/q is observed, where k is Boltzmann's constant, T is temperature, and q is elementary charge, suggesting the presence of a trap-assisted recombination.

4.1.2.4 *Film Morphology and Microstructure*

The morphology and microstructure of the blend films were characterized using atomic force microscopy (AFM), high-resolution transmission electron microscopy (HR-TEM), and grazing incidence wide-angle X-ray scattering (GIWAXS). The PTB7-Th:$PC_{71}BM$ host blend film possessed a small-length scale

morphology with a root-mean-square (RMS, R_q) roughness of 1.24 nm (Figure 4.1.7a and supporting Figure 4.1.17 of section 4.1.5). Incorporating up to 30 wt.% DR3TSBDT into the host matrix led to a gradual increase in the RMS, but the surface continued to be smooth, along with uniform features with a nanoscale phase separation. However, a further increase in DR3TSBDT caused a higher roughness with large aggregated regions. Besides, the HR-TEM images of ternary films containing 25–40 wt.% DR3TSBDT showed finely dispersed fibrils with domain sizes ranging from 10 to 15 nm, plausibly reflecting an interpenetrating network (Figure 4.1.7b). However, such features were not observed in other films.

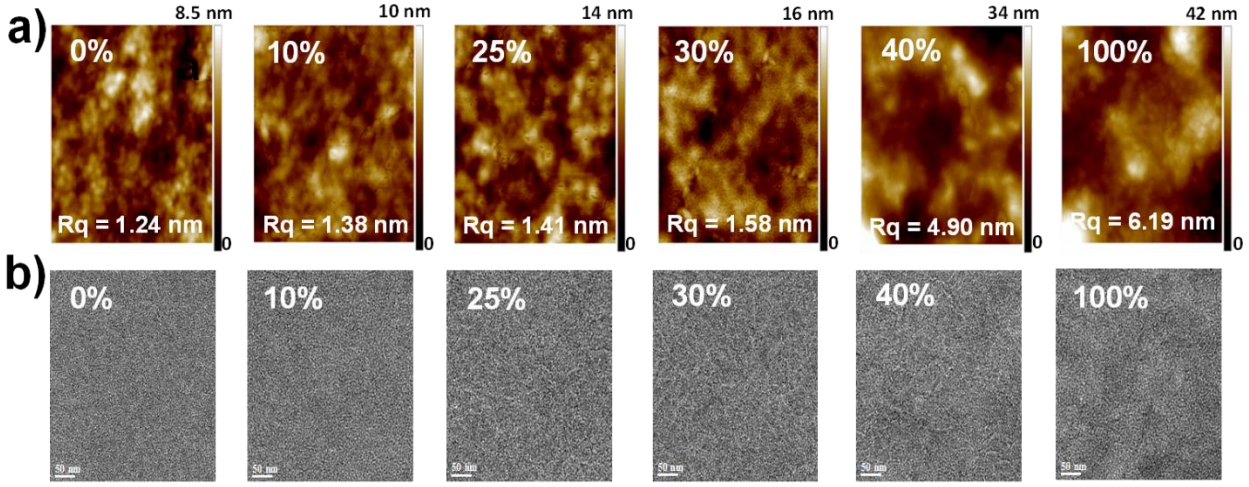

Figure 4.1.7. a) AFM topography images (scan size 1×1 μm) and b) High resolution transmission electron microscopy images (scale bar 50 nm) of blend films with different DR3TSBDT loading ratios. Different color bars are used for the height (AFM) variance.

As seen from the GIWAXS patterns in Figure 4.1.8 and supporting Figure 4.1.18 of section 4.1.5, PTB7-Th:$PC_{71}BM$ produced a (010) π-π stacking peak centered at about 1.67 $Å^{-1}$ in the out-of-plane direction (q_z) with an arc-like lamellar (100) peak along the in-plane direction (q_{xy}). This indicates a favored face-on orientation relative to the substrate (supporting Table 4.1.2 of section 4.1.5 for detailed crystallographic parameters). In contrast, in the case of DR3TSBDT:$PC_{71}BM$, another binary system, the (010) π-π stacking peak, was located along the q_{xy} direction in conjunction with highly ordered lamellar (100), (200), and (300) peaks in the q_z axis, suggesting a preferential edge-on alignment. Interestingly, adding DR3TSBDT to form the ternary films resulted in the formation of (010) π-π stacking peaks in both q_{xy} and q_z profiles, providing a conclusive evidence for the formation of mixed edge-on and face-on orientations, the so-called 3-D textured structures. In particular, we found that the intensities of both out-of-plane and in-plane (010) peaks were strengthened for the ternary film in case of the 25% DR3TSBDT blend (Figure 4.1.9a), which is largely responsible for the enhanced charge transport.

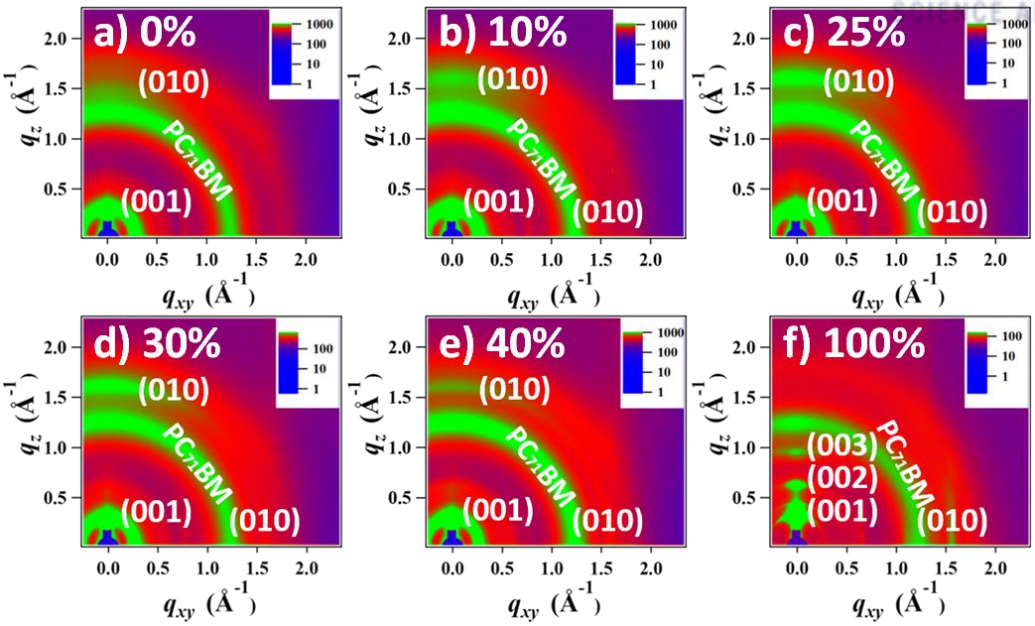

Figure 4.1.8. Grazing incidence wide angle X-ray scattering (GIWAXS) patterns of blend films with different DR3TSBDT loading ratios. Different color bars are used for the intensity variance.

Additionally, for all samples, the (010) coherence lengths (L_Cs), which are a measure of cumulative lattice distortions in both q_{xy} and q_z axes, were also calculated using the Scherrer equation[18] (Figure 4.1.9b). With the L_C values along the q_z being relatively consistent for the all cases (4–7 nm), the L_C values along the q_{xy} increased from ~6 to 20 nm with an increase in the DR3TSBDT loading ratios, illustrating that the ternary systems could form larger nanocrystallites than the PTB7-Th:$PC_{71}BM$ host. These changes in the molecular stacking and crystallinity, following the addition of a guest molecule to the host matrix, provide additional evidence for the alloy model proposed in this study.[1a, 1c, 12g, 14, 19] Another observation that needs to be emphasized is that, compared to the PTB7-Th:$PC_{71}BM$ host system, which has a predominantly face-on orientation, our data for the optimized ternary systems with 3-D textures indicate far better PCEs. This reported observation reported, for the first time, challenges the traditional assumption that face-on orientation is more favorable for photovoltaic devices because of its vertical charge transportation channel.

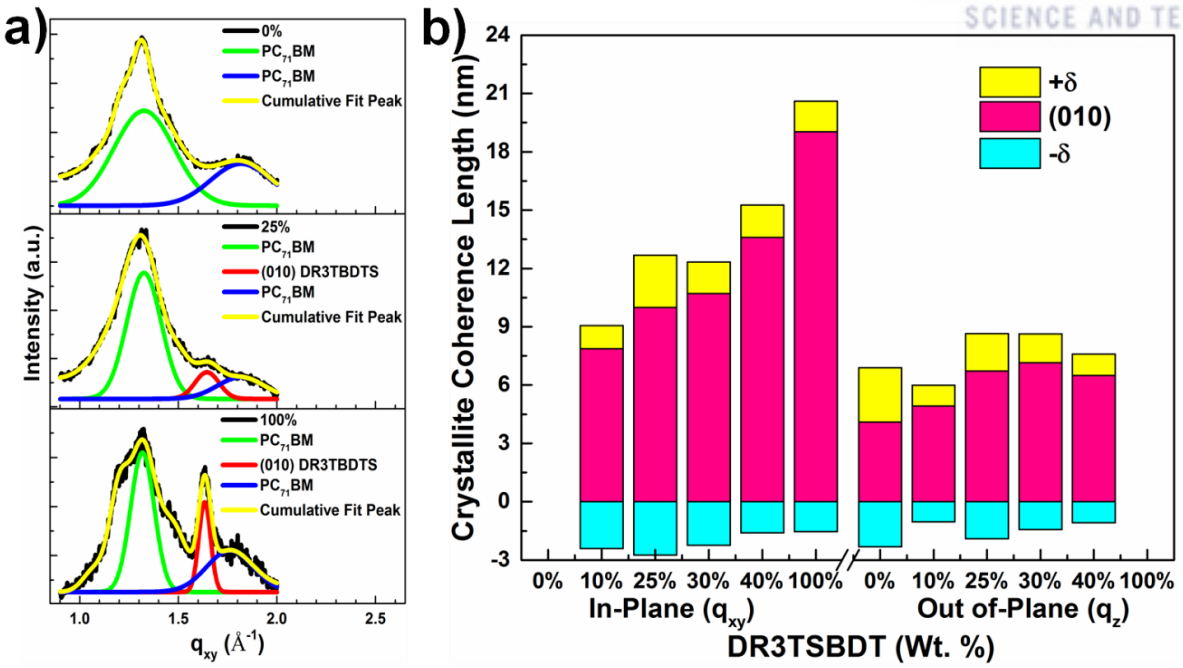

Figure 4.1.9. Exemplary fittings of the GIWAXS line cuts at higher q region in horizontal direction for PTB7-Th:PC71BM, PTB7-Th-DR3TSBDT (25%):PC71BM and DR3TSBDT:$PC_{71}BM$ blend films. b) In-plane crystallite coherence length (CCL) of π-π stacking. Gaussian fits are used to determine peak position and FWHM.

4.1.3 Conclusions

A ternary system comprising DR3TSBDT:PTB7-Th as a donor and $PC_{71}BM$ as an acceptor was investigated in detail, considering both cascaded energy levels and molecular compatibility. At low DR3TSBDT loadings (≤25 wt.%) into the host system, synergistic effects such as increased J_{SC} and FF were observed, which is attributed to enhanced light absorption and charge transport, reduced recombination, and optimized morphology. A notable PCE as high as 12.1% was obtained from ternary OSCs with 25 wt.% DR3TSBDT, which is among the highest value reported so far. The intimate mixing property of two donors enables the formation of an alloy-like model in the present ternary systems, as verified by not only elemental mapping and optical microscopy but also the V_{OC} values and molecular packing/crystallinity. Moreover, we discovered that a mixed face-on and edge-on orientation in ternary OSCs, rather than an almost entirely face-on orientation, yields a better photovoltaic performance, which challenges the fundamental idea successfully used in the past to describe high-performance OSCs. This finding provides further impetus for continued research in the field of ternary OSCs in order to understand the interesting and sometimes surprising behavior of the multiple blending systems.

4.1.4 References

1. (a) An, Q.; Zhang, F.; Zhang, J.; Tang, W.; Deng, Z.; Hu, B., Versatile ternary organic solar cells: a critical review. *Energy Environ. Sci.* **2016,** *9* (2), 281-322; (b) Subbiah, J.; Purushothaman, B.; Chen, M.; Qin, T.; Gao, M.; Vak, D.; Scholes, F. H.; Chen, X.; Watkins, S. E.; Wilson, G. J.; Holmes, A. B.; Wong, W. W. H.; Jones, D. J., Organic Solar Cells Using a High-Molecular-Weight Benzodithiophene–Benzothiadiazole Copolymer with an Efficiency of 9.4%. *Adv. Mater.* **2015,** *27* (4), 702-705; (c) Zhang, J.; Zhang, Y.; Fang, J.; Lu, K.; Wang, Z.; Ma, W.; Wei, Z., Conjugated Polymer–Small Molecule Alloy Leads to High Efficient Ternary Organic Solar Cells. *J. Am. Chem. Soc.* **2015,** *137* (25), 8176-8183; (d) Zhang, S.; Ye, L.; Hou, J., Breaking the 10% Efficiency Barrier in Organic Photovoltaics: Morphology and Device Optimization of Well-Known PBDTTT Polymers. *Adv. Energy Mater.* **2016**, n/a-n/a.

2. (a) Scharber, M. C.; Mühlbacher, D.; Koppe, M.; Denk, P.; Waldauf, C.; Heeger, A. J.; Brabec, C. J., Design Rules for Donors in Bulk-Heterojunction Solar Cells—Towards 10 % Energy-Conversion Efficiency. *Adv. Mater.* **2006,** *18* (6), 789-794; (b) Servaites, J. D.; Savoie, B. M.; Brink, J. B.; Marks, T. J.; Ratner, M. A., Modeling geminate pair dissociation in organic solar cells: high power conversion efficiencies achieved with moderate optical bandgaps. *Energy Environ. Sci.* **2012,** *5* (8), 8343-8350.

3. (a) Chen, W.; Du, Z.; Xiao, M.; Zhang, J.; Yang, C.; Han, L.; Bao, X.; Yang, R., High-Performance Small Molecule/Polymer Ternary Organic Solar Cells Based on a Layer-By-Layer Process. *ACS Appl. Mater. Interfaces* **2015,** *7* (41), 23190-23196; (b) Guo, S.; Ning, J.; Körstgens, V.; Yao, Y.; Herzig, E. M.; Roth, S. V.; Müller-Buschbaum, P., The Effect of Fluorination in Manipulating the Nanomorphology in PTB7:PC71BM Bulk Heterojunction Systems. *Adv. Energy Mater.* **2015,** *5* (4), n/a-n/a; (c) Liu, Y.; Zhao, J.; Li, Z.; Mu, C.; Ma, W.; Hu, H.; Jiang, K.; Lin, H.; Ade, H.; Yan, H., Aggregation and morphology control enables multiple cases of high-efficiency polymer solar cells. *Nature Commun.* **2014,** *5*.

4. (a) Krebs, F. C., Fabrication and processing of polymer solar cells: A review of printing and coating techniques. *Sol. Energy Mater. Sol. Cells* **2009,** *93* (4), 394-412; (b) Lee, J. M.; Lim, J.; Lee, N.; Park, H. I.; Lee, K. E.; Jeon, T.; Nam, S. A.; Kim, J.; Shin, J.; Kim, S. O., Synergistic Concurrent Enhancement of Charge Generation, Dissociation, and Transport in Organic Solar Cells with Plasmonic Metal–Carbon Nanotube Hybrids. *Adv. Mater.* **2015,** *27* (9), 1519-1525; (c) Shockley, W.; Queisser, H. J., Detailed Balance Limit of Efficiency of p-n Junction Solar Cells. *J. Appl. Phys.* **1961,** *32* (3), 510-519.

5. (a) Kan, B.; Zhang, Q.; Li, M.; Wan, X.; Ni, W.; Long, G.; Wang, Y.; Yang, X.; Feng, H.; Chen, Y., Solution-Processed Organic Solar Cells Based on Dialkylthiol-Substituted Benzodithiophene Unit with Efficiency near 10%. *J. Am. Chem. Soc.* **2014,** *136* (44), 15529-15532; (b) Liu, S.; You, P.; Li, J.; Li, J.; Lee, C.-S.; Ong, B. S.; Surya, C.; Yan, F., Enhanced efficiency of polymer solar cells by adding a high-mobility conjugated polymer. *Energy Environ. Sci.* **2015,** *8* (5), 1463-1470; (c) Liu, Y.; Zhao, J.; Li, Z.; Mu, C.; Ma, W.; Hu, H.; Jiang, K.; Lin, H.; Ade, H.; Yan, H., Aggregation and morphology control enables multiple cases of high-efficiency polymer solar cells. *Nature Commun.* **2014,** *5*, 5293; (d) Zhao, J.; Li, Y.; Yang, G.; Jiang, K.; Lin, H.; Ade, H.; Ma, W.; Yan, H., Efficient organic solar cells processed from hydrocarbon solvents. *Nature Energy* **2016,** *1*, 15027.

6. (a) Ameri, T.; Dennler, G.; Lungenschmied, C.; Brabec, C. J., Organic tandem solar cells: A review. *Energy Environ. Sci.* **2009,** *2* (4), 347-363; (b) Gilot, J.; Wienk, M. M.; Janssen, R. A. J., Double and triple junction polymer solar cells processed from solution. *Appl. Phys. Lett.* **2007,** *90* (14), 143512.

7. (a) Kotlarski, J. D.; Blom, P. W. M., Ultimate performance of polymer:fullerene bulk heterojunction tandem solar cells. *Appl. Phys. Lett.* **2011,** *98* (5), 053301; (b) You, J.; Dou, L.; Yoshimura, K.; Kato, T.; Ohya, K.; Moriarty, T.; Emery, K.; Chen, C.-C.; Gao, J.; Li, G.; Yang, Y., A polymer tandem solar cell with 10.6% power conversion efficiency. *Nature Commun.* **2013,** *4*, 1446.

8. Yang, J.; Zhu, R.; Hong, Z.; He, Y.; Kumar, A.; Li, Y.; Yang, Y., A Robust Inter-Connecting Layer for Achieving High Performance Tandem Polymer Solar Cells. *Adv. Mater.* **2011,** *23* (30), 3465-3470.

9. (a) Cha, H.; Chung, D. S.; Bae, S. Y.; Lee, M.-J.; An, T. K.; Hwang, J.; Kim, K. H.; Kim, Y.-H.; Choi, D. H.; Park, C. E., Complementary Absorbing Star-Shaped Small Molecules for the Preparation of Ternary Cascade Energy Structures in Organic Photovoltaic Cells. *Adv. Funct. Mater.* **2013,** *23* (12), 1556-1565; (b) Honda, S.; Ohkita, H.; Benten, H.; Ito, S., Multi-colored dye sensitization of polymer/fullerene bulk heterojunction solar cells. *Chem. Commun.* **2010,** *46* (35), 6596-6598; (c) Koppe, M.; Egelhaaf, H.-J.; Dennler, G.; Scharber, M. C.; Brabec, C. J.; Schilinsky, P.; Hoth, C. N., Near IR Sensitization of Organic Bulk Heterojunction Solar Cells: Towards Optimization of the Spectral Response of Organic Solar Cells. *Adv. Funct. Mater.* **2010,** *20* (2), 338-346; (d) Lu, L.; Chen, W.; Xu, T.; Yu, L., High-performance ternary blend polymer solar cells involving both energy transfer and hole relay processes. *Nature Commun.* **2015,** *6*, 7327.

10. (a) An, Q.; Zhang, F.; Li, L.; Wang, J.; Zhang, J.; Zhou, L.; Tang, W., Improved Efficiency of Bulk Heterojunction Polymer Solar Cells by Doping Low-Bandgap Small Molecules. *ACS Appl.*

Mater. Interfaces **2014,** *6* (9), 6537-6544; (b) An, Q.; Zhang, F.; Sun, Q.; Wang, J.; Li, L.; Zhang, J.; Tang, W.; Deng, Z., Efficient small molecular ternary solar cells by synergistically optimized photon harvesting and phase separation. *J. Mater. Chem. A* **2015,** *3* (32), 16653-16662; (c) Farahat, M. E.; Patra, D.; Lee, C.-H.; Chu, C.-W., Synergistic Effects of Morphological Control and Complementary Absorption in Efficient All-Small-Molecule Ternary-Blend Solar Cells. *ACS Appl. Mater. Interfaces* **2015,** *7* (40), 22542-22550; (d) Huang, J.-H.; Velusamy, M.; Ho, K.-C.; Lin, J.-T.; Chu, C.-W., A ternary cascade structure enhances the efficiency of polymer solar cells. *J. Mater. Chem.* **2010,** *20* (14), 2820-2825; (e) Huang, T.-Y.; Patra, D.; Hsiao, Y.-S.; Chang, S. H.; Wu, C.-G.; Ho, K.-C.; Chu, C.-W., Efficient ternary bulk heterojunction solar cells based on small molecules only. *J. Mater. Chem. A* **2015,** *3* (19), 10512-10518; (f) Khlyabich, P. P.; Burkhart, B.; Thompson, B. C., Efficient Ternary Blend Bulk Heterojunction Solar Cells with Tunable Open-Circuit Voltage. *J. Am. Chem. Soc.* **2011,** *133* (37), 14534-14537; (g) Yang, L.; Zhou, H.; Price, S. C.; You, W., Parallel-like Bulk Heterojunction Polymer Solar Cells. *J. Am. Chem. Soc.* **2012,** *134* (12), 5432-5435.

11. (a) Lu, L.; Kelly, M. A.; You, W.; Yu, L., Status and prospects for ternary organic photovoltaics. *Nature Photon.* **2015,** *9* (8), 491-500; (b) Savoie, B. M.; Dunaisky, S.; Marks, T. J.; Ratner, M. A., The Scope and Limitations of Ternary Blend Organic Photovoltaics. *Adv. Energy Mater.* **2015,** *5* (3), 1400891.

12. (a) Lu, H.; Zhang, X.; Li, C.; Wei, H.; Liu, Q.; Li, W.; Bo, Z., Performance Enhancement of Polymer Solar Cells by Using Two Polymer Donors with Complementary Absorption Spectra. *Macromol. Rapid Commun.* **2015,** *36* (14), 1348-1353; (b) Lu, L.; Xu, T.; Chen, W.; Landry, E. S.; Yu, L., Ternary blend polymer solar cells with enhanced power conversion efficiency. *Nature Photon.* **2014,** *8* (9), 716-722; (c) Thompson, B. C.; Kim, Y.-G.; Reynolds, J. R., Spectral Broadening in MEH-PPV:PCBM-Based Photovoltaic Devices via Blending with a Narrow Band Gap Cyanovinylene−Dioxythiophene Polymer. *Macromolecules* **2005,** *38* (13), 5359-5362; (d) Xiao, L.; Gao, K.; Zhang, Y.; Chen, X.; Hou, L.; Cao, Y.; Peng, X., A complementary absorption small molecule for efficient ternary organic solar cells. *J. Mater. Chem. A* **2016,** *4* (14), 5288-5293; (e) Zhang, S.; Zuo, L.; Chen, J.; Zhang, Z.; Mai, J.; Lau, T.-K.; Lu, X.; Shi, M.; Chen, H., Improved photon-to-electron response of ternary blend organic solar cells with a low band gap polymer sensitizer and interfacial modification. *J. Mater. Chem. A* **2016,** *4* (5), 1702-1707; (f) Gasparini, N.; Jiao, X.; Heumueller, T.; Baran, D.; Matt, G. J.; Fladischer, S.; Spiecker, E.; Ade, H.; Brabec, C. J.; Ameri, T., Designing ternary blend bulk heterojunction solar cells with reduced carrier recombination and a fill factor of 77%. *Nature Energy* **2016,** *1*, 16118; (g) Yang, L.; Yan, L.; You,

W., Organic Solar Cells beyond One Pair of Donor–Acceptor: Ternary Blends and More. *J. Phys. Chem. Lett.* **2013,** *4* (11), 1802-1810.

13. He, Z.; Xiao, B.; Liu, F.; Wu, H.; Yang, Y.; Xiao, S.; Wang, C.; Russell, T. P.; Cao, Y., Single-junction polymer solar cells with high efficiency and photovoltage. *Nature Photon.* **2015,** *9* (3), 174-179.

14. Angmo, D.; Bjerring, M.; Nielsen, N. C.; Thompson, B. C.; Krebs, F. C., Fullerene alloy formation and the benefits for efficient printing of ternary blend organic solar cells. *J. Mater. Chem. C* **2015,** *3* (21), 5541-5548.

15. (a) Holliday, S.; Ashraf, R. S.; Wadsworth, A.; Baran, D.; Yousaf, S. A.; Nielsen, C. B.; Tan, C.-H.; Dimitrov, S. D.; Shang, Z.; Gasparini, N.; Alamoudi, M.; Laquai, F.; Brabec, C. J.; Salleo, A.; Durrant, J. R.; McCulloch, I., High-efficiency and air-stable P3HT-based polymer solar cells with a new non-fullerene acceptor. *Nature Commun.* **2016,** *7*, 11585; (b) Li, N.; Machui, F.; Waller, D.; Koppe, M.; Brabec, C. J., Determination of phase diagrams of binary and ternary organic semiconductor blends for organic photovoltaic devices. *Sol. Energy Mater. Sol. Cells* **2011,** *95* (12), 3465-3471.

16. Vicente, C. M. S.; André, P. S.; Ferreira, R. A. S., Simple measurement of surface free energy using a web cam. *Rev. Bras. Ensino de Fís.* **2012,** *34*, 1-5.

17. (a) Goh, C.; Kline, R. J.; McGehee, M. D.; Kadnikova, E. N.; Fréchet, J. M. J., Molecular-weight-dependent mobilities in regioregular poly(3-hexyl-thiophene) diodes. *Appl. Phys. Lett.* **2005,** *86* (12), 122110; (b) Malliaras, G. G.; Salem, J. R.; Brock, P. J.; Scott, C., Electrical characteristics and efficiency of single-layer organic light-emitting diodes. *Phys. Rev. B* **1998,** *58* (20), R13411-R13414.

18. Kumari, T.; Moon, M.; Kang, S.-H.; Yang, C., Improved efficiency of DTGe(FBTTh2)2-based solar cells by using macromolecular additives: How macromolecular additives versus small additives influence nanoscale morphology and photovoltaic performance. *Nano Energy* **2016,** *24*, 56-62.

19. Ameri, T.; Khoram, P.; Min, J.; Brabec, C. J., Organic Ternary Solar Cells: A Review. *Adv. Mater.* **2013,** *25* (31), 4245-4266.

4.1.5 Supporting Figures

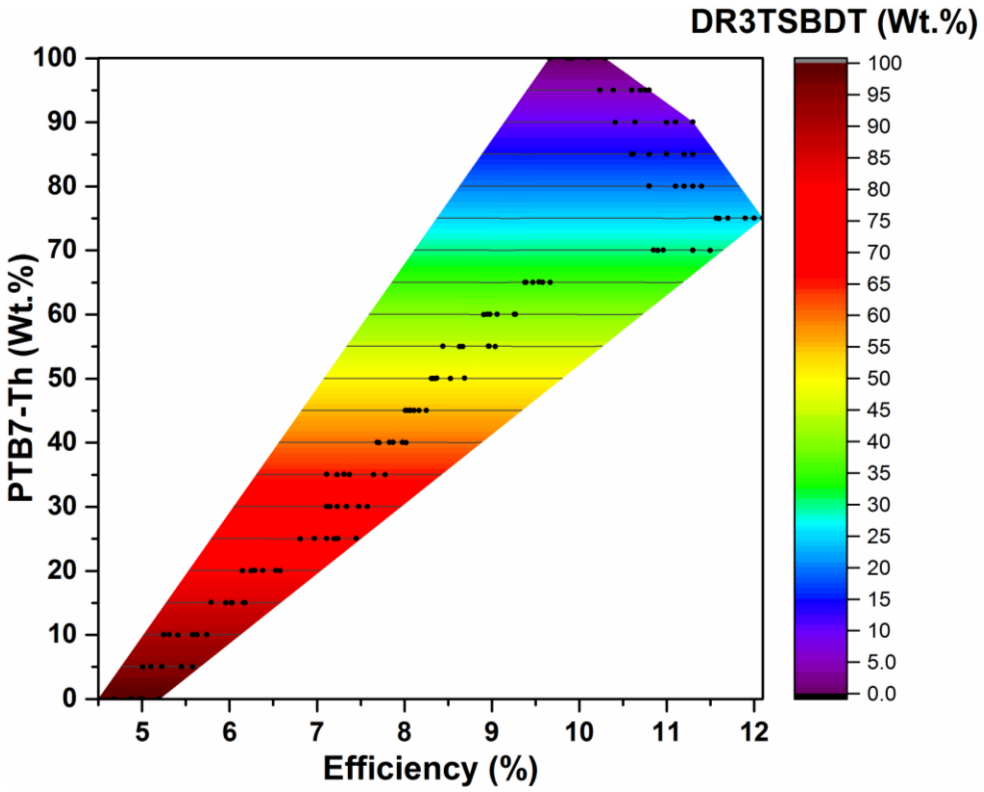

Figure 4.1.10. Contour plot showing the experimental power conversion efficiency (PCE) versus the wt.% of PTB7-Th (contour lines) and DR3TSBDT (colors) as two donor materials in the optimized ternary blends. Plotted for 6 devices in each case with maximum and minimum efficiency.

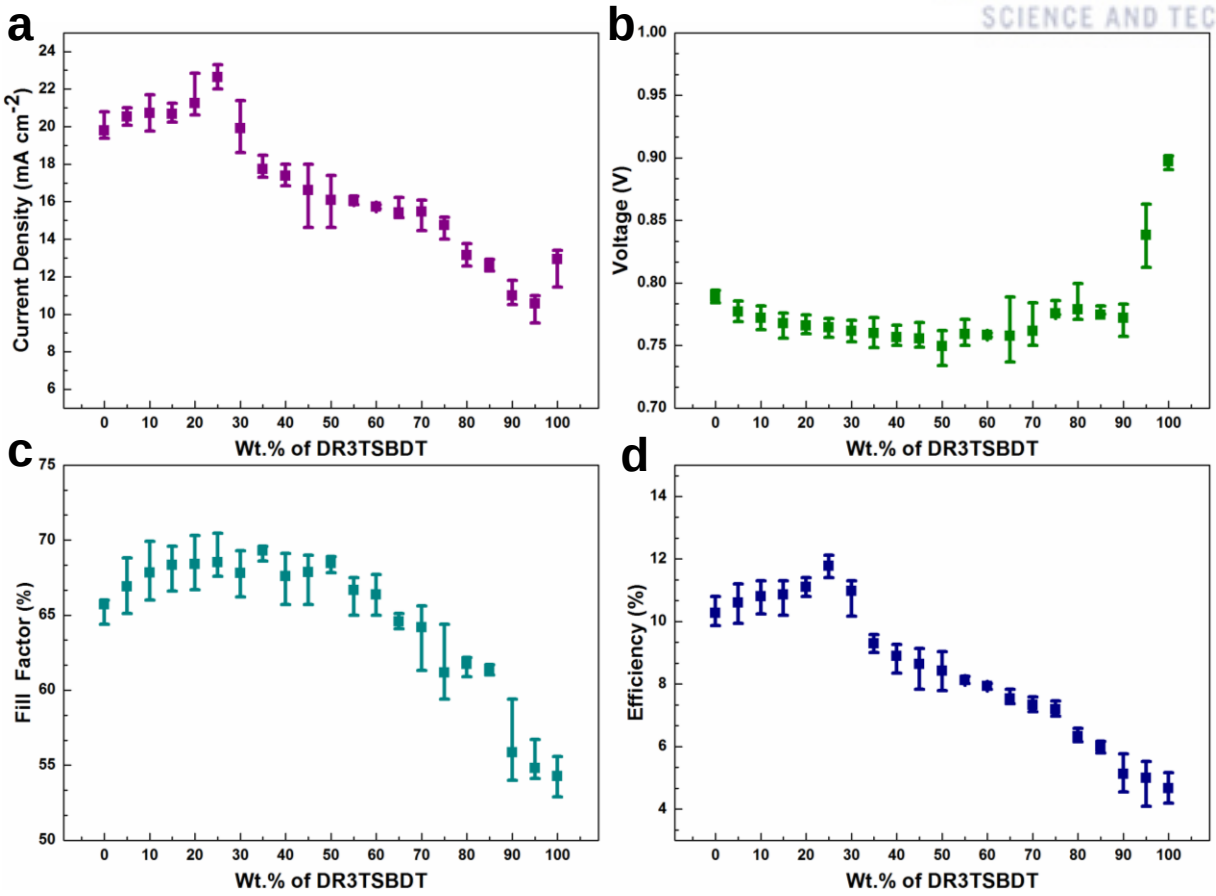

Figure 4.1.11. a) Current density. b) Voltage. c) Fill factor. d) Efficiency versus wt.% of DR3TSBDT used in the ternary blends.

(재)대구테크노파크
나노융합실용화센터
대구광역시 달서구 성서공단로 46-17
Tel : 053-602-1860 Fax : 053-602-1872

시험보고서

보고서번호: 16S-1629

1. 의 뢰 자
기 관 명: Ulsan National Institute of Science and Technology
주 소: 50, UNIST-gil, Ulsan 44919, Republic of Korea

2. 시료 설명: Organic Thin-Film Solar Cells

3. 시험기간: 16.10.27 (1일간)

4. 시험방법: 시험 장비의 측정 방법에 의함.

5. 시험결과

시험항목	결과	비고
태양전지평가시스템 기본사용 (Solar Simulator - 1kW)	Note the test results	-

이 시험보고서의 내용은 의뢰자가 제시한 시료에 한하며 용도이외의 사용을 금합니다.

확인	작성자		팀장	
	성 명 : 김 민 지	(서명)	성 명 : 안 창 현	(서명)

2016. 10. 31.

(재)대구테크노파크 나노융합실용화센터장 (인)

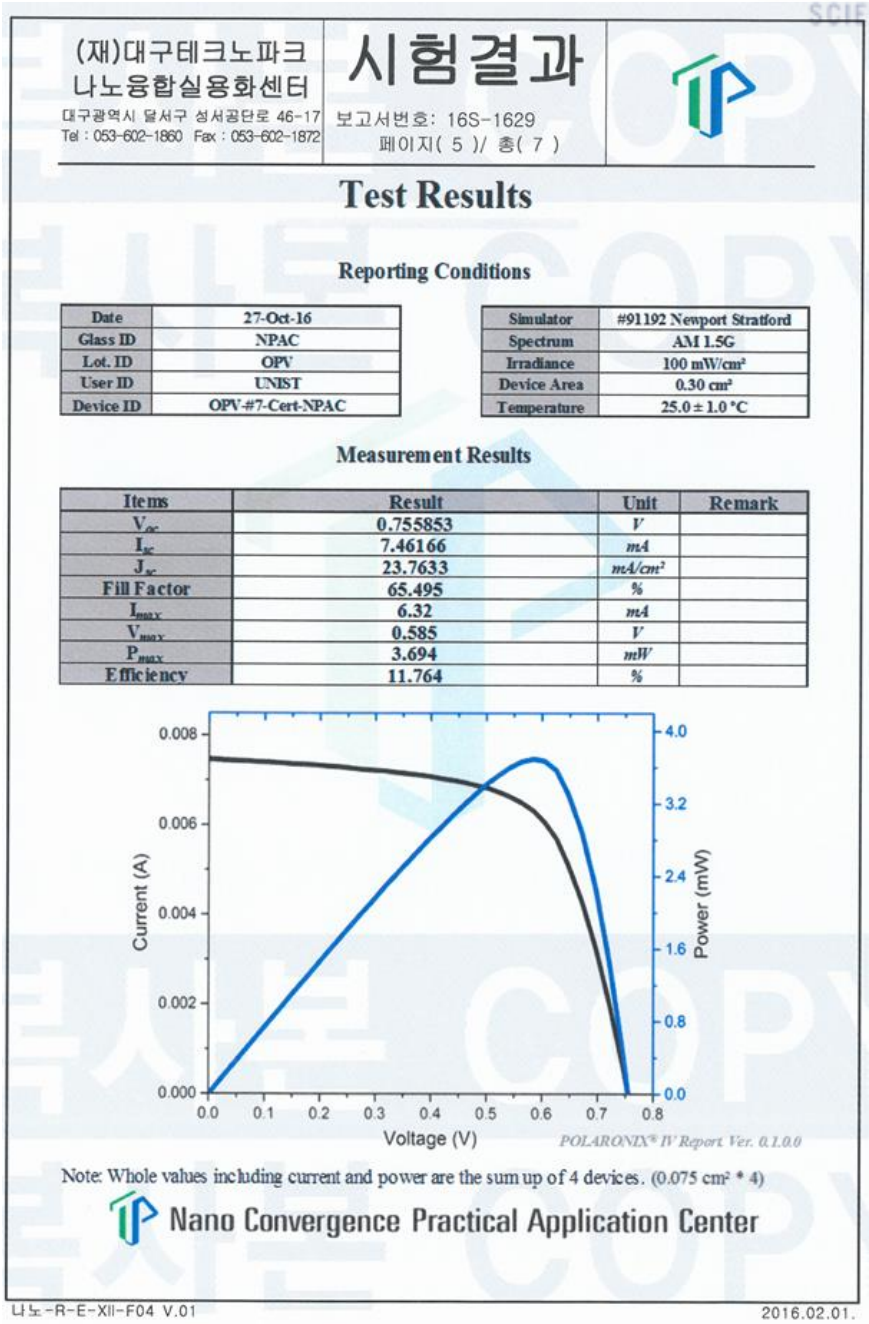

(재)대구테크노파크
나노융합실용화센터
대구광역시 달서구 성서공단로 46-17
Tel : 053-602-1860 Fax : 053-602-1872

시험결과

보고서번호: 16S-1629
페이지(5)/ 총(7)

Test Results

Reporting Conditions

Date	27-Oct-16
Glass ID	NPAC
Lot. ID	OPV
User ID	UNIST
Device ID	OPV-#7-Cert-NPAC

Simulator	#91192 Newport Stratford
Spectrum	AM 1.5G
Irradiance	100 mW/cm²
Device Area	0.30 cm²
Temperature	25.0 ± 1.0 °C

Measurement Results

Items	Result	Unit	Remark
V_{oc}	0.755853	V	
I_{sc}	7.46166	mA	
J_{sc}	23.7633	mA/cm²	
Fill Factor	65.495	%	
I_{max}	6.32	mA	
V_{max}	0.585	V	
P_{max}	3.694	mW	
Efficiency	11.764	%	

Note: Whole values including current and power are the sum up of 4 devices. (0.075 cm² * 4)

Nano Convergence Practical Application Center

나노-R-E-XII-F04 V.01 2016.02.01.

Figure 4.1.12. Independent certification confirming a power conversion efficiency of 11.76% by Nano Convergence Practical Application Center, South Korea.

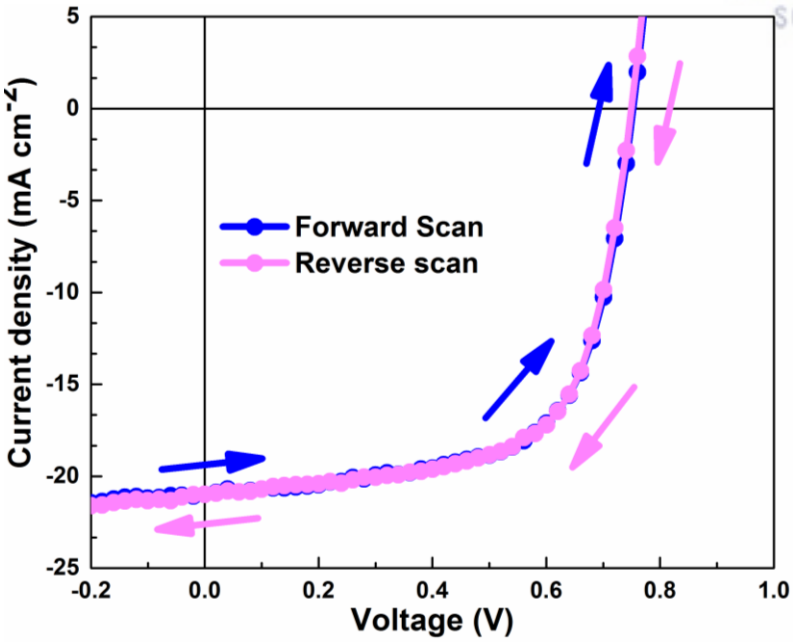

Figure 4.1.13. Hysteresis free *J-V* curve of one of the best performing ternary device (25 wt.% of DR3TSBDT loading)**.**

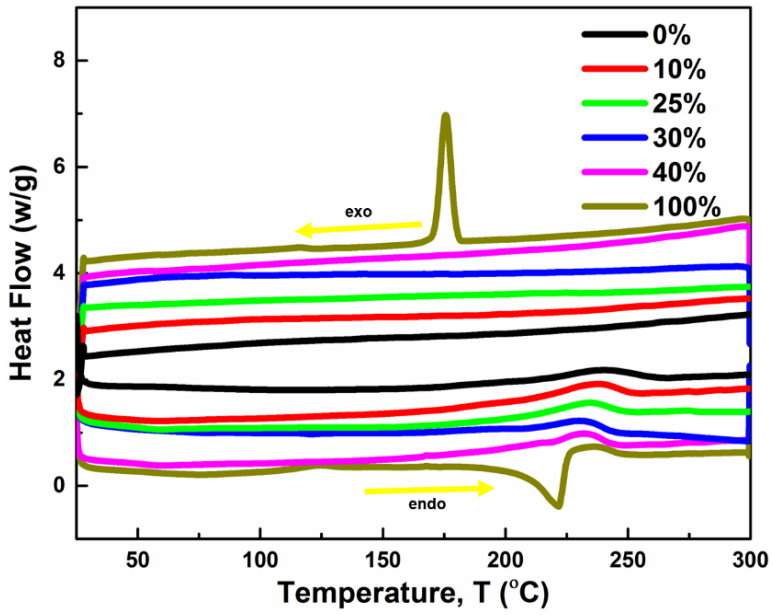

Figure 4.1.14. Differential scanning calorimetry (DSC) curves for the two donors' blend at different wt.% of DR3TSBDT loading.

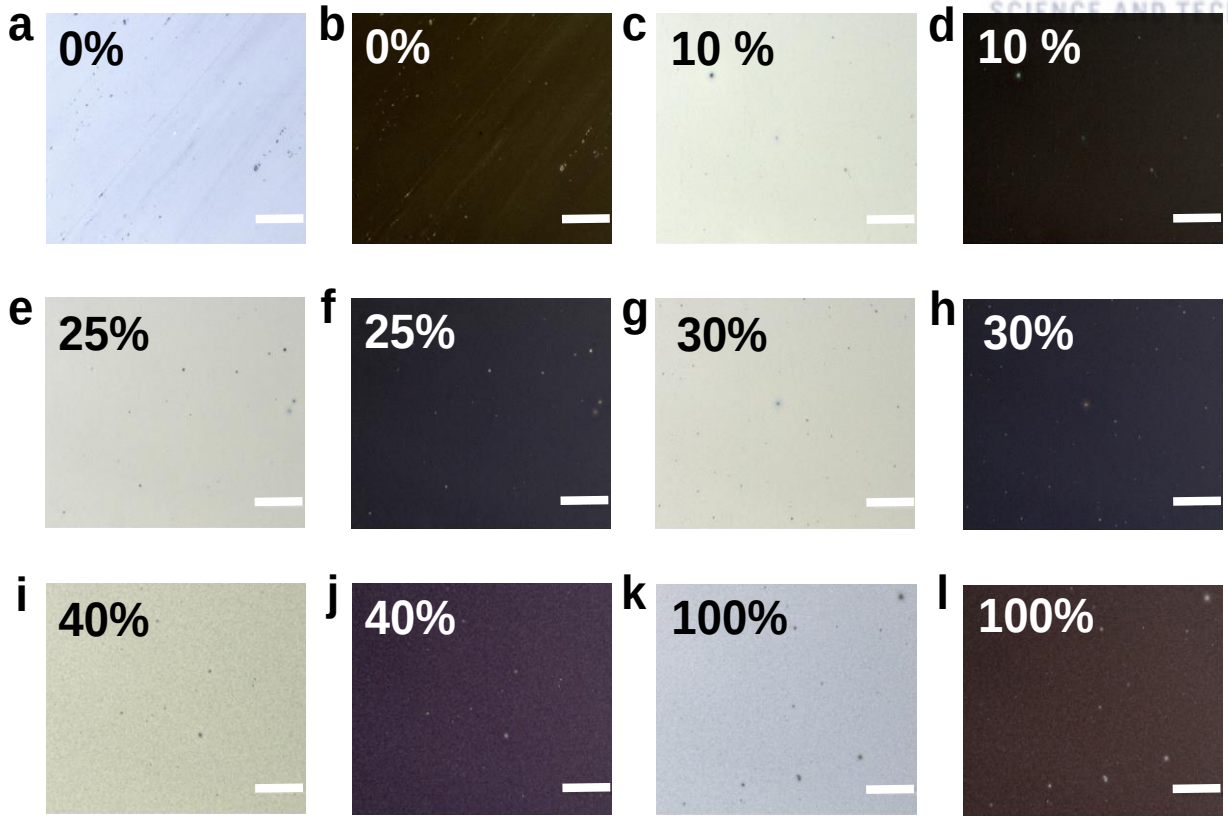

Figure 4.1.15. Optical microscopic images of ternary blends in normal and inverse color mode. a), b) 0%. c), d) 10%. e), f) 25%. g), h) 30%. i), j) 40%. k), l) 100% of DR3TSBDT in ternary blends. Scale bar is 20 μm.

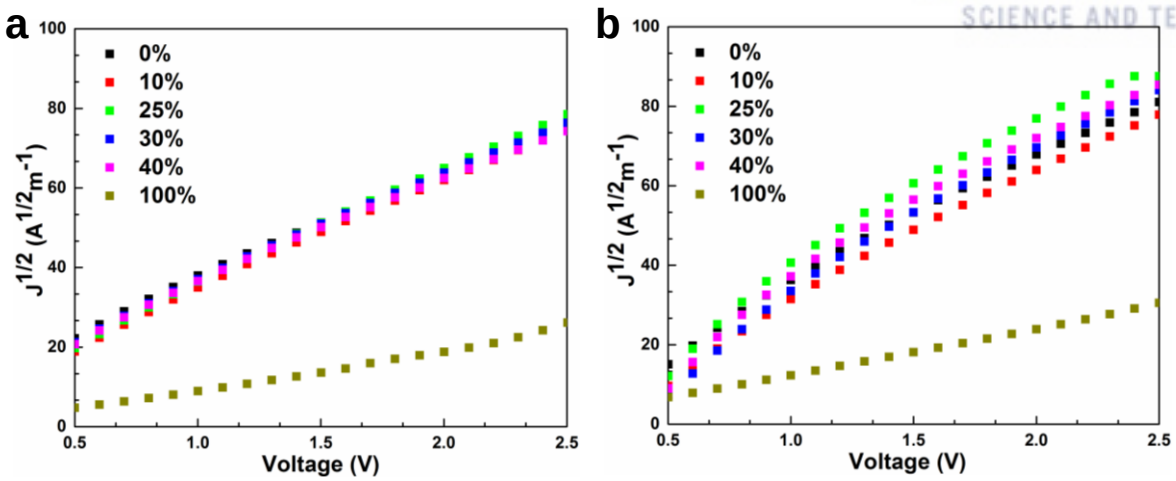

Figure 4.1.16. a) Hole mobility. b) Electron mobility of OSCs.

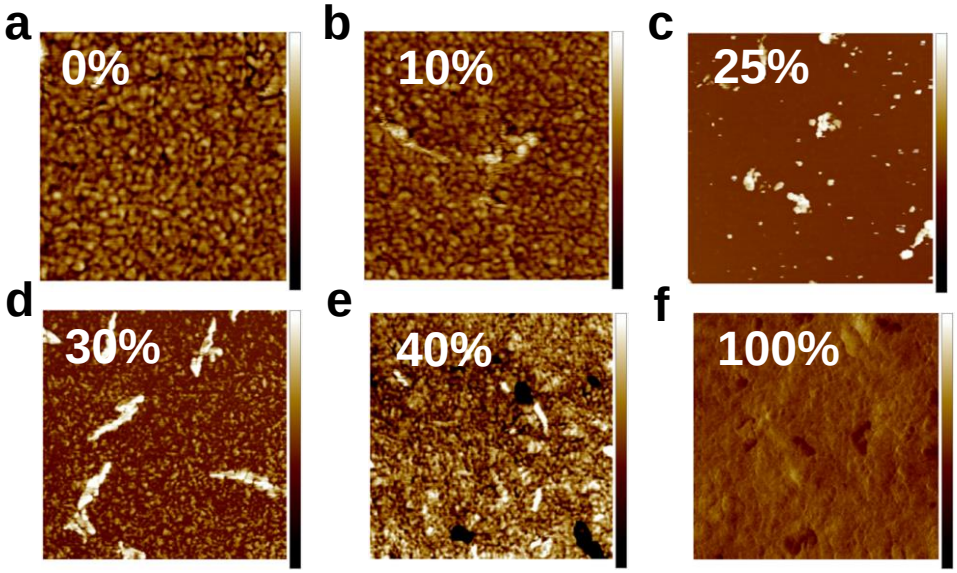

Figure 4.1.17. a) 0%, b) 10%, c) 25%, d) 30%, e) 40%, and f) 100% AFM phase images (scan size 1 × 1 μm). Different color bars are used for the phase variance.

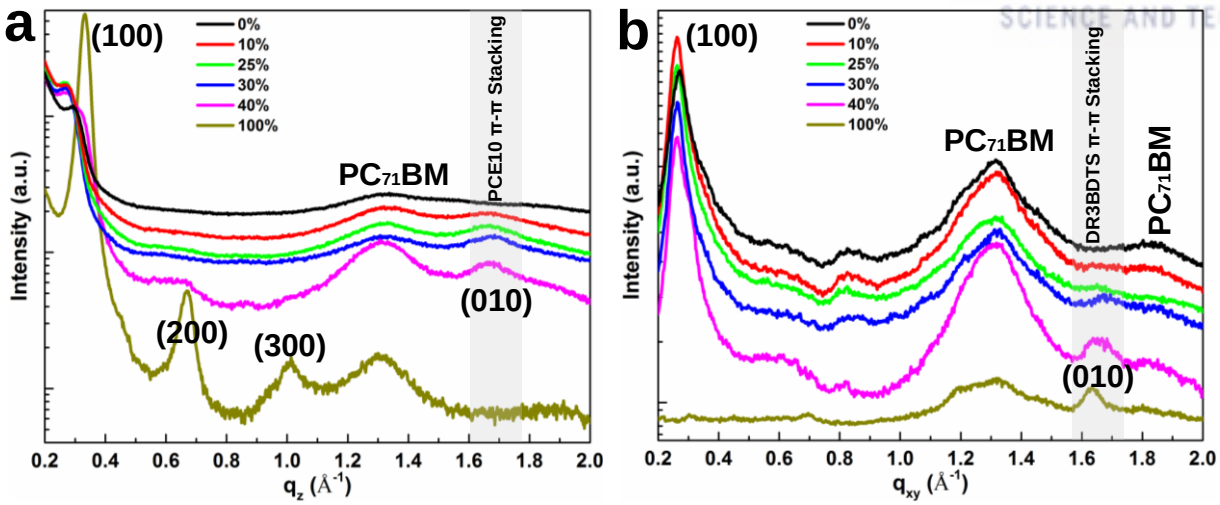

Figure 4.1.18. a) Out-of-plane. b) In-plane line cut profiles obtained from GIWAXS data.

Table 4.1.2. Lattice parameters in out-of-plane and in-plane direction for ternary system with different DR3TSBDT loading ratios.

Active layer	Unit cell long axis (100) ($Å^{-1}$)	d_{100} (Å)	π-π stacking cell axis (010) ($Å^{-1}$)	d_{010} (Å)
Out of plane				
0 %	0.2960	21.22	1.689	3.719
10 %	0.2793	22.50	1.677	3.747
25 %	0.2795	22.48	1.675	3.752
30 %	0.2748	22.86	1.674	3.753
40 %	0.2788	22.53	1.672	3.758
100 %	0.3202	19.62		
In plane				
0 %	0.2999	20.95		
10 %	0.2912	21.58	1.652	3.804
25 %	0.2881	21.81	1.648	3.813
30 %	0.2881	21.81	1.669	3.765
40 %	0.3043	20.65	1.650	3.808
100 %	0.3064	20.51	1.632	3.849

4.2 Study of Compatibility of Third component through Side Chain Engineering to Tune the Device Performance

Chapter 4.2 is reproduced in part with permission of "Harmonious Compatibility Dominates Influence of Side-Chain Engineering on Morphology and Performance of Ternary Solar Cells" from Kumari T. *et al. Adv. Energy Mater.* 2018, 8, 1800616 with permission from the John Wiley and Sons.

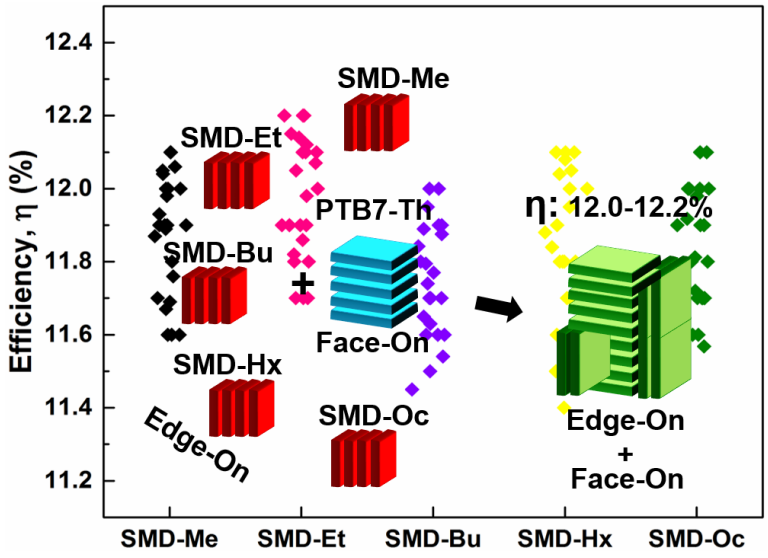

4.2.1 Introduction

Bulk-heterojunction (BHJ) binary organic solar cells (OSCs) composed of two components, such as an electron donor and electron acceptor; their power-conversion efficiency (PCE) has rapidly improved in the last decade, exceeding 11% in single- and tandem-junction architectures.[1] Based on improved understanding of the structure-property relationships, these improvements have been mainly driven by significant advances in the design and synthesis of better donor and acceptor materials.[1b, 2] It is well documented that π-conjugated backbones can determine the optoelectronic properties of the resulting semiconducting materials; hence, the development of novel π-conjugated backbones is a central issue in this field.[3] However, many recent studies have demonstrated the substantial impact of the alkyl side chains of the semiconductors on the performance of various organic electronic devices, including field-effect transistors and OSCs.[4] A series of in-depth investigations of the critical roles of side-chain engineering in the molecular design followed, shedding light on the structure-property relationship in binary OSCs.

On the contrary, the OSC community has recently developed ternary OSC structures designed to collect both high- and low-energy photons using three components in a single active layer.[5] This design is considered a promising candidate to exceed the theoretical Shockley–Queisser limit.[6] Owing to the simple single-step processing of the active layer and rapid improvements in the PCEs, an increasing amount of

research effort has been directed toward ternary OSCs. For example, various active layer compositions have been investigated, including two polymer donors blended with a fullerene acceptor, a polymer donor, and a small molecule/dye mixed with a fullerene acceptor, BHJ blend with an additional donor layer underneath, and a tri-layer containing two or more donors.[2f, 3c, 3d, 5c, 7] In spite of this interesting progress, the effect of side chains on the film morphology and OSC performance in the ternary blend systems has yet to be examined. As a result, a systematic investigation on side chain-dependent molecular packing and device performance in a given ternary system is of great importance to achieve a deep understanding of the essential role played by the side chains.

In our previous work, we reported a high-performance ternary OSC based on poly(4,8-bis(5-(2-ethylhexyl)thiophen-2-yl)benzo[1,2-*b*;4,5-*b*']dithiophene-2,6-diyl-alt-(4-(2-ethylhexyl)-3-fluorothieno[3,4-*b*]thiophene-)-2-carboxylate-2-6-diyl)) (PTB7-Th):[6,6]-phenyl-C_{71}-butyric acid methyl ester ($PC_{71}BM$) using DR3TSBDT as an additional small molecule donor (SMD).[1c, 8] In this study, we used SMDs with different terminal side-chain lengths to fabricate a series of ternary OSCs based on PTB7-Th:SMD:$PC_{71}BM$ and investigated the effects of the length of the side chains on the performance of this ternary system. Unlike the observed big dependent performance of the binary systems on the side-chain modulation, all ternary OSCs tested in this study exhibited almost identical, high PCEs of 12.0%–12.2%. The results of comprehensive electrical and morphological characterization showed good molecular compatibility between the two donors, regardless of the terminal side chains, resulting in the similar PCE values in the ternary systems.

4.2.2 Results and Discussion

4.2.2.1 *Structure and Optical Properties*

Figures 4.2.1a, b show the chemical structures of the SMD derivatives with different terminal side chains (methyl (Me), ethyl (Et), butyl (Bu), hexyl (Hx), and octyl (Oc)) (see their characterizations in the section 2.1.2a of chapter 2),[8] and the device structure showing the alloy-like structure[5e] where the two donor components are intimately mixed in the active layer. We refer to each SMD according to their side chain (SMD-Me, SMD-Et, SMD-Bu, SMD-Hx, and SMD-Oc) in the following discussions; their absorption spectra and cyclic voltammetry data are shown in supporting Figures 4.2.6a–d and Table 4.2.2 (see the section 4.2.5). We observed that tuning the terminal side chains did not cause any significant changes in the optical and electrochemical properties, even the absorption spectra of the ternary blending system (see the section 4.4.5, Figures 4.2.6b, c).

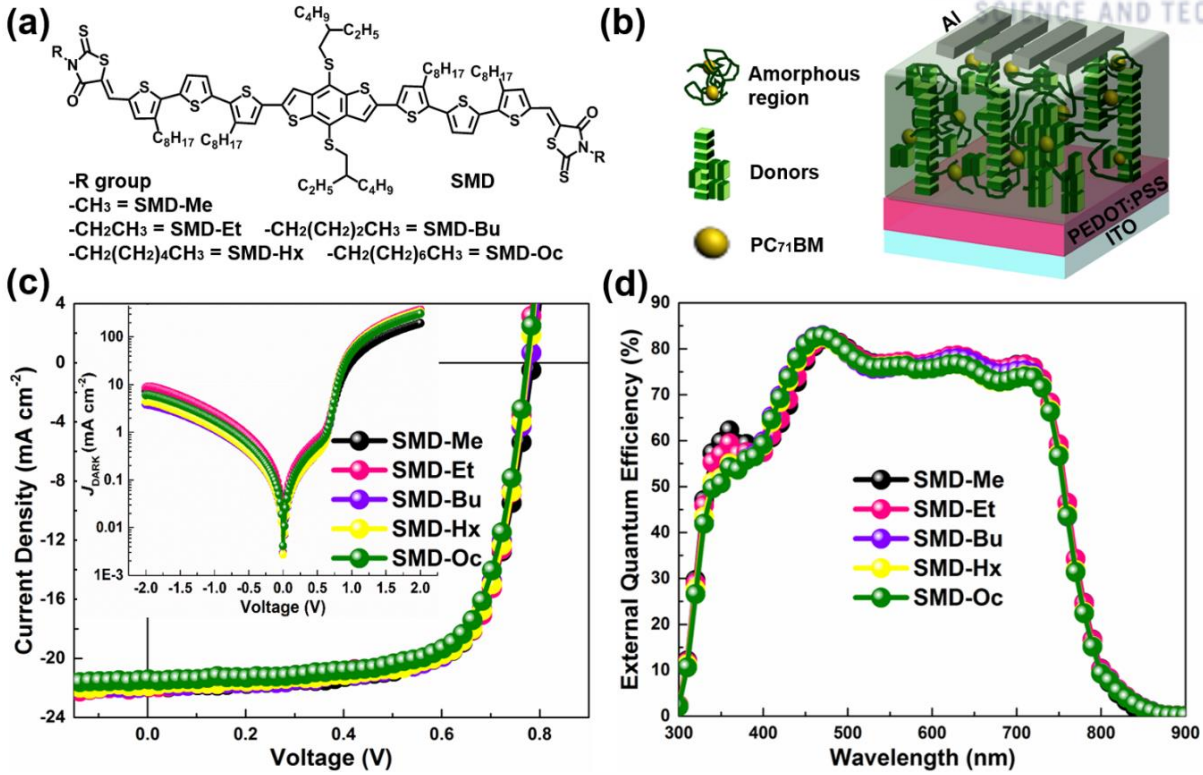

Figure 4.2.1. (a) Chemical structures of SMD derivatives with different terminal side chains used in this study. (b) Conventional device architecture. (c) *J*-*V* characteristics of ternary OSCs under AM 1.5G irradiation at 100 mW cm^{-2} (inset: *J*-*V* characteristics in the dark). (d) The corresponding EQE curves.

4.2.2.2 *Photovoltaic Performance*

The OSCs were fabricated using a conventional architecture of indium-tin oxide (ITO)/poly(3,4-ethylenedioxythiophene):poly(styrene sulfonate) (PEDOT:PSS)/active layer/Al. We carefully examined the performances of each ternary system with different weight ratio of the various SMDs (see the section 4.2.5, Tables 4.2.3–7), confirming that PTB7-Th:SMD:$PC_{71}BM$ (75:25:150 wt.%) blend cells with 1,8-diiodooctane additive (DIO, 3.0 vol.%) gave the best performances for all cases. This is consistent with the observation from our previous study.[1c] Figure 4.2.1c shows the representative current density versus voltage (*J*–*V*) characteristics of the optimized ternary OSCs under AM1.5G irradiation (100 $mWcm^{-2}$), and Table 4.2.1 summarizes the corresponding photovoltaic parameters. Before evaluating the photovoltaic properties of the ternary systems, we initially screened the performances of SMD:$PC_{71}BM$-based binary control devices fabricated from the same chlorobenzene solvent as the ternary system.

As can be seen from section 4.4.5 of supporting Figure 4.2.7 and Table 4.2.8, the binary devices showed very different behavior depending on the terminal side-chain length of the SMDs, yielding a large variation in PCE of 0.99%–5.97%. Besides, we further tested each binary system (Table 4.2.9, see section 4.2.5),

based on the optimized conditions of SMD-Et:$PC_{71}BM$-based binary devices reported by Chen et. al.,[8] still revealing significant changes in the performances as a function of the type of SDMs.

Table 4.2.1. Photovoltaic parameters and charge transport properties of OSCs using SMD derivatives with different terminal side chains.

Terminal Side	J_{SC} (mA cm^{-2})	V_{OC} (V)	FF (%)	PCE (%)	R_S (Ω)	R_{SH} ×10^4 (Ω)
SMD-Me	21.83 (22.00)	0.778 (0.780)	69.90 (70.43)	11.87 (12.1)	19.5 (20.2)	1.49 (3.73)
SMD-Et	21.75 (21.95)	0.777 (0.778)	70.88 (71.44)	11.98 (12.2)	16.5 (17.9)	1.76 (2.25)
SMD-Bu	21.82 (21.87)	0.775 (0.776)	69.65 (70.72)	11.78 (12.0)	14.9 (16.8)	1.37 (1.81)
SMD-Hx	21.86 (21.90)	0.776 (0.776)	69.78 (71.20)	11.84 (12.1)	19.1 (17.4)	1.16 (1.52)
SMD-Oc	21.69 (21.73)	0.774 (0.775)	69.85 (71.24)	11.73 (12.0)	18.3 (20.7)	1.42 (1.68)

*Average values obtained from at least 20 devices. The data in parentheses are the highest values.

Further information on the binary device fabrication can be found in the device fabrication section of chapter 2. Note also that despite the observed similarity between SMD frontier molecular orbital energies (see section 4.2.5, Figure 4.2.6d), the binary devices displayed very different V_{OC} values, and this might be due to the varied bend morphologies arising from the terminal side-chain engineering. However, very interestingly, all the ternary devices exhibited very similar, high PCE values of 12.0%–12.2% with a short-circuit current density (J_{SC}) of 21.73–22.00 mAcm^{-2}, open-circuit voltage (V_{OC}) of 0.775–0.780 V, devices also showed nearly identical external quantum efficiency curves (Figure 4.2.1d), consistent with the observed similarity between the absorption spectra of the ternary blends. The best device is certified from an independent laboratory (Nano Convergence Practical Application Center, South Korea) with a PCE of 11.918%, (see section 4.2.5, Figure 4.2.8). The average PCEs were achieved for 20 identical devices for each system, and the corresponding parameters (i.e., PCE, J_{SC}, V_{OC}, and FF) were also analyzed independently (see section 4.2.5, Figure 4.2.9). It is reasonable to believe that regardless of the lengths of the terminal side chains in SMDs, the channels formed by the good molecular compatibility of the two donors (PTB7-Th:SMD), as demonstrated by our previous result,[1c] were responsible for the similar behavior of all ternary blends. Note that for all devices, we also observed similar low leakage currents (~10^{-3} mAcm^{-2}) under reverse bias and high rectification ratios (~10^5) in the dark J−V characteristics (inset of Figure 4.2.1c), indicating similar charge extraction efficiencies.

4.2.2.3 *Charge Carrier Transport and Recombination Dynamics*

Next, we characterized the charge-carrier mobilities of the hole- and electron-only ternary devices to examine the vertical charge transport properties using a space-charge limited curve (SCLC).[9] All ternary blend systems showed similar SCLC hole (μ_h) and electron (μ_e) mobilities of 1.17–1.49 $\times 10^{-4}$ $cm^2V^{-1}s^{-1}$ and 0.60–0.80 $\times 10^{-4}$ $cm^2V^{-1}s^{-1}$, respectively (see section 4.2.5, Figure 4.2.10 and Table 4.2.10), resulting in adequately balanced μ_h/μ_e ratios of 1.51–2.38.

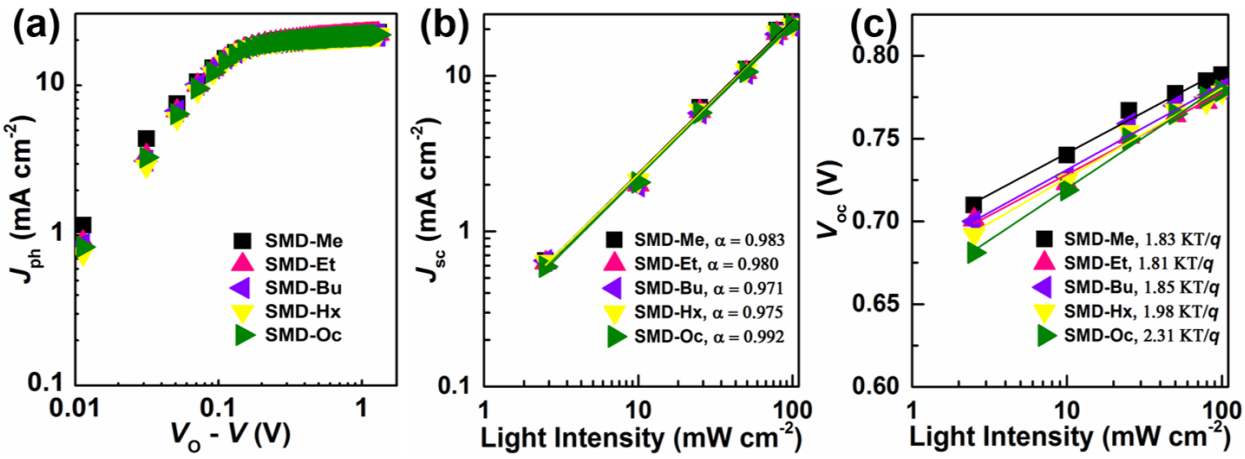

Figure 4.2.2. (a) Photo current measurement of ternary devices. (b) Dependence of current density (J_{SC}). (c) Open-circuit voltage (V_{OC}) on light intensity of OSCs using SMD derivatives with different terminal side chains.

To gain a deeper insight into the photovoltaic responses of the ternary blends as a function of the length of the terminal side chains, we firstly quantitatively analyzed the dependence of the net photocurrent (J_{ph}) on the effective applied voltage (V_{eff}) using $J_{ph} = J_L - J_D$ (where J_L is the current under illumination, and J_D is the dark current) and $V_{eff} = V_0 - V$ (where V_0 is the voltage at $J_{ph} = 0$, and V is the applied bias voltage).[1d, 10] As shown in Figure 4.2.2a and Table 4.2.4 of section 4.2.5, for all samples, the J_{ph} values became saturated at a V_{eff} of ~0.3 V and J_{ph}/saturation current density (J_{sat}) ratios in the low effective voltage range of V_{eff} > 0.3 were similar (~98%), implying similar charge dissociation and collection efficiencies. The recombination kinetics were also investigated by plotting the variations in J_{SC} and V_{OC} as functions of the applied light intensity in range of 10–100 $mWcm^{-2}$.[11] As shown in Figures 4.2.2b, c, all the devices showed a linear dependence of J_{SC} with light intensity and similar coefficients (α) of 0.97–0.99, corresponding to the power law fit $J_{SC} \propto I^{\alpha}$ (where I is the light intensity). In addition, the slopes (kT/q) of V_{OC} vs. the natural logarithm of the light intensity of the devices were measured, where k, T, and q are Boltzmann's constant, temperature in Kelvin, and the elementary charge, respectively; for samples SMD-Me, SMD-Et, SMD-Bu, SMD-Hx, and SMD-Oc, these values were 1.83, 1.81, 1.85, 1.98, and 2.31, respectively. These results

suggest that all the ternary devices had very weak bimolecular recombination with slightly different degrees of Shockley-Read-Hall (trap-assisted recombination).

The series resistance (R_S) and shunt resistance (R_{SH}) are also important parameters for explaining OSC device characteristics; R_S is derived from the bulk resistances of the active layer and electrodes and from the contact resistances between the active layer and electrodes, while R_{SH} originates from the leakage current from the edge of the device or that induced by pinholes in the cell. Therefore, we also characterized the R_S and R_{SH} of each optimized device at various illumination intensities (see section 4.2.5, Figure 4.2.11).[12] The R_S and R_{SH} values at 100 mWcm^{-2} are summarized in Table 4.2.1. All the devices gave similar, small R_S values (less than 20 Ωcm^2) and high R_{SH} values (more than 11 KΩcm^2), suggesting a suppressed leakage current and improved diode behavior; this is consistent with the usual high FF values obtained from the ternary OSCs.

To further quantify resistive and capacitive contributions to the overall electrical response of the OSCs, we undertook electrochemical impedance spectroscopy of the ternary systems.[9d, 13] Figure 4.2.3 shows Nyquist plots of the ternary devices at V_{OC} both in the dark and at 100 mWcm^{-2} illumination over the frequency range of 1 KHz to 1 MHz, where no direct current is allowed, so that transport mechanisms play a secondary role. All Nyquist plots showed a single semicircle in the complex plot of the imaginary part versus the real part of the complex impedance. We observed almost no variation in the diameters of the semicircles obtained from the impedance spectra. The fitted curves are shown in Figure 4.2.3a, d as dashed lines together with the experimental data (denoted as symbols), where a simplified circuit model was used to fit these curves (see the inset of Figure 4.2.3a). The corresponding parameters are listed in the section 4.2.5, Table 4.2.11. In this circuit, R_{OS} represents the Ohmic series resistance including the electrodes and bulk resistance in the active layer. R_{CT} is associated with the interface charge transport process, defined by the charge-transfer resistance, and the constant phase element (CPE) suggests a non-ideal behavior of the capacitor. The CPE can be used in place of a capacitance-like element to compensate for inhomogeneity at the interfaces of the active layer components. The CPE is commonly defined by two values, CPE-T and CPE-P. When CPE-P equals 1, then the CPE is identical to an ideal capacitor without defects and/or grain boundaries.[13d, 14] All the ternary devices showed similar CPE-P values (~0.95 in the dark and ~0.85 under illumination) and R_{CT} values (~16 Ω in the dark and ~160 Ω under illumination), indicating that the interface capacitance between the compatible donors and $PC_{71}BM$ acceptor in the active layer was electrically excellent with a homogenous manner, allowing for efficient charge transport in the tested devices.

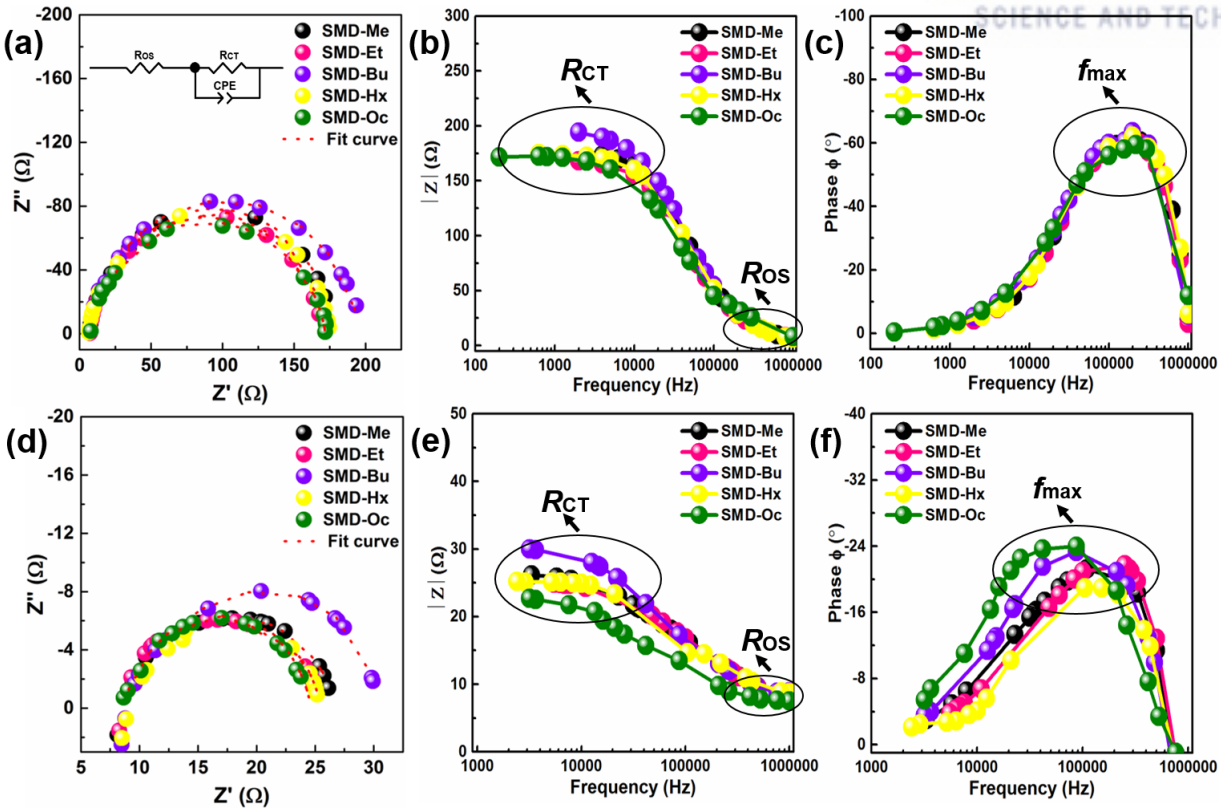

Figure 4.2.3. Nyquist plots of the ternary devices in (a) dark (d) illumination condition. Inset of (a) is an equivalent circuit employed in fitting different impedance curves. (b), (e) The frequency-dependent real parts and (c), (f) the frequency-dependent imaginary parts in the impedance spectra of the ternary devices using SMD derivatives with different terminal side chains where (b), (c) in the dark and (e), (f) under illumination.

In addition, Figures 4.2.3b, e show the frequency-dependent real parts of the impedance of the ternary devices. We observed two plateaus in the low-frequency (<10 kHz) and high-frequency (>5 MHz) regions under both conditions. The plateau in the low-frequency region corresponded to R_{CT}, while the high-frequency plateau was ascribed to R_{OS}. The R_{CT} and R_{OS} values obtained for all ternary devices were similar. As can be seen from the corresponding imaginary parts shown in Figures 4.2.3c, f, the maximum frequency (f_{max}) values in the highest virtual step impedance were nearly identical for all conditions, except for the SMD-Oc-based device under illumination, for which the f_{max} slightly shifted to lower frequencies compared with that in the other samples. The f_{max} is related to the relaxation time (τ) by $f_{max} \propto 1/\tau$; this implies that all devices had similar electron lifetimes and diffusion rates, with only a weak variation in the case of SMD-Oc.

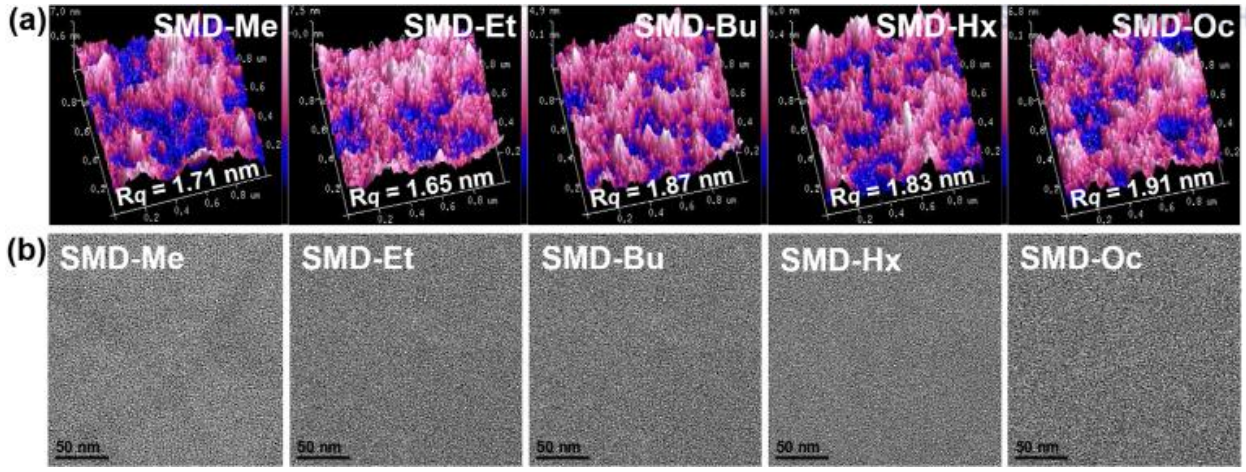

Figure 4.2.4. (a) AFM topography height images (scan size 1×1 μm) and, (b) TEM images of ternary blend films using SMD derivatives with different terminal side chains.

4.2.2.4 *Film Morphology and Microstructure*

As we observed a strong morphology–performance relationship, detailed investigation of the morphology and molecular packing was performed using various structural characterization techniques. All of the ternary films exhibited similar nanostructured morphologies with a surface roughness of 1.65−1.91 nm, as shown by atomic force microscopy images (Figure 4.2.4a and Figure 4.2.12 of the section 4.2.5). Transmission electron microscopy images of the blend films (Figure 4.2.4b) also showed similar, smooth features with phase separation on the nanometer scale, where the bright and dark regions correspond to the two donors and $PC_{71}BM$-rich domains, respectively. These findings showed that all ternary blends had a similar morphology, regardless of the type of terminal side chain of the SMD material, which is attributed to the good molecular compatibility between the two donors in the blend with $PC_{71}BM$. The similar morphological characteristics of the ternary blends were further confirmed by energy dispersive X-ray elemental mapping and optical florescence microscopy measurements (see the section 4.2.5, Figure 4.2.13 and 4.2.14). Note that the florescence images of the ternary films revealed a well-mixed and homogenous structure, while images of the binary blends (SMD:$PC_{71}BM$) showed that the morphology was highly dependent on the SMD structure (see the section 4.2.5, Figure 4.2.15), which is consistent with the different performances observed for the ternary and binary OSCs. From the differential scanning calorimetry (DSC) (see the section 4.2.5, Figure 4.2.16), it is apparent that, during the heating/cooling cycles, all the pure SMDs undergo endothermic and exothermic transitions, while no such peaks are observed in all of the two donor blend systems, supporting excellent compatibility between the two donor components.[5e, 15]

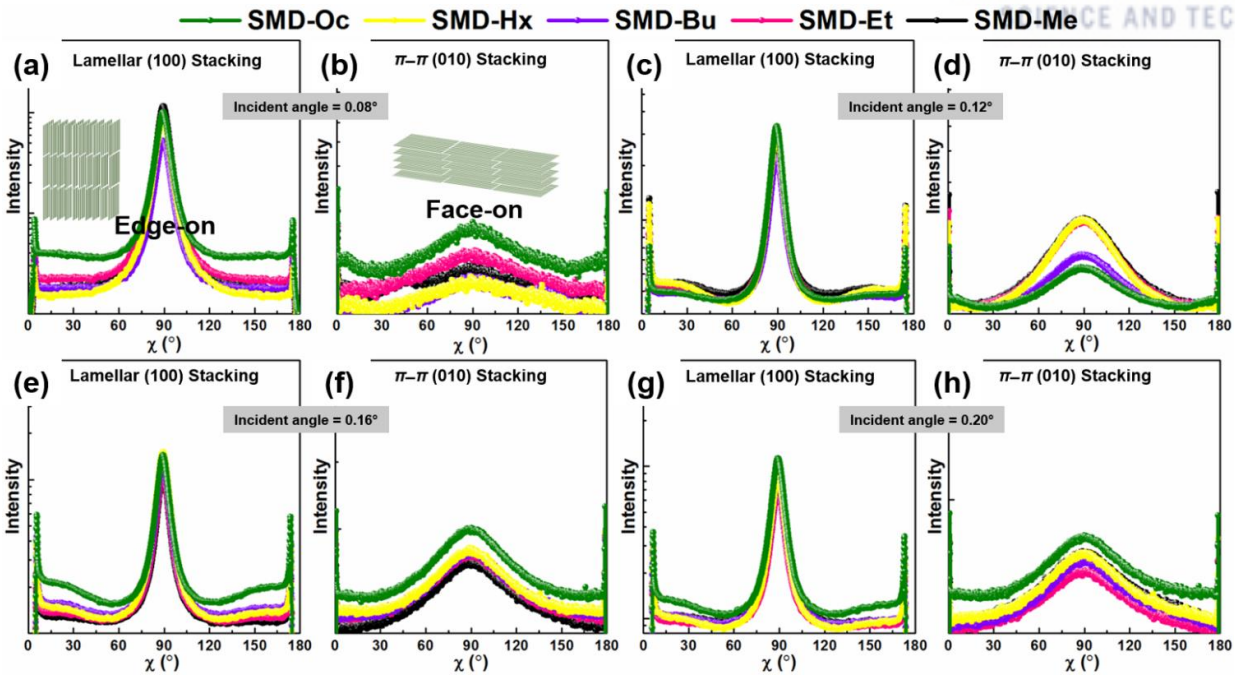

Figure 4.2.5. (a) Circular cut profiles. (a), (c), (e), and (g) Lamellar (*100*) stacking. (b), (d), (f), and (h) *π*–*π* (*010*) stacking obtained from GIWAXS data measured at different angle for ternary blend films using SMD derivatives with different terminal side chains. Inset of (a) and (b) are the corresponding stacking illustration diagram.

Finally, we conducted grazing-incidence wide-angle X-ray scattering (GIWAXS) experiments to further elucidate the structural order in the ternary blend films and quantitatively characterize the depth-dependent structural changes in the ternary films; the experiments were performed at various incidence angles (α_i) of 0.08°, 0.12°, 0.16°, and 0.20°.[16] As seen from the Figure 4.2.17 of section 4.2.5, a bimodal texture of mixed edge-on and face-on orientations was observed for all ternary films at all incident angles, with evident *(010)* *π*–*π* stacking and *(100)* lamellar *d*-spacing reflections along both the in-plane and out of-plane directions. Note that the strong edge-on *(010)* *π*–*π* stacking peak is present for both pure SMD and binary blend (SMD:$PC_{71}BM$) films (Figure 4.2.18, see the section 4.2.5), indicating that the edge-on molecular orientation in the ternary films is mainly originated from the crystallinity of SMDs. Figure 4.2.5 shows the circular cut profiles of the (*100*) and (*010*) diffraction peaks, where the intensity of the azimuthal angle (χ) of 45°–135° was attributed to the parallel (//) *π*–*π* stacking of the substrate and χ of 0°–45° and 135°–180° to the perpendicular (⊥) *π*–*π* stacking and vice versa for the lamellar stacking, respectively, as shown in the inset slab diagram in Figures 4.2.5a, b. In all cases, the nearly identical GIWAXS data proved that all ternary blends had similar molecular orientation and crystallinity, independent of the depth. It is worth noting that as compared to ternary blend (see the section 4.2.5, Figure 4.2.19), we observed significant

changes in the diffraction patterns for both pure SMD and binary blend (SMD:$PC_{71}BM$) films as a function of SMD structures (see the section 4.2.5, Figures 4.2.19, 4.2.20, and Table 4.2.12).

4.2.3 Conclusion

In conclusion, we demonstrated high-performance ternary OSCs using various SMDs with different terminal side chains incorporated into a PTB7-Th:$PC_{71}BM$ host blend. The performance of all ternary OSCs was obviously different from those of the SMD-based control binary OSCs and was highly independent of the side chains of SMD material. As a result, similar, unprecedented PCE values of 12.0%–12.2% were achieved for all ternary OSCs. Despite the fact that a variation in the terminal side-chain length of SMDs has a profound impact on both the morphology and OSC performance for the binary OSCs, the present PCE behavior in the ternary systems was due to good molecular compatibility between the PTB7-Th and SMD materials, regardless of the side-chain length of the SMDs. This was evidenced by a combination of electrical measurements of the internal resistance, recombination properties, and interfacial charge-transfer kinetics, as well as morphological characterization. This work demonstrates that the alloy-like structure induced by the high compatibility of donor molecules in the ternary systems can dominate any possible performance differences related to the side-chain engineering, contributing judicious molecular design rules and working mechanisms for the further development of such OSCs.

4.2.4 References

1. (a) Gasparini, N.; Lucera, L.; Salvador, M.; Prosa, M.; Spyropoulos, G. D.; Kubis, P.; Egelhaaf, H.-J.; Brabec, C. J.; Ameri, T., High-performance ternary organic solar cells with thick active layer exceeding 11% efficiency. *Energy Environ. Sci.* **2017,** *10* (4), 885-892; (b) Jiang, W.; Yu, R.; Liu, Z.; Peng, R.; Mi, D.; Hong, L.; Wei, Q.; Hou, J.; Kuang, Y.; Ge, Z., Ternary Nonfullerene Polymer Solar Cells with 12.16% Efficiency by Introducing One Acceptor with Cascading Energy Level and Complementary Absorption. *Adv. Mater.* **2018,** *30* (1), 1703005-n/a; (c) Kumari, T.; Lee, S. M.; Kang, S.-H.; Chen, S.; Yang, C., Ternary solar cells with a mixed face-on and edge-on orientation enable an unprecedented efficiency of 12.1%. *Energy Environ. Sci.* **2017,** *10* (1), 258-265; (d) Nian, L.; Gao, K.; Liu, F.; Kan, Y.; Jiang, X.; Liu, L.; Xie, Z.; Peng, X.; Russell, T. P.; Ma, Y., 11% Efficient Ternary Organic Solar Cells with High Composition Tolerance via Integrated Near-IR Sensitization and Interface Engineering. *Adv. Mater.* **2016,** *28* (37), 8184-8190; (e) Xu, X.; Yu, T.; Bi, Z.; Ma, W.; Li, Y.; Peng, Q., Realizing Over 13% Efficiency in Green-Solvent-Processed Nonfullerene Organic Solar Cells Enabled by 1,3,4-Thiadiazole-Based Wide-Bandgap

Copolymers. *Adv. Mater.* **2018,** *30* (3), 1703973-n/a; (f) Zhang, T.; Zhao, X.; Yang, D.; Tian, Y.; Yang, X., Ternary Organic Solar Cells with >11% Efficiency Incorporating Thick Photoactive Layer and Nonfullerene Small Molecule Acceptor. *Adv. Energy Mater.* **2018,** *8* (4), 1701691-n/a; (g) Zhao, W.; Li, S.; Yao, H.; Zhang, S.; Zhang, Y.; Yang, B.; Hou, J., Molecular Optimization Enables over 13% Efficiency in Organic Solar Cells. *J. Am. Chem. Soc.* **2017,** *139* (21), 7148-7151; (h) Zhao, W.; Li, S.; Zhang, S.; Liu, X.; Hou, J., Ternary Polymer Solar Cells based on Two Acceptors and One Donor for Achieving 12.2% Efficiency. *Adv. Mater.* **2017,** *29* (2), 1604059; (i) Su, Y.-W.; Lan, S.-C.; Wei, K.-H., Organic photovoltaics. *Mater. Today* **2012,** *15* (12), 554-562.

2. (a) An, Q.; Zhang, F.; Sun, Q.; Zhang, M.; Zhang, J.; Tang, W.; Yin, X.; Deng, Z., Efficient organic ternary solar cells with the third component as energy acceptor. *Nano Energy* **2016,** *26*, 180-191; (b) Benten, H.; Nishida, T.; Mori, D.; Xu, H.; Ohkita, H.; Ito, S., High-performance ternary blend all-polymer solar cells with complementary absorption bands from visible to near-infrared wavelengths. *Energy Environ. Sci.* **2016,** *9* (1), 135-140; (c) Chen, Y.; Ye, P.; Zhu, Z.-G.; Wang, X.; Yang, L.; Xu, X.; Wu, X.; Dong, T.; Zhang, H.; Hou, J.; Liu, F.; Huang, H., Achieving High-Performance Ternary Organic Solar Cells through Tuning Acceptor Alloy. *Adv. Mater.* **2017,** *29* (6), 1603154; (d) Gasparini, N.; Jiao, X.; Heumueller, T.; Baran, D.; Matt, G. J.; Fladischer, S.; Spiecker, E.; Ade, H.; Brabec, C. J.; Ameri, T., Designing ternary blend bulk heterojunction solar cells with reduced carrier recombination and a fill factor of 77%. *Nat. Energy* **2016,** *1*, 16118; (e) Liu, T.; Guo, Y.; Yi, Y.; Huo, L.; Xue, X.; Sun, X.; Fu, H.; Xiong, W.; Meng, D.; Wang, Z.; Liu, F.; Russell, T. P.; Sun, Y., Ternary Organic Solar Cells Based on Two Compatible Nonfullerene Acceptors with Power Conversion Efficiency >10%. *Adv. Mater.* **2016,** *28* (45), 10008-10015; (f) Xiao, L.; Gao, K.; Zhang, Y.; Chen, X.; Hou, L.; Cao, Y.; Peng, X., A complementary absorption small molecule for efficient ternary organic solar cells. *J. Mater. Chem. A* **2016,** *4* (14), 5288-5293; (g) Su, Y.-W.; Lin, Y.-C.; Wei, K.-H., Evolving molecular architectures of donor-acceptor conjugated polymers for photovoltaic applications: from one-dimensional to branched to two-dimensional structures. *J. Mater. Chem. A* **2017,** *5* (46), 24051-24075.

3. (a) Facchetti, A., π-Conjugated Polymers for Organic Electronics and Photovoltaic Cell Applications. *Chem. Mater.* **2011,** *23* (3), 733-758; (b) Guo, X.; Baumgarten, M.; Müllen, K., Designing π-conjugated polymers for organic electronics. *Prog. Polym. Sci.* **2013,** *38* (12), 1832-1908; (c) Ke, L.; Min, J.; Adam, M.; Gasparini, N.; Hou, Y.; Perea, J. D.; Chen, W.; Zhang, H.; Fladischer, S.; Sale, A.-C.; Spiecker, E.; Tykwinski, R. R.; Brabec, C. J.; Ameri, T., A Series of Pyrene-Substituted Silicon Phthalocyanines as Near-IR Sensitizers in Organic Ternary Solar Cells. *Adv. Energy Mater.* **2016,** *6* (7), 1502355; (d) Koppe, M.; Egelhaaf, H.-J.; Dennler, G.; Scharber, M. C.; Brabec, C. J.; Schilinsky, P.; Hoth, C. N., Near IR Sensitization of Organic Bulk Heterojunction Solar Cells: Towards Optimization of the Spectral Response of Organic Solar Cells. *Adv. Funct. Mater.* **2010,** *20* (2), 338-346; (e) Liu, S.; You, P.; Li, J.; Li, J.; Lee,

C.-S.; Ong, B. S.; Surya, C.; Yan, F., Enhanced efficiency of polymer solar cells by adding a high-mobility conjugated polymer. *Energy Environ. Sci.* **2015,** *8* (5), 1463-1470; (f) Lu, H.; Zhang, X.; Li, C.; Wei, H.; Liu, Q.; Li, W.; Bo, Z., Performance Enhancement of Polymer Solar Cells by Using Two Polymer Donors with Complementary Absorption Spectra. *Macromol. Rapid Commun.* **2015,** *36* (14), 1348-1353; (g) Scharber, M. C.; Mühlbacher, D.; Koppe, M.; Denk, P.; Waldauf, C.; Heeger, A. J.; Brabec, C. J., Design Rules for Donors in Bulk-Heterojunction Solar Cells—Towards 10 % Energy-Conversion Efficiency. *Adv. Mater.* **2006,** *18* (6), 789-794.

4. (a) Aldrich, T. J.; Swick, S. M.; Melkonyan, F. S.; Marks, T. J., Enhancing Indacenodithiophene Acceptor Crystallinity via Substituent Manipulation Increases Organic Solar Cell Efficiency. *Chem. Mater.* **2017,** *29* (24), 10294-10298; (b) Cabanetos, C.; El Labban, A.; Bartelt, J. A.; Douglas, J. D.; Mateker, W. R.; Fréchet, J. M. J.; McGehee, M. D.; Beaujuge, P. M., Linear Side Chains in Benzo[1,2-b:4,5-b′]dithiophene–Thieno[3,4-c]pyrrole-4,6-dione Polymers Direct Self-Assembly and Solar Cell Performance. *J. Am. Chem. Soc.* **2013,** *135* (12), 4656-4659; (c) Duan, C.; Willems, R. E. M.; van Franeker, J. J.; Bruijnaers, B. J.; Wienk, M. M.; Janssen, R. A. J., Effect of side chain length on the charge transport, morphology, and photovoltaic performance of conjugated polymers in bulk heterojunction solar cells. *J. Mater. Chem. A* **2016,** *4* (5), 1855-1866; (d) Friedel, B.; McNeill, C. R.; Greenham, N. C., Influence of Alkyl Side-Chain Length on the Performance of Poly(3-alkylthiophene)/Polyfluorene All-Polymer Solar Cells. *Chem. Mater.* **2010,** *22* (11), 3389-3398; (e) Lee, M.-H.; Kim, J.; Kang, M.; Kim, J.; Kang, B.; Hwang, H.; Cho, K.; Kim, D.-Y., Precise Side-Chain Engineering of Thienylenevinylene–Benzotriazole-Based Conjugated Polymers with Coplanar Backbone for Organic Field Effect Transistors and CMOS-like Inverters. *ACS Appl. Mater. Interfaces* **2017,** *9* (3), 2758-2766; (f) Min, J.; Luponosov, Y. N.; Gerl, A.; Polinskaya, M. S.; Peregudova, S. M.; Dmitryakov, P. V.; Bakirov, A. V.; Shcherbina, M. A.; Chvalun, S. N.; Grigorian, S.; Kaush-Busies, N.; Ponomarenko, S. A.; Ameri, T.; Brabec, C. J., Alkyl Chain Engineering of Solution-Processable Star-Shaped Molecules for High-Performance Organic Solar Cells. *Adv. Energy Mater.* **2014,** *4* (5), 1301234; (g) Yin, X.; An, Q.; Yu, J.; Guo, F.; Geng, Y.; Bian, L.; Xu, Z.; Zhou, B.; Xie, L.; Zhang, F.; Tang, W., Side-chain Engineering of Benzo[1,2-b:4,5-b']dithiophene Core-structured Small Molecules for High-Performance Organic Solar Cells. *Sci. Rep.* **2016,** *6*, 25355; (h) Lin, Y.-C.; Cheng, H.-W.; Su, Y.-W.; Lin, B.-H.; Lu, Y.-J.; Chen, C.-H.; Chen, H.-C.; Yang, Y.; Wei, K.-H., Molecular engineering of side chain architecture of conjugated polymers enhances performance of photovoltaics by tuning ternary blend structures. *Nano Energy* **2018,** *43*, 138-148.

5. (a) Ameri, T.; Khoram, P.; Min, J.; Brabec, C. J., Organic Ternary Solar Cells: A Review. *Adv. Mater.* **2013,** *25* (31), 4245-4266; (b) An, Q.; Zhang, F.; Zhang, J.; Tang, W.; Deng, Z.; Hu, B., Versatile ternary organic solar cells: a critical review. *Energy Environ. Sci.* **2016,** *9* (2), 281-322; (c) Yang, L.; Yan, L.; You, W., Organic Solar Cells beyond One Pair of Donor–Acceptor: Ternary Blends and More. *J. Phys. Chem.*

Lett. **2013,** *4* (11), 1802-1810; (d) Zhang, G.; Zhang, K.; Yin, Q.; Jiang, X.-F.; Wang, Z.; Xin, J.; Ma, W.; Yan, H.; Huang, F.; Cao, Y., High-Performance Ternary Organic Solar Cell Enabled by a Thick Active Layer Containing a Liquid Crystalline Small Molecule Donor. *J. Am. Chem. Soc.* **2017,** *139* (6), 2387-2395; (e) Zhang, J.; Zhang, Y.; Fang, J.; Lu, K.; Wang, Z.; Ma, W.; Wei, Z., Conjugated Polymer–Small Molecule Alloy Leads to High Efficient Ternary Organic Solar Cells. *J. Am. Chem. Soc.* **2015,** *137* (25), 8176-8183; (f) Zhao, F.; Li, Y.; Wang, Z.; Yang, Y.; Wang, Z.; He, G.; Zhang, J.; Jiang, L.; Wang, T.; Wei, Z.; Ma, W.; Li, B.; Xia, A.; Li, Y.; Wang, C., Combining Energy Transfer and Optimized Morphology for Highly Efficient Ternary Polymer Solar Cells. *Adv. Energy Mater.* **2017,** *7* (13), 1602552; (g) Lin, Y.-C.; Su, Y.-W.; Li, J.-X.; Lin, B.-H.; Chen, C.-H.; Chen, H.-C.; Wu, K.-H.; Yang, Y.; Wei, K.-H., Energy transfer within small molecule/conjugated polymer blends enhances photovoltaic efficiency. *J. Mater. Chem. A* **2017,** *5* (34), 18053-18063.

6. (a) Lu, L.; Kelly, M. A.; You, W.; Yu, L., Status and prospects for ternary organic photovoltaics. *Nat. Photon.* **2015,** *9* (8), 491-500; (b) Savoie, B. M.; Dunaisky, S.; Marks, T. J.; Ratner, M. A., The Scope and Limitations of Ternary Blend Organic Photovoltaics. *Adv. Energy Mater.* **2015,** *5* (3), 1400891; (c) Shockley, W.; Queisser, H. J., Detailed Balance Limit of Efficiency of p-n Junction Solar Cells. *J. Appl. Phys.* **1961,** *32* (3), 510-519.

7. (a) Fan, B.; Zhong, W.; Jiang, X.-F.; Yin, Q.; Ying, L.; Huang, F.; Cao, Y., Improved Performance of Ternary Polymer Solar Cells Based on A Nonfullerene Electron Cascade Acceptor. *Adv. Energy Mater.* **2017,** *7* (11), 1602127; (b) Ghasemi, M.; Ye, L.; Zhang, Q.; Yan, L.; Kim, J.-H.; Awartani, O.; You, W.; Gadisa, A.; Ade, H., Panchromatic Sequentially Cast Ternary Polymer Solar Cells. *Adv. Mater.* **2017,** *29* (4), 1604603; (c) Honda, S.; Ohkita, H.; Benten, H.; Ito, S., Multi-colored dye sensitization of polymer/fullerene bulk heterojunction solar cells. *Chem. Commun.* **2010,** *46* (35), 6596-6598; (d) Li, H.; Lu, K.; Wei, Z., Polymer/Small Molecule/Fullerene Based Ternary Solar Cells. *Adv. Energy Mater.* **2017,** *7*, 1602540; (e) Zhang, M.; Zhang, F.; An, Q.; Sun, Q.; Wang, W.; Ma, X.; Zhang, J.; Tang, W., Nematic liquid crystal materials as a morphology regulator for ternary small molecule solar cells with power conversion efficiency exceeding 10%. *J. Mater. Chem. A* **2017,** *5* (7), 3589-3598.

8. Kan, B.; Zhang, Q.; Li, M.; Wan, X.; Ni, W.; Long, G.; Wang, Y.; Yang, X.; Feng, H.; Chen, Y., Solution-Processed Organic Solar Cells Based on Dialkylthiol-Substituted Benzodithiophene Unit with Efficiency near 10%. *J. Am. Chem. Soc.* **2014,** *136* (44), 15529-15532.

9. (a) Ebenhoch, B.; Thomson, S. A. J.; Genevičius, K.; Juška, G.; Samuel, I. D. W., Charge carrier mobility of the organic photovoltaic materials PTB7 and PC71BM and its influence on device performance. *Org. Electron.* **2015,** *22* (Supplement C), 62-68; (b) Reid, O. G.; Munechika, K.; Ginger, D. S., Space Charge Limited Current Measurements on Conjugated Polymer Films using Conductive Atomic Force Microscopy. *Nano Lett.* **2008,** *8* (6), 1602-1609; (c) Seki, K., Overall current-voltage characteristics of space charge

controlled currents for thin films by a single carrier species. *J. Appl. Phys.* **2014,** *116* (6), 063716; (d) Sharma, R.; Lee, H.; Gupta, V.; Kim, H.; Kumar, M.; Sharma, C.; Chand, S.; Yoo, S.; Gupta, D., Photo-physics of PTB7, PCBM and ICBA based ternary solar cells. *Org. Electron.* **2016,** *34*, 111-117.

10. (a) Kim, G.; Song, S.; Lee, J.; Kim, T.; Lee, T. H.; Walker, B.; Kim, J. Y.; Yang, C., Control of Charge Dynamics via Use of Nonionic Phosphonate Chains and Their Effectiveness for Inverted Structure Solar Cells. *Adv. Energy Mater.* **2015,** *5* (18), 1500844; (b) Uddin, M. A.; Lee, T. H.; Xu, S.; Park, S. Y.; Kim, T.; Song, S.; Nguyen, T. L.; Ko, S.-j.; Hwang, S.; Kim, J. Y.; Woo, H. Y., Interplay of Intramolecular Noncovalent Coulomb Interactions for Semicrystalline Photovoltaic Polymers. *Chem. Mater.* **2015,** *27* (17), 5997-6007.

11. (a) Koster, L. J. A.; Mihailetchi, V. D.; Ramaker, R.; Blom, P. W. M., Light intensity dependence of open-circuit voltage of polymer:fullerene solar cells. *Appl. Phys. Lett.* **2005,** *86* (12), 123509; (b) Kyaw, A. K. K.; Wang, D. H.; Gupta, V.; Leong, W. L.; Ke, L.; Bazan, G. C.; Heeger, A. J., Intensity Dependence of Current–Voltage Characteristics and Recombination in High-Efficiency Solution-Processed Small-Molecule Solar Cells. *ACS Nano* **2013,** *7* (5), 4569-4577; (c) Riedel, I.; Parisi, J.; Dyakonov, V.; Lutsen, L.; Vanderzande, D.; Hummelen, J. C., Effect of Temperature and Illumination on the Electrical Characteristics of Polymer–Fullerene Bulk-Heterojunction Solar Cells. *Adv. Funct. Mater.* **2004,** *14* (1), 38-44.

12. (a) Guerrero, A.; Ripolles-Sanchis, T.; Boix, P. P.; Garcia-Belmonte, G., Series resistance in organic bulk-heterojunction solar devices: Modulating carrier transport with fullerene electron traps. *Org. Electron.* **2012,** *13* (11), 2326-2332; (b) Proctor, C. M.; Nguyen, T.-Q., Effect of leakage current and shunt resistance on the light intensity dependence of organic solar cells. *Appl. Phys. Lett.* **2015,** *106* (8), 083301; (c) Zhang, J.; Lee, S.-T.; Sun, B., Effect of Series and Shunt Resistance on Organic-Inorganic Hybrid Solar Cells Performance. *Electrochim. Acta* **2014,** *146* (Supplement C), 845-849.

13. (a) Bisquert, J.; Bertoluzzi, L.; Mora-Sero, I.; Garcia-Belmonte, G., Theory of Impedance and Capacitance Spectroscopy of Solar Cells with Dielectric Relaxation, Drift-Diffusion Transport, and Recombination. *J. Phys. Chem. C* **2014,** *118* (33), 18983-18991; (b) Fabregat-Santiago, F.; Garcia-Belmonte, G.; Mora-Sero, I.; Bisquert, J., Characterization of nanostructured hybrid and organic solar cells by impedance spectroscopy. *Phys. Chem. Chem. Phys.* **2011,** *13* (20), 9083-9118; (c) Glatthaar, M.; Mingirulli, N.; Zimmermann, B.; Ziegler, T.; Kern, R.; Niggemann, M.; Hinsch, A.; Gombert, A., Impedance spectroscopy on organic bulk-heterojunction solar cells. *Phys. Stat. Sol. (a)* **2005,** *202* (11), R125-R127; (d) Zhang, Y.; Li, L.; Yuan, S.; Li, G.; Zhang, W., Electrical properties of the interfaces in bulk heterojunction organic solar cells investigated by electrochemical impedance spectroscopy. *Electrochim. Acta* **2013,** *109* (Supplement C), 221-225.

14. Arredondo, B.; Romero, B.; Del Pozo, G.; Sessler, M.; Veit, C.; Würfel, U., Impedance spectroscopy analysis of small molecule solution processed organic solar cell. *Sol. Energy Mater. Sol. Cells* **2014,** *128* (Supplement C), 351-356.

15. (a) Holliday, S.; Ashraf, R. S.; Wadsworth, A.; Baran, D.; Yousaf, S. A.; Nielsen, C. B.; Tan, C.-H.; Dimitrov, S. D.; Shang, Z.; Gasparini, N.; Alamoudi, M.; Laquai, F.; Brabec, C. J.; Salleo, A.; Durrant, J. R.; McCulloch, I., High-efficiency and air-stable P3HT-based polymer solar cells with a new non-fullerene acceptor. *Nat. Commun.* **2016,** *7*, 11585; (b) Li, N.; Machui, F.; Waller, D.; Koppe, M.; Brabec, C. J., Determination of phase diagrams of binary and ternary organic semiconductor blends for organic photovoltaic devices. *Sol. Energy Mater. Sol. Cells* **2011,** *95* (12), 3465-3471.

16. (a) Juraić, K.; Gracin, D.; Šantić, B.; Meljanac, D.; Zorić, N.; Gajović, A.; Dubček, P.; Bernstorff, S.; Čeh, M., GISAXS and GIWAXS analysis of amorphous–nanocrystalline silicon thin films. *Nucl. Instrum. Methods Phys. Res. B* **2010,** *268* (3), 259-262; (b) Kim, Y.; Long, D. X.; Lee, J.; Kim, G.; Shin, T. J.; Nam, K.-W.; Noh, Y.-Y.; Yang, C., A Balanced Face-On to Edge-On Texture Ratio in Naphthalene Diimide-Based Polymers with Hybrid Siloxane Chains Directs Highly Efficient Electron Transport. *Macromolecules* **2015,** *48* (15), 5179-5187; (c) Müller-Buschbaum, P., The Active Layer Morphology of Organic Solar Cells Probed with Grazing Incidence Scattering Techniques. *Adv. Mater.* **2014,** *26* (46), 7692-7709.

4.2.5. Supporting Figures and Tables

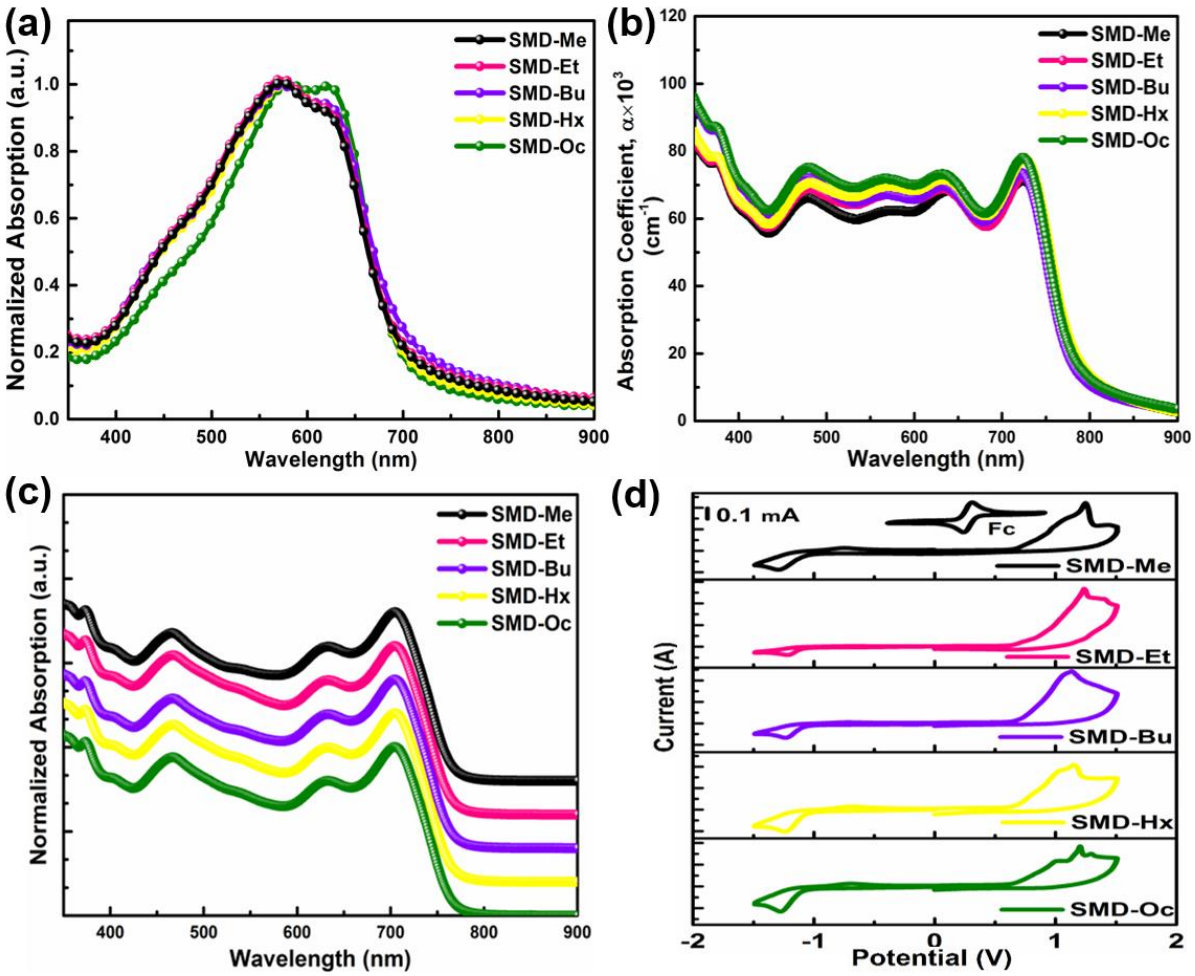

Figure 4.2.6. (a) Normalized UV-Vis absorption of thin films of pure SMD derivatives with different terminal side chains. (b) Absorption coefficient of ternary films. (c) Normalized UV-Vis absorption of ternary blend solution (in stacked format) using SMD derivatives with different terminal side chains. (d) Cyclic voltammetry of SMD derivatives with different terminal side chains.

Table 4.2.2. Optical and electrochemical properties of various SMDs.

Compounds	λ_{max}^{sol} (nm)[a]	λ_{max}^{film} (nm)[a]	E_g (eV)[b]	E_{HOMO} (eV)[c]	E_{LUMO} (eV)[c]	E_g (eV)[d]
Me	324, 507	573, 615	1.81	-5.38	-3.63	1.75
Et	324, 507	577, 623	1.78	-5.38	-3.65	1.73
Bu	324, 507	573, 622	1.78	-5.38	-3.65	1.73
Hx	324, 507	573, 623	1.78	-5.37	-3.64	1.73
Oc	324, 507	574, 623	1.78	-5.38	-3.64	1.74

[a] Solutions were prepared in chloroform and the films were spin-coated on glass substrates; b determined from the onset of the electronic absorption spectra; c measured from thin films by cyclic voltammetry following the equation, $E_{HOMO/LUMO} = -4.8 - (E_{ox/red} - E_{ferrocene})$); [d]$Eg = E_{LUMO} - E_{HOMO}$.

Table 4.2.3. Summary of photovoltaic parameters of ternary PTB7-Th:SMD-Me:$PC_{71}BM$ based devices in chlorobenzene with different SMD-Me loading ratios.

SMD-Me ratio	**J_{SC} (mA cm^{-2})**	**V_{OC} (V)**	**FF (%)**	**PCE (%)**
15%	19.9 (20.14)	0.783 (0.785)	68.31 (69.11)	10.64 (10.93)
20%	21.0 (21.45)	0.780 (0.781)	69.10 (69.82)	11.32 (11.7)
25%	21.83 (22.00)	0.778 (0.780)	69.90 (70.43)	11.87 (12.1)
30%	20.14 (20.96)	0.777 (0.778)	68.93 (69.90)	10.79 (11.4)
35%	19.31 (19.74)	0.770 (0.772)	68.63 (69.30)	10.20 (10.56)

*The data in parentheses are the highest values.

Table 4.2.4. Summary of photovoltaic parameters of ternary PTB7-Th:SMD-Et:$PC_{71}BM$ based devices in chlorobenzene with different SMD-Et loading ratios.

SMD-Et ratio	J_{SC} (mA cm^{-2})	V_{OC} (V)	FF (%)	PCE (%)
15%	19.64 (19.96)	0.781 (0.783)	68.86 (69.40)	10.56 (10.85)
20%	20.87 (21.38)	0.779 (0.780)	69.54 (70.15)	11.31 (11.70)
25%	21.75 (21.95)	0.777 (0.778)	70.88 (71.44)	11.98 (12.2)
30%	20.93 (21.37)	0.774 (0.775)	69.45 (70.02)	11.25 (11.6)
35%	19.27 (19.95)	0.771 (0.773)	68.83 (69.57)	10.23 (10.73)

*The data in parentheses are the highest values.

Table 4.2.5. Summary of photovoltaic parameters of ternary PTB7-Th:SMD-Bu:$PC_{71}BM$ based devices in chlorobenzene with different SMD-Bu loading ratios.

SMD-Bu ratio	J_{SC} (mA cm^{-2})	V_{OC} (V)	FF (%)	PCE (%)
15%	19.41 (19.87)	0.779 (0.780)	68.12 (68.91)	10.30 (10.68)
20%	21.17 (21.39)	0.776 (0.778)	69.20 (69.70)	11.36 (11.6)
25%	21.82 (21.87)	0.775 (0.776)	69.65 (70.72)	11.78 (12.0)
30%	20.24 (20.88)	0.772 (0.773)	69.34 (70.00)	10.83 (11.3)
35%	19.35 (19.71)	0.770 (0.771)	68.39 (69.17)	10.19 (10.51)

*The data in parentheses are the highest values.

Table 4.2.6. Summary of photovoltaic parameters of ternary PTB7-Th:SMD-Hx:$PC_{71}BM$ based devices in chlorobenzene with different SMD-Hx loading ratios.

SMD-Hx ratio	J_{SC} (mA cm^{-2})	V_{OC} (V)	FF (%)	PCE (%)
15%	19.05 (19.6)	0.777 (0.779)	69.14 (69.71)	10.23 (10.64)
20%	20.79 (21.29)	0.777 (0.778)	69.46 (70.03)	11.22 (11.60)
25%	21.86 (21.90)	0.776 (0.776)	69.78 (71.20)	11.84 (12.1)
30%	20.13 (20.95)	0.771 (0.773)	69.93 (70.38)	10.85 (11.4)
35%	18.84 (19.32)	0.770 (0.771)	69.87 (70.14)	10.14 (10.45)

*The data in parentheses are the highest values.

Table 4.2.7. Summary of photovoltaic parameters of ternary PTB7-Th:SMD-Oc:$PC_{71}BM$ based devices in chlorobenzene with different SMD-Oc loading ratios.

SMD-Oc ratio	J_{SC} (mA cm^{-2})	V_{OC} (V)	FF (%)	PCE (%)
15%	18.94 (19.53)	0.777 (0.778)	68.90 (69.42)	10.14 (10.55)
20%	19.78 (21.01)	0.774 (0.776)	69.32 (69.91)	10.61 (11.4)
25%	21.69 (21.73)	0.774 (0.775)	69.85 (71.24)	11.73 (12.0)
30%	20.21 (20.89)	0.771 (0.772)	69.58 (70.05)	10.84 (11.3)
35%	18.79 (19.29)	0.769 (0.770)	69.63 (69.87)	10.06 (10.38)

*The data in parentheses are the highest values.

Table 4.2.8. The photovoltaic parameters of binary SMD:$PC_{71}BM$ based devices in chlorobenzene using SMD derivatives with different terminal side chains.

Terminal Side	J_{SC} (mA cm^{-2})	V_{OC} (V)	FF (%)	PCE (%)
SMD-Me	4.38 (5.38)	0.720 (0.808)	25.5 (27.0)	0.957 (0.999)
SMD-Et	13.6 (14.7)	0.927 (0.939)	43.0 (44.3)	5.61 (5.97)
SMD-Bu	14.0 (14.6)	0.959 (0.965)	37.1 (40.1)	5.03 (5.21)
SMD-Hx	6.65 (7.08)	0.940 (0.946)	34.0 (35.5)	2.26 (2.53)
SMD-Oc	6.09 (6.64)	0.897 (0.901)	39.6 (40.2)	2.20 (2.37)

The average values obtained from 7 devices. The data in parentheses are the highest values.

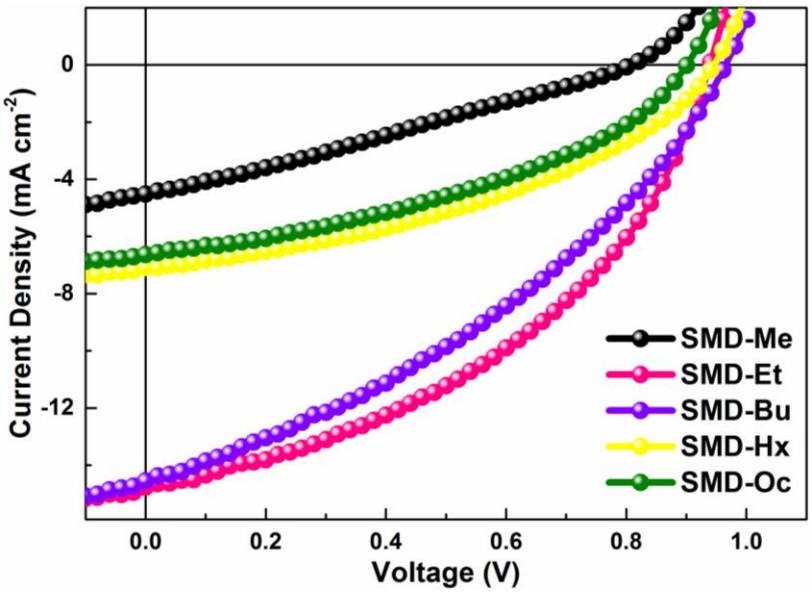

Figure 4.2.7. *J-V* characteristics of binary SMD:$PC_{71}BM$ based OSCs in chlorobenzene under AM 1.5G irradiation at 100 mW cm^{-2} using SMD derivatives with different terminal side chains.

Table 4.2.9. Summary of photovoltaic parameters of binary SMD:$PC_{71}BM$ based devices optimized using, chloroform solvent, thermal annealing, solvent vapor annealing, and ETL (PDINO) coating.

Terminal side	Spin rate (rpm)	J_{SC} (mA cm^{-2})	V_{OC} (V)	FF (%)	PCE (%)
SMD-Me	1800	5.47 (5.83)	0.887 (0.890)	44.32 (45.50)	2.15 (2.36)
	2000	5.84 (6.19)	0. 876 (0.879)	40.04 (41.00)	2.05 (2.23)
SMD-Et	1800	12.93 (13.38)	0.947 (0.950)	68.34 (69.90)	8.37 (8.89)
	2000	13.27 (13.64)	0.946 (0.948)	69.87 (70.20)	8.77 (9.07)
SMD-Bu	1800	11.78 (12.27)	0.947 (0.950)	59.84 (60.80)	6.67 (7.09)
	2000	11.82 (12.11)	0.952 (0.954)	60.55 (61.90)	6.81 (7.15)
SMD-Hx	1800	11.94 (12.30)	0.931 (0.933)	49.73 (50.80)	5.53 (5.82)
	2000	12.18 (12.73)	0.932 (0.936)	53.37 (54.10)	6.06 (6.44)
SMD-Oc	1800	9.77 (10.28)	0.927 (0.929)	49.83 (50.40)	4.51 (4.82)
	2000	9.91 (10.44)	0.928 (0.931)	51.72 (52.70)	4.76 (5.13)

*The data in parentheses are the highest values.

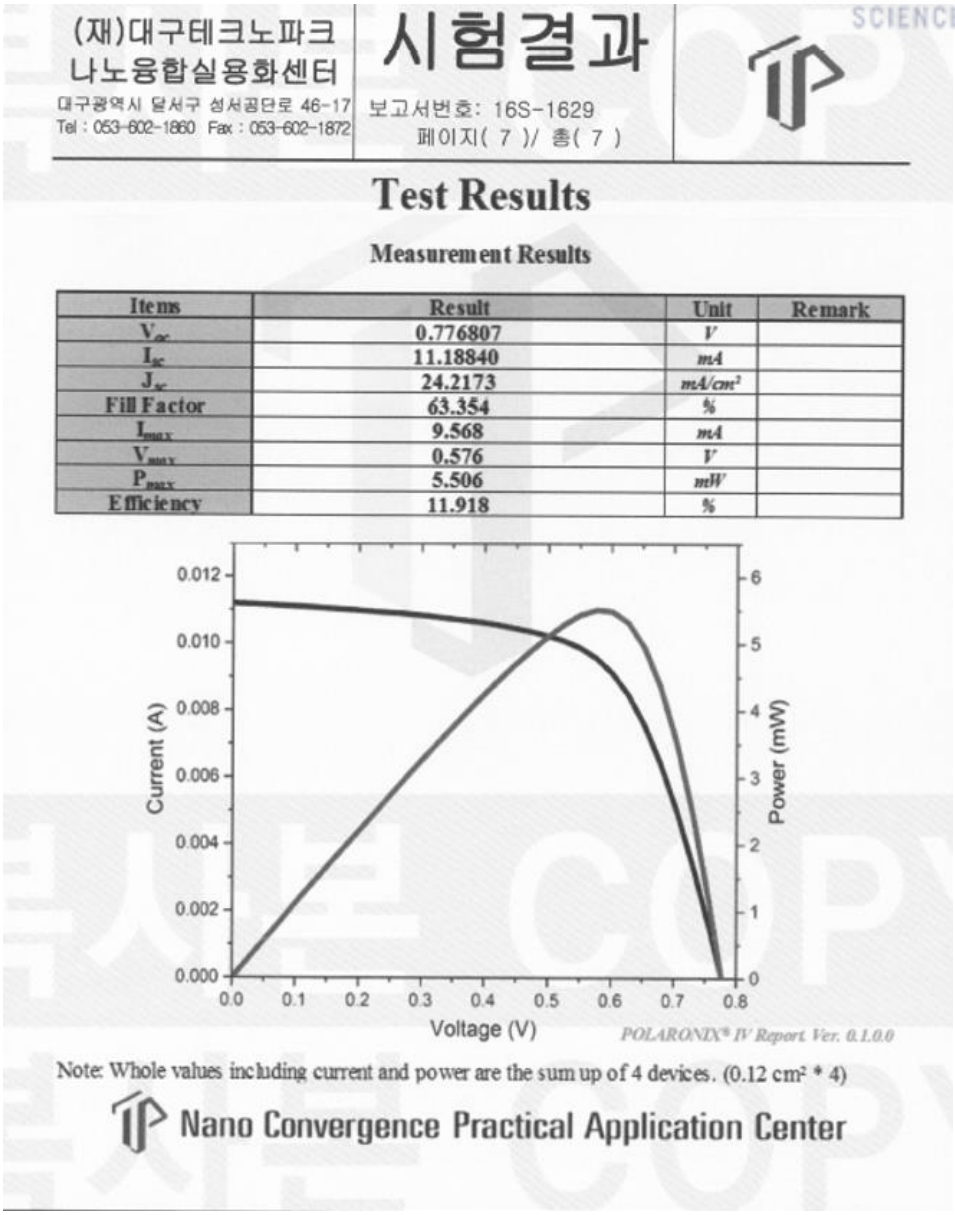

(재)대구테크노파크
나노융합실용화센터
대구광역시 달서구 성서공단로 46-17
Tel : 053-602-1860 Fax : 053-602-1872

시험결과

보고서번호: 16S-1629
페이지(7)/ 총(7)

Test Results

Measurement Results

Items	Result	Unit	Remark
V_{oc}	0.776807	V	
I_{sc}	11.18840	mA	
J_{sc}	24.2173	mA/cm²	
Fill Factor	63.354	%	
I_{max}	9.568	mA	
V_{max}	0.576	V	
P_{max}	5.506	mW	
Efficiency	11.918	%	

Note: Whole values including current and power are the sum up of 4 devices. (0.12 cm² * 4)

Nano Convergence Practical Application Center

Figure 4.2.8. Independent certification confirming a power conversion efficiency of 11.918% by Nano Convergence Practical Application Center, South Korea.

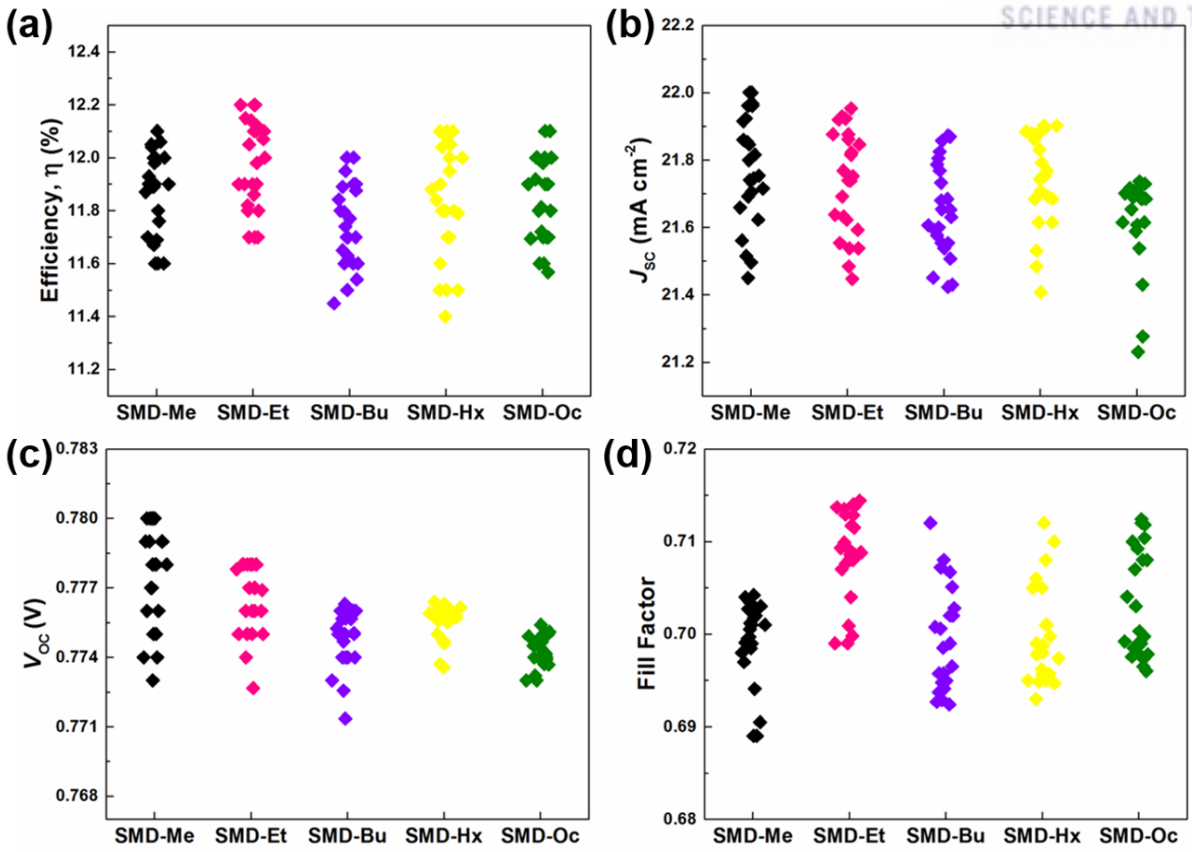

Figure 4.2.9. Scatter plot of device parameters. (a) Efficiency (η), (b) JSC (Current density), (c) VOC (Open Circuit Voltage), and (d) Fill factor of ternary OSCs (75:25:150 wt.%) using SMD derivatives with different terminal side chains for 24 devices in each case.

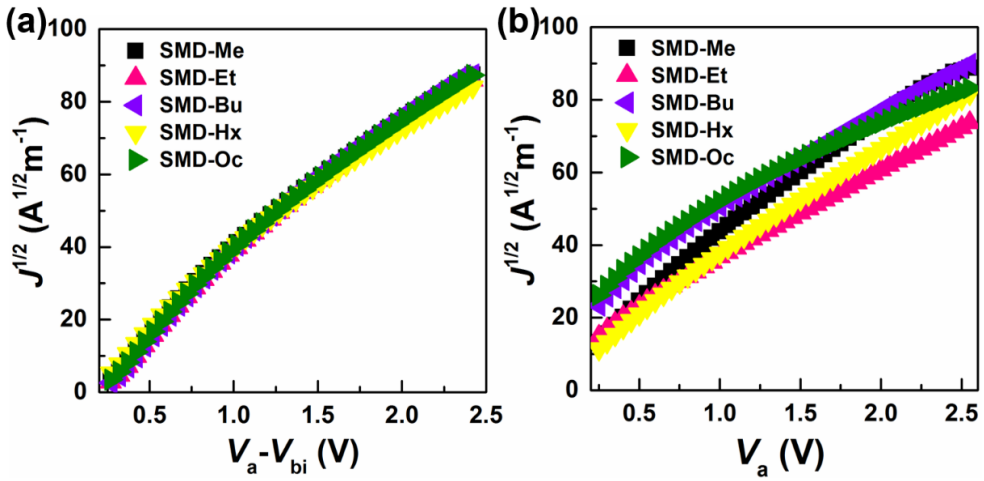

Figure 4.2.10. (a) Hole only. (b) Electron only mobility of ternary blend using SMD derivatives with different terminal side chains.

Table 4.2.10. Summary of mobilities for hole only and electron only ternary blend using SMD derivatives with different terminal side chains.

Terminal Side	μ_h ($cm^2 V^{-1} s^{-1}$)	μ_e ($cm^2 V^{-1} s^{-1}$)	μ_h/μ_e	J_{ph}/J_{sat}
SMD-Me	1.305×10^{-4}	0.800×10^{-4}	1.630	0.979
SMD-Et	1.489×10^{-4}	0.772×10^{-4}	1.923	0.986
SMD-Bu	1.443×10^{-4}	0.705×10^{-4}	2.047	0.978
SMD-Hx	1.165×10^{-4}	0.771×10^{-4}	1.511	0.985
SMD-Oc	1.350×10^{-4}	0.565×10^{-4}	2.388	0.975

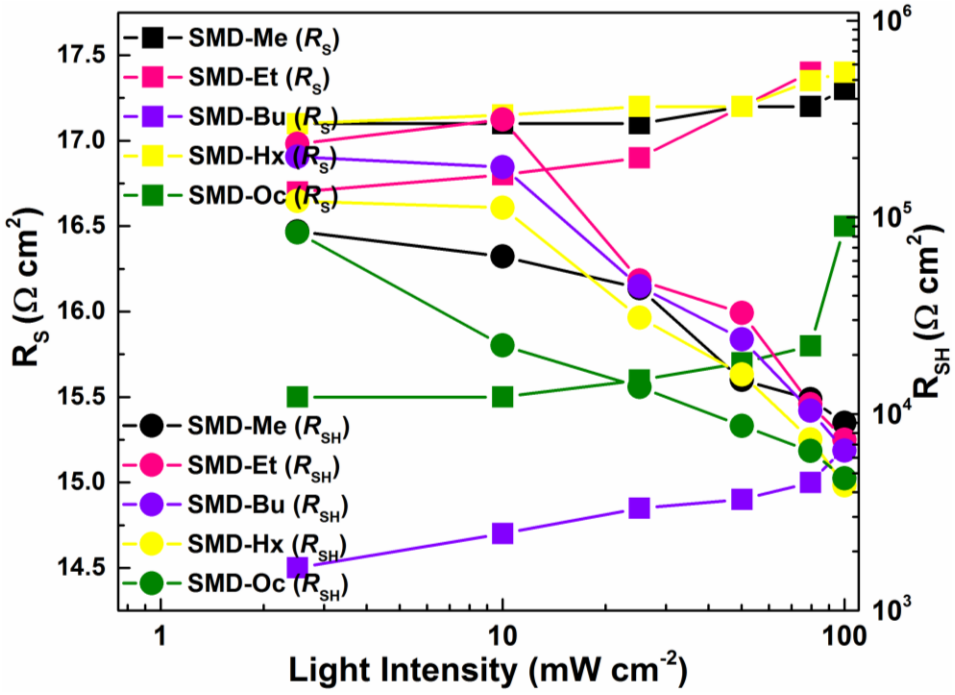

Figure 4.2.11. Series and shunt resistance dependence on light intensity for ternary OSCs using SMD derivatives with different terminal side chains.

Table 4.2.11. Charge transport properties of OSCs using SMD derivatives with different terminal side chains.

Terminal Side	J_{SC} (mA cm^{-2})	R_{OS} (Ω)	R_{CT} (Ω)	CPE-T (F)	CPE-P	f_{max} (Hz)*
SMD-Me	Dark	10.9	165	4.782 x10^{-8}	0.968	3.512 ± 0.392 x10^{5}
	Illumination	9.6	18.3	2.256 x10^{-6}	0.804	2.373 ± 0.209 x10^{5}
SMD-Et	Dark	9.50	159	1.597 x10^{-9}	0.954	2.926 ± 0.335 x10^{5}
	Illumination	10.3	16.2	2.028 x10^{-7}	0.853	2.615 ± 0.230 x10^{5}
SMD-Bu	Dark	7.77	188	7.478 x10^{-8}	0.927	2.082 ± 0.212 x10^{5}
	Illumination	11.4	20.0	1.848 x10^{-7}	0.905	2.290 ± 0.250 x10^{5}
SMD-Hx	Dark	10.0	164	5.641 x10^{-8}	0.956	3.183 ± 0.398 x10^{5}
	Illumination	11.8	16.6	1.098 x10^{-6}	0.895	2.504 ± 0.145 x10^{5}
SMD-Oc	Dark	8.23	164	1.320 x10^{-7}	0.901	3.001 ± 0.399 x10^{5}
	Illumination	7.92	14.7	4.512 x10^{-6}	0.886	1.613 ± 0.226 x10^{5}

*fmax approximated for Figure 7 in the main text.

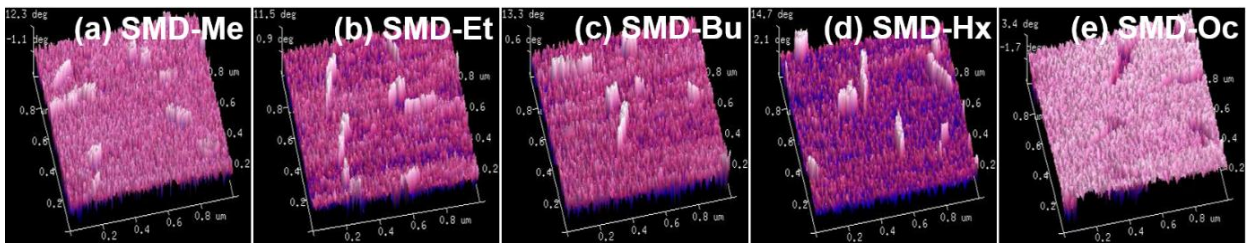

Figure 4.2.12. AFM topography phase images (scan size 1×1 μm) of ternary blend films using SMD derivatives with different terminal side chains.

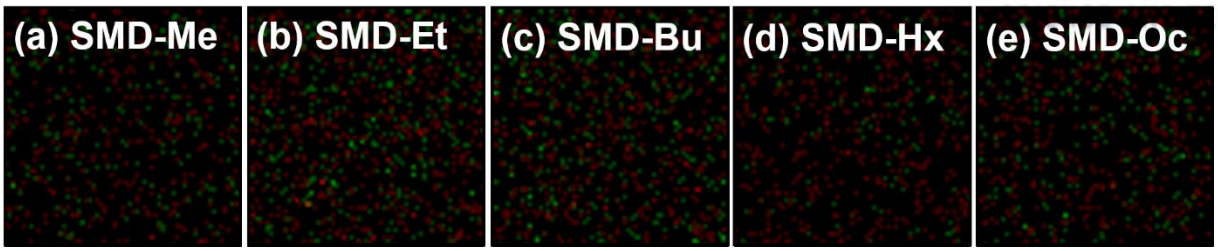

Figure 4.2.13. Elemental mapping by EDAX analysis of ternary blend films using SMD derivatives with different terminal side chains. Red corresponds to Nitrogen and green to fluorine representing DR3TSBDT and PTB7-Th respectively.

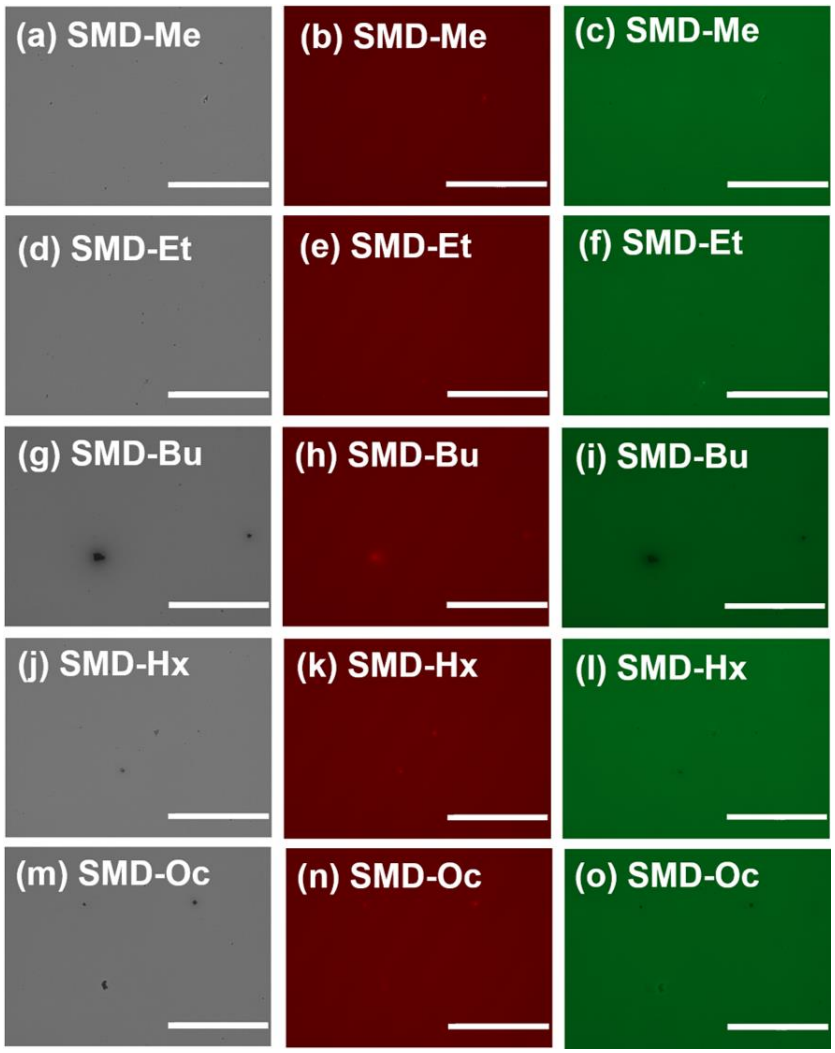

Figure 4.2.14. Fluorescence microscopy of the optimized ternary system using SMD derivatives with different terminal side chains investigated using white light ((a), (d), (g), (j), and (m)), red light ((b), (e), (h), (k), and (n)), and blue light ((c), (f), (i), (l), and (o)). Scale bar is 20 μm.

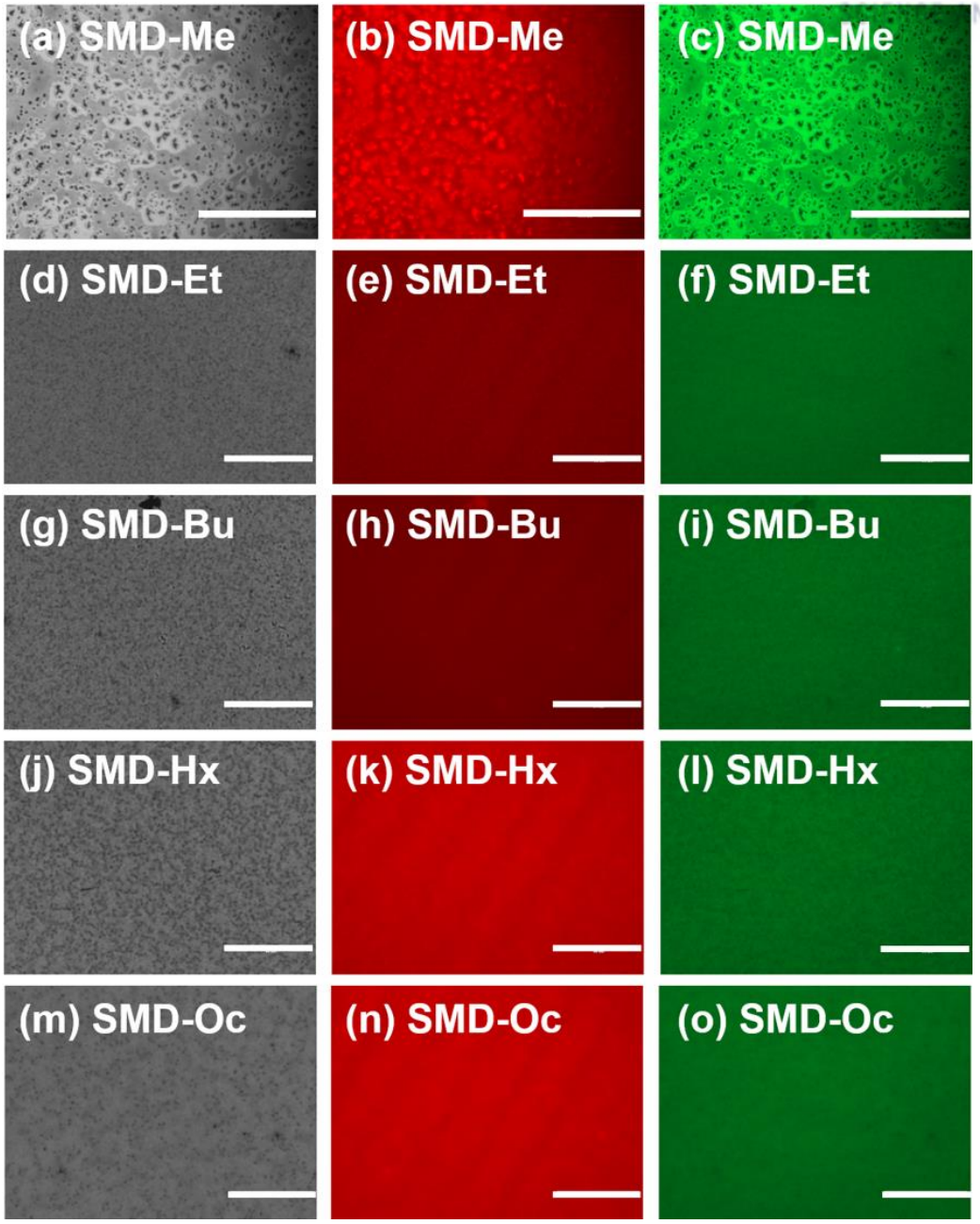

Figure 4.2.15. Fluorescence microscopy of the optimized binary system using SMD derivatives with different terminal side chains investigated using white light ((a), (d), (g), (j), and (m)), red light ((b), (e), (h), (k), and (n)), and blue light ((c), (f), (i), (l), and (o)). Scale bar is 20 μm.

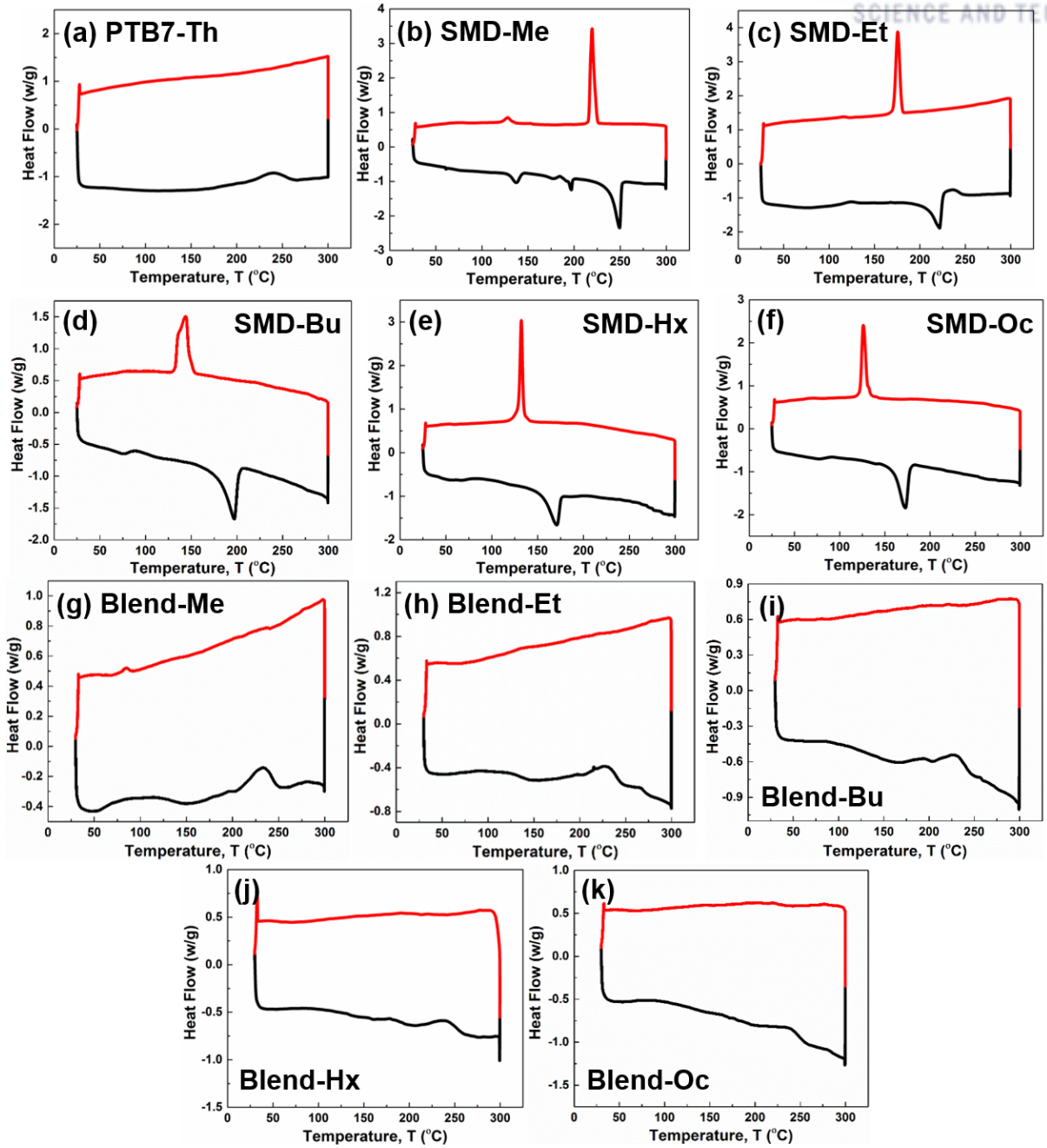

Figure 4.2.16. Differential scanning calorimetry (DSC) curves of (a) PTB7-Th, (b) SMD-Me, (c) SMD-Et, (d) SMD-Bu, (e) SMD-Hx, (f) SMD-Oc, (g), (h), (i), (j), and (k) binary blends of PTB7-Th:SMD (75:25 wt/wt). Black and red curve corresponds to endothermic and exothermic curves respectively.

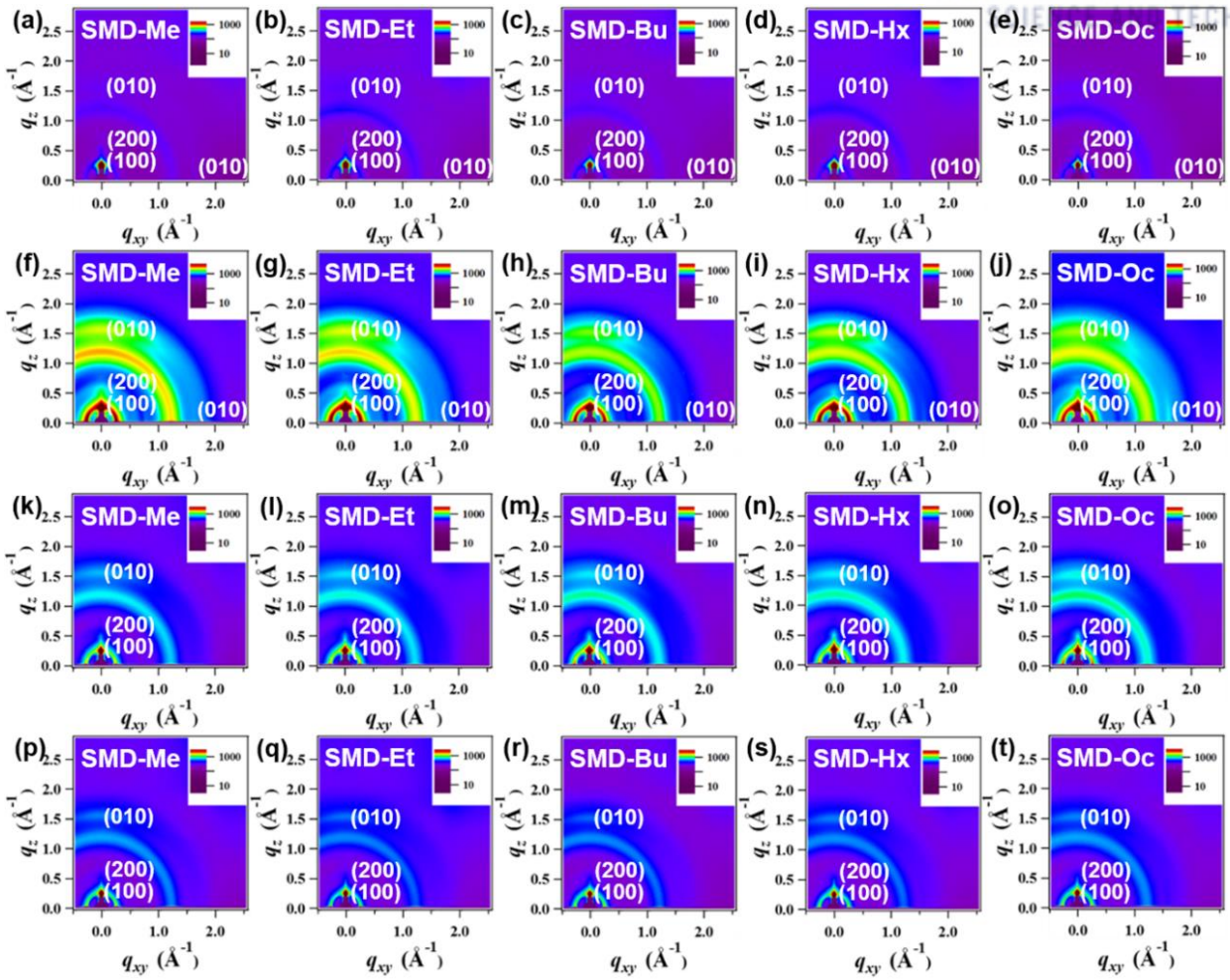

Figure 4.2.17. GIWAXS pattern of ternary blend films using SMD derivatives with different terminal side chains measured at different incident angles. (a)-(e) 0.08°, (f)-(j) 0.12°, (f)-(j) 0.16°, and (f)-(j) 0.20°. Different color bars represent intensity variance.

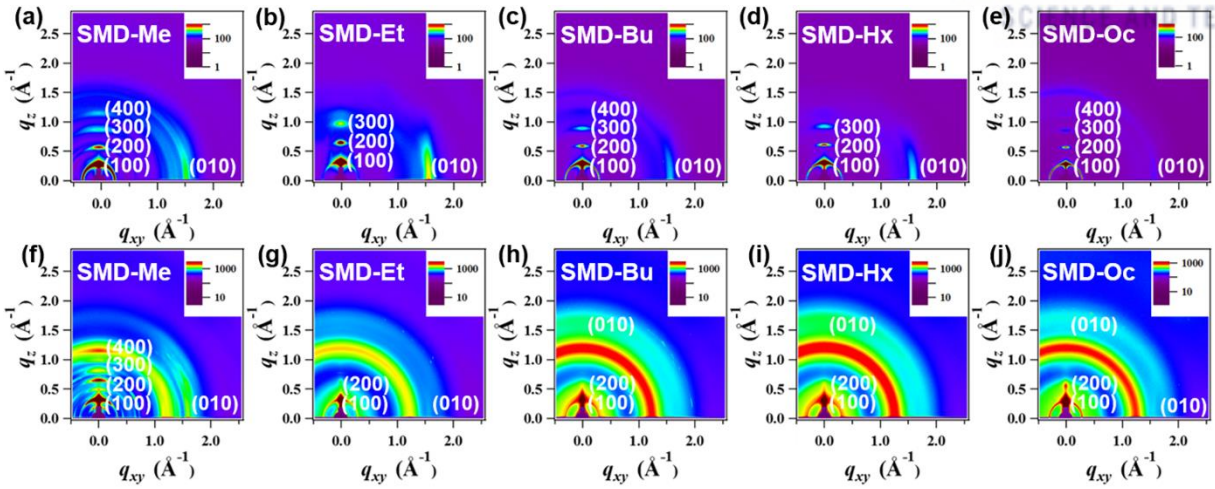

Figure 4.2.18. GIWAXS pattern. (a)-(e) Pure SMD film. (f)-(j) Binary SMD:PC71BM film using SMD derivatives with different terminal side chains. Different color bars represent intensity variance.

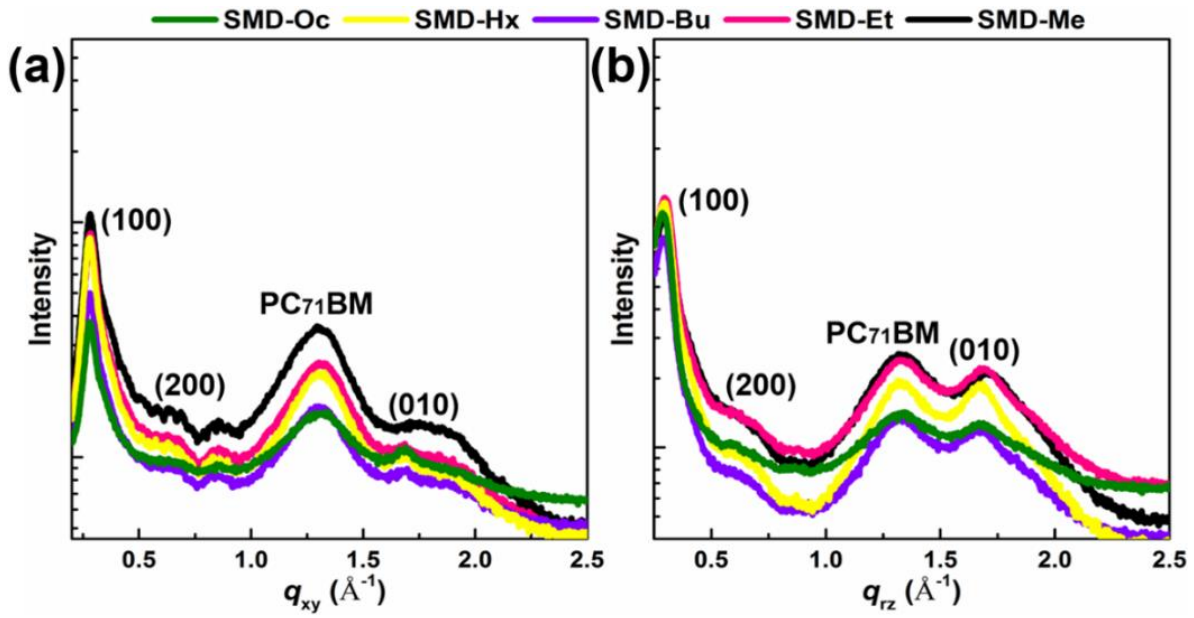

Figure 4.2.19. (a) In-plane. (b) Out-of-plane line cut profiles obtained from GIWAXS data of ternary blend films using SMD derivatives with different terminal side chains.

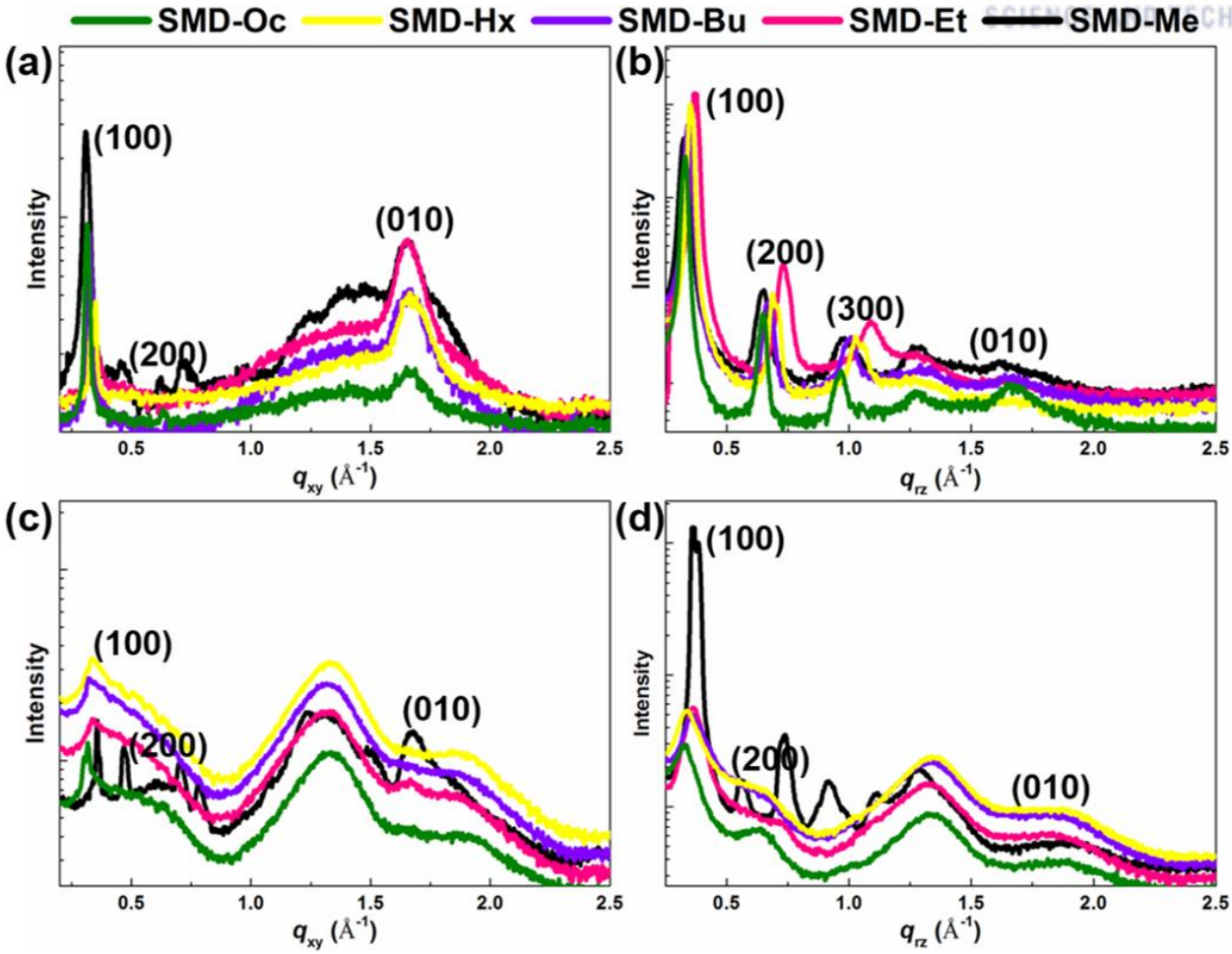

Figure 4.2.20. (a), (c) In-plane. (b), (d) Out-of-plane line cut profiles obtained from GIWAXS data. (a), (b) Pure SMD film, and (c), (d) SMD:PC71BM film using SMD derivatives with different terminal side chains.

Table 4.2.12. Lattice parameters in out-of-plane and in-plane direction using SMD derivatives with different terminal side chains for ternary, pure and binary blend system.

	In-plane		Out of-plane	
Terminal Side	**Unit cell long axis (*100*) ($Å^{-1}$)**	**d_{100} (Å)**	**Unit cell long axis (*100*) ($Å^{-1}$)**	**d_{100} (Å)**
		Ternary Blend		
SMD-Me	0.282	22.28	0.296	21.27
SMD-Et	0.282	22.28	0.296	21.27
SMD-Bu	0.279	22.53	0.296	21.27
SMD-Hx	0.279	22.52	0.296	21.27
SMD-Oc	0.279	22.52	0.289	21.74
		Binary Blend		
SMD-Me	0.356	17.65	0.365	17.21
SMD-Et	0.340	18.48	0.362	17.36
SMD-Bu	0.320	19.63	0.36	17.45
SMD-Hx	0.331	18.98	0.333	18.87
SMD-Oc	0.318	19.76	0.325	19.33
		Pure Material		
SMD-Me	0.309	20.33	0.325	19.33
SMD-Et	0.339	18.53	0.37	16.98
SMD-Bu	0.326	19.26	0.341	18.42
SMD-Hx	0.344	18.26	0.352	17.85
SMD-Oc	0.315	19.94	0.331	18.98
	π-π stacking cell axis (*010*) ($Å^{-1}$)	**d_{010} (Å)**	**π-π stacking cell axis (*010*) ($Å^{-1}$)**	**d_{010} (Å)**
		Ternary blend		
SMD-Me	1.707	3.681	1.711	3.672
SMD-Et	1.696	3.704	1.694	3.709
SMD-Bu	1.689	3.720	1.684	3.731
SMD-Hx	1.685	3.728	1.680	3.740
SMD-Oc	1.692	3.713	1.676	3.749
		Pure Material		
SMD-Me	1.699	3.698		
SMD-Et	1.699	3.698		
SMD-Bu	1.696	3.704		
SMD-Hx	1.696	3.704		
SMD-Oc	1.696	3.704		

Chapter 5. Study of Material–Solvent Interaction Leading to the Evolution of Bimolecular Cubic Crystal

In this study, we determine the solubility properties of a given ternary blend set, in which two donors (PTB7-Th and DR3TSBDT) and one acceptor ($PC_{71}BM$) are used, in a series of solvents, and use active material–solvent interactions as an aid for finding suitable non-chlorinated solvents to achieve effective ternary OSCs based on PTB7-Th:DR3TSBDT:$PC_{71}BM$. An exceptional power conversion efficiency (PCE) as high as 12.3% (a certified PCE of 11.94%) is obtained using the developed non-halogenated processing system. In-depth investigations (morphology, charge mobility, recombination dynamics, and OSC characteristics) uncover the underlying structure–property relationships as a function of the chosen non-halogenated systems. In addition, another intriguing finding of this study is the formation of a cubic bimolecular crystal structure of PTB7-Th:$PC_{71}BM$ in a non-halogenated system, which is the first such demonstration in blend films. This sheds light upon the fact that the physical properties of a material applied from different solutions may surpass the variation in the properties between two material having totally different molecular structure. Therefore, this work not only offers important scientific insights into developing highly efficient and eco-friendly OSCs but also improves our understanding of achievable bimolecular crystals with an intercalated structure.

Chapter 5 is reproduced in part with permission of "Cubic-Like Bimolecular Crystal Evolution and Over 12% Efficiency in Halogen-Free Ternary Solar Cells" from Kumari T. *et al. Adv. Funct. Mater.* **2018**, 28, 1707278 with permission from the John Wiley and Sons.

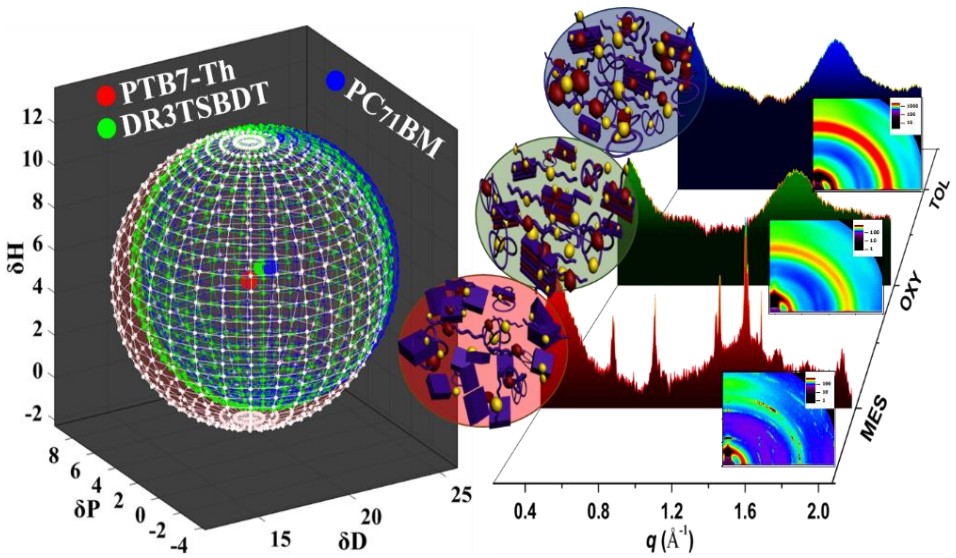

5.1 Introduction

In principle, a high-performance bulk-heterojunction organic solar cell (OSC) system requires finely interpenetrating phase-separated domains between the donor and the acceptor, which enable a large specific inner surface area to effectively split excitons and provide bi-continuous pathways for efficient charge carrier transport.[1] The choice of processing solvents and additives plays a vital role in producing such an ideal morphology in the blended thin films,[2] since they not only affect the thermodynamic interactions between the donor and the acceptor but also cause differences in kinetic parameters such as the rate of solvent evaporation, boiling point, and solubility during the film formation process.[3] At present, the fabrication of the most state-of-the-art OSCs involves the use of halogenated (typically chlorinated) solvents and/or additives that are toxic, environmentally hazardous, or incompatible with roll-to-roll processing under ambient conditions, all of which prevent their mass deployment. Although many researchers have recently devoted great effort to developing OSCs processed by more environment-friendly solvents, very limited success has been achieved.[4] Moreover, the body of knowledge relating to the active material–solvent interactions within the field of OSCs remains scarce,[3d, 5] and thus, establishing a better understanding of the structure–performance correlation for halogen-free processing systems has become an urgent task for advancing to environmentally friendly ink formulations for OSCs.[2f, 6]

It is widely recognized that the solvent quality is a critical parameter influencing the chain conformation of materials and the statistical distribution of their segments in "solution," which is due to the difference in material–solvent interactions.[3a, 7] Even more meaningful is the fact that the memory of certain conformations in the solution is somehow preserved through the film-forming process, leading to different underlying chain packing morphologies in the films.[1a, 7b, 8]

Therefore, in addition to considering whether the solubilities of all active components are high enough, the interactions between the solvents and materials should be quantified, which enables rational selection of environmentally friendly processing solvents and subsequent achievement of the best morphology and OSC performance using non-halogenated solvents.

Recently, we demonstrated high-performance ternary OSCs comprising two benzo[1,2-*b*;4,5-*b*']dithiophene-based donors (PTB7-Th polymer and DR3TSBDT small molecule) and a [6,6]-phenyl-C_{71}-butyric acid methyl ester ($PC_{71}BM$) acceptor, by using chlorobenzene (CB) and 1,8-diiodooctane (DIO), a commonly used solvent−additive pair.[1d] Our ongoing high interest in the environment-friendly processing of OSCs and the successful example of ternary OSCs based on PTB7-Th:DR3TSBDT:$PC_{71}BM$ prompted us to investigate high-efficiency ternary OSCs prepared without using halogenated solvents and additives.

In this contribution, as the first step of the journey toward achieving our goal of halogen-free OSC processing, we not only analyze the solubility properties of the three active components in various sol-vents but also characterize the interactions between the potential non-halogenated solvents and each active

component. An outstanding power conversion efficiency (PCE) of 12.3%, is achieved for OSCs based on non-halogenated solvent/additive combinations, outperforming the OSCs using the aforementioned CB/DIO pair. In addition, we discover a cubic bimolecular crystal of amorphous PTB7-Th:$PC_{71}BM$ with an intercalated structure beyond that achievable using the previous halogenated solvent/additive system.

5.2 Results and Discussion

Figure 5.1a presents the chemical structures of PTB7-Th, DR3TSBDT, and $PC_{71}BM$ used in the ternary device, together with a schematic illustration of the film morphologies (Figure 5.1b) with different non-chlorinated processing solvents, as identified by the various characterization techniques below.

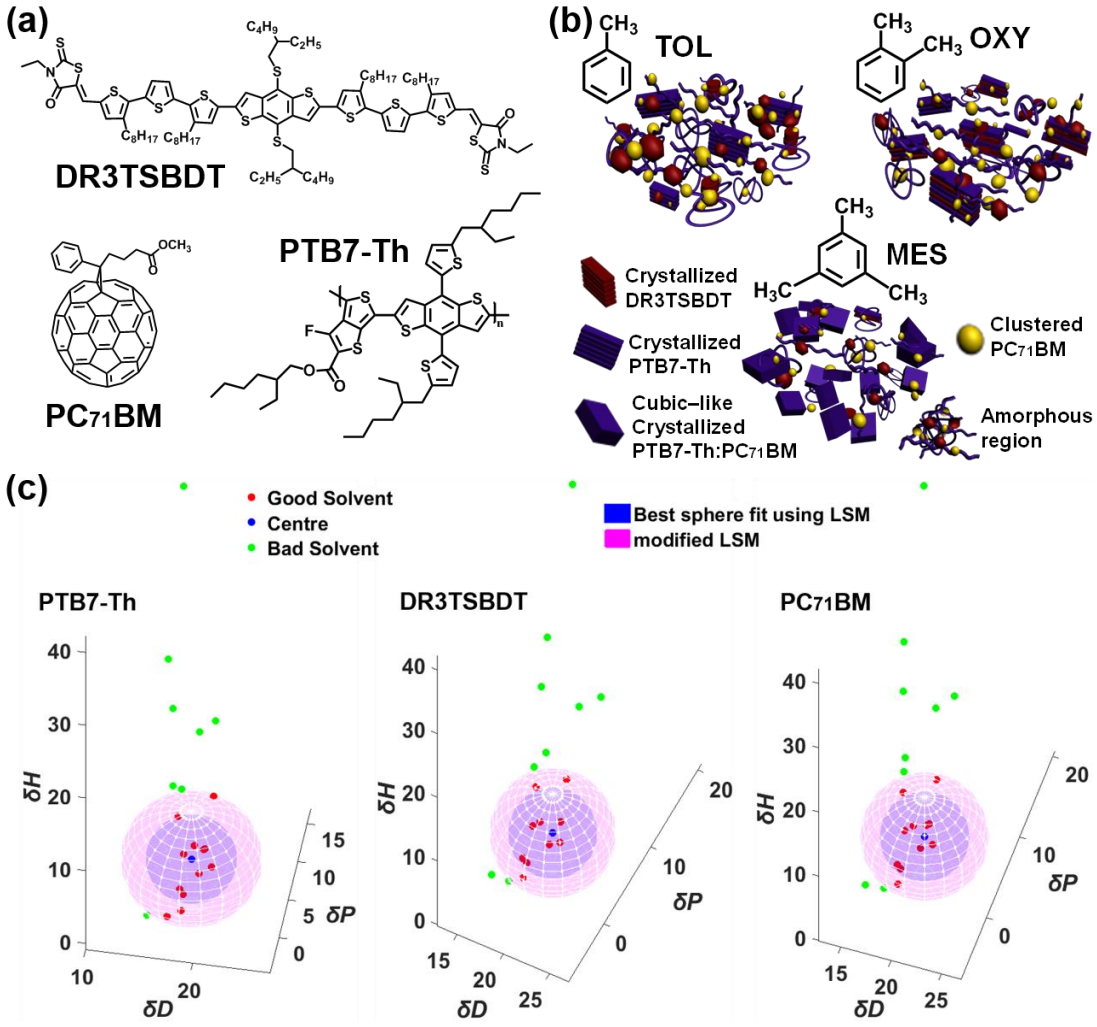

Figure 5.1. (a) Chemical structures of PTB7-Th, DR3TSBDT, and $PC_{71}BM$. (b) Illustration of the active layer of the ternary device. (c) The 3-D plots of good and bad solvents versus δD, δP, and δH as well as the Hansen Solubility Parameters for PTB7-Th, DR3TSBDT, and $PC_{71}BM$ calculated using sphere fit program written in MATLAB.

5.2.1 *Active Material–Solvent Interactions*

a. *Hansen Solubility Parameters*

We quantified the solubility of PTB7-Th, DR3TSBDT, and $PC_{71}BM$ in various solvents at room temperature. First, a set of standard absorption spectra were taken for each active material in CB at certain concentrations and the absorbance was plotted against the concentration (see the section 5.5, for supporting texts and Figures 5.7−5.9). Next, the solubility values of each active material in different solvents were analyzed by comparing the absorbances with the corresponding standard linear fit curves, which are summarized in the section 5.5, Table 5.2. Based on the estimated solubility values, toluene (TOL), o-xylene (OXY), and mesitylene (MES) were chosen as the proper non-chlorinated solvents for our ternary sys-tem since they can well dissolve both PTB7-Th (>12 mg mL^{-1}) and $PC_{71}BM$ (>20 mg mL^{-1}) with moderate solubility for DR3TSBDT (>3.4 mg mL^{-1}), being necessary to enable the fabrication of the best-performing ternary system (PTB7-Th:DR3TSBDT:$PC_{71}BM$ = 75:25:150 wt.%) as demonstrated in our previous work. Details of the solubility experiments are provided in the Supporting.

Furthermore, we employed Hansen solubility parameters (HSPs)[9] to quantify the interaction between processing solvents and the three active components. The HSPs comprise three parameters: δD (energy from dispersion forces), δP (energy from dipolar intermolecular forces), and δH (energy from hydrogen bonding). The total Hildebrand parameter (δ) is defined according to Eq. 1[5, 9a] as the square root of the cohesion energy density.

$$\delta^2 = \delta^2D+\delta^2P+\delta^2H \quad (1)$$

By using a sphere fit program written in MATLAB, as detailed in the supporting texts of section 5.5, the solubility parameters can be visualized in 2-D and 3-D coordinate systems with δD, δP, and δH axes. The derived HSP locations and solubility spheres of PTB7-Th, DR3TSBDT, and $PC_{71}BM$ are presented in Figure 5.1c and Figures 5.10−5.12 (see the section 5.5), respectively. The interactions between the solvent and the active materials can be discerned from their HSP locations. The radius of the sphere (R_0) indicates the maximum difference for solubility.[5, 9a] A sol-vent with an HSP located within the solubility sphere of a material shows good solvation (solubility >2 mg mL^{-1}) of the material. A closer HSP location between the solvent and the material results in greater solubility and a larger interaction strength. The fitted solubility parameters, δD, δP, and δH, for PTB7-Th are 18.60, 2.56, and 5.71; for DR3TSBDT are 19.95, 3.09, and 5.89; and for $PC_{71}BM$ are 19.88, 2.85, and 6.00 $MPa^{1/2}$, respectively.

b. *Relative Energy Difference*

The relative energy difference (RED) between two materials is defined by Eq. 2[7a, 9a] and acts as a measure of the tendency for two materials to dissolve each other, where the radius of interaction (R_a) is the distance between their coordinates in Hansen space (see the Supporting texts of section 5.5 for details).

$$RED = R_a/R_0 \quad (2)$$

Good solvents have an RED value smaller than 1, indicating a high affinity for one another, whereas bad solvents have a value larger than 1, suggesting a decreased affinity for each other.

The HSP and RED values of the active materials in the selected solvents for this study are given in Figure 5.2a and summarized in the section 5.5, Table 5.3. The RED values clearly suggest that both TOL and OXY have sufficient affinity for dissolving all three components compared to MES, which has RED values greater than 1.1 for DR3TSBDT and $PC_{71}BM$ and 0.8 for PTB7-Th, suggesting the possibility of strong phase separation due to the different affinity.

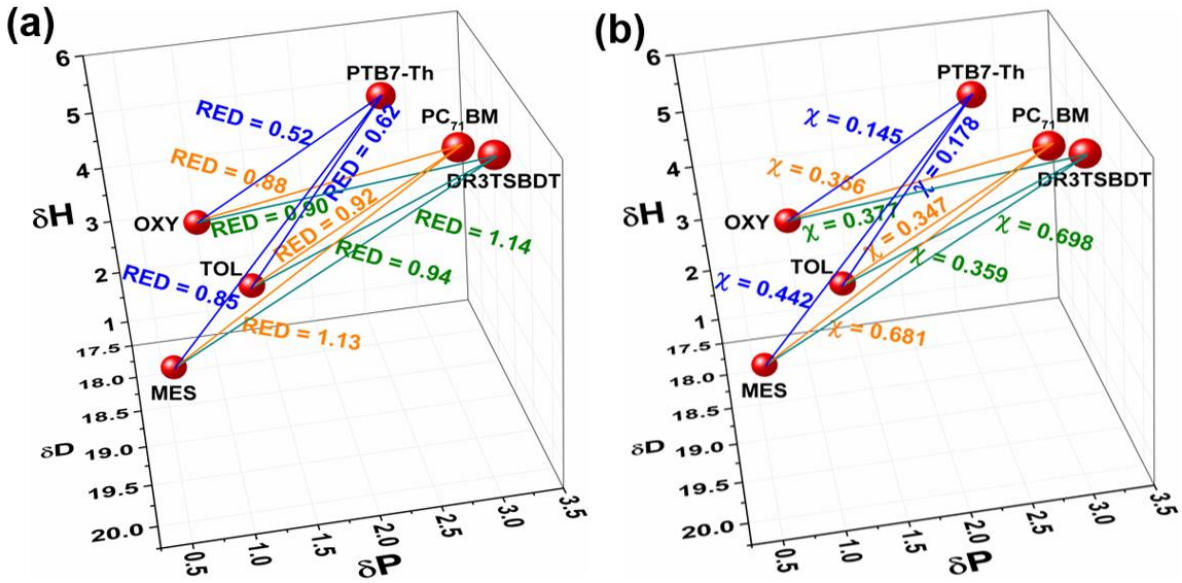

Figure 5.2. (a) The relative energy difference (RED). (b) Chi parameters calculated using Hansen solubility parameters for PTB7-Th, DR3TSBDT, and $PC_{71}BM$ in TOL, OXY, and MES.

c. *Flory–Huggins Interaction Parameter*

Additionally, we calculated the Flory–Huggins interaction parameter (χ)[7c-f, 8b, 9a, 10] (Figure 5.2b and Table S2), which is a relatively good predictor for thermodynamic miscibility. A low χ means a good sol-vent, and χ equal to 0.5 represents the theta state (θ), wherein the interactions disappear in the component pairs. The equations used for calculation are provided in the Supporting. The χ values for the three active materials in all tested solvents are below 0.5, except for $PC_{71}BM$ and DR3TSBDT in MES, where χ is greater than 0.6. On the basis of the χ values, one can conclude that there are very different interactions in $PC_{71}BM$−MES and DR3TSBDT−MES pairs, in which severe phase separation compared to other systems will most likely occur. This is a possible reason for the unexpected formation of a cubic crystal in the blend systems processed in MES, as discussed later.

5.2.2 Optical Properties

Although changing the solvents of neat PTB7-Th and DR3TSBDT solutions did not alter their absorption significantly, the ternary blending films (PTB7-Th:DR3TSBDT:$PC_{71}BM$ = 75:25:150 wt.%) were considerably different depending on the chosen non-chlorinated solvents (see the section 5.5, Figure 5.13). For example, similar to the CB/DIO-cast films in our previous study, the ternary films by using either TOL or OXY exhibited high and uniform absorption intensities in the whole range of 300−800 nm.[1d] However, in the case of MES-cast films, the absorption intensities from 300 to 600 nm, originating from the combined absorption characteristics of the DR3TSBDT and $PC_{71}BM$ chromophores, decreased significantly, together with a slight increase in the maximum ab-sorption of PTB7-Th at 704 nm. This observation supports the existence of the solvent-dependent interaction mentioned above. In addition, the photoluminescence emissions of the neat PTB7-Th:DR3TSBDT solutions were quenched significantly upon blending with $PC_{71}BM$ regardless of the solvent (see the section 5.5, Figure 5.14), confirming that proficient charge transfer occurs in all of the ternary films.[11]

5.2.3 Photovoltaic Performance

The photovoltaic performance of OSCs fabricated with different solvents (TOL, OXY, and MES) was evaluated in a conventional architecture of indium-tin oxide (ITO)/poly(3,4-ethylenedioxythiophene):poly(styrene sulfonate) (PEDOT:PSS)/active layer/Al under simulated AM 1.5G irradiation (100 mW cm^{-2}). We kept the previously optimized ratio of PTB7-Th:DR3TSBDT:$PC_{71}BM$ (75:25:150 wt.%), but used N-methyl pyrrolidone (NMP) as a halogen-free additive instead of DIO to optimize the morphology of the active layer. In addition to the requirement that the final OSC production process involves no toxic solvents, the selection of NMP was due to its high boiling point and selective solubility for $PC_{71}BM$, as confirmed by our solubility tests (see the section 5.5, Table 5.2). Photovoltaic devices with different amounts of NMP were evaluated.

The representative current density–voltage (*J*–*V*) characteristics of the best ternary OSCs are shown in Figure 5.3a, and the corresponding device parameters are summarized in Table 5.1 (see the section 5.5, Tables 5.4-5.5 for other data tested under different conditions). The TOL-processed ternary OSCs with NMP exhibited a remarkably high PCE of up to 11.8%; more surprisingly, the OXY-processed ones with optimal NMP delivered an even superior PCE of 12.3% (average PCE = 11.75 ± 0.55%), with a short-circuit current density (J_{SC}) of 21.7 ± 0.80 mA cm^{-2}, an open-circuit voltage (V_{OC}) of 0.779 ± 0.002 V, and a fill factor (FF) of 69.5 ± 1.2 %. This is comparable to the highest PCEs reported to date for OSCs processed from non-halogenated solvents.[12] One of the best OSCs was sent to an independent solar cell

calibration laboratory (Nano Convergence Practical Application Center, South Korea) for certification, which confirmed a PCE of 11.942% (see the section 5.5, Figure 5.15).

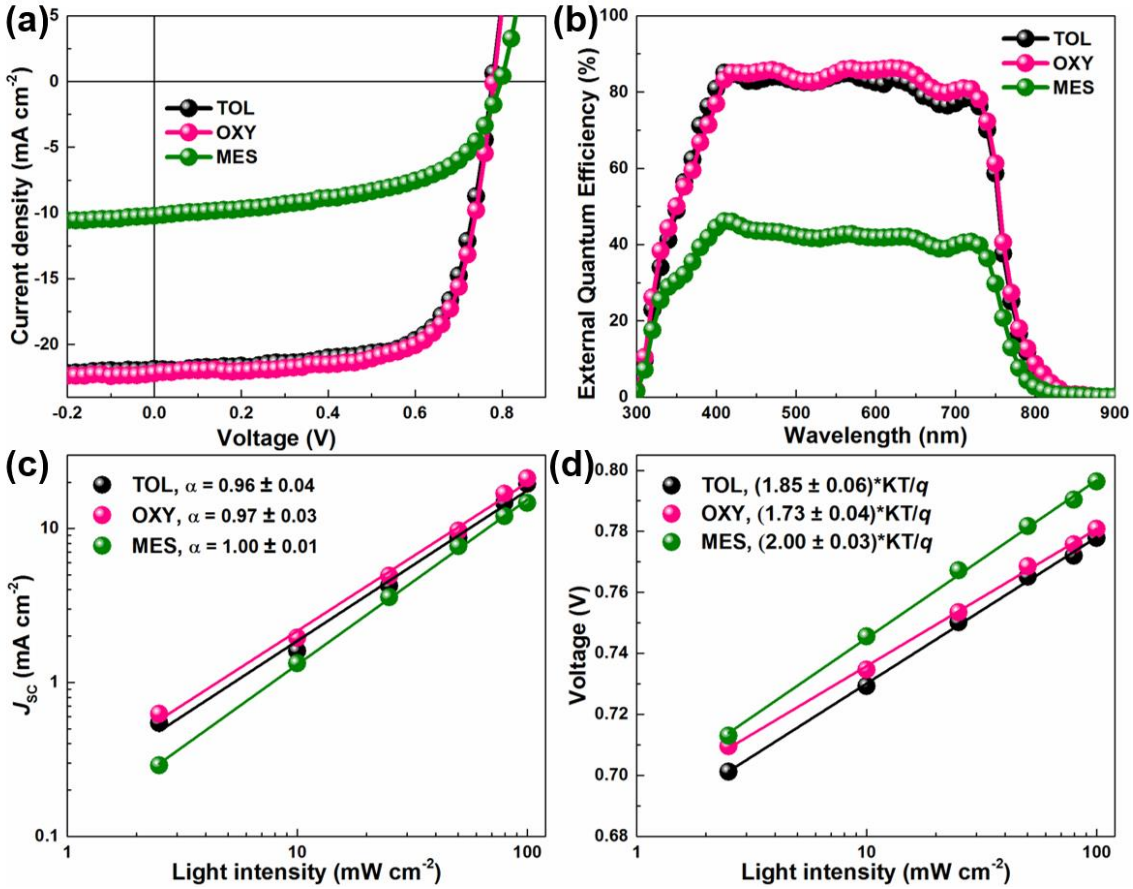

Figure 5.3. (a) *J*–*V* characteristics of ternary OSCs under AM 1.5G irradiation at 100 mW cm^{-2}. (b) The corresponding EQE curves. (c) Dependence of current density (J_{SC}) and (d) open-circuit voltage (V_{OC}) on light intensity of OSCs processed in TOL, OXY, and MES.

Table 5.1. Photovoltaic parameters of ternary OSCs with different NMP ratios in TOL, OXY, and MES.

Solvents	NMP	J_{SC} (mA cm^{-2})	V_{OC} (V)	FF (%)	PCE (%)	R_S (Ω)	R_{SH} (Ω)
TOL	2.0 vol%	21.31 (22.3)	0.777 (0.778)	68.1 (68.8)	11.28 (11.8)	1.94E+01 (1.93E+01)	3.73E+04 (4.08E+04)
OXY	2.25 vol%	21.70 (22.5)	0.779 (0.781)	69.5 (70.7)	11.75 (12.3)	2.35E+01 (1.56E+01)	2.54E+03 (6.93E+03)
MES	0.75 vol%	9.69 (10.30)	0.794 (0.799)	54.9 (55.3)	4.22 (4.57)	2.61E+01 (2.37E+01)	2.29E+03 (3.22E+03)

*Average values obtained from at least 25 devices. The data in parentheses are the highest values.

On the other hand, the ternary OSCs prepared using MES showed a much poorer performance of 4.57%, highlighting the marked impact of the chosen processing solvents on OSC performance. As shown in Figure 5.3b, the external quantum efficiencies (EQEs) of both TOL- and OXY-processed devices clearly revealed far better photo responses from 300 to 800 nm than those of MES-processed devices. This behavior is similar to that observed in the above absorption spectra of the ternary blending films with different solvents. Therefore, one can conclude that a properly chosen processing solvent is a key to realize controllable interactions between the solvent and the active components to achieve an optimal blending film morphology.

5.2.4 Carrier Transport and Recombination Dynamics

To unveil the role played by choice of the processing solvents in governing photovoltaic properties of the OSCs, we characterized the charge transport properties and recombination dynamics. First, the charge carrier mobilities of the hole- and electron-only devices were estimated using a space charge-limited curve (SCLC)[13] (see the section 5.5, Figure 5.16 and Table 5.6). The hole and electron mobilities were found to be similar for the two films processed from TOL and OXY, but much higher than those of the film processed from MES. Higher and more balanced mobility values imply better percolation pathways for the charge carriers, most likely due to the optimized morphology, which will be discussed later. In addition, this should be an important reason for the higher J_{SC} and FF values of both TOL- and OXY-processed devices.

Second, we analyzed the dependence of *J*–*V* characteristics of the devices on light intensity (*I*). In principle, J_{SC} has a power-law dependence on *I* ($J_{SC} \propto I^{\alpha}$), where the bimolecular recombination should be minimum ($\alpha \approx 1$) for maximum carrier sweep out.[14] As shown in Figure 5.3c, the log–log scale fitting of the data yielded $\alpha = 0.96$–1.00 for all devices, suggesting that the bimolecular recombination loss is minor for all devices. Next, we analyzed the slope of V_{OC} versus ln(*I*), reflecting the nature of the monomolecular recombination[15] (Figure 5.3d). The slopes of kT/*q* are 1.85, 1.73, and 2.00 for TOL-, OXY-, and MES-processed films, respectively, where k is Boltzmann's constant, T is the temperature, and *q* is the elementary charge. Collectively, the above results suggest that the monomolecular recombination process is predominantly involved in all devices. In particular, the MES-processed device had a higher monomolecular recombination probability with the highest slope of kT/*q*, which could be due to the presence of severe phase separation.

5.2.5 Film Morphology and Microstructure

The influence of the processing solvents on the morphology and microstructure of the blend films was further studied by a combination of techniques, including fluorescence microscopy, high-resolution

transmission electron microscopy (HR-TEM), atomic force microscopy (AFM), energy-dispersive X-ray analysis (EDAX), and grazing incidence wide-angle X-ray scattering (GIWAXS).

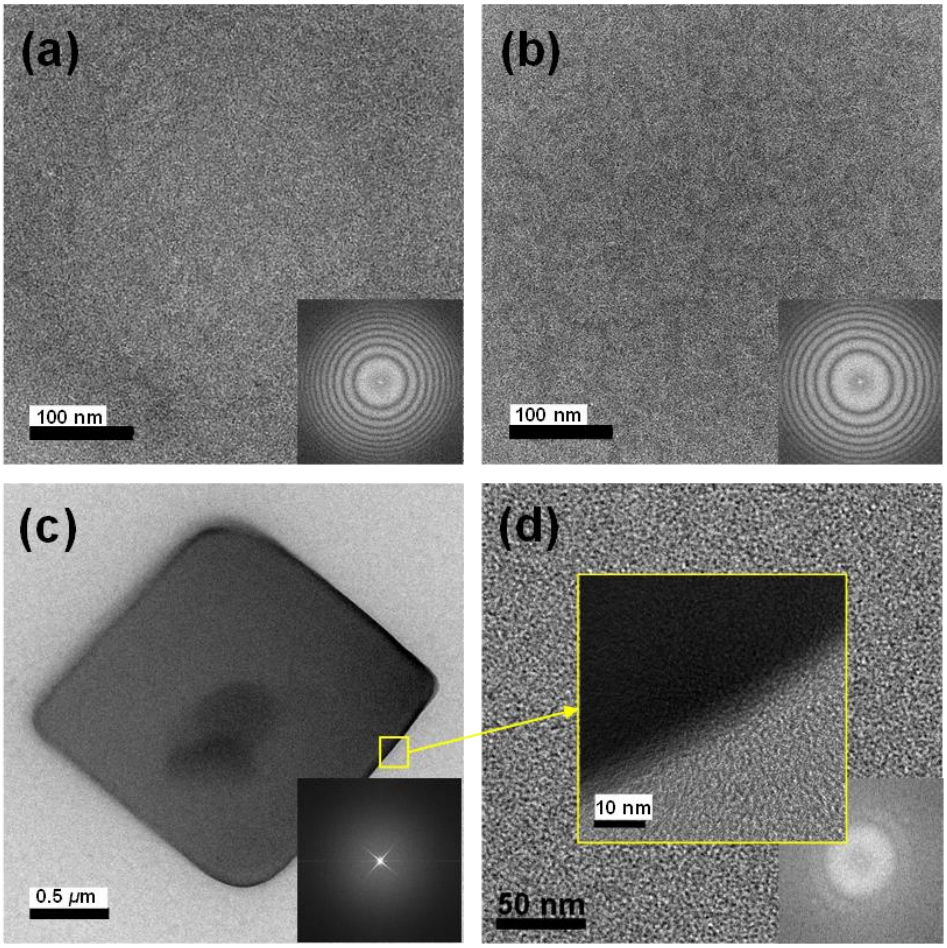

Figure 5.4. HR-TEM images. (a) In TOL. (b) In OXY. (c) In MES. (d) A zoomed view of the cubic crystal observed in MES, where the background is from the center of the crystal and the highlighted area is from the interface. Inset images (bottom right) in each figure are the corresponding diffractograms.

As shown in the Figure 5.17 of section 5.5, in the full excitation scan, the fluorescence microscopy images for the blend films processed from both TOL and OXY showed a featureless finely structured intermix, whereas the film processed from MES exhibited large dark bulk clusters of a cubic crystal structure, as clearly visualized by scanning electron microscopy (SEM) (see the section 5.5, Figure 5.18). To further analyze such crystal structures, the red, green, and blue channels were also recorded using appropriate excitation filters (~639 nm, ~555 nm, and ~488 nm, respectively), which produced similar phenomena as that observed in full light. Figure 5.4 shows the HR-TEM images of films cast with different solvents. All films presented a fibril morphology and exhibited phase separation on the nanometer scale, which was also

observed in both the topography and phase AFM images (see the section 5.5, Figure 5.19). Note that the cubic crystals were also pre-sent in the TEM image of the MES-processed film, which is consistent with the SEM image above.

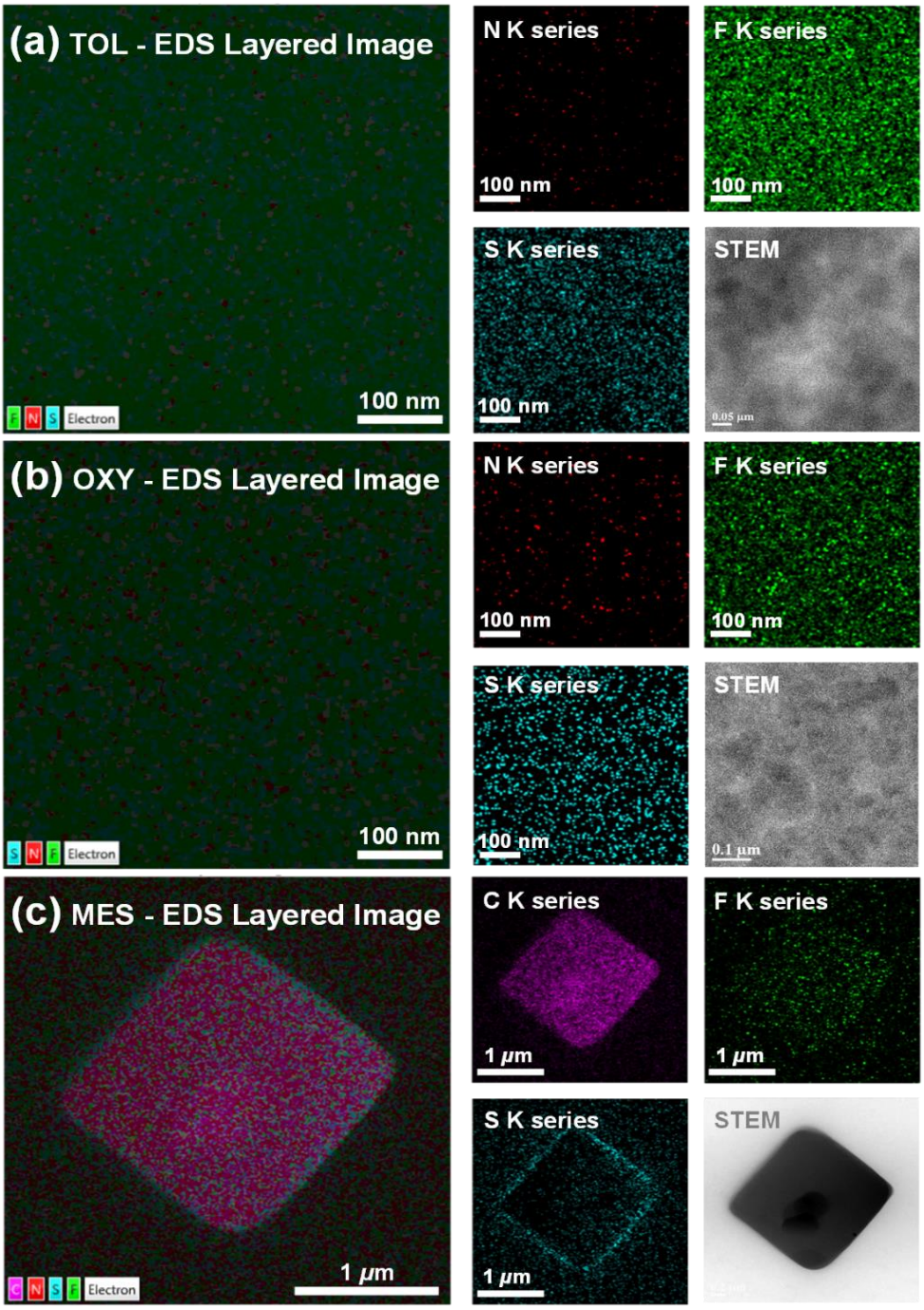

Figure 5.5. Elemental mapping by EDAX analysis along with STEM images of ternary blends. (a) In TOL. (b) In OXY. (c) In MES. Nitrogen and fluorine represent DR3TSBDT and PTB7-Th, respectively, and sulfur indicates the absence of $PC_{71}BM$.

The morphological differences induced by processing solvents were further supported by EDAX elemental mapping, where red, green, blue, and pink indicate nitrogen, fluoride, sulfur, and carbon signals, respectively, as shown in Figure 5.5. The elemental analysis of both TOL- and OXY-processed films clearly revealed well-dispersed dots with a homogenous distribution throughout the whole area, whereas the MES-processed film showed highly pink cubic crystals. This implies that the crystal is mainly composed of $PC_{71}BM$ crystallites in which some PTB7-Th chains are embedded into the $PC_{71}BM$ domains, as evidenced by the green and blue dots within the crystal.

In addition, the surface energy of PTB7-Th is 23.76 mJ m^{-2}, which is far closer to that of $PC_{71}BM$ (23.75 mJ m^{-2}) than that of DR3TSBDT (28.38 mJ m^{-2}) (see the section 5.5, Figure 5.20). This fact explains how PTB7-Th molecules can be easily located in the $PC_{71}BM$ domains, well supporting the above observation by EDAX. This was further evidenced by optical microscopy images of the pure and binary films of $PC_{71}BM$ with either PTB7-Th or DR3TSBDT (see the section 5.5, Figure 5.21), where such a crystal is only observed in PTB7-Th:$PC_{71}BM$. We also investigated the effect of the NMP additive on the formation of the crystals in MES-processed films. For all the cases, the similar crystals were observed, implying that they are independent of the presence of NMP in the MES films (see the section 5.5, Figure 5.22). Note also that in order to obtain a complete picture of the bimolecular crystal structure in the solid state via single crystal X-ray diffraction study, unfortunately, it is difficult to separate the pure cubic-like crystal in powder state. This is due to the presence of the amorphous PTB7-Th and $PC_{71}BM$ fractions in the solution (see the section 5.5, Figure 5.23).

For both TOL- and OXY-based processing systems, the GIWAXS patterns exhibited a similar bimodal texture of mixed edge-on and face-on orientations, with (100) lamellar and (010) π–π stacking peaks in both out-of-plane and in-plane directions (see Figure 5.6a and the section 5.5, Table 5.7 for the corresponding lattice parameters), which is quite similar to what was previously observed in the CB/DIO-based processing system.[1d] However, the GIWAXS patterns of the MES-processed films were significantly different due to the presence of the cubic crystals; as shown in Figure 5.6b, for the given MES-processed film sample, in addition to the broad (100) and (010) peaks, many scattering spots with irregular spacing were found in the GIWAXS image, and several distinct narrow peaks in the line-cut profiles were found in both out-of-plane and in-plane directions. Note that we clearly observed a strong and sharp peak at ~1.4 $Å^{-1}$ as-signed to $PC_{71}BM$ in the in-plane direction, reflecting the favored perpendicular orientation relative to the substrate. Additionally, we calculated the crystallite correlation length (CCL) of $PC_{71}BM$ lattice planes along the in-plane axis by using Debye Scherrer's equation.[16] Both TOL- and OXY-processed films had nearly similar small CCL values in the range 7−8 nm, whereas a very large CCL of 230 nm was obtained in the MES-processed film (see the section 5.5, Figure 5.24). To further clarify the crystals, we also measured GIWAXS

for the substrate side of the MES-processed film by using a float-off technique. The detailed process is given in the Methods and graphical illustration (see the section 5.5, Figure 5.25).

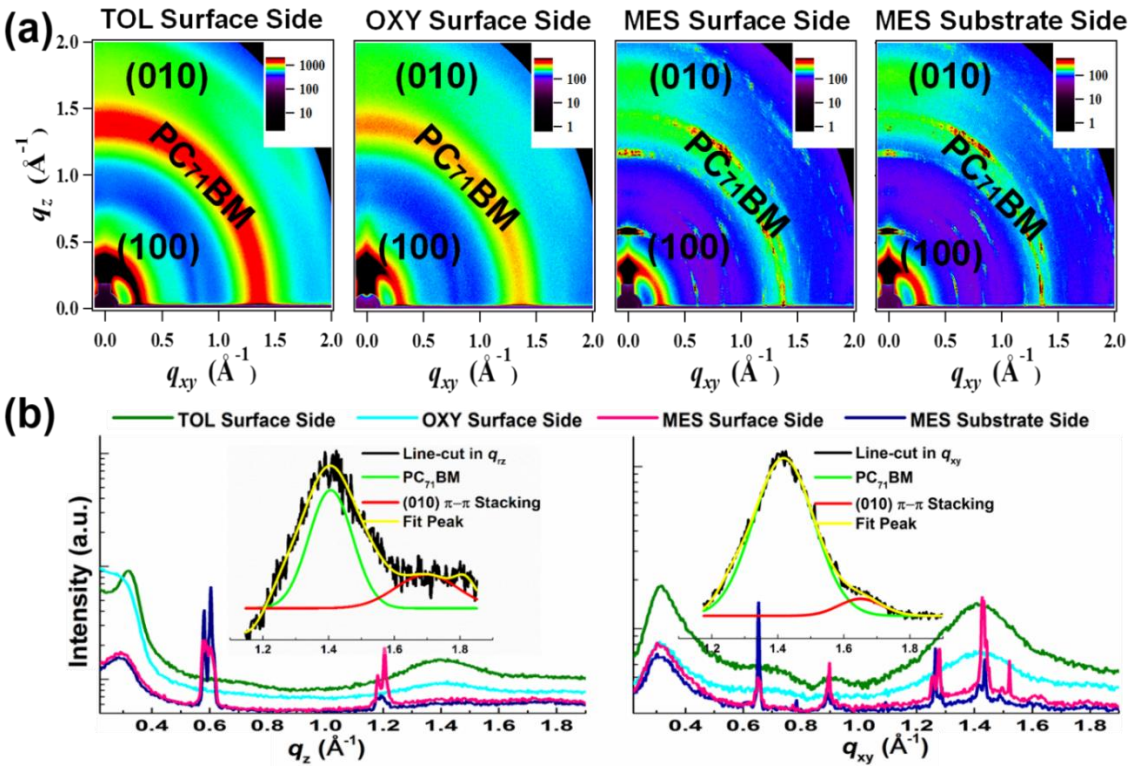

Figure 5.6. (a) GIWAXS pattern for ternary systems. (b) Out-of-plane and in-plane line cut profiles obtained from GIWAXS data processed in TOL, OXY, and MES. Insets in the line cuts are exemplary curve fittings in the corresponding higher *q* region. In MES, the surface and substrate sides of the films are exposed to beamline for in-depth analysis of the formed cubic structure throughout the volume. Different color bars represent intensity variance.

Compared to the surface-side measurement, the peak patterns of the substrate side showed some similarity, but the intensities of the narrow peaks assigned to the crystals were very different. Although as-signing the lattice structure of the crystals is difficult at this point in time, based on all the above results, one can conclude that PTB7-Th:$PC_{71}BM$ intercalating bimolecular crystals with an anisotropic lattice are grown on the MES-processed films.[17] We also envisage that the low performance is likely due to the intermolecular deconstruction between the bimolecular crystals (see Supporting Figure S11 and S15), leading to the inefficient charge transfer, and ultimately low FF and J_{SC} values. However, the size and thickness of the bimolecular crystals can be controllable by the kinetics of crystal growth process. This maybe create a new possibility of increased polymer-chain-mobility within thick nanocomposite thin-films, due to a combination of the increased connectivity and anisotropic lattice structure. Therefore, such features can

make a good candidate for applications in p-n crystal junction-based optoelectronics and ambipolar organic transistor.

5.3 Conclusion

In summary, we undertook an investigation to find a suitable non-chlorinated processing system for efficient ternary OSCs based on PTB7-Th:DR3TSBDT:$PC_{71}BM$ by determining the solubility properties of the active materials in various solvents and active material–solvent interactions. On the basis of these results, we successfully developed ternary OSCs processed from OXY having a high PCE of 12.3% (a certified PCE of 11.94%), which exceeds the record PCE of OSCs using a CB/DIO pair previously demonstrated by our group. The effects of non-halogenated solvents on the morphology, charge mobility, recombination dynamics, and OSC performance have been thoroughly studied. Another interesting point that this study uncovered is that the MES-based blend film shows a cubic-like bimolecular crystal structure of PTB7-Th:$PC_{71}BM$, although it has a negative effect on OSC performance. This study can inspire the community in the quest to further improve the performance of eco-friendly OSCs and to advance understanding of the solvent-dependent bimolecular crystal growth mechanism in blend systems.

5.4 References

1. (a) Schwartz, B. J., CONJUGATED POLYMERS AS MOLECULAR MATERIALS: How Chain Conformation and Film Morphology Influence Energy Transfer and Interchain Interactions. *Annu. Rev. Phys. Chem.* **2003,** *54* (1), 141-172; (b) Huang, Y.; Kramer, E. J.; Heeger, A. J.; Bazan, G. C., Bulk Heterojunction Solar Cells: Morphology and Performance Relationships. *Chem. Rev.* **2014,** *114* (14), 7006-7043; (c) An, Q.; Zhang, F.; Li, L.; Wang, J.; Sun, Q.; Zhang, J.; Tang, W.; Deng, Z., Simultaneous Improvement in Short Circuit Current, Open Circuit Voltage, and Fill Factor of Polymer Solar Cells through Ternary Strategy. *ACS Appl. Mater. Interfaces* **2015,** *7* (6), 3691-3698; (d) Kumari, T.; Lee, S. M.; Kang, S.-H.; Chen, S.; Yang, C., Ternary solar cells with a mixed face-on and edge-on orientation enable an unprecedented efficiency of 12.1%. *Energy Environ. Sci.* **2017,** *10* (1), 258-265; (e) Gasparini, N.; Jiao, X.; Heumueller, T.; Baran, D.; Matt, G. J.; Fladischer, S.; Spiecker, E.; Ade, H.; Brabec, C. J.; Ameri, T., Designing ternary blend bulk heterojunction solar cells with reduced carrier recombination and a fill factor of 77%. *Nat. Energy* **2016,** *1*, 16118; (f) Li, G.; Shrotriya, V.; Huang, J.; Yao, Y.; Moriarty, T.; Emery, K.; Yang, Y., High-efficiency solution processable polymer photovoltaic cells by self-organization of polymer blends. *Nat. Mater.* **2005,** *4* (11), 864-868.

2. (a) Guo, X.; Zhang, M.; Cui, C.; Hou, J.; Li, Y., Efficient Polymer Solar Cells Based on Poly(3-hexylthiophene) and Indene–C60 Bisadduct Fabricated with Non-halogenated Solvents. *ACS Appl. Mater. Interfaces* **2014,** *6* (11), 8190-8198; (b) Hoppe, H.; Niggemann, M.; Winder, C.; Kraut, J.; Hiesgen, R.;

Hinsch, A.; Meissner, D.; Sariciftci, N. S., Nanoscale Morphology of Conjugated Polymer/Fullerene-Based Bulk- Heterojunction Solar Cells. *Adv. Funct. Mater.* **2004,** *14* (10), 1005-1011; (c) Wan, Q.; Guo, X.; Wang, Z.; Li, W.; Guo, B.; Ma, W.; Zhang, M.; Li, Y., 10.8% Efficiency Polymer Solar Cells Based on PTB7-Th and PC71BM via Binary Solvent Additives Treatment. *Adv. Funct. Mater.* **2016,** *26* (36), 6635-6640; (d) Chen, Y.; Zhang, S.; Wu, Y.; Hou, J., Molecular Design and Morphology Control Towards Efficient Polymer Solar Cells Processed using Non-aromatic and Non-chlorinated Solvents. *Adv. Mater.* **2014,** *26* (17), 2744-2749; (e) Zhou, Y.; Gu, K. L.; Gu, X.; Kurosawa, T.; Yan, H.; Guo, Y.; Koleilat, G. I.; Zhao, D.; Toney, M. F.; Bao, Z., All-Polymer Solar Cells Employing Non-Halogenated Solvent and Additive. *Chem. Mater.* **2016,** *28* (14), 5037-5042; (f) Zhang, S.; Ye, L.; Zhang, H.; Hou, J., Green-solvent-processable organic solar cells. *Mater. Today* **2016,** *19* (9), 533-543; (g) Zhang, G.; Zhang, K.; Yin, Q.; Jiang, X.-F.; Wang, Z.; Xin, J.; Ma, W.; Yan, H.; Huang, F.; Cao, Y., High-Performance Ternary Organic Solar Cell Enabled by a Thick Active Layer Containing a Liquid Crystalline Small Molecule Donor. *J. Am. Chem. Soc.* **2017,** *139* (6), 2387-2395.

3. (a) Flory, P. J., *Principles of Polymer Chemistry*. Cornell University Press: 1953; Vol. chap. 14; (b) Cai, W.; Liu, P.; Jin, Y.; Xue, Q.; Liu, F.; Russell, T. P.; Huang, F.; Yip, H.-L.; Cao, Y., Morphology Evolution in High-Performance Polymer Solar Cells Processed from Nonhalogenated Solvent. *Adv. Sci.* **2015,** *2* (8), 1500095-n/a; (c) Rispens, M. T.; Meetsma, A.; Rittberger, R.; Brabec, C. J.; Sariciftci, N. S.; Hummelen, J. C., Influence of the solvent on the crystal structure of PCBM and the efficiency of MDMO-PPV:PCBM 'plastic' solar cells. *Chem. Commun.* **2003,** (17), 2116-2118; (d) Rothberg, L., Conjugated polymers: Watching polymers dance. *Nat. Chem.* **2011,** *3* (6), 425-426; (e) Miller-Chou, B. A.; Koenig, J. L., A review of polymer dissolution. *Prog. Polym. Sci.* **2003,** *28* (8), 1223-1270.

4. (a) Li, S.; Zhang, H.; Zhao, W.; Ye, L.; Yao, H.; Yang, B.; Zhang, S.; Hou, J., Green-Solvent-Processed All-Polymer Solar Cells Containing a Perylene Diimide-Based Acceptor with an Efficiency over 6.5%. *Adv. Energy Mater.* **2016,** *6* (5), 1501991-n/a; (b) Zhang, H.; Yao, H.; Zhao, W.; Ye, L.; Hou, J., High-Efficiency Polymer Solar Cells Enabled by Environment-Friendly Single-Solvent Processing. *Adv. Energy Mater.* **2016,** *6* (6), 1502177-n/a; (c) Chueh, C.-C.; Yao, K.; Yip, H.-L.; Chang, C.-Y.; Xu, Y.-X.; Chen, K.-S.; Li, C.-Z.; Liu, P.; Huang, F.; Chen, Y.; Chen, W.-C.; Jen, A. K. Y., Non-halogenated solvents for environmentally friendly processing of high-performance bulk-heterojunction polymer solar cells. *Energy Environ. Sci.* **2013,** *6* (11), 3241-3248; (d) Sprau, C.; Buss, F.; Wagner, M.; Landerer, D.; Koppitz, M.; Schulz, A.; Bahro, D.; Schabel, W.; Scharfer, P.; Colsmann, A., Highly efficient polymer solar cells cast from non-halogenated xylene/anisaldehyde solution. *Energy Environ. Sci.* **2015,** *8* (9), 2744-2752; (e) Zhao, W.; Ye, L.; Zhang, S.; Sun, M.; Hou, J., A universal halogen-free solvent system for highly efficient polymer solar cells. *J. Mater. Chem. A* **2015,** *3* (24), 12723-12729; (f) Zhao, J.; Li, Y.; Yang, G.; Jiang, K.;

Lin, H.; Ade, H.; Ma, W.; Yan, H., Efficient organic solar cells processed from hydrocarbon solvents. *Nat. Energy* **2016,** *1*, 15027.

5. Walker, B.; Tamayo, A.; Duong, D. T.; Dang, X.-D.; Kim, C.; Granstrom, J.; Nguyen, T.-Q., A Systematic Approach to Solvent Selection Based on Cohesive Energy Densities in a Molecular Bulk Heterojunction System. *Adv. Energy Mater.* **2011,** *1* (2), 221-229.

6. (a) Chen, K.-S.; Yip, H.-L.; Schlenker, C. W.; Ginger, D. S.; Jen, A. K. Y., Halogen-free solvent processing for sustainable development of high efficiency organic solar cells. *Org. Electron.* **2012,** *13* (12), 2870-2878; (b) Matsushima, T.; Sandanayaka, A. S. D.; Esaki, Y.; Adachi, C., Vacuum-and-solvent-free fabrication of organic semiconductor layers for field-effect transistors. *Sci. Rep.* **2015,** *5*, 14547; (c) Kaduwal, D.; Schleiermacher, H.-F.; Schulz-Gericke, J.; Kroyer, T.; Zimmermann, B.; Würfel, U., ITO-free organic solar cells with roll-to-roll coated organic functional layers from non-halogenated solvents. *Sol. Energy Mater. Sol. Cells* **2014,** *124*, 92-97; (d) Schmidt-Hansberg, B.; Sanyal, M.; Grossiord, N.; Galagan, Y.; Baunach, M.; Klein, M. F. G.; Colsmann, A.; Scharfer, P.; Lemmer, U.; Dosch, H.; Michels, J.; Barrena, E.; Schabel, W., Investigation of non-halogenated solvent mixtures for high throughput fabrication of polymer–fullerene solar cells. *Sol. Energy Mater. Sol. Cells* **2012,** *96*, 195-201; (e) Fan, B.; Ying, L.; Zhu, P.; Pan, F.; Liu, F.; Chen, J.; Huang, F.; Cao, Y., All-Polymer Solar Cells Based on a Conjugated Polymer Containing Siloxane-Functionalized Side Chains with Efficiency over 10%. *Adv. Mater.* **2017,** *29* (47), 1703906; (f) Fan, B.; Ying, L.; Wang, Z.; He, B.; Jiang, X.-F.; Huang, F.; Cao, Y., Optimisation of processing solvent and molecular weight for the production of green-solvent-processed all-polymer solar cells with a power conversion efficiency over 9%. *Energy Environ. Sci.* **2017,** *10* (5), 1243-1251.

7. (a) Fu, B.; Wang, C.-Y.; Rose, B. D.; Jiang, Y.; Chang, M.; Chu, P.-H.; Yuan, Z.; Fuentes-Hernandez, C.; Kippelen, B.; Brédas, J.-L.; Collard, D. M.; Reichmanis, E., Molecular Engineering of Nonhalogenated Solution-Processable Bithiazole-Based Electron-Transport Polymeric Semiconductors. *Chem. Mater.* **2015,** *27* (8), 2928-2937; (b) Schreiber, H. P.; Croucher, M. D., Surface characteristics of solvent-cast polymers. *J. Appl. Polym. Sci.* **1980,** *25* (9), 1961-1968; (c) Huggins, M. L., Solutions of Long Chain Compounds. *J. Chem. Phys.* **1941,** *9* (5), 440-440; (d) Huggins, M. L., Some Properties of Solutions of Long-chain Compounds. *J. Chem. Phys.* **1942,** *46* (1), 151-158; (e) Etxabarren, C.; Iriarte, M.; Uriarte, C.; Etxeberría, A.; Iruin, J. J., Polymer–solvent interaction parameters in polymer solutions at high polymer concentrations. *J. Chromatogr. A* **2002,** *969* (1–2), 245-254; (f) Pajula, K.; Taskinen, M.; Lehto, V.-P.; Ketolainen, J.; Korhonen, O., Predicting the Formation and Stability of Amorphous Small Molecule Binary Mixtures from Computationally Determined Flory−Huggins Interaction Parameter and Phase Diagram. *Mol. Pharm.* **2010,** *7* (3), 795-804; (g) Gaikwad, A. M.; Khan, Y.; Ostfeld, A. E.; Pandya, S.; Abraham, S.;

Arias, A. C., Identifying orthogonal solvents for solution processed organic transistors. *Org. Electron.* **2016,** *30*, 18-29.

8. (a) Chen, X.; Liu, X.; Burgers, M. A.; Huang, Y.; Bazan, G. C., Green-Solvent-Processed Molecular Solar Cells. *Angew. Chem. Int. Ed.* **2014,** *53* (52), 14378-14381; (b) Kozub, D. R.; Vakhshouri, K.; Orme, L. M.; Wang, C.; Hexemer, A.; Gomez, E. D., Polymer Crystallization of Partially Miscible Polythiophene/Fullerene Mixtures Controls Morphology. *Macromolecules* **2011,** *44* (14), 5722-5726; (c) Olayemi, J. Y.; Adeyeye, A. A., Some properties of polyvinyl acetate films cast from methanol, acetone and chloroform as solvent. *Polym. Test.* **1982,** *3* (1), 25-35.

9. (a) Hansen, C. M., *Hansen solubility parameters: a user's handbook*. CRC press: 2007; (b) Machui, F.; Abbott, S.; Waller, D.; Koppe, M.; Brabec, C. J., Determination of Solubility Parameters for Organic Semiconductor Formulations. *Macromol. Chem. Phys* **2011,** *212* (19), 2159-2165.

10. (a) Bawendi, M. G.; Freed, K. F.; Mohanty, U., A lattice field theory for polymer systems with nearest-neighbor interaction energies. *J. Chem. Phys.* **1987,** *87* (9), 5534-5540; (b) Flory, P. J., Thermodynamics of High Polymer Solutions. *J. Chem. Phys.* **1941,** *9* (8), 660-660; (c) Flory, P. J., Thermodynamics of High Polymer Solutions. *J. Chem. Phys.* **1942,** *10* (1), 51-61; (d) Orwoll, R. A.; Arnold, P. A., Polymer–Solvent Interaction Parameter χ. In *Physical Properties of Polymers Handbook*, Mark, J. E., Ed. Springer New York: New York, NY, 2007; pp 233-257.

11. Huang, T.-Y.; Patra, D.; Hsiao, Y.-S.; Chang, S. H.; Wu, C.-G.; Ho, K.-C.; Chu, C.-W., Efficient ternary bulk heterojunction solar cells based on small molecules only. *J. Mater. Chem. A* **2015,** *3* (19), 10512-10518.

12. (a) Xu, X.; Yu, T.; Bi, Z.; Ma, W.; Li, Y.; Peng, Q., Realizing Over 13% Efficiency in Green-Solvent-Processed Nonfullerene Organic Solar Cells Enabled by 1,3,4-Thiadiazole-Based Wide-Bandgap Copolymers. *Adv. Mater.* **2018,** *30* (3), 1703973-n/a; (b) Zhao, W.; Zhang, S.; Zhang, Y.; Li, S.; Liu, X.; He, C.; Zheng, Z.; Hou, J., Environmentally Friendly Solvent-Processed Organic Solar Cells that are Highly Efficient and Adaptable for the Blade-Coating Method. *Adv. Mater.*, 1704837-n/a; (c) Zhao, W.; Li, S.; Yao, H.; Zhang, S.; Zhang, Y.; Yang, B.; Hou, J., Molecular Optimization Enables over 13% Efficiency in Organic Solar Cells. *J. Am. Chem. Soc.* **2017,** *139* (21), 7148-7151.

13. (a) Armin, A.; Juska, G.; Ullah, M.; Velusamy, M.; Burn, P. L.; Meredith, P.; Pivrikas, A., Balanced Carrier Mobilities: Not a Necessary Condition for High-Efficiency Thin Organic Solar Cells as Determined by MIS-CELIV. *Adv. Energy Mater.* **2014,** *4* (4), 1300954-n/a; (b) Kline, R. J.; McGehee, M. D.; Kadnikova, E. N.; Liu, J.; Fréchet, J. M. J., Controlling the Field-Effect Mobility of Regioregular Polythiophene by Changing the Molecular Weight. *Adv. Mater.* **2003,** *15* (18), 1519-1522; (c) Goh, C.; Kline, R. J.; McGehee, M. D.; Kadnikova, E. N.; Fréchet, J. M. J., Molecular-weight-dependent mobilities in regioregular poly(3-hexyl-thiophene) diodes. *Appl. Phys. Lett.* **2005,** *86* (12), 122110.

14. (a) Schilinsky, P.; Waldauf, C.; Brabec, C. J., Recombination and loss analysis in polythiophene based bulk heterojunction photodetectors. *Appl. Phys. Lett.* **2002,** *81* (20), 3885-3887; (b) Seki, K., Overall current-voltage characteristics of space charge controlled currents for thin films by a single carrier species. *J. Appl. Phys.* **2014,** *116* (6), 063716.

15. (a) Kyaw, A. K. K.; Wang, D. H.; Gupta, V.; Leong, W. L.; Ke, L.; Bazan, G. C.; Heeger, A. J., Intensity Dependence of Current–Voltage Characteristics and Recombination in High-Efficiency Solution-Processed Small-Molecule Solar Cells. *ACS Nano* **2013,** *7* (5), 4569-4577; (b) Riedel, I.; Parisi, J.; Dyakonov, V.; Lutsen, L.; Vanderzande, D.; Hummelen, J. C., Effect of Temperature and Illumination on the Electrical Characteristics of Polymer–Fullerene Bulk-Heterojunction Solar Cells. *Adv. Funct. Mater.* **2004,** *14* (1), 38-44.

16. (a) Kumari, T.; Moon, M.; Kang, S.-H.; Yang, C., Improved efficiency of DTGe(FBTTh2)2-based solar cells by using macromolecular additives: How macromolecular additives versus small additives influence nanoscale morphology and photovoltaic performance. *Nano Energy* **2016,** *24*, 56-62; (b) Lilliu, S.; Alsari, M.; Bikondoa, O.; Emyr Macdonald, J.; Dahlem, M. S., Absence of Structural Impact of Noble Nanoparticles on P3HT:PCBM Blends for Plasmon-Enhanced Bulk-Heterojunction Organic Solar Cells Probed by Synchrotron GI-XRD. *Sci. Rep.* **2015,** *5*, 10633.

17. (a) Wang, Y.; Chan, S. L. I.; Amal, R.; Shen, Y. R.; Kiatkittipong, K., XRD ANISOTROPIC BROADENING OF NANO-CRYSTALLITES; (b) Haware, R. V.; Kim, P.; Ruffino, L.; Nimi, B.; Fadrowsky, C.; Doyle, M.; Boerrigter, S. X. M.; Cuitino, A.; Morris, K., Anisotropic crystal deformation measurements determined using powder X-ray diffraction and a new in situ compression stage. *Int. J. Pharm.* **2011,** *418* (2), 199-206.

5.5 Supporting Texts and Figures

Solubility Measurement

The solubility's of PTB7-Th, DR3TSBDT and $PC_{71}BM$ in various solvents were measured optically. First, a set of standard absorption spectra were taken for PTB7-Th, DR3TSBDT and $PC_{71}BM$ in chlorobenzene (CB) at known concentrations and diluted with 100 to 10,000 volumes of CB in order to achieve an optical density suitable for absorption measurement (SI Figs. S1a, S2a, and S3a respectively).[4] The optical density of PTB7-Th (at 704 nm) and DR3TSBDT (at 505 nm) solutions exhibit a linear relationship with concentration between 1.05 - 21 μg mL^{-1} (SI Figs. S1b and S2b respectively) and $PC_{71}BM$ (at 463 nm) solutions shows a linear relationship with concentration between 2.1 - 42 μg mL^{-1} (SI Fig. S3b).

Secondly, for determining solubility in various solvents, solutions were prepared by mixing 14 mg mL^{-1} of solid material in case of PTB7-Th or DR3TSBDT and 21 mg mL^{-1} of solid material in case of $PC_{71}BM$ with a small volume (200 μL) of each test solvent. It was followed by stirring for 15 minutes and then allowed to stand for at least 6 hours at room temperature. It should be noted that the maximum concentrations in mg mL^{-1} for each material are chosen as per our device fabrication conditions. The saturated solutions were then diluted in same ratio as the standard solutions. The optical density of the diluted solutions are measured and their solubility was calculated using the slope of linearly fitted graphs (SI Figs. S1b, S2b, and S3b) of standard curves with known concentrations.

2-D and 3-D plots in Hansen space.

The solubility parameters for PTB7-Th, DR3TSBDT and $PC_{71}BM$ were calculated with the help of MATLAB programming. The solvating power of each solvent was ranked as 1 (> 2 mg mL^{-1}) and 0 (< 2 mg mL^{-1}). Using MATLAB programming, all the good points (1s) and the bad points (0s) were stored in separate matrix and their plots versus δD, δP, and δH in 2-D and 3-D spaces were plotted. Next, for fitting spheres through good solvents points, sphere-fit algorithm[5] was written in MATLAB. Since the best fit of sphere through number (≥ 4) of δD, δP, and δH data points were needed to be done therefore, the written algorithm fits the sphere through set of data using least square method (LSM).[6] The written program returns the center and radius of the best fitted sphere after minimizing its distance from each points in 3-D space. Using this center and radius, best fit sphere (called LSM sphere) for PTB7-Th, DR3TSBDT and $PC_{71}BM$ were plotted (inner purple color sphere in 3-D plots). To fit all the good points inside or on the sphere, second sphere (called modified LSM) is plotted (outer pink color sphere in 3-D plots) such that all the good points are either inside or on the surface of the sphere while the center remain unchanged (to be noted). To clearly visualize the modified LSM sphere fit, 2-D plots of good solvent points versus (δD δP), (δP δH), and (δH δD) are also demonstrated with circle fit using the center and radius from the modified LSM. Figure 1c contains RED value calculated from the radius of the modified LSM data as the modified

LSM sphere encloses all the good data points and the radius predicted is the maximum radius for the given set of solvent data in each material case. For RED calculation, the radius of interaction, R_a is calculated using the following equation:[7]

$$[(R_a)]^2 = [4(\delta D_1 - \delta D_2)]^2 + [(\delta P_1 - \delta P_2)]^2 + [(\delta H_1 - \delta H_2)]^2$$

Where, the radius of interaction (R_a) for two substances with Hansen parameters (δD_i, δP_i, δH_i) is defined as the distance between their coordinates in Hansen space as above and is the ability of one substance to dissolve another.

In order to calculate the polymer-solvent interaction parameter χ using the HSP,[7] the following equations for χ_{12} have been used:

$$\chi_{12} = V^*A_{12}/RT$$

Where, $A_{12} = [(\delta D_1 - \delta D_2)]^2 + 0.25[(\delta P_1 - \delta P_2)]^2 + 0.25[(\delta H_1 - \delta H_2)]^2$, V is the molar volume of the solvent (see SI Table S1).

References

[1] B. Kan, Q. Zhang, M. Li, X. Wan, W. Ni, G. Long, Y. Wang, X. Yang, H. Feng, Y. Chen, *J. Am. Chem. Soc.* **2014**, *136*, 15529-15532.

[2] T. Kumari, S. M. Lee, S.-H. Kang, S. Chen, C. Yang, *Energy Environ. Sci.* **2017**, *10*, 258-265.

[3] a) J. You, L. Dou, K. Yoshimura, T. Kato, K. Ohya, T. Moriarty, K. Emery, C.-C. Chen, J. Gao, G. Li, Y. Yang, *Nat. Commun.* **2013**, *4*, 1446; b) Y. B. Zhu, L. K. Ang, *Sci. Rep.* **2015**, *5*, 9173.

[4] B. Walker, A. Tamayo, D. T. Duong, X.-D. Dang, C. Kim, J. Granstrom, T.-Q. Nguyen, *Adv. Energy Mater.* **2011**, *1*, 221-229.

[5] a) V. Pratt, *ACM SIGGRAPH Comput. Graph.* **1987**, *21*, 145-152; b) L. Moura, R. Kitney, *Comput. Phys. Commun.* **1991**, *64*, 57-63; c) F. Machui, S. Abbott, D. Waller, M. Koppe, C. J. Brabec, *Macromol. Chem. Phys* **2011**, *212*, 2159-2165; d) S. J. Ahn, W. Rauh, H.-J. Warnecke, *Pattern Recognition* **2001**, *34*, 2283-2303.

[6] K. J. Cross, J. W. McBride, J. J. Lifton, *Prec. Eng.* **2014**, *38*, 499-505.

[7] C. M. Hansen, *Hansen solubility parameters: a user's handbook*, CRC press, **2007**.

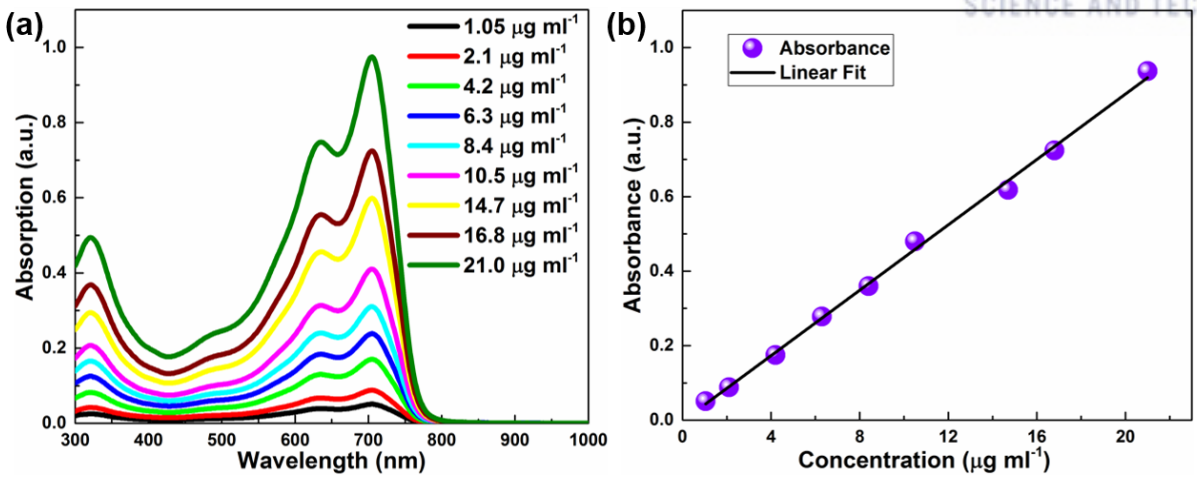

Figure 5.7. (a) Reference U-V Vis. absorbance for PTB7-Th taken at various known concentrations. (b) The linear fit for PTB7-Th at the absorption maximum (704 nm).

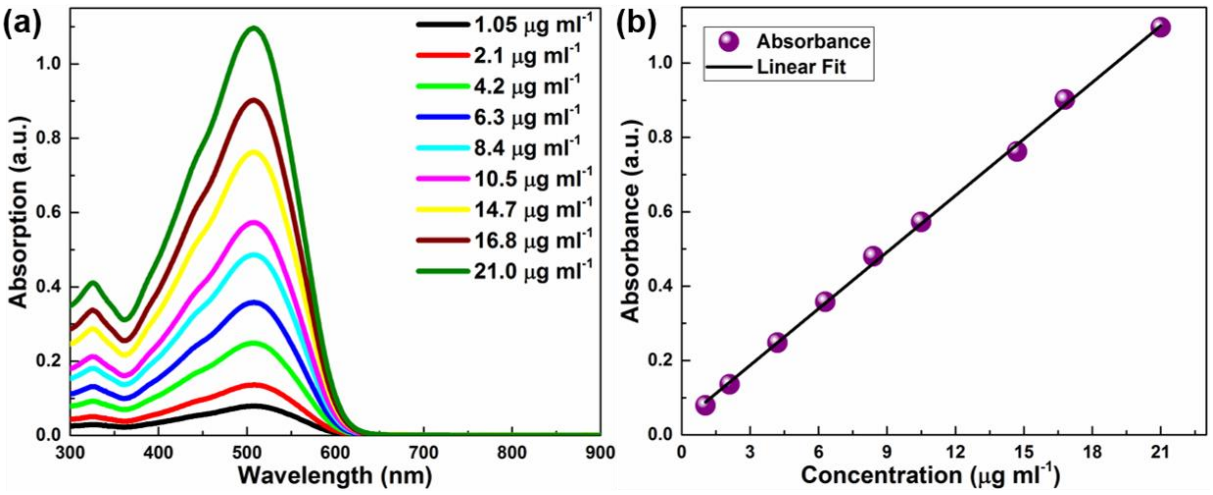

Figure 5.8. (a) Reference U-V Vis. absorbance for DR3TSBDT taken at various known concentrations. (b) The linear fit for DR3TSBDT at the absorption maximum (505 nm).

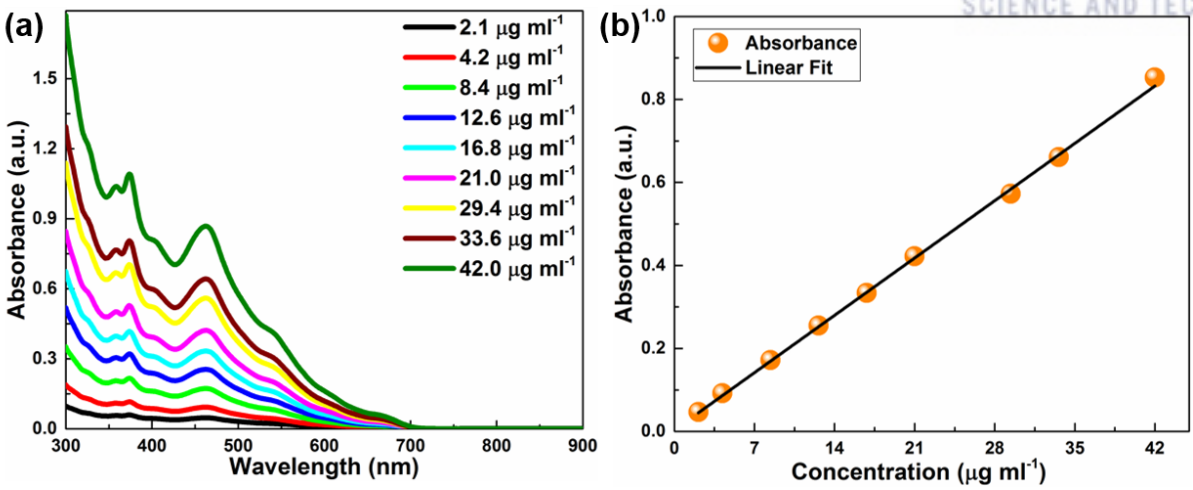

Figure 5.9. (a) Reference U-V Vis. absorbance for $PC_{71}BM$ taken at various known concentrations. (b) The linear fit for $PC_{71}BM$ at the absorption maximum (463 nm).

Table 5.2. Room temperature solubility of PTB7-Th, DR3TSBDT, and $PC_{71}BM$ in different solvents along with some thermodynamic properties.

Solvents	δD	δP	δH	Molar Vol.	Boiling Point (°C)	Vapor Pressure	PTB7-Th solubility (mg mL^{-1})	DR3TSBDT solubility (mg mL^{-1})	$PC_{71}BM$ solubility (mg mL^{-1})
1,2,4-Trichlorobenzene	20.2	4.2	3.2	125.5	213	0.29	13.5±0.47	>14.0	>21.0
o-Dichlorobenzene	19.2	6.3	3.3	113	180.42	1.38	>14.0	10.32±0.36	>21.0
Chlorobenzene	19	4.3	2	102.1	131.72	12.01	>14.0	>14.0	>21.0
Mesitylene	18	0.6	0.6	139.5	164.74	2.39	10.5±0.47	3.41±0.36	>21.0
Acetone	15.5	10.4	7	73.8	56.29	231.79	0	0	0
Chloroform	17.8	3.1	5.7	80.5	61.18	194.68	>14.0	>14.0	>21.0
Ethanol	15.8	8.8	19.4	58.6	78.29	59.15	0	0	0
p-Xylene	17.8	1	3.1	121.1	138.36	8.78	6.94±0.47	5.56±0.36	20.22±0.58

o-Xylene	17.8	1	3.1	121.1	144.43	6.64	12.56±0.47	5.41±0.36	20.19±0.58
Toluene	18	1.4	2	106.6	110.63	28.4	12.24±0.47	6.67±0.36	>21.0
Cyclohexane	16.8	0	0.2	108.9	80.72	97.49	< 0.5	< 0.2	1.65±0.58
Dimethyl Sulfoxide (DMSO)	18.4	16.4	10.2	71.3	190.85	0.48	0	0	1.07±0.58
Dimethyl Formamide (DMF)	17.4	13.7	11.3	77.4	152	3.68	0	0	1.75±0.58
Tetrahydrofuran (THF)	16.8	5.7	8	81.9	65.97	180.98	>14.0	6.31±0.36	4.46±0.58
Hexane	14.9	0	0	131.4	68.73	151.35	< 0.1	0	0
N-Methyl-2-Pyrrolidone (NMP)	18	12.3	7.2	96.6	204.27	0.09	0	< 0.1	>21.0
Thiophene	18.9	2.4	7.8	79.5	84.16	79.81	>14.0	12.64±0.36	15.18±0.58
Methanol	14.7	12.3	22.3	40.6	64.7	127.74	0	0	0
Water	15.5	16	42.3	18	100	21.8	0	0	0
Cyclohexanol	17.4	4.1	13.5	105.7	160.85	0.91	0	0	0
Aniline	20.1	5.8	11.2	91.6	184	0.6	0	11.77±0.36	>21.0
Bromobenzene	19.2	5.5	4.1	105.6	156.09	4.14	>14.0	12.29±0.36	>21.0

*Note: the > symbol designates larger than the initial concentrations.

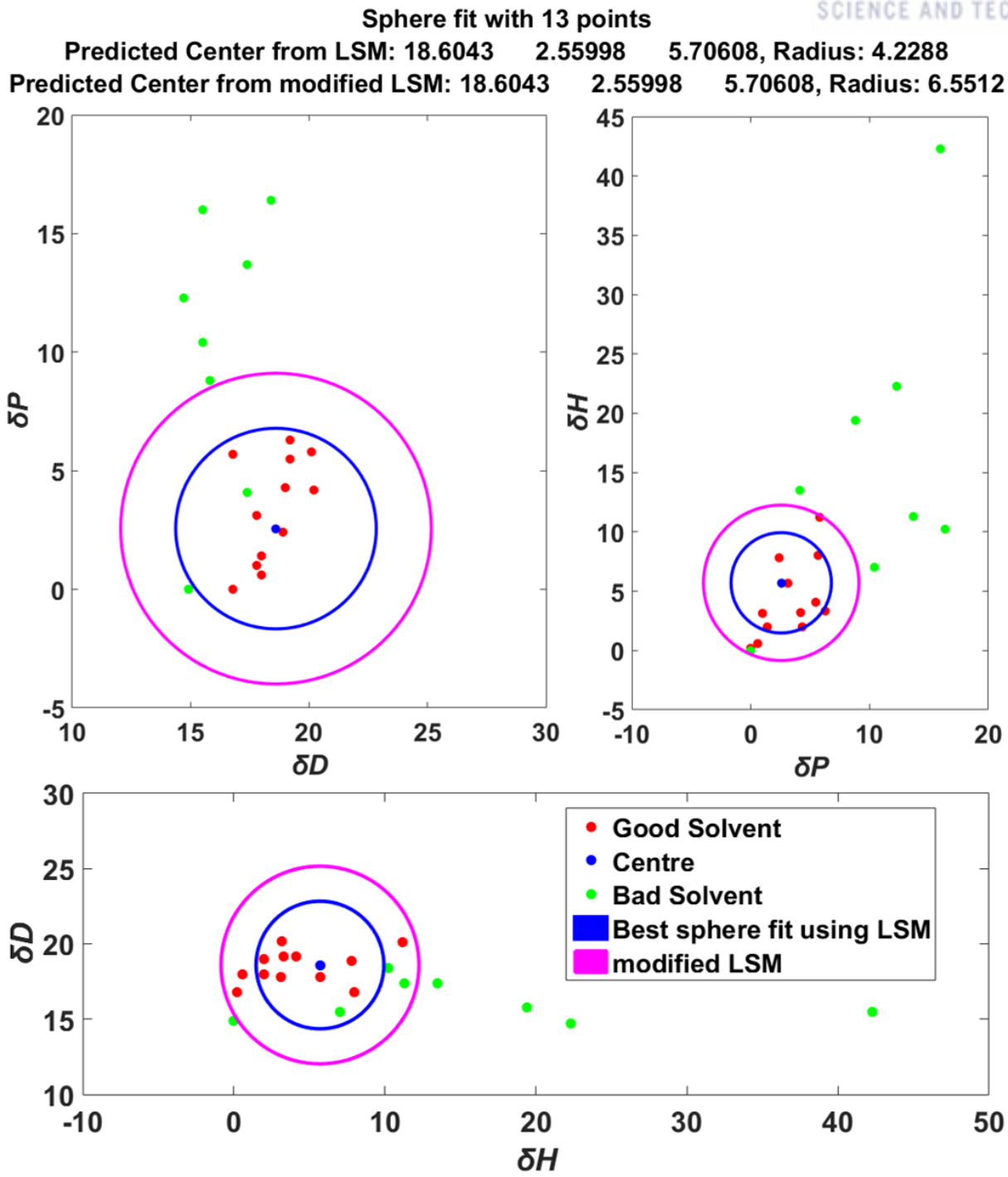

Figure 5.10. The 2-D plots of good and bad solvents versus δD, δP, and δH as well as the Hansen Solubility Parameters for PTB7-Th calculated using sphere fit program written in MATLAB.

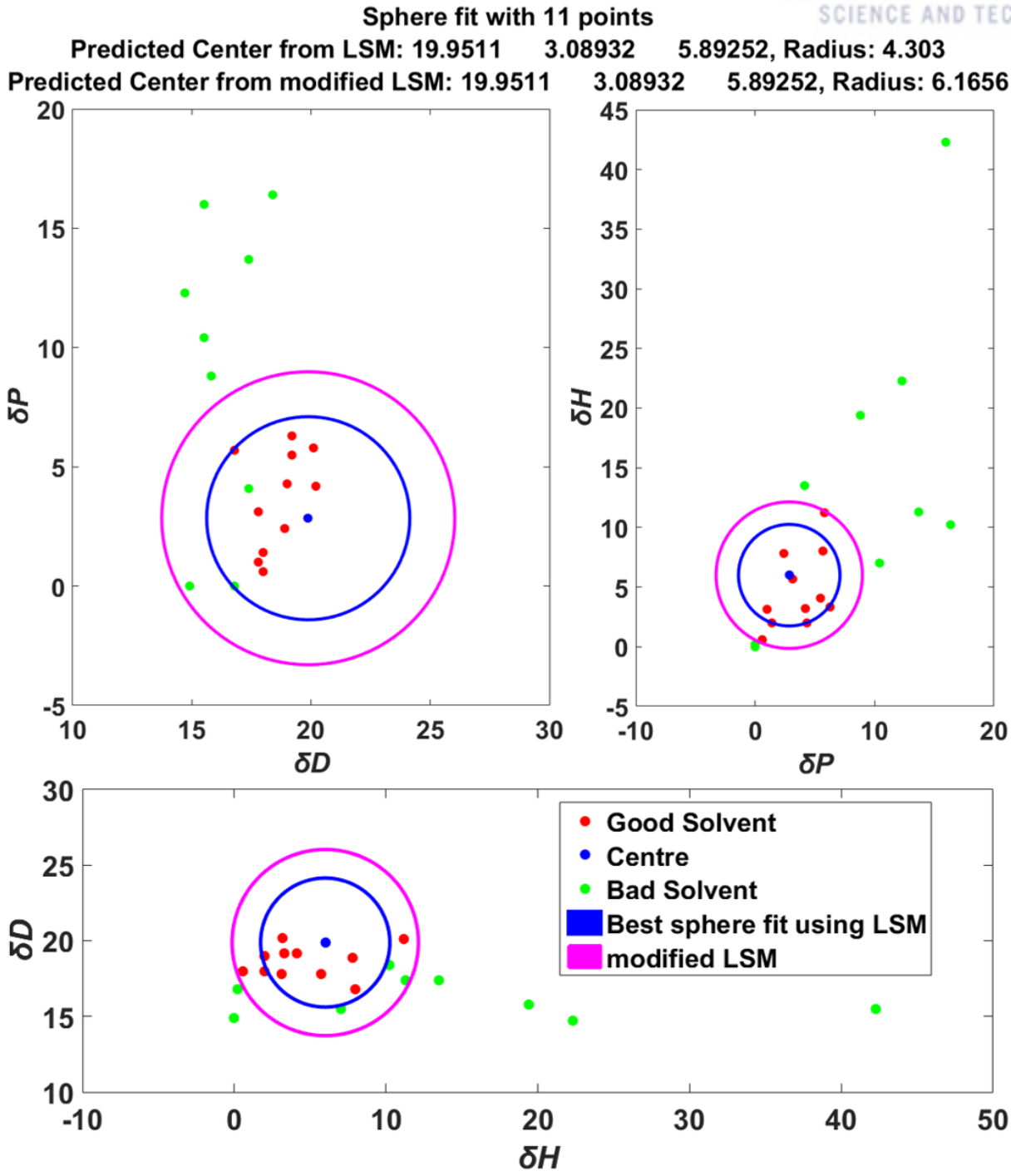

Figure 5.11. The 2-D plots of good and bad solvents versus δD, δP, and δH as well as the Hansen Solubility Parameters for DR3TSBDT calculated using sphere fit program written in MATLAB.

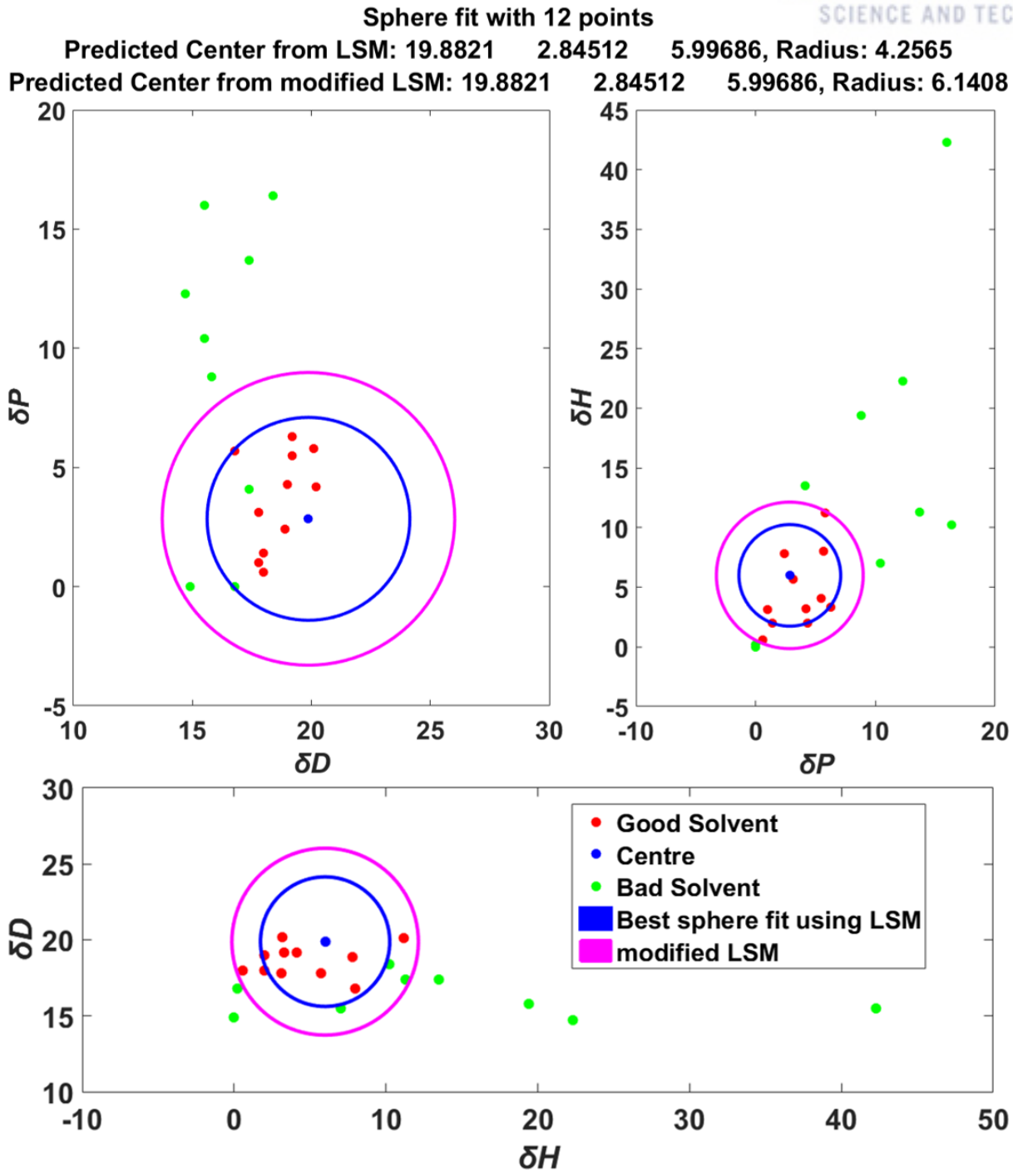

Figure 5.12. The 2-D plots of good and bad solvents versus δD, δP, and δH as well as the Hansen Solubility Parameters for $PC_{71}BM$ calculated using sphere fit program written in MATLAB.

Table 5.3. RED and χ values of PTB7-Th, DR3TSBDT, and $PC_{71}BM$ in TOL, OXY, and MES.

Solvent	Material	RED From Modified LSM	χ Parameter
TOL	PTB7-Th	0.621	0.178
OXY		0.525	0.144
MES		0.855	0.442
TOL	DR3TSBDT	0.937	0.359
OXY		0.900	0.377
MES		1.142	0.698
TOL	$PC_{71}BM$	0.924	0.347
OXY		0.879	0.356
MES		1.132	0.681

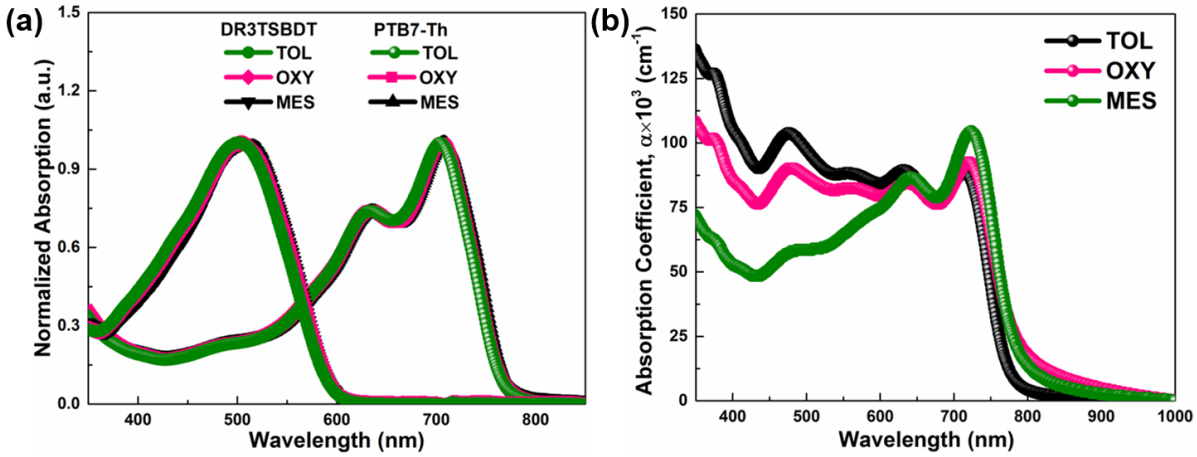

Figure 5.13. U-V Vis. absorption of (a) neat PTB7-Th and DR3TSBDT solutions, and (b) ternary blend (25 wt.%) thin films in TOL, OXY, and MES.

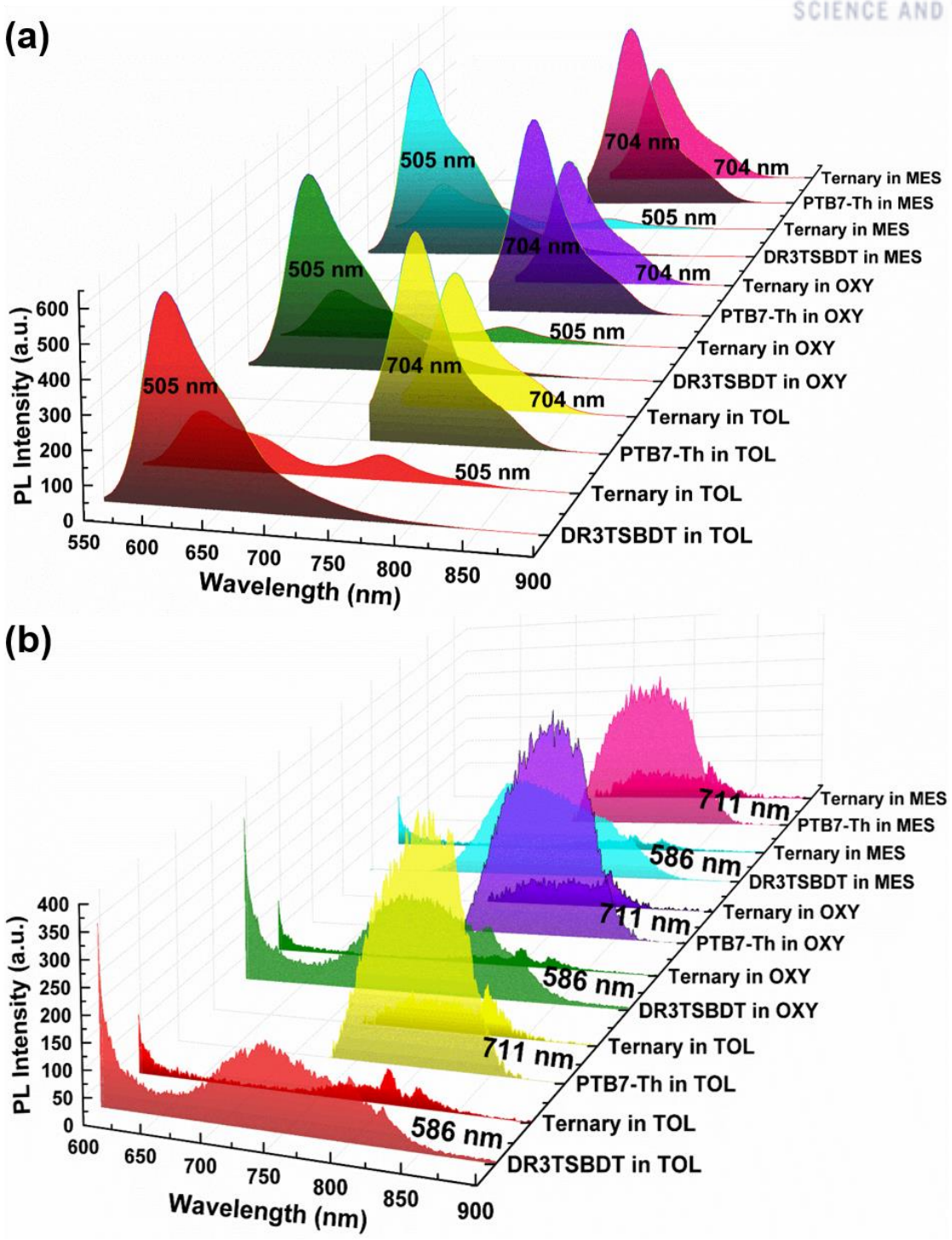

Figure 5.14. Photoluminescence spectra of pure DR3TSBDT, PTB7-Th, and ternary blend (25 wt.%). (a) Solutions, and (b) films in TOL, OXY, and MES.

Table 5.4. The photovoltaic parameters of ternary OSCs with different NMP ratios in TOL, OXY, and MES.

Solvents	**NMP**	J_{SC} **(mA cm^{-2})**	V_{OC} **(V)**	**FF (%)**	**PCE (%)**	R_S **(Ω)**	R_{SH} **(Ω)**
TOL	0 vol%	9.89 (10.0)	0.783 (0.787)	50.9 (55.5)	4.00 (4.33)	2.70E+01 (2.43E+01)	2.78E+03 (3.24E+03)
TOL	1.5 vol%	21.9 (22.3)	0.765 (0.776)	67.1 (68.6)	11.35 (11.6)	2.19E+01 (2.17E+01)	4.37E+03 (6.54E+03)
TOL	2.25 vol%	21.2 (22.2)	0.758 (0.772)	67.3 (68.4)	11.14 (11.3)	2.55E+01 (2.35E+01)	2.77E+03 (7.22E+03)
OXY	0 vol%	9.96 (10.3)	0.779 (0.782)	56.3 (57.2)	4.27 (4.60)	2.77E+01 (2.61E+01)	1.50E+03 1.64E+03)
OXY	2.0 vol%	21.8 (22.2)	0.778 (0.780)	68.8 (70.5)	11.83 (12.1)	1.91E+01 (1.74E+01)	1.45E+03 (6.32E+03)
OXY	2.5 vol%	21.8 (22.1)	0.777 (0.779)	68.6 (69.9)	11.70 (12.0)	2.15E+01 (2.05E+01)	2.93E+03 (4.61E+03)
MES	0 vol%	9.0 (9.46)	0.779 (0.801)	43.3 (44.4)	3.11 (3.37)	4.67E+01 (4.07E+01)	1.52E+03 (1.65E+03)
MES	0.5 vol%	9.92 (10.8)	0.778 (0.794)	43.2 (49.3)	3.60 (3.87)	4.33E+01 (2.73E+01)	2.66E+03 (2.78E+03)
MES	1.0 vol%	10.3 (10.6)	0.779 (0.801)	40.0 (41.3)	3.30 (3.42)	5.33E+01 (4.93E+01)	1.16E+03 (1.67E+03)

*Average values obtained from at least 15 devices. The data in parentheses are the highest values.

Table 5.5. The photovoltaic parameters of binary PTB7-Th:$PC_{71}BM$ and DR3TSBDT:$PC_{71}BM$ based devices in TOL, OXY, and MES.

Solvents	**Binary System**	**NMP**	J_{SC} **(mA cm^{-2})**	V_{OC} **(V)**	**FF (%)**	**PCE (%)**
TOL	PTB7-Th:$PC_{71}BM$	2.0 vol%	17.8 (19.0)	0.799 (0.812)	65.8 (66.2)	9.52 (10.0)
TOL	DR3TSBDT:$PC_{71}BM$	2.0 vol%	13.4 (14.8)	0.921 (0.942)	41.6 (45.8)	5.68 (5.78)
OXY	PTB7-Th:$PC_{71}BM$	2.25 vol%	18.2 (19.1)	0.790 (0.802)	65.4 (66.9)	9.64 (10.1)
OXY	DR3TSBDT:$PC_{71}BM$	2.25 vol%	12.4 (13.7)	0.937 (0.938)	45.8 (47.0)	5.76 (5.99)
MES	PTB7-Th:$PC_{71}BM$	0.75 Vol%	13.8 (14.4)	0.791 (0.801)	38.0 (38.4)	4.12 (4.44)
MES	DR3TSBDT:$PC_{71}BM$	0.75 Vol%	×	×	×	×

Note: Binary device of DR3TSBDT:$PC_{71}BM$ processed in mesitylene cannot be measured due to large aggregation and non-uniform film formation. Average values obtained from at least 8 devices with standard deviation. The data in parentheses are the highest values.

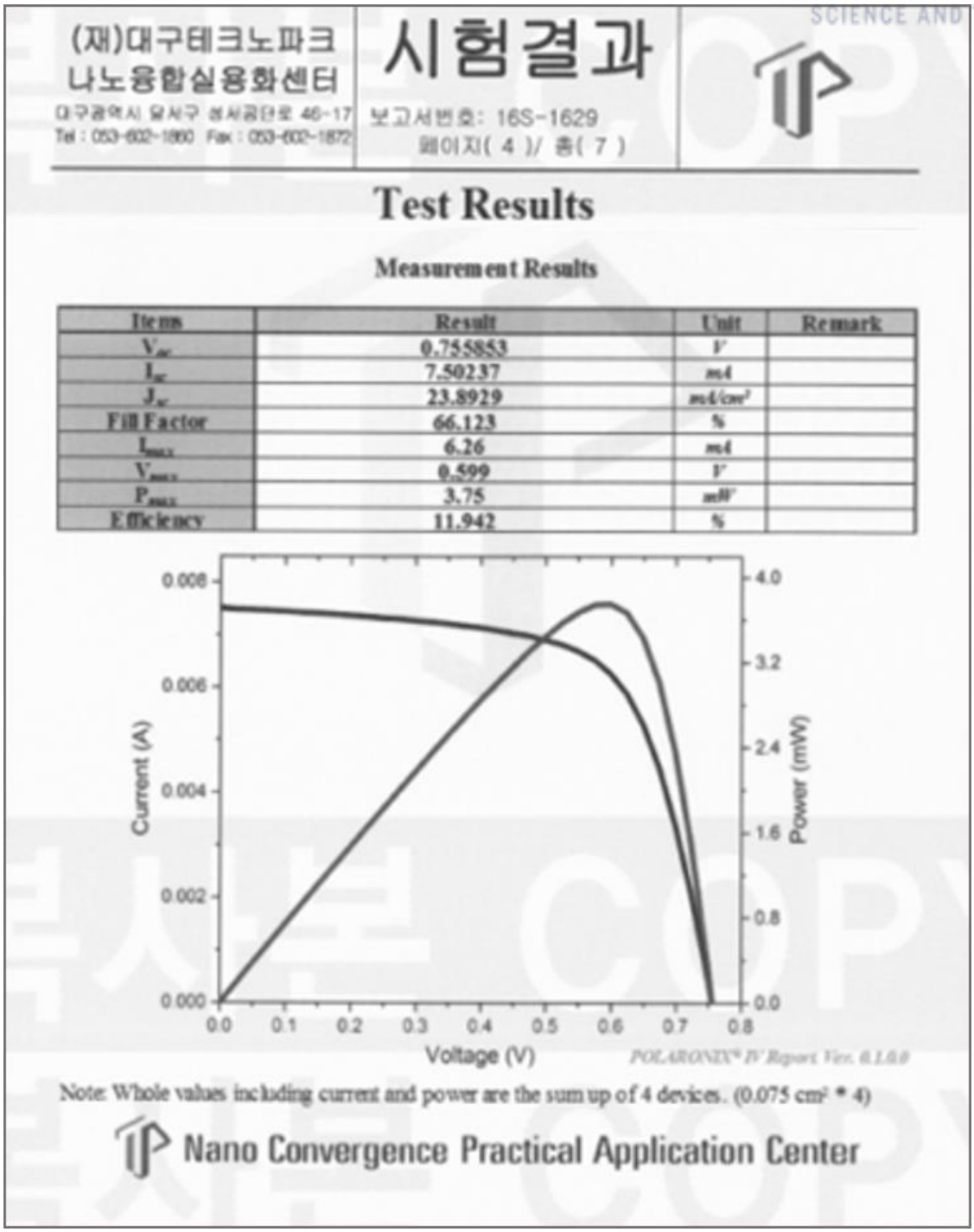

(재)대구테크노파크
나노융합실용화센터
대구광역시 달서구 성서공단로 46-17
Tel : 053-602-1860 Fax : 053-602-1872

시험결과

보고서번호: 16S-1629
페이지(4)/ 총(7)

Test Results

Measurement Results

Items	Result	Unit	Remark
V_{oc}	0.755853	V	
I_{sc}	7.50237	mA	
J_{sc}	23.8929	mA/cm²	
Fill Factor	66.123	%	
I_{max}	6.26	mA	
V_{max}	0.599	V	
P_{max}	3.75	mW	
Efficiency	11.942	%	

POLARONIX® IV Report Ver. 6.1.0.0

Note: Whole values including current and power are the sum up of 4 devices. (0.075 cm² * 4)

Nano Convergence Practical Application Center

Figure 5.15. Independent certification confirming a power conversion efficiency of 11.94% by Nano Convergence Practical Application Center, South Korea.

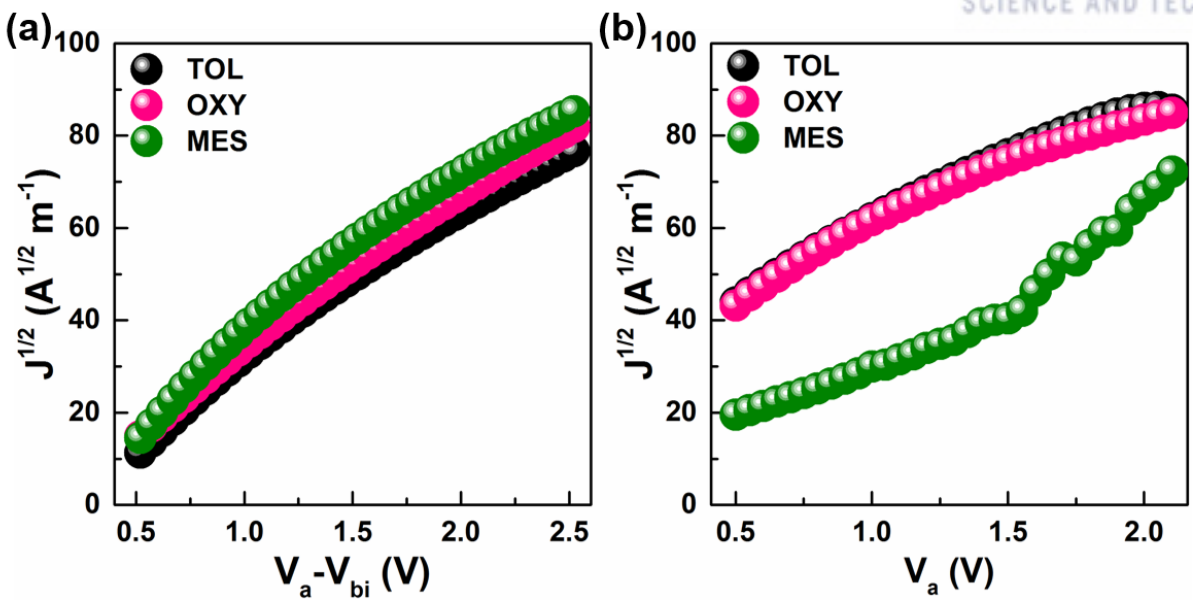

Figure 5.16. (a) Hole only. (b) Electron only mobility of ternary blend (25 wt.%) active layer in TOL, OXY, and MES.

Table 5.6. Summary of mobilities for hole only and electron only ternary blend (25 wt.%) active layer and the calculated J_{cal} from EQE curve in TOL, OXY, and MES.

Solvent System	**$\mu_h \times 10^{-4}$ (cm^2 V^{-1} S^{-1})**	**$\mu_e \times 10^{-4}$ (cm^2 V^{-1} S^{-1})**	**μ_h/μ_e**	**J_{cal} from EQE**
TOL	2.02	0.897	2.25	19.87
OXY	2.25	1.01	2.23	20.35
MES	0.085	0.099	0.857	10.13

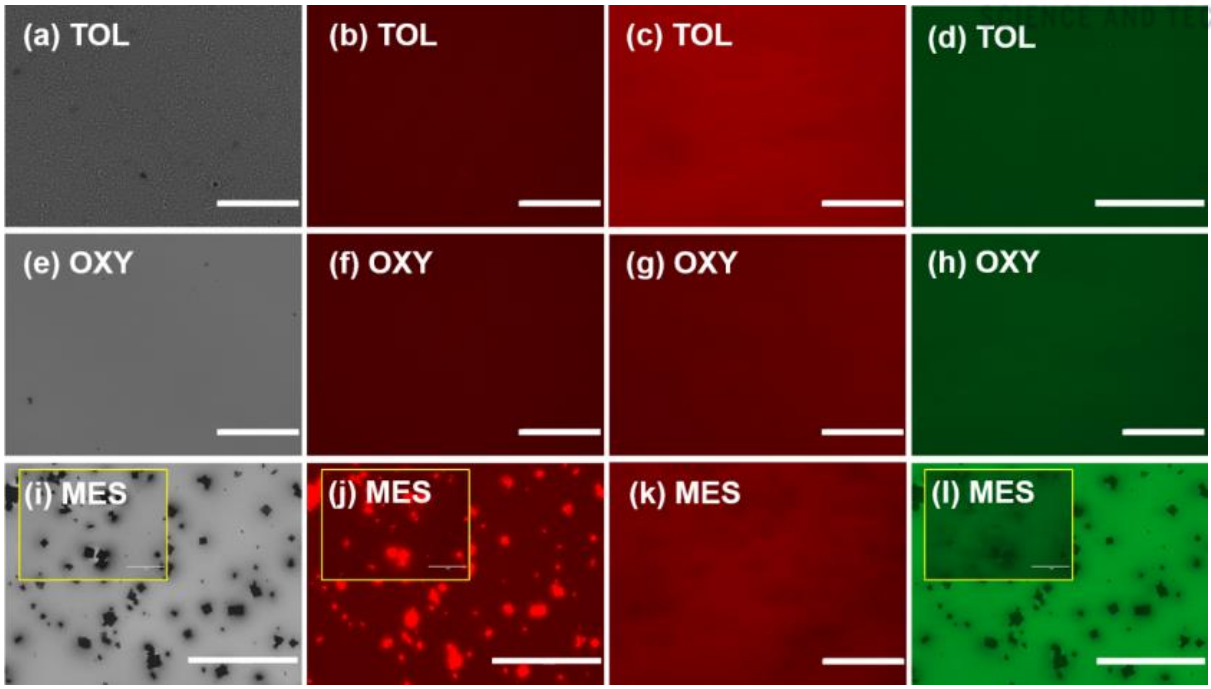

Figure 5.17. Fluorescence microscopy of the optimized ternary system (25 wt.%) thin film investigated using white light ((a), (e), and (i)), red light ((b), (f), and (j)), green light ((c), (g), and (k)), and blue light ((d), (h), and (l)). (a),(b),(c), and (d) in TOL. (e), (f), (g), and (h) in OXY. (i), (j) (k) (l) in MES. Scale bar is 50 μm (inset scale bar is 20 μm).

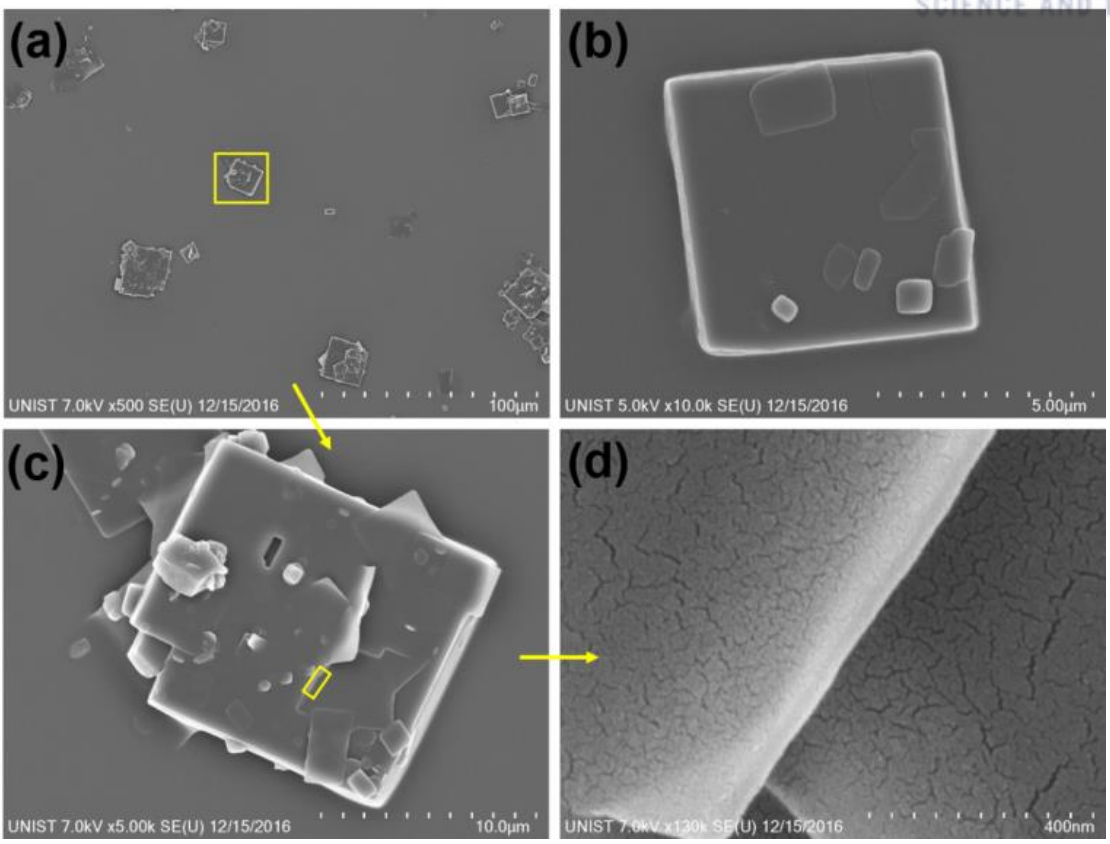

Figure 5.18. SEM images. (a), (b), (c), and (d) are the view of cubic bimolecular crystal observed in MES at different resolution scale. Highlighted area in each figure refers to the subsequent zoomed imaging present as indicated through the arrow.

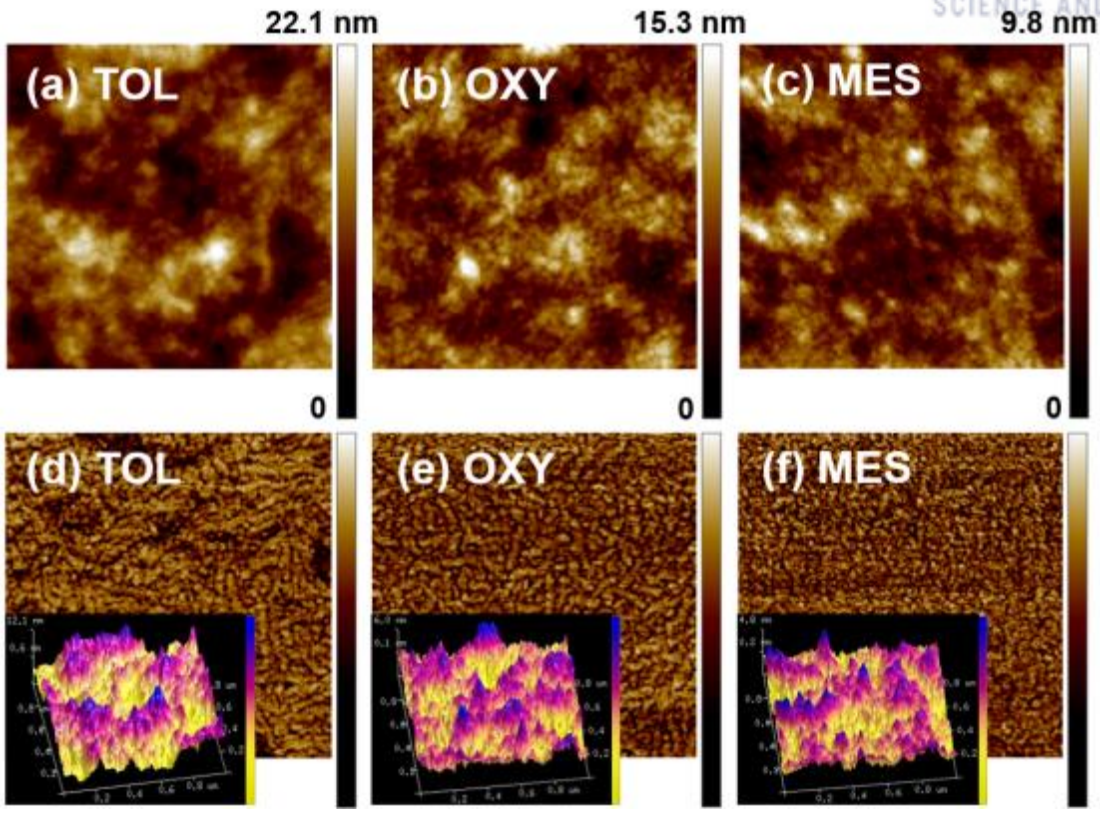

Figure 5.19. AFM topography images (scan size 1×1 mm). AFM Height images (a) in TOL. (b) In OXY. (c) In MES. Phase images (d) in TOL. (e) In OXY. (f) In MES. Inset 3-D height Images respectively. Different color bars are used for height and phase variance.

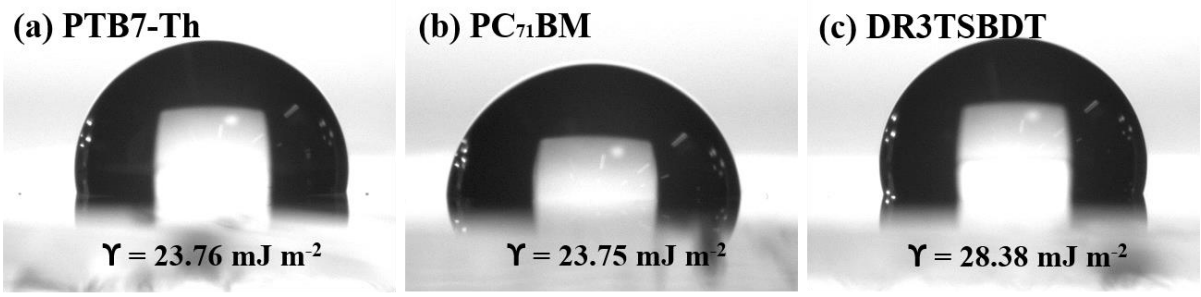

Figure 5.20. Surface energy measurement. Photographs of the drop of water on the surface of (a) PTB7-Th, (b) $PC_{71}BM$, and (c) DR3TSBDT films on a glass substrate along with the calculated surface energy respectively in each case.

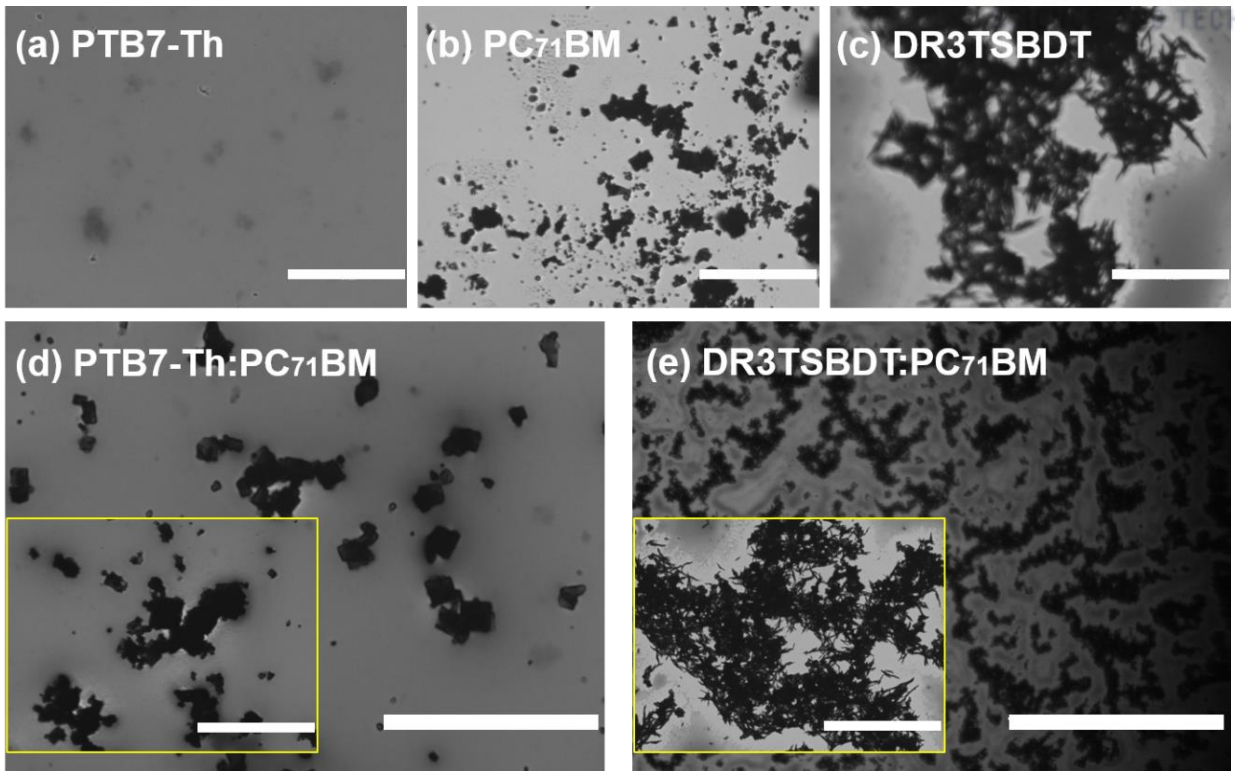

Figure 5.21. Optical microscopy of the pure (a) PTB7-Th (b) $PC_{71}BM$ (c) DR3TSBDT as well as optimized binary systems (d) PTB7-Th:$PC_{71}BM$ (e) DR3TSBDT:$PC_{71}BM$ thin film in MES. Scale bar is 50 μm (inset scale bar is 20 μm).

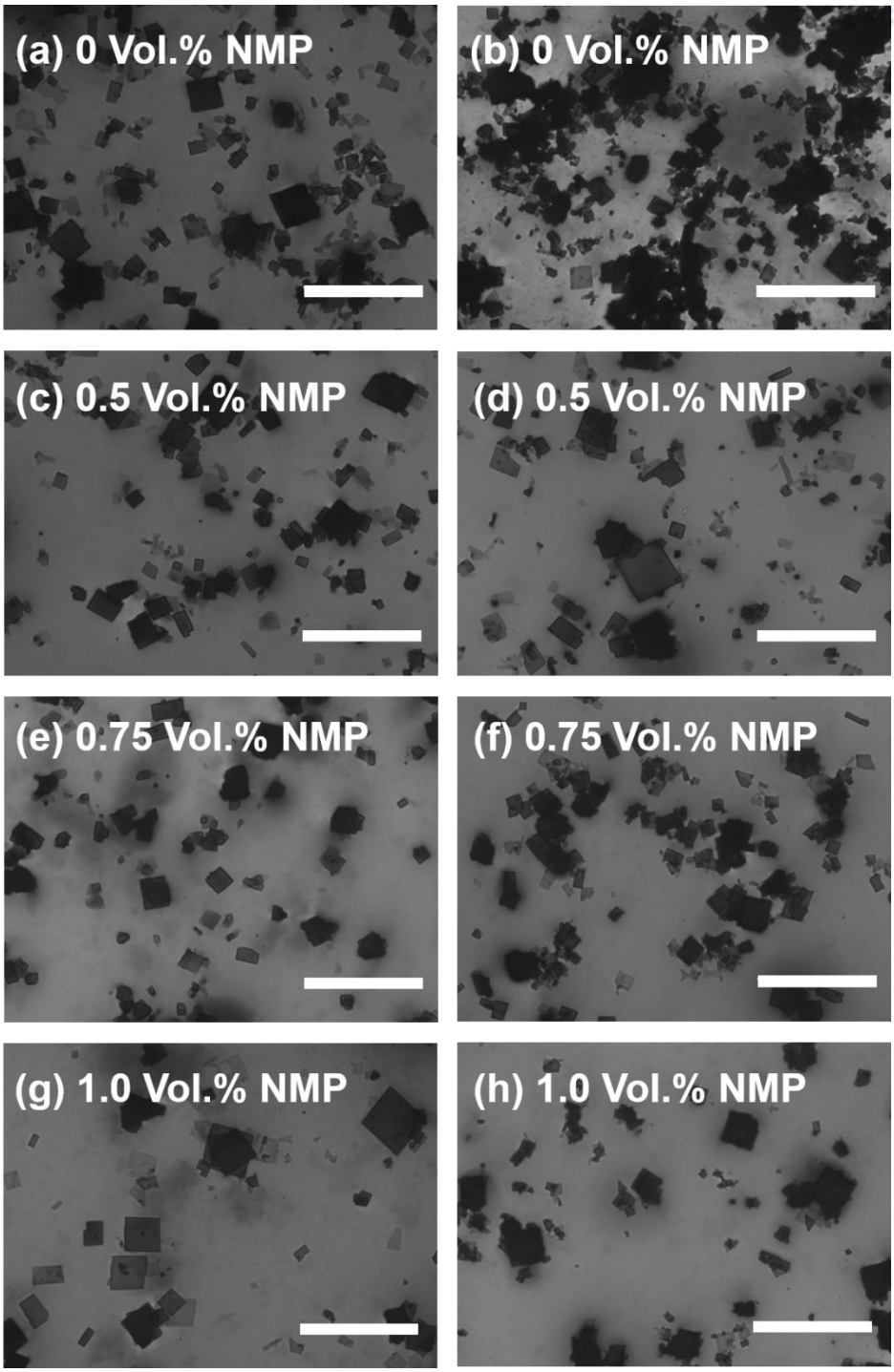

Figure 5.22. Optical microscopy of the binary PTB7-Th:$PC_{71}BM$ (a), (c), (e), (g) and ternary systems PTB7-Th:DR3TSBDT:$PC_{71}BM$ (25 wt.%) (b), (d), (f), (h) thin films in MES processed with different Vol. % of NMP. Scale bar is 50 μm.

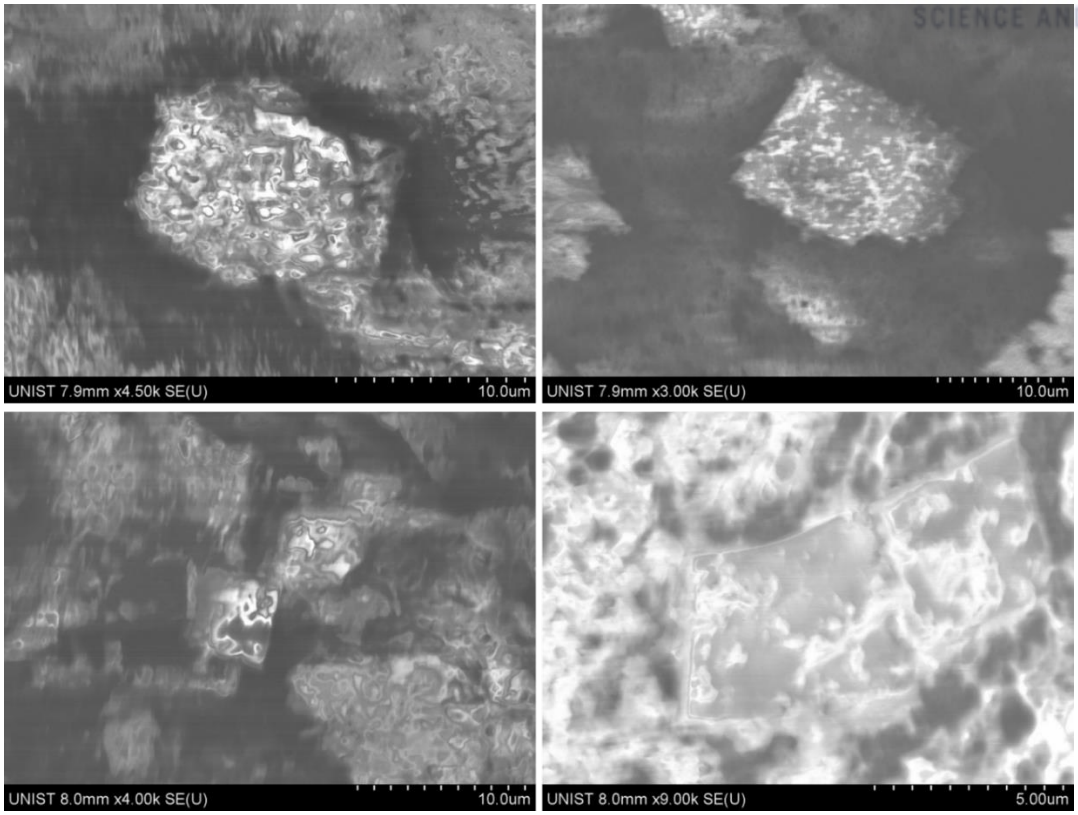

Figure 5.23. SEM images of bimolecular cubic crystals taken in powder states at various location. It should be noted that on filtering the solution non homogeneous mixture of cubic crystal and amorphous PTB7-Th and $PC_{71}BM$ is obtained.

Table 5.7. Lattice parameters in out-of-plane and in-plane direction for ternary system processed in TOL, OXY, and MES.

Solvent	**Beamline exposure direction**	q_{100} (Å^{-1})	d_{100} (Å)	q_{010} (Å^{-1})	d_{100} (Å)
Out-of-plane					
TOL	Surface side exposed	0.320	19.63	1.71	3.674
OXY	Surface side exposed	0.301	20.87	1.71	3.674
MES	Surface side exposed	0.295	21.30	1.73	3.631
MES	Substrate side exposed	0.297	21.16	1.74	3.611
In-plane					
TOL	Surface side exposed	0.312	20.14	1.64	3.831
OXY	Surface side exposed	0.306	20.53	1.71	3.674
MES	Surface side exposed	0.310	20.27	1.78	3.530
MES	Substrate side exposed	0.312	20.14	1.78	3.530

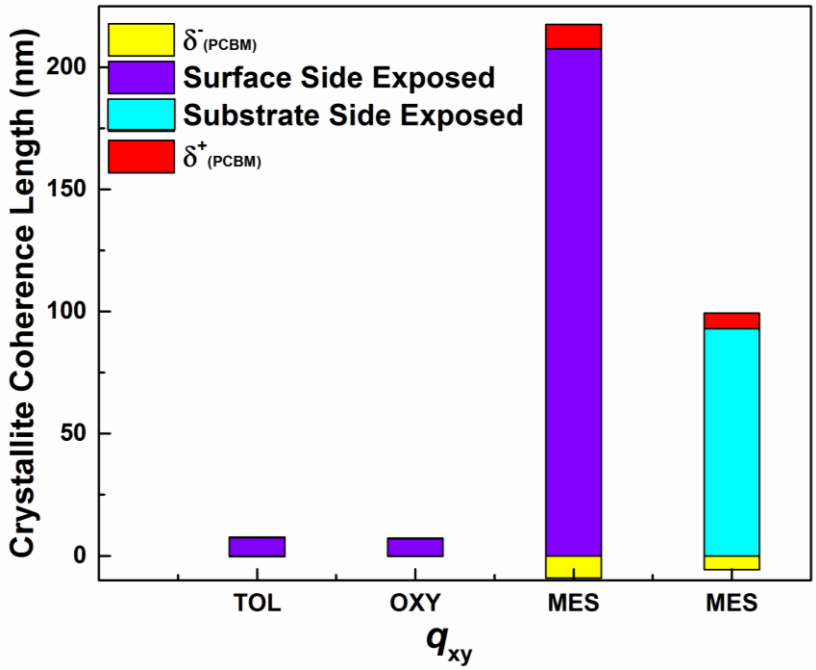

Figure 5.24. Crystallite coherence length (L_{CS}) of $PC_{71}BM$ along the in-plane direction obtained from the corresponding line cut profiles. Gaussian fits were used to determine the peak position and FWHM.

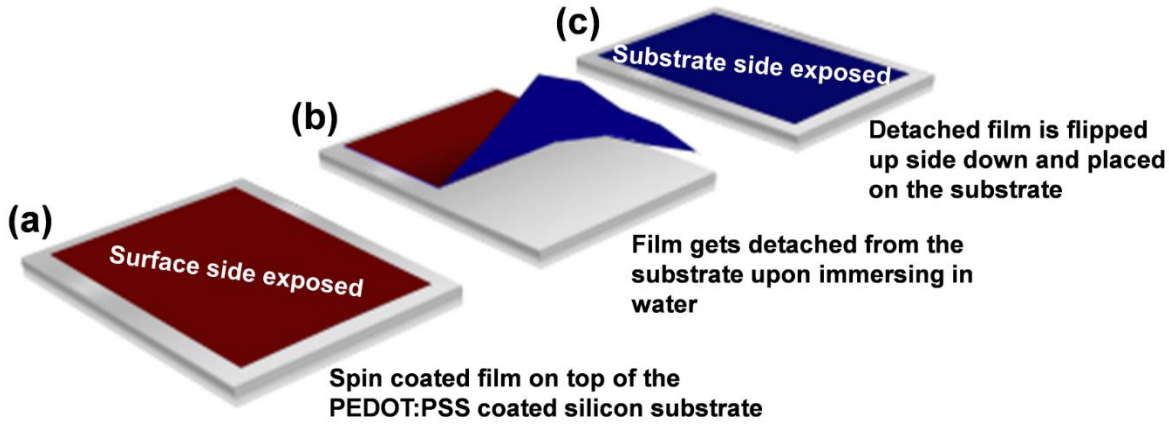

Figure 5.25. Graphical demonstration of film preparation with surface/substrate side exposed for GIWAXS measurement.

Chapter 6. Incorporation of Ferroelectric Additives Enhances Built-in Electric Field for Higher Efficiency in BHJ Solar Cells

In principle, an internal electric field induced by ferroelectric materials directly can affect the photovoltaic properties, though it is still seeking to develop the complete mechanistic understanding. Here, we show that locally built-in electric field can be ensured by introducing ferroelectric additives (P1, P2, P3, and P4) into an active layer of organic solar cells (OSCs). The use of *o*-xylene (good solvent for the active components yet anti solvent for the ferroelectric additives)/*N*-methylpyrrolidone (their inverse solubility trend) pair induces recrystallization of the ferroelectric additives into the active layer matrix, enabling to create the ferroelectric polarization without poling process. The P2-processed OSC exhibits a best performance with efficiency up to 11.02%. A comparative study exploring the role of the ferroelectric polarization surrounding the active layer matrix is performed by a series of structural, electrical, and morphological techniques, shedding light on the underlying understanding of the ferroelectric polarization's effects on OSCs. The use of the ferroelectric additives discovered in this study should be widely to percolate into related organic semiconductor fields, beyond sole consideration of its efficiency enhancement.

Chapter 6 is the completed work from the manuscript "Incorporation of Ferroelectric Additives enhances built-in electric field for better efficiency in BHJ Solar Cells" currently under submission.

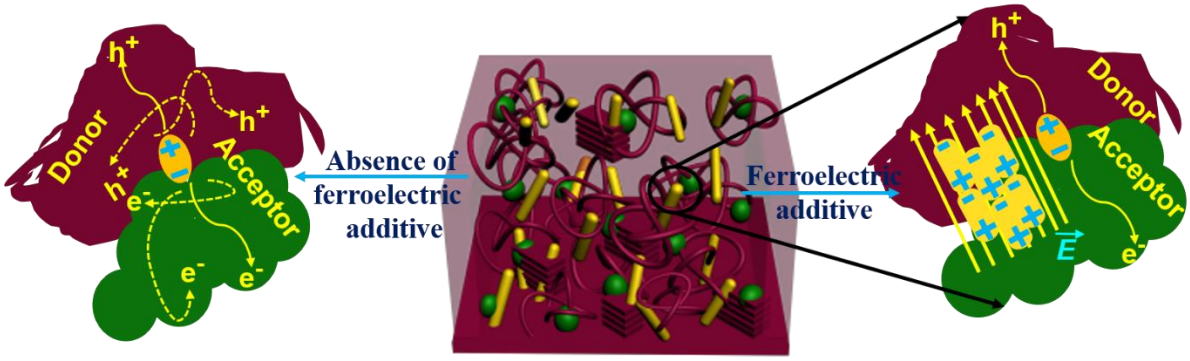

6.1 Introduction

Ferroelectric materials−that feature a spontaneous electric polarization, so-called ferroelectricity, that can be switched by external electric field−, have remained one of the most fascinating areas of modern.[1] Organic solar cells (OSCs) coverts the absorbed photon into electrical charges by forming a potential across heterojunction to separate holes and electrons apart. After the exciton dissociation on charge transfer states (CTS) at the donor/acceptor (D/A) interface, the fate of electron-hole pairs is mainly governed by the competing processes of charge collection and recombination. The photo-generated charge carriers are

separated by the internal electric field of the p–n junction and thus, collected by the respective electrodes.[2] The strengthening of the internal (built-in) electric field by doping with ferroelectric materials is one of the innovative approach to quickly separate the charges prior to recombination for achieving efficient solar cells.

In particular, the discovery of ferroelectric phenomenon in organic polymers in early 1970s has electrified astounding research interests in these soft materials with appealing physical properties, giving rise to a plethora of applications ranging from transistors and sensors to to several other information technology devices,[3] which soon captured rapid attention from the worldwide research communities leading to the discovery of a number of ferroelectric polymers beyond the PVDF homopolymer, such as PVDF-based grafted copolymers, terpolymers.[4] Since then, as boosted by the ever-increasing demand for state-of-the-art energy technologies, recent attempts have been made to utilize the built-in electric field provided by the electric polarization of a ferroelectric polymer to improve the PCE in OSCs.[5, 1d, 1e] For example, Huang *et al*. incorporated a thin interfacial layer of poled ferroelectric poly(vinylidene fluoride-trifluoroethylene) (PVDF-TrFE) at electrode interface to generate an extra electric field in the active layer, demonstrating an increase in PCE of OSCs after polling the PVDF-TrFE layer by applying a large voltage pulse on the electrode.[1d] More recently, by mixing a small amount of PVDF-TrFE polymer into the active layer, Chaudhary *et al*. enhanced the charge collection efficiency and achieved a very high internal quantum efficiency of 100%, consequently leading to improved device performance.[1e] Nonetheless, the former method has limitation in applying to the many state-of-the-art low-bandgap polymers recently developed since the Langmuir–Blodgett (LB) deposition used to fabricate the PVDF-TrFE monolayers is incompatible with their process due to the high-temperature annealing (over 130 °C) needed to convert the high-quality PVDF-TrFE LB film into the ferroelectric phase. For such polymers, the high-temperature annealing directly after casting can give rise to the micrometer-sized phase segregation, dramatically reducing donor-acceptor interfacial area and device performance. In the case of the latter approach, despite the improved PCE as a result of the a local build-in electric field within the unpoled PVDF-TrFE mixed active layer, the positively poled OSC did not show additional enhancement and even the negative poling adversely degraded the device performance. Thereby, the role of PVDF-TrFE and the working mechanisms behind ferroelectric induced electric fields in OSCs are still not completely understood. In addition, both the research works mostly focused on a traditional poly(3-hexylthiophene):[6,6]-phenyl-C_{61}-butyric acid methyl ester (P3HT:PC_{61}BM) system referred to as the 'fruit fly' platform of OSCs. As a consequence, despite the synergistic effects of electric fields induced by the electric polarization on photovoltaic properties, the achieved maxima PCEs were below 5%.

The large electronegativity difference between the carbon and fluorine atoms give rise to a highly polar C-F bond with a large dipole moment of $>6.0 \times 10^{-30}$ C m leading to the strong electric polarization of PVDF

crystals generated from the regularly packing of polymer chains such that dipole internal moments are not cancelled out.[5b, 5d, 6] The PVDF-based polymers are a semi-crystalline polymer with polymorphs referred to as α, β, γ, δ-phases (directly related to the ferroelectric properties), which are sensitive to external stimuli such as temperature, stress, electric field, strain, or chemical substances.[5c, 6-7] Recently, it was reported that their crystal structures and phase transitions can be easy to tune via grafting one polymer onto PVDF-based polymers. Therefore, several studies have been devoted to increase the *β* crystal phase in PVDF either through copolymerization of vinylidenefluoride (VDF) with trifluoroethylene (TrFE), bromotrifluoroethylene (BTFE), chlorotrifluoroethylene (CTFE) etc. or grafting with low polarizable polymer side chains such as polystyrene (PS), poly(*tert*-butyl acrylate) (P*t*BA).[5b, 5c, 7b, 8] Like other organic polymers, these materials have several benefits like light weight, ease of processing, and flexibility over their inorganic ferroelectric counterparts offering several opportunities in various electronic devices including organic solar cells, field effect transistors, triboelectric nanogenerator, capacitors, piezo-, and pyroelectric applications.[1d, 5b, 8e, 9] Apart from the materials design, innovative device engineering and effective morphology control also play very important roles in increasing the power conversion efficiency (PCE) of OSCs. Currently OSCs have shown very promising PCE beyond 12% through fully optimizing the given binary/ternary system.[10] In this study, to advance and forward our understanding of the ferroelectric photovoltaic mechanism, we systematically examine the effects of a family of PVDF-based ferroelectric polymers (PVDF, poly(vinylidene fluoride)-*graft*-poly(*tert*-butyl acrylate) (PVDF-*g*-PBA), PVDF-TrFE, and poly(vinylidene fluoride-trifluoroethylene)-*graft*-poly(*tert*-butyl acrylate) (PVDF-TrFE-*g*-PBA)) as an additive on photovoltaic property of an archetype of high-performance poly(4,8-bis(5-(2-ethylhexyl)thiophen-2-yl)benzo[1,2-*b*;4,5-*b*']dithiophene-2,6-diyl-*alt*-(4-(2-ethylhexyl)-3-fluorothieno[3,4-*b*]thiophene-)-2-carboxylate-2-6-diyl)) (PTB7-Th):[6,6]-phenyl-C_{71}-butyric acid methyl ester ($PC_{71}BM$) system. On the basis of high-performance OSCs based on *o*-xylene (OXY)/*N*-methylpyrrolidone (NMP) combination previously reported, the OXY/NMP pair was used as the processing solvent for making OSCs in this study. Note that the solubility of the ferroelectric polymers in NMP is satisfactory but poor in OXY. Thereby, OXY/NMP pair drives the recrystallization of the ferroelectric additives into the active layer matrix, not only yielding built-in electric fields but also a large enhancement of the PCE up to 11.02%. The ferroelectric polarization induced by the simple recrystallization tool requires no additional fabrication step, and is readily applicable to various organic optoelectronic devices. Till now external electric fields are applied (called poling) to polarize the PVDF based ferroelectric material prior to device operation, such that remnant polarizations are left behind after removing the applied field.[1d, 9a, 9e, 11] However, these four ferroelectric insulating polymer additives having different dielectric constant display permanent remnant polarization in the host matrix without poling providing a unique approach to strengthen the built-in field.

6.2 Results and Discussion

To make the polymers' names more reader-friendly, the ferroelectric polymers (PVDF, PVDF-*g*-PBA, PVDF-TrFE, and PVDF-TrFE-*g*-PBA) are henceforth designated as simple ones (P1, P2, P3, and P4) respectively, where the chemical structures are shown in Figure 6.1a; P1 and P3 were commercial available materials and P2 and P4 were prepared from grafting PBA onto the corresponding main backbones via atom transfer radical polymerization (ATRP) technique, respectively. The details of synthesis and characterization (see in the section 6.5, Figure 6.7), including the grafting ratios are provided in the supporting texts of section 6.5.

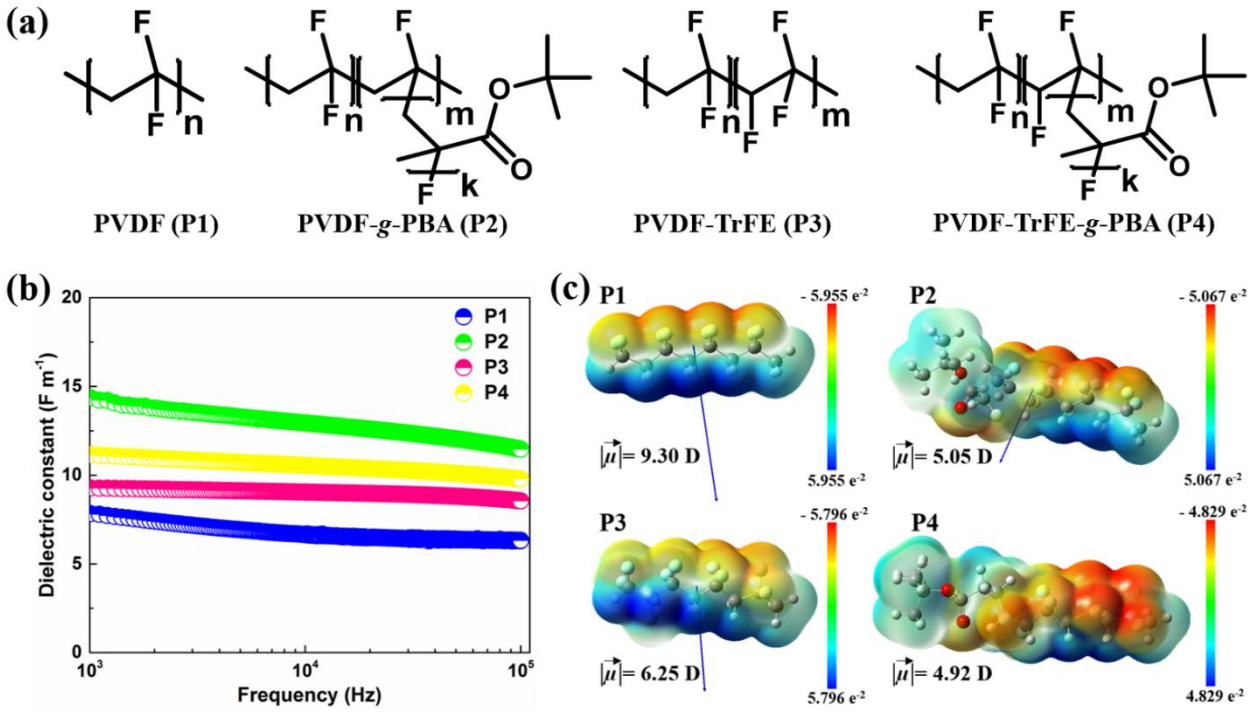

Figure 6.1. (a) Chemical structures of P1, P2, P3, and P4. (b) Dielectric constant of PVDF-based ferroelectric polymer's thin-film capacitors. (c) Electrostatic surface potential (ESP) due to the charge distribution and dipole direction (by blue arrow) with magnitude for structural models of PVDF-based ferroelectric polymers $(VDF)_4$, $(VDF)_3$-$(VDF\text{-}BA)_1$, $(VDF)_3$-$(TrFE)_1$, and $(VDF)_3$-$(TrFE\text{-}BA)_1$ in all-trans (*tttt*) conformation. The scale bar shows the colors scheme for the ESP. Red indicates electron rich (partially negative charge) region; yellow indicates slightly electron rich region; green indicates neutral region; light blue indicates slightly electron deficient region; and blue indicates electron deficient (partially positive charge) region, respectively.

We determined the relative dielectric property of the ferroelectric polymers using a frequency-dependent capacitance measurement over the frequency range of 10^3 to 10^5 Hz. The relative dielectric constants (ε_r)

were calculated from the equation of $\varepsilon_r = Cd/\varepsilon_0 A$, where C is the capacitance, d is the thickness of the tested film, ε_0 is the permittivity of free space, and A is the area. Figure 6.1b shows the frequency dependent dielectric constant plots for the ferroelectric polymers. The constant values are manifested in the sequence of P1 < P3 < P4 < P2 in the testing frequency ranges, verifying that grafting of PBA in the PVDF-based backbones increases the dielectric constant values. Therefore, we anticipate that the existence of an optimal amount of P2 or P4 surrounding the host active components would facilitate efficient charge transport property, being attractive for improving the performance of OSCs. The thermal transition behaviors of the ferroelectric polymers were evaluated via differential scanning calorimetry (DSC) (see the section 6.5, Figure 6.8). In the heating and cooling processes, the PVDF-based polymers (P1 and P2) underwent an endothermic melting peak at ~170 °C and an exothermic crystallization transition at ~135 °C, while for P(VDF-TrFE)-based based polymers (P3 and P4),[12] there were two endothermic peaks with the corresponding two endothermic events; the low-temperature one is associated with a ferroelectric-to-paraelectric Curie transition and the high-temperature one is ascribed to the melting phase transition. [12b, 12f, 12g] Note that the changes in the transition temperatures and relative integrating peaks exist in P2 and P4 compared to the corresponding parent polymers P1 and P3, indicating that incorporating PBA into the backbones influences the polymorph phases and crystallinity by tuning the structural conformations, which will account for the varied ferroelectric effects on the photovoltaic behavior in the following OSC section.

6.2.1 Energy Orbitals and Electrostatic Potential

Molecular simulation on model compounds with the four repeating units for each polymer was performed through density functional theory (DFT) at BLYP/6-31G level. Three different conformation namely all-*trans (tttt)* for β-phase, *trans-gauche–trans-gauche* (*tgtg*) for α- and δ- phases, and *trans–trans–trans-gauche* (*tttg*) for γ- and ε- phases are calculated.[5b, 6, 7c]. The structural models, $(VDF)_4$, $(VDF)_3$-$(VDF\text{-}BA)_1$, $(VDF)_3$-$(TrFE)_1$, and $(VDF)_3$-$(TrFE\text{-}BA)_1$ were used for the calculations, where only conformation with all-trans planar zigzag β-phase was taken because it is responsible for the ferroelectric property. The electrostatic potential (ESP) distribution and orientation of the electric dipole at the molecular levels were visualized in Figure 6.1c (see the section 6.5, Figure 6.9 for other conformation cases). The DFT calculations indicate that the presence of BA unit in the backbones can bring the variations in charge polarization and direction and magnitude of dipole moments (μ), being well-correlated with what observed in DSC data above. Optimized geometries of all the four ferroelectric polymers of each conformation are provided in detail with the HOMO-LUMO levels and dipole moment values (see the Table 6.2 of the section 6.5).

6.2.2 Hysteresis Measurement

The polarization behavior of each ferroelectric polymer film fabricated from NMP solution was characterized by electrical polarization versus electric field (*P*-*E*) loops using the triangular waveform of the voltage at 1 Hz. As we can see from Figure 6.2 (the insets of Figure 6.2 and Figure 6.10 of the section 6.5 provides optical visualization of films), all the ferroelectric polymer films exhibit a banana hysteresis loop with similar remnant polarization (0.02 – 0.07 μC cm^{-2}) and coercive field (75 – 100 kV cm^{-1}) values, suggesting that incorporating PBA blocks into the PVDF-based polymers seems not to play a role of limiting their intrinsic ferroelectric property.

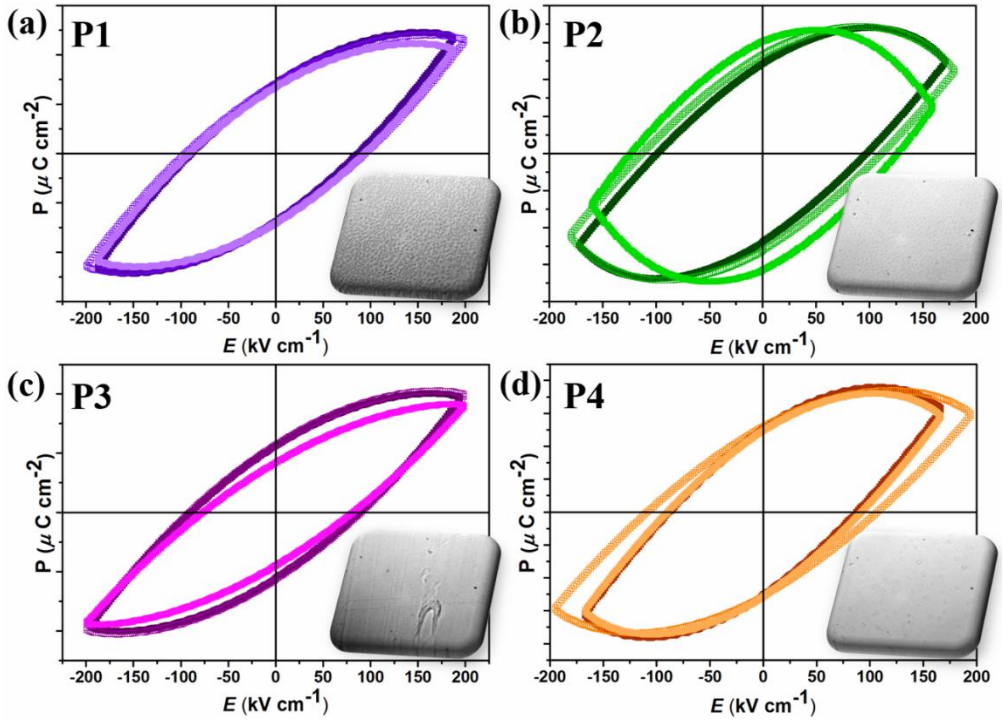

Figure 6.2. Ferroelectricity of PVDF-based ferroelectric polymers based thin-film capacitors. Hysteresis loops without poling measured at different locations for (a) P1, (b) P2, (c) P3, and (d) P4. Insets are the corresponding optical microscopy images for the illustration of reason behind similar hysteresis loops in the case of pure additive films.

Next, we set out to investigate the effect of the ferroelectric polymers as an additive on the PTB7-Th:$PC_{71}BM$ OSC based on OXY/NMP pair, in which, as mentioned before, the OXY serves as good solvent for active components and NMP acts as a good solvent for ferroelectric polymers. The *P*-*E* loops of the

films without and with optimal amount of ferroelectric additives prepared from the same optimized OSC condition are measured at various locations, and shown in Figure 6.3; the details regarding the device optimization including the donor:acceptor ratios and amounts of NMP and ferroelectric additives are discussed in the following OSC part and supporting texts of the section 6.5.

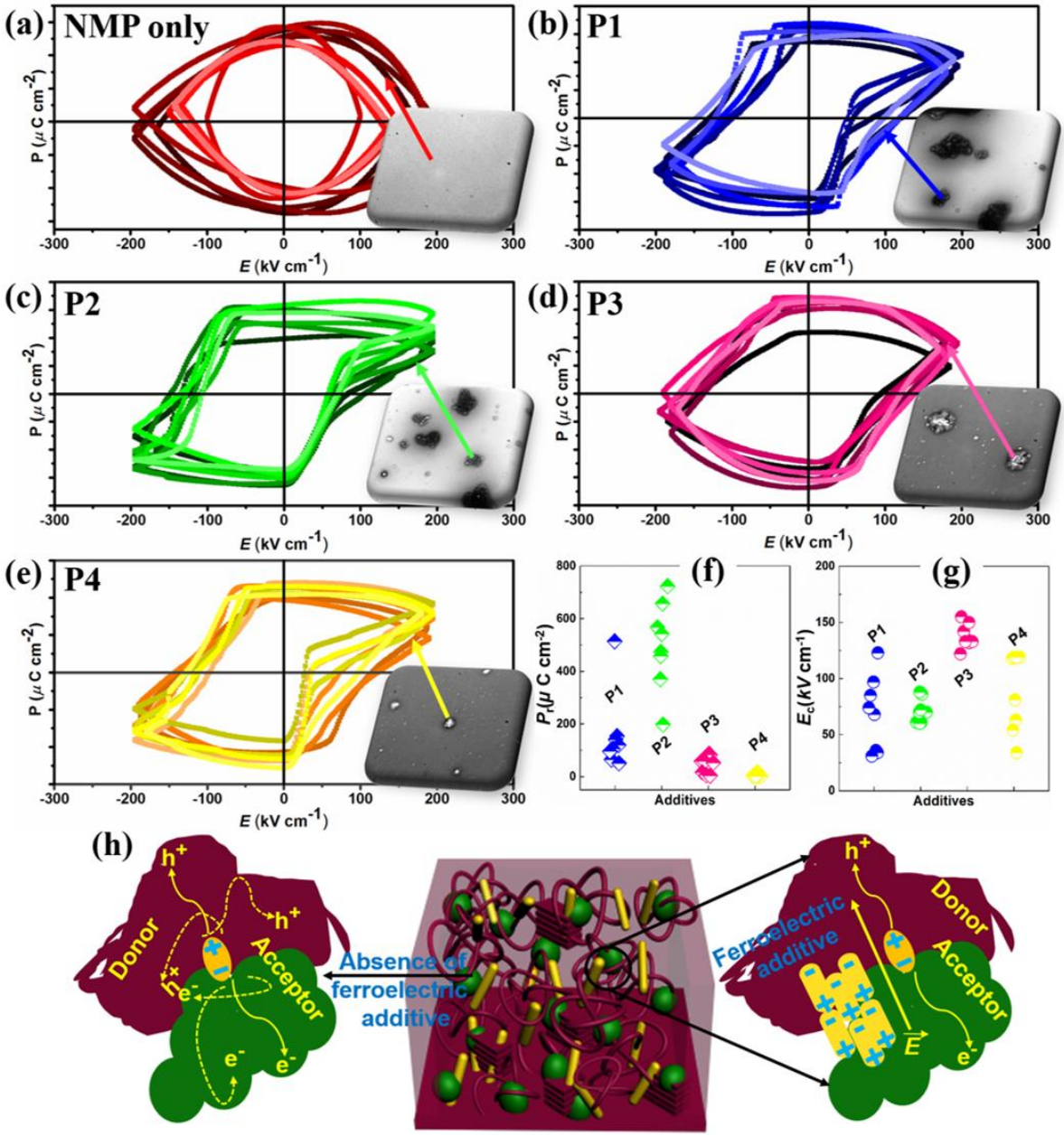

Figure 6.3. Ferroelectricity of active layer based thin-film capacitors using PVDF-based ferroelectric polymers as an additive in binary host matrix. Hysteresis loops without poling measured at various locations for (a) NMP only, (b) P1, (c) P2, (d) P3, (e) P4. Insets are the corresponding optical microscopy images for the illustration of reason behind different hysteresis loops in the case of active layers with additives. Scatter

plots of (f) remanent polarization, *P*r (μ C cm^{-2}), and (g) the corresponding coercive field, *E*c (kV cm^{-1}) in each case. (h) Illustration of the active layer morphology in absence/presence of ferroelectric additive.

There is hardly any ferroelectric characteristics in the only OXY/NMP-processed active layer film, while a typical ferroelectric behavior with a rectangular-shaped hysteresis loop is obviously obtained from all the active layer films with the ferroelectric additives measured at various locations. These results demonstrate that the β-phase crystals of the ferroelectric additives are enhanced by using the mixed OXY/NMP pair as a co-solvent recrystallization process, which in turn can strongly invigorate their ferroelectric nature even without poling treatment. Fluorescence microscopy images of the ferroelectric additives-processed active layer films by OXY/NMP showed a direct evidence of partially formed crystalline chunks of the ferroelectric additives via recrystallization within the active layer matrix (the insets of Figure 6.3 and Figure 6.11 of the section 6.5). One can expect that the ferroelectricity induced by the sporadically and locally formed permanent polarization at nanoscale is to efficiently separate the holes and electrons within the active layer matrix, as schematically illustrated in Figure 6.3h. The extracted values of the remnant polarization (P_r) and coercive field (E_c) of the ferroelectric additives-processed films are summarized and compared in Figure 6.3f,g, where the E_c is related to the size of ferroelectric domains whereas P_r is associated with the number of dipoles locked in the ferroelectric crystals. The P2-processed active layer film showed overall higher P_r (over 200 μC cm^{-2}) yet lower E_c values compared to those observed for other additives-processed ones, being taken as an indication of the more ordered microstructure with high β-phase content.

6.2.3 Photovoltaic Performance

The photovoltaic properties of OSCs based on PTB7-Th:$PC_{71}BM$ active layer using OXY/NMP pair were investigated in a conventional device architecture of ITO/ PEDOT:PSS/active layer/Al, where the PTB7-Th to $PC_{71}BM$ ratio was kept at 1:1.5 in this work. The best-performing current-density-voltage (*J*–*V*) characteristics are displayed in Figure 6.4a and the performance parameters are summarized in Table 6.1. The as-cast PTB7-Th:$PC_{71}BM$ control device gave a low PCE of 4.67% (average PCE = 4.23%), with a short-circuit current density (J_{SC}) of 12.52 mA/cm^2, an open-circuit voltage (V_{OC}) of 0.795 V, and a fill factor (FF) of 46.8%. On the other hand, the J_{SC} and FF were significantly improved by adding optimal amount of NMP (3.0 vol%), resulting in a high PCE of up to 10.20% (average PCE = 9.96%). Note that V_{OC} values remain at similar 0.795 – 0.799 V levels for the two optimized devices without and with NMP. And then, we began to evaluate the photovoltaic performances with various weight percentages of the ferroelectric additives (0.5 – 4.0 wt% with respect to total active layer concentration (35 mg/mL)), where they were dissolved in the NMP prior to the addition to the OXY active layer solution. The performance

characteristics as a function of NMP/ferroelectric additive concentration are presented in Figures 6.12-6.16 and the corresponding device parameters are summarized in Tables 6.3-6.7 as well as Figure 6.17 of the section 6.5 for all NMP/ferroelectric additives applied.

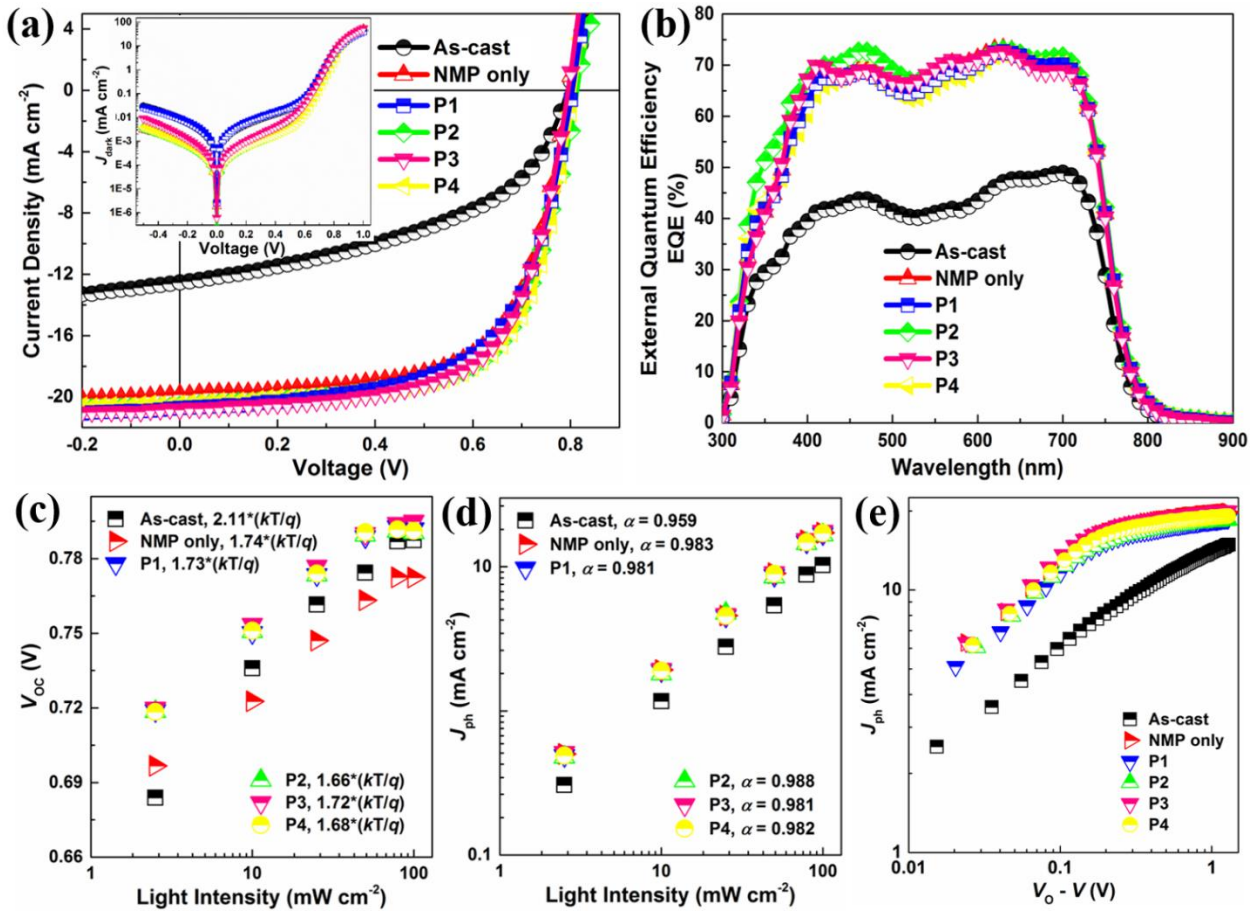

Figure 6.4. (a) *J*–*V* characteristics (inset: *J*–*V* characteristics in the dark). (b) The corresponding EQE curves. (c) Dependence of open-circuit voltage (V_{OC}), (d) current density (J_{SC}) on light intensity and (e) photocurrent measurement of binary devices w/ and w/o PVDF-based ferroelectric polymers as an additive under AM 1.5G irradiation at 100 mW cm^{-2}.

The optimized photovoltaic performances were obtained by using 1.5 wt% for all the cases except for P3 showing 2.0 wt%. We observed that except for P1-processed device (PCE = 10.10%), in which a PCE was slightly decreased compared with that of the NMP only-processed optimized one, an increase in the device performance was observed upon the addition of the ferroelectric additives. Specially, all the parameters including J_{SC}, V_{OC}, and FF were simultaneously improved for the P2-processed device, delivering the champion PCE of 11.02 % (J_{SC} = 20.30 mA cm^{-2}, V_{OC} = 0.812 V, and FF = 66.50%), which is by far the highest PCE reported to date for PTB7 derivatives-based binary OSCs. Such performance improvements

in the devices with the ferroelectric additives can be explained by the enhanced local build-in electric field of ferroelectric dipoles embedded within the active layer, as observed from the above polarization study. From the *J*–*V* curves in dark (the inset of Figure 6.4a), we found that both as-cast control and P1-processed devices displayed higher current density at reverse bias, leading to lower diode rectification ratios compared to other systems, which reflects the relatively lower FFs of the two devices.

It should be noteworthy that the optical effects are ruled out as the performance enhancing mechanisms, being evident in nearly identical optical spectra of the host system upon adding ferroelectric additives (see the section 6.5m Figures 6.18-6.19). Compared to other systems, there is the form of the aggressively large aggregation in the case of P1, as evidenced by the fluorescence microscopy images above, which is a rationale reason for the observation of the relatively inferior performance. In addition, the external quantum efficiency (EQE) for all the devices displayed a broad photo-response from 300 to 800 nm, well-matching the trends of the measured J_{SC} values (Figure 6.4b).

Table 6.1. Summary of device parameters for binary OSCs w and w/o PVDF-based ferroelectric polymers as additives under AM 1.5G irradiation at 100 mW cm^{-2}.

Additive	Concentration	J_{SC} (mA cm^{-2})	V_{OC} (V)	FF (%)	PCE (%)
As-cast	0 vol%	12.52 (11.84)	0.795 (0.790)	46.8 (45.3)	4.67 (4.23)
NMP only	3 vol%	19.43 (19.13)	0.799 (0.796)	65.7 (65.4)	10.20 (9.96)
P1	1.5 wt%	20.30 (20.01)	0.812 (0.810)	66.5 (66.1)	11.02 (10.72)
P2	1.5 wt%	20.09 (19.78)	0.807 (0.805)	66.8 (66.4)	10.83 (10.58)
P3	1.5 wt%	20.19 (19.83)	0.804 (0.803)	62.2 (61.5)	10.10 (9.79)
P4	2.0 wt%	20.07 (19.75)	0.795 (0.794)	65.8 (65.0)	10.50 (10.20)

6.2.4 Study of Charge Transport and Recombination Behavior

In order to understand the charge recombination behavior as a function of the used ferroelectric additives, we measured light intensity dependence of the *J*–*V* characteristics for the optimized devices with and without ferroelectric additives (Figure 6.4c,d). In principle, the relationship between the J_{SC} values and the incident light intensity (P_{light}) values follows the power-law dependence $J_{SC} \propto P_{light}^{\alpha}$, whereas the V_{OC} values depend on the natural logarithm of P_{light} with a slope of nkT/q, where k = Boltzmann's constant, T = the temperature, q = the elementary charge, and n is an ideality factor.[13]

All the devices have similar, high α (0.96 – 0.99) and n (1.66 – 2.11) values, suggesting that geminate or trap-assisted Shockley-Read-Hall recombination predominates the loss of free-charge carriers.[14] Note that

P2-processed system shows the α closest to unity with the smallest n slope, verifying the weakest loss of any types of the recombination kinetics.

Photogenerated current density (J_{ph}) versus effective voltage (V_{eff}) curves were also plotted to evaluate the exciton dissociation and charge collection in the devices (Figure 6.4e).[15] The J_{ph} reached the saturation value (J_{sat}) at a high V_{eff} (over 0.3 V) for all the devices, except for as-cast control one. Under the short-circuit condition, exciton dissociation probability ($P_{diss} = J_{ph}/J_{sat}$, where J_{sat} is the saturation photocurrent density) of the as-cast control one is 88%, while distinctly higher P_{diss} values of ~97% are achieved in the other devices (see the section 6.5, Table 6.8). Taken together, these results suggest that more efficient exciton dissociations and charge collections occur in the NMP only- and ferroelectric additives-processed devices, which could contribute largely to their higher J_{SC} values observed from the OSCs.

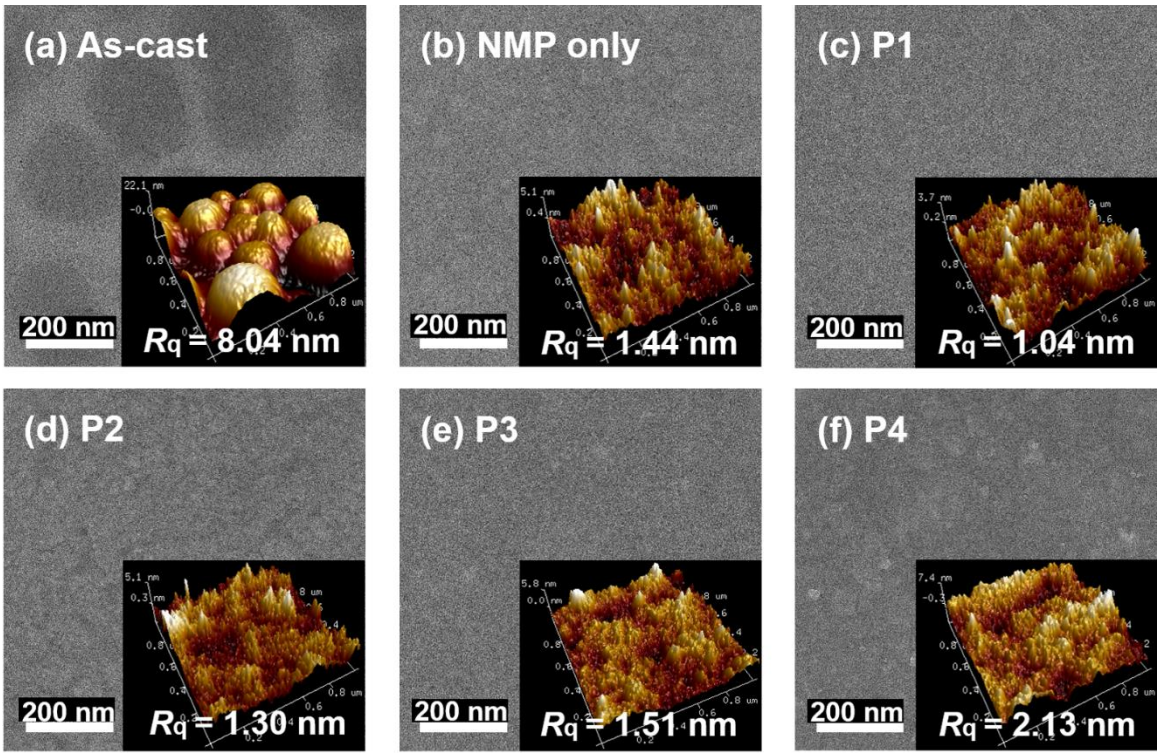

Figure 6.5. HR-TEM images and AFM topography height images in 3D view (inset, scan size 1 × 1 μm) for binary blend films w/ and w/o PVDF-based ferroelectric polymers as additives. (a) As-cast, (b) NMP only, (c) P1, (d) P2, (e) P3, and (f) P4.

The hole and electron mobilities of the blend films were also determined by fitting the dark current to the model of a single carrier space-charge limited curve (SCLC) (see Figure 6.20 and Table 6.8 of the section 6.5), as described by the Mott-Gurney equation. For the as-cast film, the hole/electron mobilities were calculated to be $8.96 \times 10^{-5}/9.56 \times 10^{-5}$ $cm^2V^{-1}s^{-1}$, whereas for the NMP only-processed film the

corresponding values were improved to be $1.93 \times 10^{-4}/2.24 \times 10^{-4}$ $cm^2V^{-1}s^{-1}$, respectively. Upon adding the ferroelectric additives, both hole/electron mobilities were further improved, especially for P2-processed film that has the highest hole/electron mobilities ($2.94 \times 10^{-4}/3.93 \times 10^{-4}$ $cm^2V^{-1}s^{-1}$), which could partially account for the lowest recombination loss as well as enhanced J_{SC} and FF values observed above. We note that the changed trends in the charge dynamics and transport properties may not be sufficiently enough to explain the enhanced device performance by adding small amount of the ferroelectric additives since the ferroelectric dipoles sporadically form only small spots within the large active area, which was already discussed in the above microscopy images in Figure 6.3.

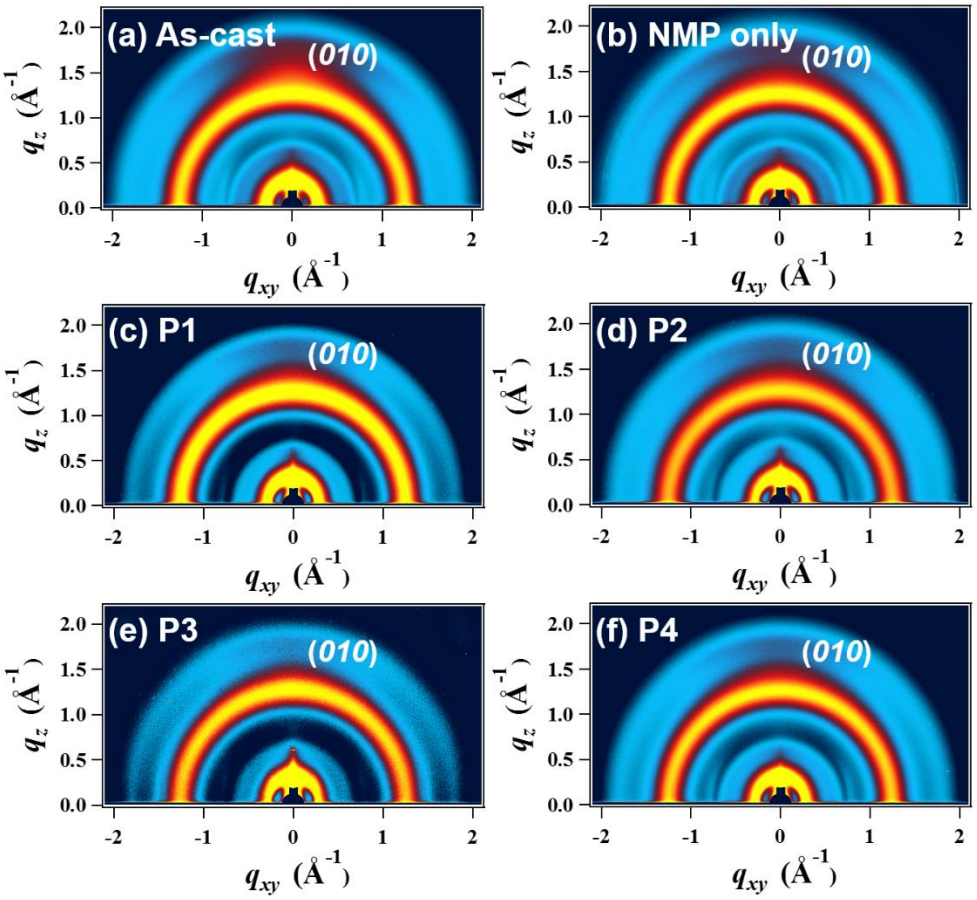

Figure 6.6. Grazing incidence wide angle X-ray scattering (GIWAXS) patterns of binary blend films w/ and w/o PVDF-based ferroelectric as an additive (a) As-cast, (b) NMP only, (c) P1, (d) P2, (e) P3, and (f) P4.

6.2.5 Study of Microstructures and Surface Morphologies of the Active Layer Films

The microstructure and surface morphology of the blend films are thoroughly investigated by using high-resolution transmission electron microscopy (HR-TEM), tapping-mode atomic force microscopy (AFM),

and grazing incident wide-angle X-ray diffraction (GIXD). The HR-TEM images of the blend films (Figure 6.5) with NMP only and ferroelectric additives show homogeneous morphology with finely phase-separated domains compared to as-cast blend film having the oversized dark regions, corresponding to $PC_{71}BM$-rich domains. In addition, from AFM images (the insets of Figure 6.5 and Figure 6.21 in the section 6.5), the surface of the as-cast film was relatively coarser with a large root mean square surface roughness (RMS) of 8.04 nm, whereas the blend films with NMP only and ferroelectric additives exhibited a smooth surface and uniform morphology with small RMS of 1.04 – 2.13 nm. The AFM data agreed well with the TEM results. The packing orientation and crystallinity of the donor and acceptor in the optimized binary blend upon incorporating various additives are studied via GIXD measurement. Shown in Figure 6.6 (and Figure 6.22 of the section 6.5) are GIXD images and line-cut profiles of the blend films. Figure 6.23 (see the section 6.5) shows GIXD images of pure additive films. All the blend films exhibited preferentially face-on orientation with respect to the substrates, as evidenced by the intensified out-of-plane π–π stacking (010) peak at $q \approx 1.85$ Å^{-1} with a no defused ring-like (100) peak at $q \approx 0.31$ Å^{-1} (Table 6.9, see the section 6.5). Besides, the locations of the diffraction peaks are nearly identical in all the cases, providing additional evidence for the fact that the improved OSC performance with ferroelectric additives is due to the ferroelectric dipoles rather than the molecular packing and orientation change.

6.3 Conclusion

In summary, we have successfully demonstrated high-performance OSCs using the built-in local electric field induced by a simple addition of ferroelectric additives (P1, P2, P3, and P4) into the PTB7-Th:$PC_{71}BM$ active layer, where the PBA-grafted P2 and P4 were prepared by ATRP for this study. The recrystallization of the ferroelectric additives with an OXY/NMP solvent pair into active layer matrix is a driving force for vitalizing their ferroelectric polarization without poling treatment, as evidenced by the advent of the rectangular-shaped *P-E* hysteresis loops after using such a co-solvent combination. A notable PCE as high as 11.02% was achieved for the P2-processed OSC, because of its enhanced permanent polarizations originated from high β-phase ordered microstructure. This value is one of the highest PCEs reported for the PTB7 derivatives-containing binary OSCs. The in-depth structural, electrical, and morphological analyses performed in our study indicate that the ferroelectric dipoles locally embedded in the active layer matrix rather than the morphological changes can affect the ultimate device performance, though the mechanism of the ferroelectric additives still needs to be borne out by further investigations. Our study can facilitate the practical application of many ferroelectric materials as an additive for various optoelectronic fields, being an effective strategy for affecting desired properties even as the considerations expend beyond that of raw efficiency.

6.4 References

1. (a) Armin, A.; Juska, G.; Philippa, B. W.; Burn, P. L.; Meredith, P.; White, R. D.; Pivrikas, A., Doping-Induced Screening of the Built-in-Field in Organic Solar Cells: Effect on Charge Transport and Recombination. *Adv. Energy Mater.* **2013,** *3* (3), 321-327; (b) Elumalai, N. K.; Uddin, A., Open circuit voltage of organic solar cells: an in-depth review. *Energy Environ. Sci.* **2016,** *9* (2), 391-410; (c) Karak, S.; Page, Z. A.; Tinkham, J. S.; Lahti, P. M.; Emrick, T.; Duzhko, V. V., Raising efficiency of organic solar cells with electrotropic additives. *Appl. Phys. Lett.* **2015,** *106* (10), 103303; (d) Yuan, Y.; Reece, T. J.; Sharma, P.; Poddar, S.; Ducharme, S.; Gruverman, A.; Yang, Y.; Huang, J., Efficiency enhancement in organic solar cells with ferroelectric polymers. *Nat. Mater.* **2011,** *10*, 296; (e) Nalwa, K. S.; Carr, J. A.; Mahadevapuram, R. C.; Kodali, H. K.; Bose, S.; Chen, Y.; Petrich, J. W.; Ganapathysubramanian, B.; Chaudhary, S., Enhanced charge separation in organic photovoltaic films doped with ferroelectric dipoles. *Energy Environ. Sci.* **2012,** *5* (5), 7042-7049; (f) Tessler, N., Adding 0.2 V to the open circuit voltage of organic solar cells by enhancing the built-in potential. *J. Appl. Phys.* **2015,** *118* (21), 215501.

2. (a) Chen, S.; Hu, Y.; Meng, S.; Fu, X., Study on the separation mechanisms of photogenerated electrons and holes for composite photocatalysts g-C3N4-WO3. *Appl. Catal. B-Environ.* **2014,** *150-151*, 564-573; (b) Vaynzof, Y.; Kabra, D.; Zhao, L.; Ho, P. K. H.; Wee, A. T.-S.; Friend, R. H., Improved photoinduced charge carriers separation in organic-inorganic hybrid photovoltaic devices. *Appl. Phys. Lett.* **2010,** *97* (3), 033309; (c) Würfel, U.; Cuevas, A.; Würfel, P., Charge Carrier Separation in Solar Cells. *IEEE J. Photovolt.* **2015,** *5* (1), 461-469; (d) Xu, T.; Qiao, Q., Conjugated polymer–inorganic semiconductor hybrid solar cells. *Energy Environ. Sci.* **2011,** *4* (8), 2700-2720.

3. (a) Fukada, E.; Furukawa, T., Piezoelectricity and ferroelectricity in polyvinylidene fluoride. *Ultrasonics* **1981,** *19* (1), 31-39; (b) Kaji, K., Increase of the crystallite size by application of tensile stress for highly oriented polymer. *Makromol. Chem.* **1974,** *175* (1), 311-325; (c) Kepler, R. G.; Anderson, R. A., Ferroelectricity in polyvinylidene fluoride. *J. Appl. Phys.* **1978,** *49* (3), 1232-1235; (d) McFee, J. H.; Bergman, J. G.; Crane, G. R., Pyroelectric and nonlinear optical properties of poled polyvinylidene fluoride films. *Ferroelectrics* **1972,** *3* (1), 305-313; (e) Murayama, N.; Oikawa, T.; Katto, T.; Nakamura, K. i., Persistent polarization in poly(vinylidene fluoride). II. Piezoelectricity of poly(vinylidene fluoride) thermoelectrets. *J. Polym. Sci. Poly. Phys. Ed.* **1975,** *13* (5), 1033-1047; (f) Nakamura, K. i.; Wada, Y., Piezoelectricity, pyroelectricity, and the electrostriction constant of poly(vinylidene fluoride). *J. Polym. Sci., Part A-2* **1971,** *9* (1), 161-173.

4. (a) Hester, J. F.; Banerjee, P.; Won, Y. Y.; Akthakul, A.; Acar, M. H.; Mayes, A. M., ATRP of Amphiphilic Graft Copolymers Based on PVDF and Their Use as Membrane Additives. *Macromolecules* **2002,** *35* (20), 7652-7661; (b) Zhang, Q. M.; Bharti, V.; Kavarnos, G., Poly(Vinylidene Fluoride) (PVDF) and its Copolymers. In *Encyclopedia of Smart Materials*, Wiley: New York: 2002; pp 807– 825; (c) Zhu, L.; Wang, Q., Novel Ferroelectric Polymers for High Energy Density and Low Loss Dielectrics. *Macromolecules* **2012,** *45* (7), 2937-2954.

5. (a) Li, Q.; Wang, Q., Ferroelectric Polymers and Their Energy-Related Applications. *Macromol. Chem. Phys.* **2016,** *217* (11), 1228-1244.

6. Ma, W.; Zhang, J.; Chen, S.; Wang, X., Crystalline Phase Formation of Poly(vinylidene fluoride) from Tetrahydrofuran/N,N-dimethylformamide Mixed Solutions. *J. Macromol. Sci. B.* **2008,** *47* (3), 434-449.

7. (a) Abdalla, S.; Obaid, A.; Al-Marzouki, F. M., Preparation and characterization of poly(vinylidene fluoride): A high dielectric performance nano-composite for electrical storage. *Results Phys.* **2016,** *6*, 617-626; (b) Bohlén, M.; Bolton, K., Conformational studies of poly(vinylidene fluoride), poly(trifluoroethylene) and poly(vinylidene fluoride-co-trifluoroethylene) using density functional theory. *Phys. Chem. Chem. Phys.* **2014,** *16* (25), 12929-12939; (c) Buensuceso, J. G. G.; Cuan, A.; Castillo, R. V.; Cortes-Romero, C. M. In *DFT study of PVDF as polymer composite precursor*, 2016 12th Congreso Internacional de Ingeniería (CONIIN), 1-6 May 2016; IEEE: 2016; pp 1-6; (d) Lovinger, A. J., Unit cell of the γ phase of poly(vinylidene fluoride). *Macromolecules* **1981,** *14* (2), 322-325; (e) Manna, S.; Nandi, A. K., Piezoelectric β Polymorph in Poly(vinylidene fluoride)-Functionalized Multiwalled Carbon Nanotube Nanocomposite Films. *J. Phys. Chem. C* **2007,** *111* (40), 14670-14680; (f) Pei, Y.; Zeng, X. C., Elastic properties of poly(vinyldene fluoride) (PVDF) crystals: A density functional theory study. *J. Appl. Phys.* **2011,** *109* (9), 093514; (g) Wolff, S.; Jirasek, F.; Beuermann, S.; Türk, M., Crystal phase transformation of α into β phase poly(vinylidene fluoride) via particle formation caused by rapid expansion of supercritical solutions. *RSC Adv.* **2015,** *5* (82), 66644-66649; (h) Yu, S.; Zheng, W.; Yu, W.; Zhang, Y.; Jiang, Q.; Zhao, Z., Formation Mechanism of β-Phase in PVDF/CNT Composite Prepared by the Sonication Method. *Macromolecules* **2009,** *42* (22), 8870-8874.

8. (a) Gadinski, M. R.; Han, K.; Li, Q.; Zhang, G.; Reainthippayasakul, W.; Wang, Q., High Energy Density and Breakdown Strength from β and γ Phases in Poly(vinylidene fluoride-co-bromotrifluoroethylene) Copolymers. *ACS Appl. Mater. Interfaces* **2014,** *6* (21), 18981-18988; (b) Guan, F.; Pan, J.; Wang, J.; Wang, Q.; Zhu, L., Crystal Orientation Effect on Electric Energy Storage in Poly(vinylidene fluoride-co-hexafluoropropylene) Copolymers. *Macromolecules* **2010,** *43* (1), 384-392; (c) Guan, F.; Wang, J.; Yang, L.; Tseng, J.-K.; Han, K.; Wang, Q.; Zhu, L., Confinement-Induced High-Field Antiferroelectric-like Behavior in a Poly(vinylidene fluoride-co-trifluoroethylene-co-chlorotrifluoroethylene)-graft-polystyrene Graft Copolymer. *Macromolecules* **2011,** *44* (7), 2190-2199; (d) Guan, F.; Yang, L.; Wang, J.; Guan, B.; Han, K.; Wang, Q.; Zhu, L., Confined Ferroelectric Properties in Poly(Vinylidene Fluoride-co-Chlorotrifluoroethylene)-graft-Polystyrene Graft Copolymers for Electric Energy Storage Applications. *Adv. Funct. Mater.* **2011,** *21* (16), 3176-3188; (e) Lee, J. W.; Cho, H. J.; Chun, J.; Kim, K. N.; Kim, S.; Ahn, C. W.; Kim, I. W.; Kim, J.-Y.; Kim, S.-W.; Yang, C.; Baik, J. M., Robust nanogenerators based on graft copolymers via control of dielectrics for remarkable output power enhancement. *Sci. Adv.* **2017,** *3* (5); (f) Li, Z.; Wang, Y.; Cheng, Z.-Y., Electromechanical properties of poly(vinylidene-fluoride-chlorotrifluoroethylene) copolymer. *Appl. Phys. Lett.* **2006,** *88* (6), 062904.

9. (a) Chen, X.; Han, X.; Shen, Q.-D., PVDF-Based Ferroelectric Polymers in Modern Flexible Electronics. *Adv. Electron. Mater.* **2017,** *3* (5), 1600460; (b) Gerber, A.; Fitsilis, M.; Waser, R.; Reece, T. J.; Rije, E.; Ducharme, S.; Kohlstedt, H., Ferroelectric field effect transistors using very thin ferroelectric polyvinylidene fluoride copolymer films as gate dielectrics. *J. Appl. Phys.* **2010,** *107* (12), 124119; (c) Kim, G.; Kang, S.-J.; Dutta, G. K.; Han, Y.-K.; Shin, T. J.; Noh, Y.-Y.; Yang, C., A Thienoisoindigo-Naphthalene Polymer with Ultrahigh Mobility of 14.4 cm2/V·s That Substantially Exceeds Benchmark Values for Amorphous Silicon Semiconductors. *J. Am. Chem. Soc.* **2014,** *136* (26), 9477-9483; (d) Mai, M.; Ke, S.; Lin, P.; Zeng, X., Ferroelectric Polymer Thin Films for Organic Electronics. *J. Nanomater.* **2015,** *2015*, 14; (e) Yuan, Y.; Xiao, Z.; Yang, B.; Huang, J., Arising applications of ferroelectric materials in photovoltaic devices. *J. Mater. Chem. A* **2014,** *2* (17), 6027-6041.

10. (a) Jiang, W.; Yu, R.; Liu, Z.; Peng, R.; Mi, D.; Hong, L.; Wei, Q.; Hou, J.; Kuang, Y.; Ge, Z., Ternary Nonfullerene Polymer Solar Cells with 12.16% Efficiency by Introducing One Acceptor with Cascading Energy Level and Complementary Absorption. *Adv. Mater.* **2018,** *30* (1), 1703005-n/a; (b) Kumari, T.; Lee, S. M.; Kang, S.-H.; Chen, S.; Yang, C., Ternary solar cells with a mixed face-on and edge-on orientation enable an unprecedented efficiency of 12.1%. *Energy Environ. Sci.* **2017,** *10* (1), 258-265; (c) Kumari, T.; Lee, S. M.; Lee, K. C.; Cho, Y.; Yang, C., Harmonious Compatibility Dominates Influence of Side-Chain Engineering on Morphology and Performance of Ternary Solar Cells. *Adv. Energy Mater.* **2018,** *8* (22), 1800616; (d) Kumari, T.; Lee, S. M.; Yang, C., Cubic-Like Bimolecular Crystal Evolution and over 12% Efficiency in Halogen-Free Ternary Solar Cells. *Adv. Funct. Mater.* **2018,** *28* (19), 1707278; (e) Xu, X.; Yu, T.; Bi, Z.; Ma, W.; Li, Y.; Peng, Q., Realizing Over 13% Efficiency in Green-Solvent-Processed Nonfullerene Organic Solar Cells Enabled by 1,3,4-Thiadiazole-Based Wide-Bandgap Copolymers. *Adv. Mater.* **2018,** *30* (3), 1703973; (f) Zhao, W.; Li, S.; Yao, H.; Zhang, S.; Zhang, Y.; Yang, B.; Hou, J., Molecular Optimization Enables over 13% Efficiency in Organic Solar Cells. *J. Am. Chem. Soc.* **2017,** *139* (21), 7148-7151; (g) Zhao, W.; Li, S.; Zhang, S.; Liu, X.; Hou, J., Ternary Polymer Solar Cells based on Two Acceptors and One Donor for Achieving 12.2% Efficiency. *Adv. Mater.* **2017,** *29* (2), 1604059.

11. (a) Eskandari, R.; Zhang, X.; Malkinski, L. M., Polarization-dependent photovoltaic effect in ferroelectric-semiconductor system. *Appl. Phys. Lett.* **2017,** *110* (12), 121105.

12. (a) Chen, Y.; Chen, X.; Zhou, D.; Shen, Q.-D.; Hu, W., Low-temperature crystallization of P(VDF-TrFE-CFE) studied by Flash DSC. *Polymer* **2016,** *84*, 319-327; (b) Feng, T.; Xie, D.; Zang, Y.; Wu, X.; Ren, T.; Pan, W., Temperature Control of P(VDF-TrFE) Copolymer Thin Films. *Integr. Ferroelectrics* **2013,** *141* (1), 187-194; (c) Fu, Z.; Xia, W.; Chen, W.; Weng, J.; Zhang, J.; Zhang, J.; Jiang, Y.; Zhu, G., Improved Thermal Stability of Ferroelectric Phase in Epitaxially Grown P(VDF-TrFE) Thin Films. *Macromolecules* **2016,** *49* (10), 3818-3825; (d) Lang, M. H.; Zhang, J., Morphology and properties of poly(vinylidene fluoride) (PVDF)/ethylene–vinyl acetate copolymer (EVA) blends. *Plast. Rubb. Compos.* **2014,** *43* (1), 8-14; (e) Le, M. Q.; Capsal, J.-F.; Galineau, J.; Ganet, F.; Yin, X.; Yang, M.; Chateaux, J.-F.; Renaud, L.; Malhaire, C.; Cottinet, P.-J.; Liang, R., All-organic

electrostrictive polymer composites with low driving electrical voltages for micro-fluidic pump applications. *Sci. Rep.* **2015,** *5*, 11814; (f) Teyssedre, G.; Bernes, A.; Lacabanne, C., DSC and TSC study of a VDF/TrFE copolymer. *Thermochimica Acta* **1993,** *226*, 65-75; (g) Teyssèdre, G.; Lacabanne, C., Study of the thermal and dielectric behavior of P(VDF-TrFE) copolymers in relation with their electroactive properties. *Ferroelectrics* **1995,** *171* (1), 125-144.

13. (a) He, Z.; Xiao, B.; Liu, F.; Wu, H.; Yang, Y.; Xiao, S.; Wang, C.; Russell, T. P.; Cao, Y., Single-junction polymer solar cells with high efficiency and photovoltage. *Nat. Photonics* **2015,** *9*, 174; (b) Kyaw, A. K. K.; Wang, D. H.; Gupta, V.; Leong, W. L.; Ke, L.; Bazan, G. C.; Heeger, A. J., Intensity Dependence of Current–Voltage Characteristics and Recombination in High-Efficiency Solution-Processed Small-Molecule Solar Cells. *ACS Nano* **2013,** *7* (5), 4569-4577; (c) Schilinsky, P.; Waldauf, C.; Brabec, C. J., Recombination and loss analysis in polythiophene based bulk heterojunction photodetectors. *Appl. Phys. Lett.* **2002,** *81* (20), 3885-3887.

14. (a) Gao, L.; Zhang, Z.-G.; Xue, L.; Min, J.; Zhang, J.; Wei, Z.; Li, Y., All-Polymer Solar Cells Based on Absorption-Complementary Polymer Donor and Acceptor with High Power Conversion Efficiency of 8.27%. *Adv. Mater.* **2016,** *28* (9), 1884-1890; (b) Riedel, I.; Parisi, J.; Dyakonov, V.; Lutsen, L.; Vanderzande, D.; Hummelen, J. C., Effect of Temperature and Illumination on the Electrical Characteristics of Polymer–Fullerene Bulk-Heterojunction Solar Cells. *Adv. Funct. Mater.* **2004,** *14* (1), 38-44.

15. (a) Guo, B.; Li, W.; Guo, X.; Meng, X.; Ma, W.; Zhang, M.; Li, Y., High Efficiency Nonfullerene Polymer Solar Cells with Thick Active Layer and Large Area. *Adv. Mater.* **2017,** *29* (36), 1702291; (b) Kim, G.; Song, S.; Lee, J.; Kim, T.; Lee, T. H.; Walker, B.; Kim, J. Y.; Yang, C., Control of Charge Dynamics via Use of Nonionic Phosphonate Chains and Their Effectiveness for Inverted Structure Solar Cells. *Adv. Energy Mater.* **2015,** *5* (18), 1500844; (c) Nian, L.; Gao, K.; Liu, F.; Kan, Y.; Jiang, X.; Liu, L.; Xie, Z.; Peng, X.; Russell, T. P.; Ma, Y., 11% Efficient Ternary Organic Solar Cells with High Composition Tolerance via Integrated Near-IR Sensitization and Interface Engineering. *Adv. Mater.* **2016,** *28* (37), 8184-8190.

16. (a) Armin, A.; Juska, G.; Ullah, M.; Velusamy, M.; Burn, P. L.; Meredith, P.; Pivrikas, A., Balanced Carrier Mobilities: Not a Necessary Condition for High-Efficiency Thin Organic Solar Cells as Determined by MIS-CELIV. *Adv. Energy Mater.* **2014,** *4* (4), 1300954; (b) Goh, C.; Kline, R. J.; McGehee, M. D.; Kadnikova, E. N.; Fréchet, J. M. J., Molecular-weight-dependent mobilities in regioregular poly(3-hexyl-thiophene) diodes. *Appl. Phys. Lett.* **2005,** *86* (12), 122110.

6.5 Supporting Texts and Figures

General Procedure for grafting Using Atom Transfer Radical Polymerization

In a round flask, PVDF (3.0 g) or P(VDF-TrFE) (3.0 g) was dissolved completely in NMP at 60°C, and BA (18.02g, 93.5 mmol), CuCl (0.03g, 0.202 mmol) and PMDETA (0.096g, 0.553 mmol) were added to the solution at room temperature, and purge with argon for 15min. Then, the reaction mixture was stirred at 120 °C for 72 h. After the reaction had completed, the copolymer solution was precipitated into water/methanol (1:4, v/v) and filtered off. The precipitated copolymer was stirred overnight in a large volume of hexane and chloroform for removing the PBA homopolymer and impurities. The copolymer was then recovered by filtration, re-dissolved in NMP, and precipitated into water/methanol (1:4, v/v). Finally, the graft copolymers were obtained under a vacuum.

PVDF-g-PBA (P2)

M_n = 102 kDa, PDI = 2.55. F-H decoupled ^{1}H NMR (400MHz, $(CD_3)_2CO$), δ (ppm): 2.9–3.2 (br, –$CF_2CH_2CF_2CH_2$–), 2.3–2.5 (br, −$CF_2CH_2CH_2CF_2$–), 1.5–2.0 (-C(COO)H_2-CH_2-), 0.8–1.4 (-C(COO)H_2-CH_2-) and 1.4–1.65 (br, 9H, −$C(CH_3)_3$).

P(VDF-TrFE)-g-PBA (P4)

M_n = 174 kDa, PDI = 2.53. F-H decoupled ^{1}H NMR (400MHz, $(CD_3)_2CO$), δ (ppm): 5.3–5.7 (br, -CF*H*CF_2-), 2.7–3.2 (br, -$CF_2CH_2CF_2CH_2$-), 2.2–2.7 (br, -$CF_2CH_2CH_2CF_2$-), 1.5–2.0 (-C(COO)H_2-CH_2-), 0.8–1.4 (-C(COO)H_2-CH_2-) and 1.4–1.6 (br, −$OC(CH_3)_3$).

Calculation of the molar compositions

In F-H decoupled ^{1}H NMR spectra, the mol % of PBA in PVDF and P(VDF-TrFE) were ascertained by integrating the ratio of the BA peak at 1.4–1.6 ppm to the VDF peaks at 2.1–2.4, 2.9–3.1 ppm and 2.2–2.7, 2.7–3.2 ppm, respectively, corresponding to head-to-head and head-to-tail configurations through the following equations.

PVDF-g-PBA

$$x = \frac{(\text{Integral}_{1.4-1.65})/9}{(\text{Integral}_{2.3-2.5} + \text{Integral}_{2.9-32})/2}$$

(1) BA mol percent (mol %) $= \frac{x}{1+x} \times 100$

(2) x = 0.3172

(3) mol% = 24.08 ± 5.00 %

P(VDF-TrFE)-g-PBA

$$x = \frac{(\text{Integral}_{1.4-1.6})/9}{(\text{Integral}_{2.2-2.7} + \text{Integral}_{2.7-3.2})/2}$$

(1) BA mol percent (mol %) $= \frac{x}{1+x} \times 100$

(2) x = 0.4996

(3) mol% = 33.31 ± 5.00 %

Solar cell fabrication

PTB7-Th:$PC_{71}BM$ (1:1.5 ratio) based devices were fabricated in the conventional device structure of glass/ITO/PEDOT:PSS/active layer/Al. On the pre-cleaned ITO substrate, a PEDOT:PSS layer (Clevios P VP AI. 4083) was spin-coated at 4000 rpm for 60 s and then thermally annealed at 140 °C for 20 min. The substrates were immediately transferred to glovebox and the active layer was spin-coated yielding thickness in the range of 160-200 nm for different additives (see Figure 6.24). The films were subsequently treated by vacuum annealing for 15 minutes. Finally, a 100 nm thick layer of Al was deposited using a shadow mask (device area: 0.13 cm^2) under high vacuum (< 3×10^{-6} Pa). For active layer preparation, PTB7-Th:$PC_{71}BM$ (35 mg ml^{-1}) were dissolved in anhydrous OXY and stirred at 60 °C for overnight. P1, P2, P3, and P4 with same as total active layer concentration were dissolved separately in NMP and stirred at 60 °C for overnight. Next day, different wt. % of additives were added separately in the active layer solution and again stirred at 60 °C for 2 hrs. For the hysteresis measurement using P-E loop, the thickness of binary blend films w or w/o additives as well as of pure additive films are provided in Figures 6.25 and 6.26, respectively.

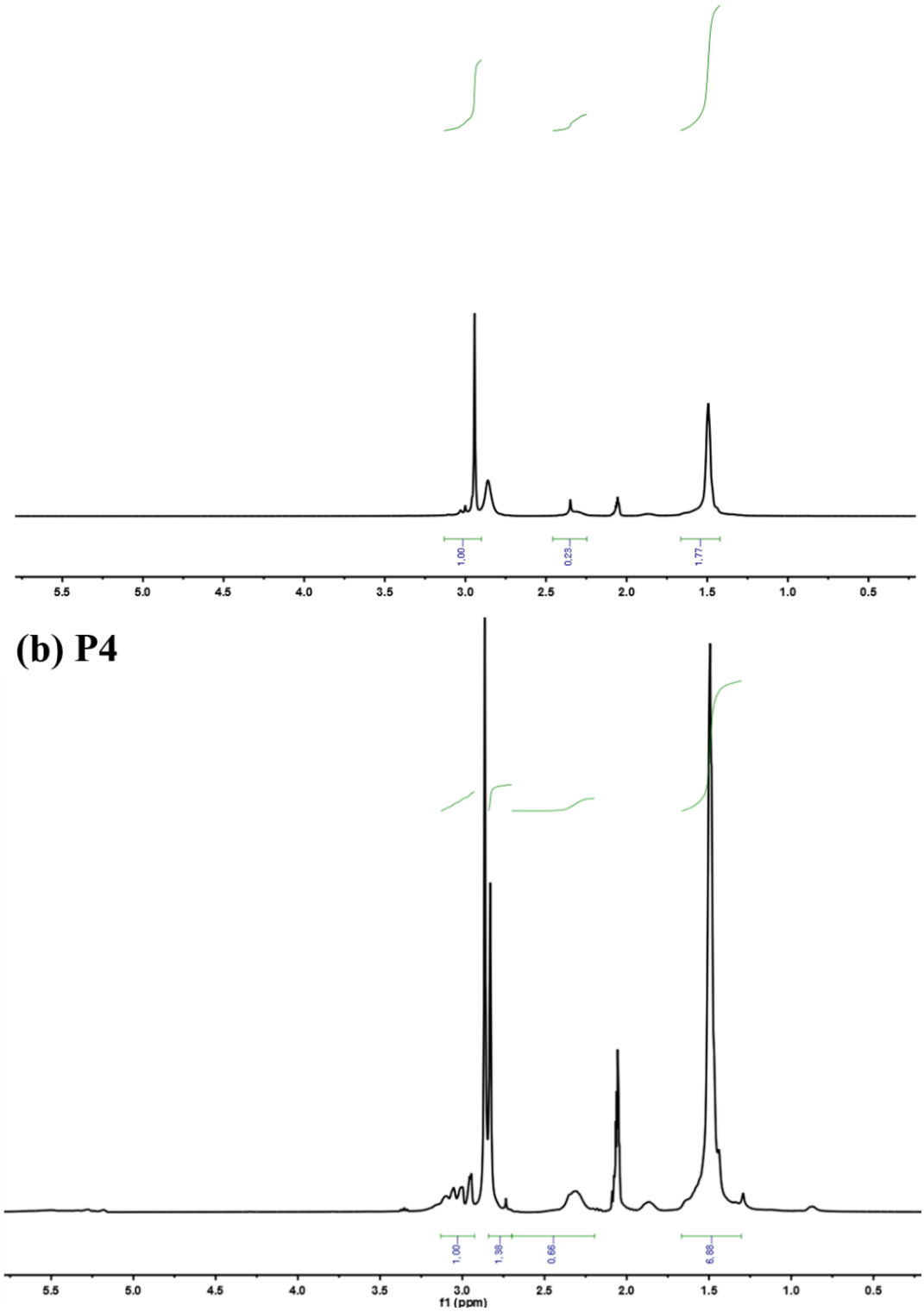

Figure 6.7. ^{1}H NMR result of (a) P1, and (b) P2 ferroelectric polymers.

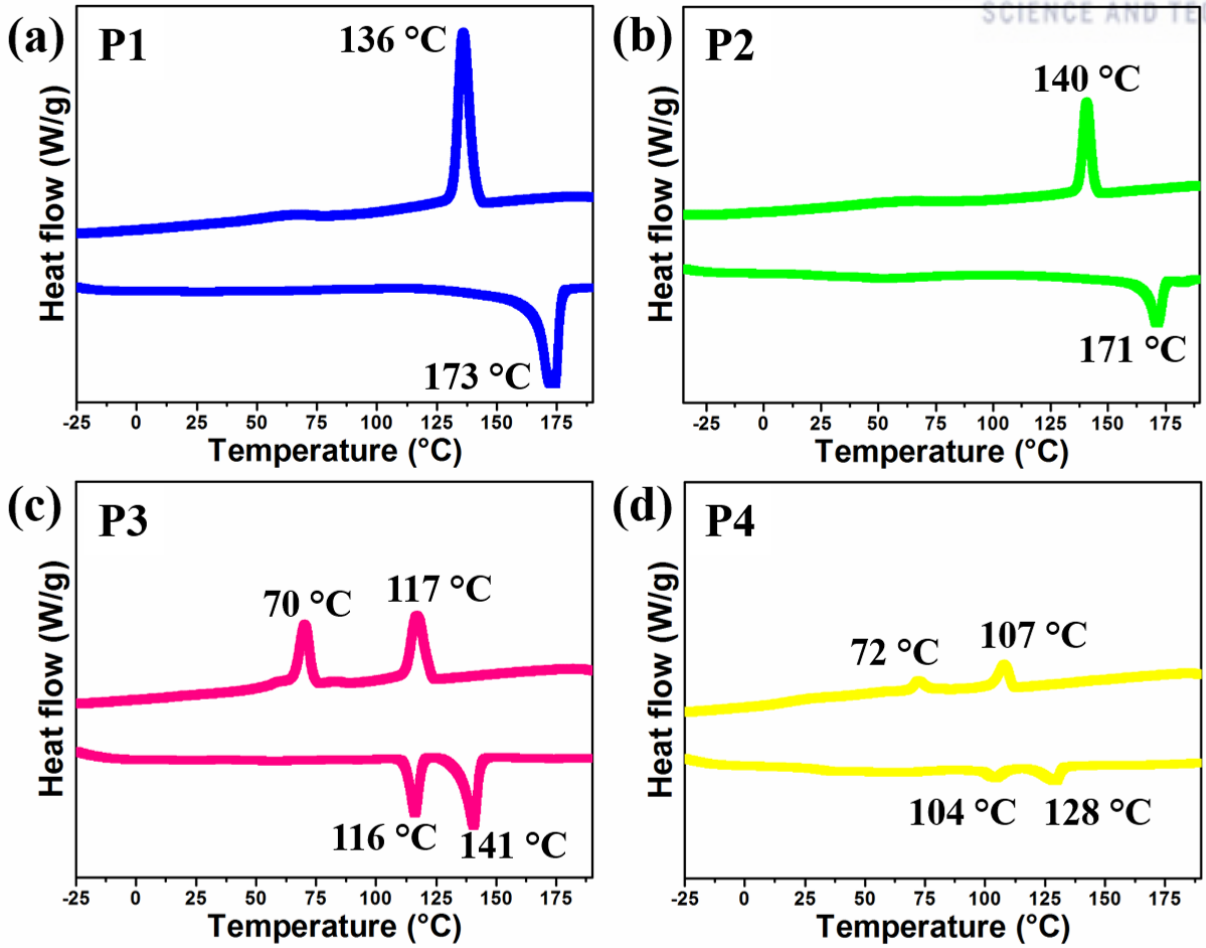

Figure 6.8. Differential scanning calorimetry data of PVDF-based ferroelectric polymers. (a) P1, (b) P2, (c) P3, and (d) P4.

Table 6.2. Optimized geometries by DFT calculation, the charge density isosurfaces for LUMO and HOMO levels of PVDF-based ferroelectric polymers, the LUMO-HOMO levels and the dipole moment values of PVDF-based ferroelectric polymers. Red and green color scheme refers to the positive and negative wave functions, respectively.

Conformation	Structure (LUMO, HOMO)	Dipole moment	LUMO (eV)	HOMO (eV)
P1				
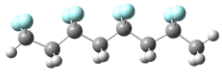 tttt	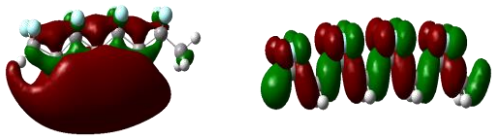	9.298 D	-0.756	-9.056
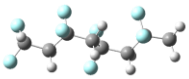 tgtg	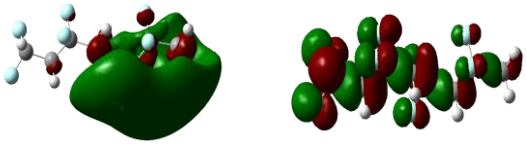	6.100 D	-0.354	-9.318
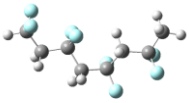 tttg	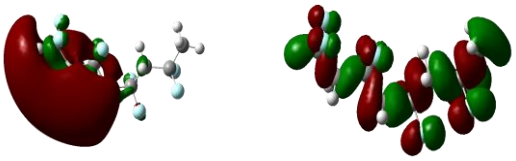	3.619 D	-0.517	-9.070
P2				
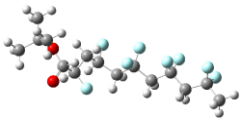 tttt (1)	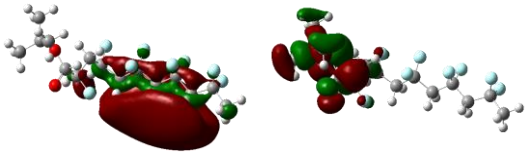	5.048 D	-0.468	-7.743
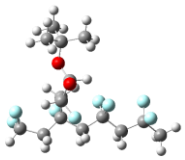 tttt (2)	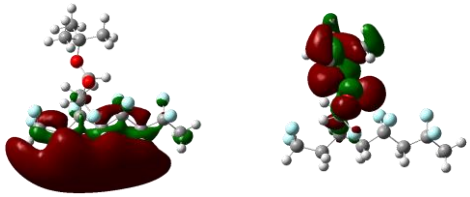	4.149 D	-0.483	-7.558
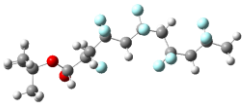 tgtg (1)		4.347 D	-0.245	-7.807
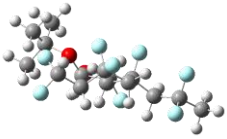 tgtg (2)	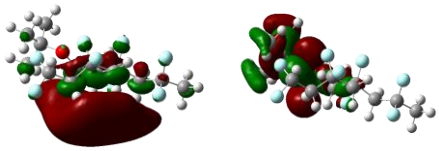	3.048 D	-0.392	-7.739

tttg (1) 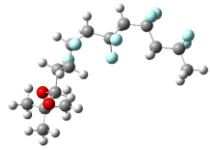	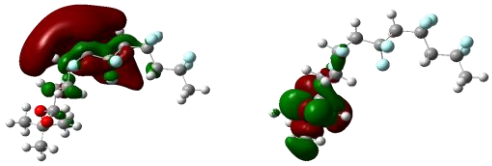	5.439 D	-0.374	-7.930
tttg (2) 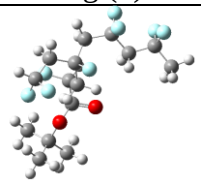	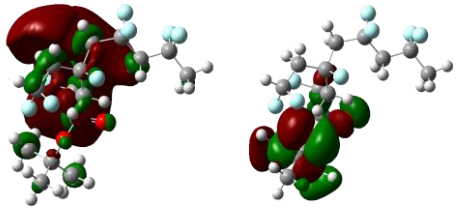	5.451 D	-0.362	-7.998
P3				
tttt (1) 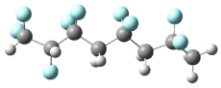	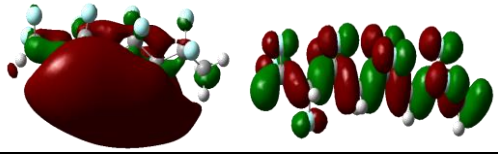	6.248 D	-0.578	-9.111
tttt (2) 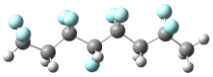	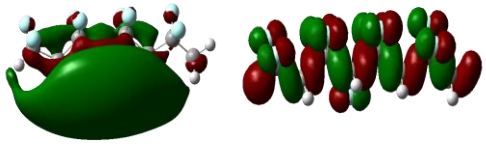	7.209 D	-0.612	-9.111
tgtg (1) 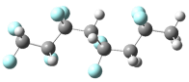	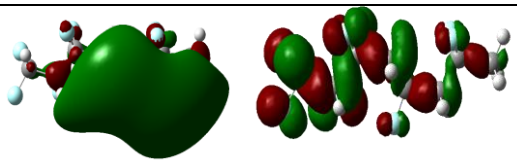	6.366 D	-0.384	-9.387
tgtg (2) 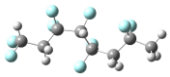	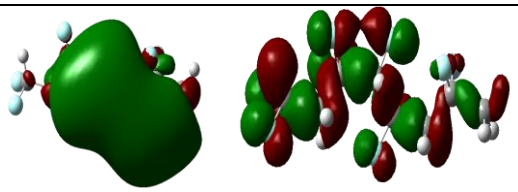	6.073 D	-0.482	-9.418
tttg (1) 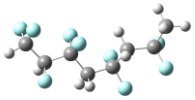	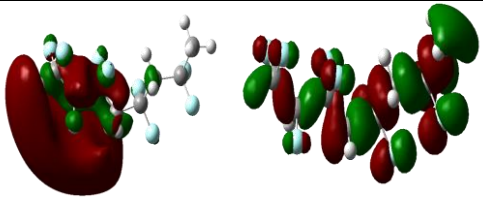	2.979 D	-0.408	-9.174
tttg (2) 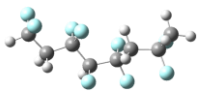	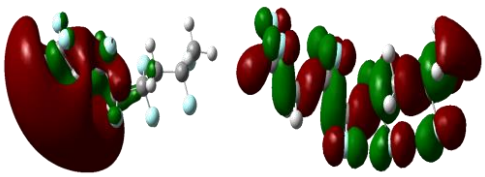	3.375 D	-0.452	-9.186
P4				

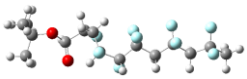 tttt (1)	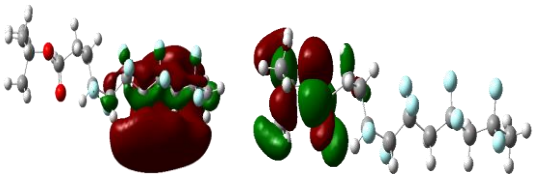	4.916 D	-0.392	-7.980
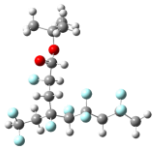 tttt (2)	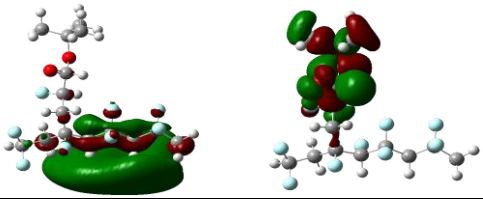	5.589 D	-0.529	-7.505
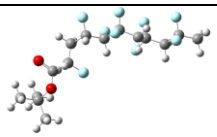 tgtg (1)	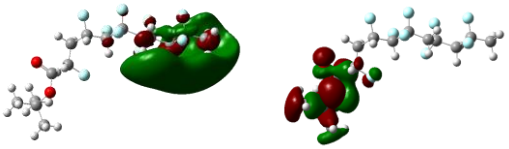	6.061 D	-0.217	-7.778
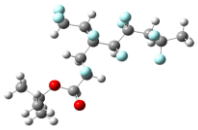 tgtg (2)	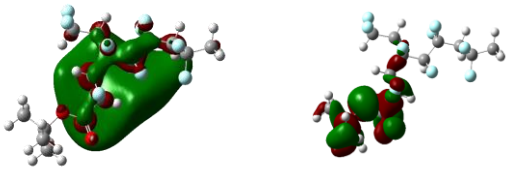	6.864 D	-0.691	-7.634
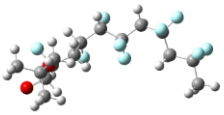 tttg (1)	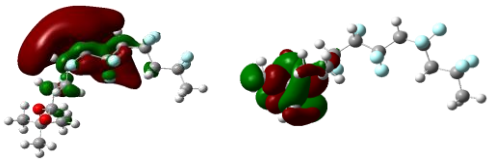	3.141 D	-0.408	-7.785
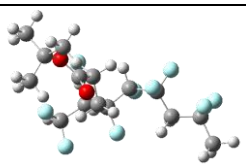 tttg (2)	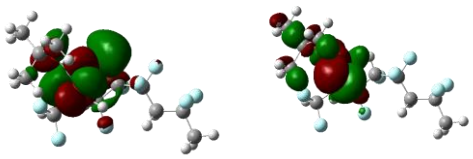	2.844 D	-0.594	-7.808

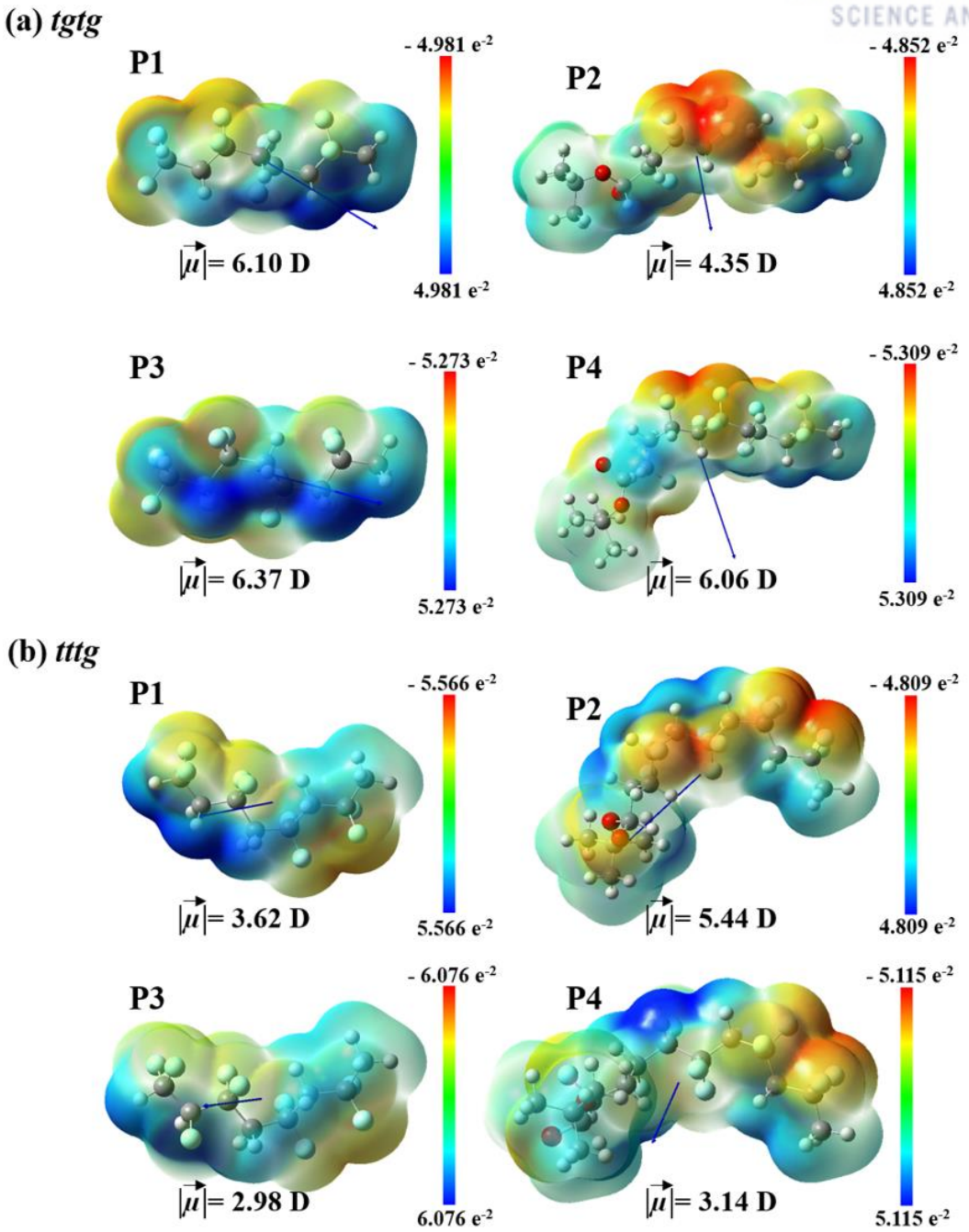

Figure 6.9. Electrostatic charge distribution and dipole direction (by blue arrow) with magnitude for structural models of PVDF-based ferroelectric polymers $(VDF)_4$, $(VDF)_3$-$(VDF\text{-}BA)_1$, $(VDF)_3$-$(TrFE)_1$, and $(VDF)_3$-$(TrFE\text{-}BA)_1$ in (a) (*tgtg*) and (b) (*tttg*) conformations. The scale bar shows the colors scheme for the ESP. Red indicates electron rich (partially negative charge) region; yellow indicates slightly electron rich region; green indicates neutral region; light blue indicates slightly electron deficient region; and blue indicates electron deficient (partially positive charge) region, respectively.

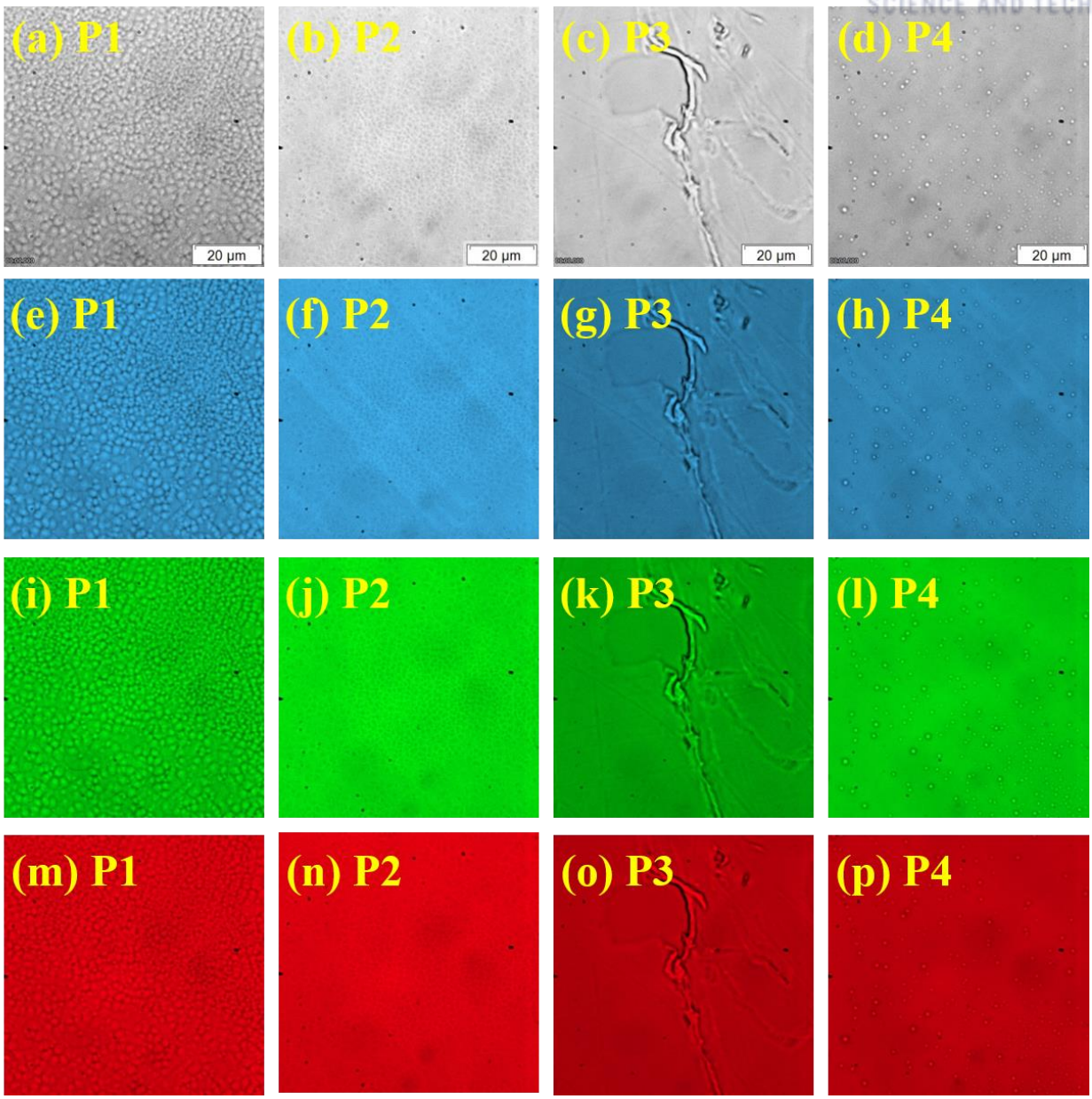

Figure 6.10. Fluorescence microscopy of the pure PVDF-based ferroelectric polymer films investigated using white light ((a), (b), (c), and (d)), blue light ((e), (f), (g), and (h)), green light ((i), (j), (k), and (l)), and red light ((m), (n), (o), and (p)). Scale bar is 20 μm.

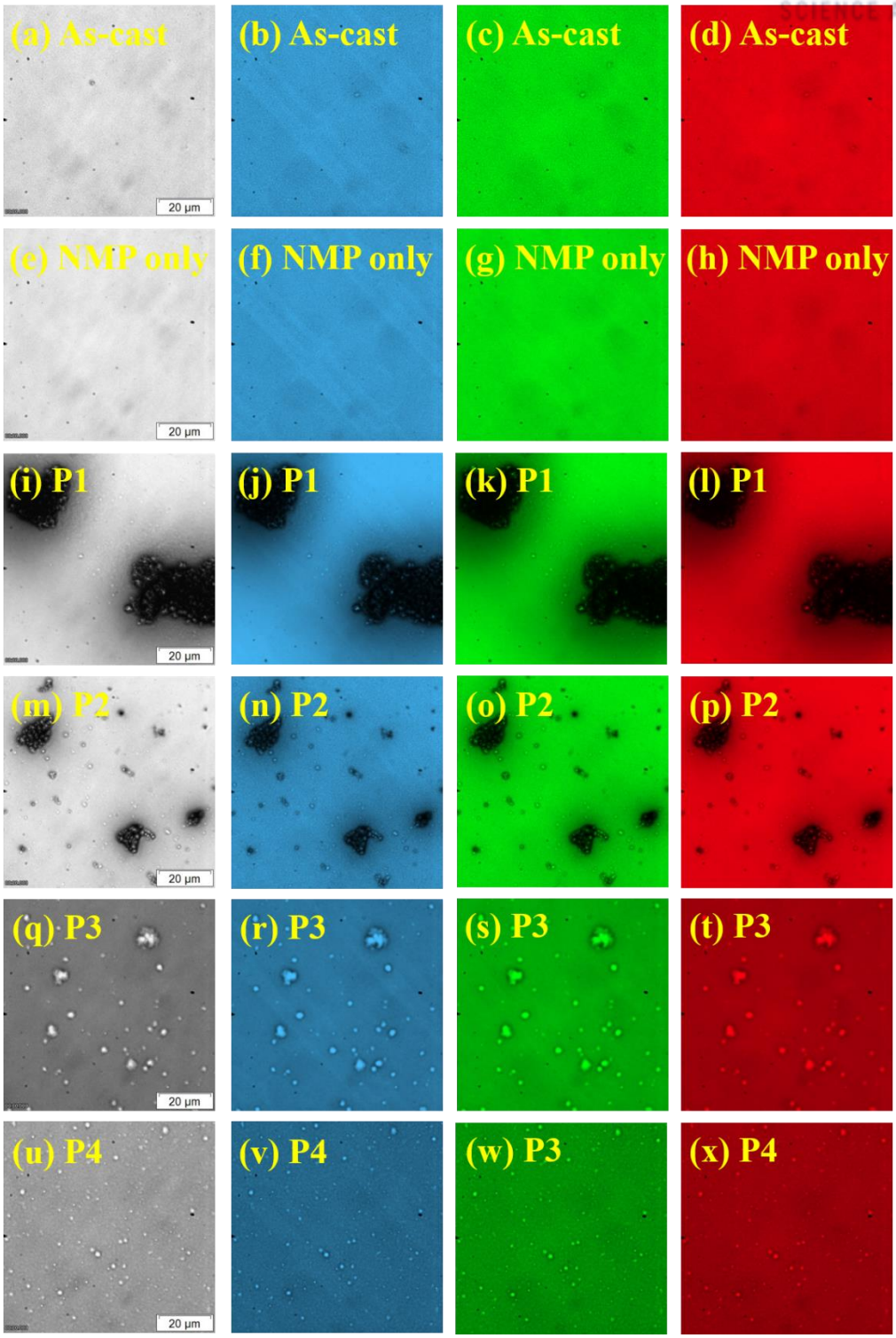

Figure 6.11. Fluorescence microscopy of the optimized of binary blend films w/ and w/o various PVDF-based ferroelectric polymers as an additive investigated using white light ((a), (e), (i), (m), (q), and (u)), blue light ((b), (f), (j), (n), (r), and (v)), green light ((c), (g), (k), (o), (s), and (w)), and red light ((d), (h), (l), (p), (t), and (x). Scale bar is 20 μm.

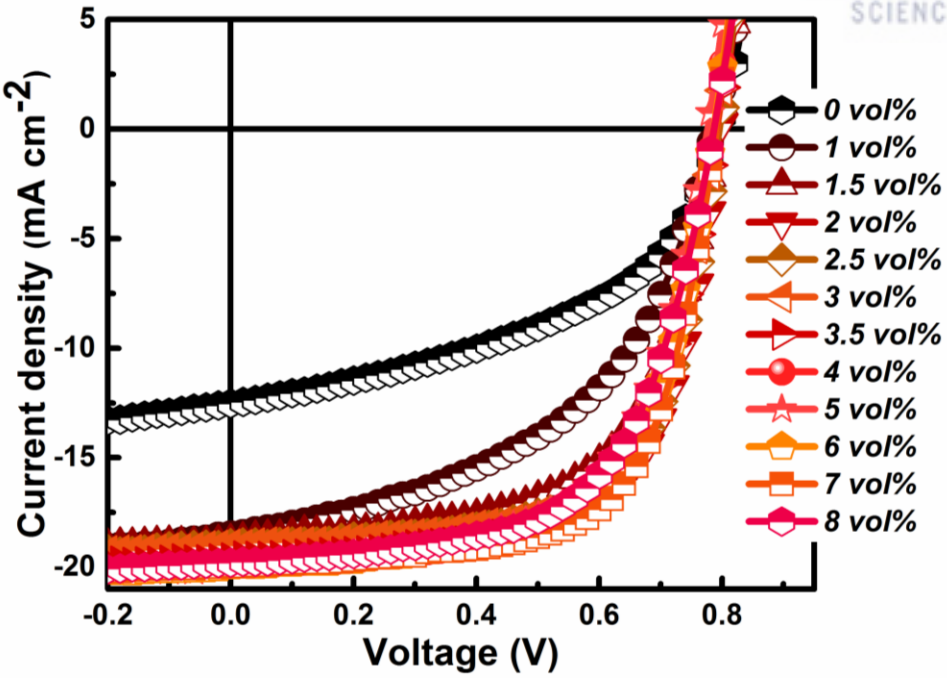

Figure 6.12. *J–V* characteristics of binary devices with different vol% of NMP only under AM 1.5G irradiation at 100 mW cm^{-2}.

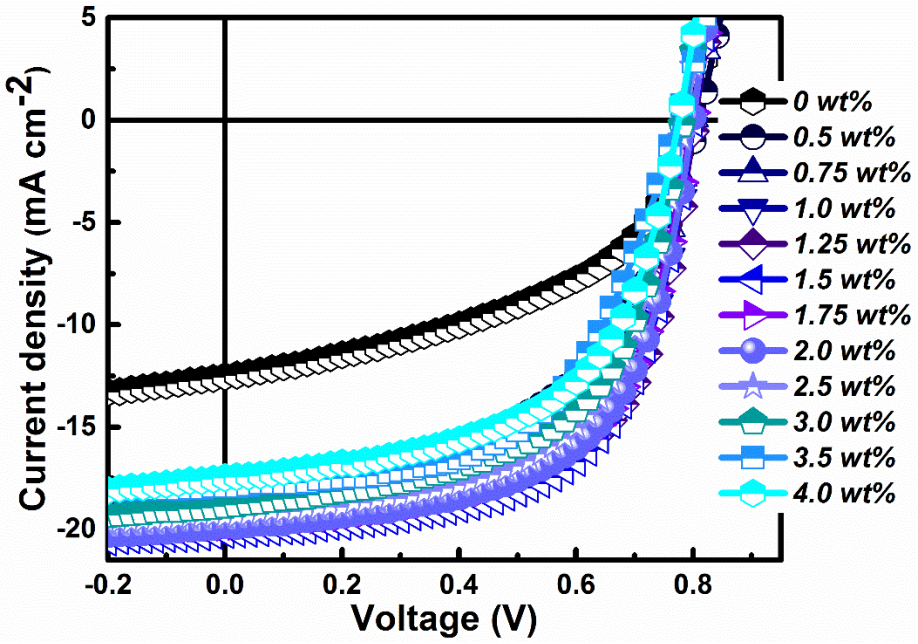

Figure 6.13. *J–V* characteristics of binary devices with different wt% of P1 as an additive under AM 1.5G irradiation at 100 mW cm^{-2}.

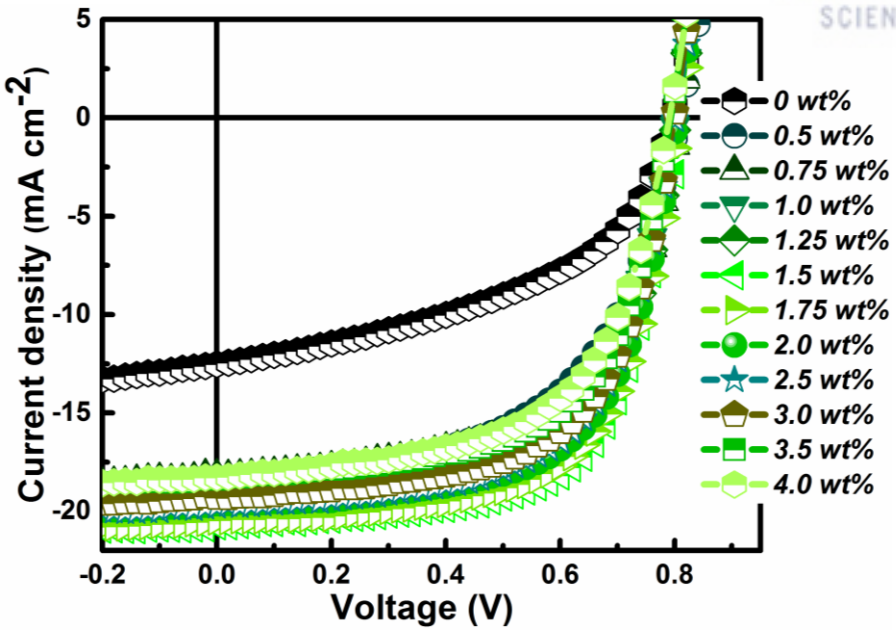

Figure 6.14. *J–V* characteristics of binary devices with different wt% of P2 as an additive under AM 1.5G irradiation at 100 mW cm^{-2}.

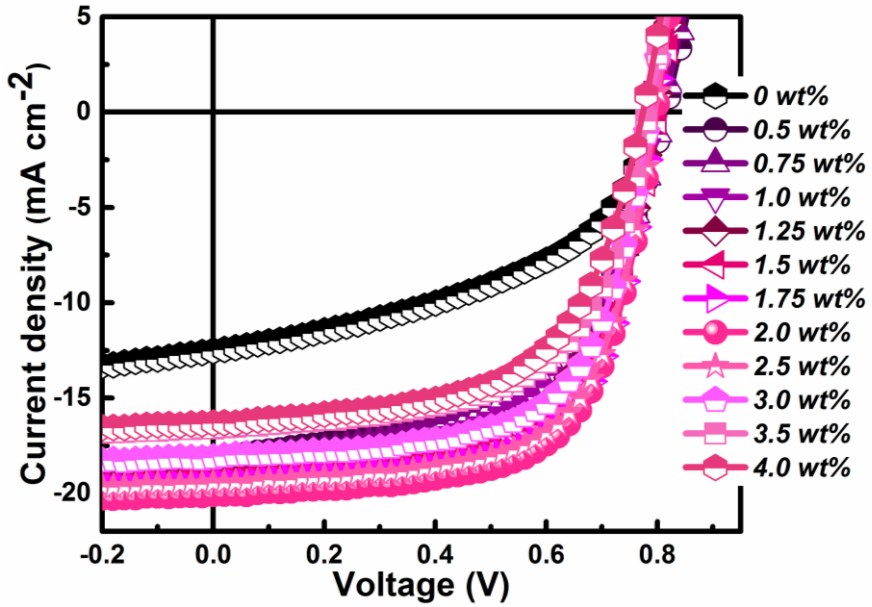

Figure 6.15. *J–V* characteristics of binary devices with different wt% of P3 as an additive under AM 1.5G irradiation at 100 mW cm^{-2}.

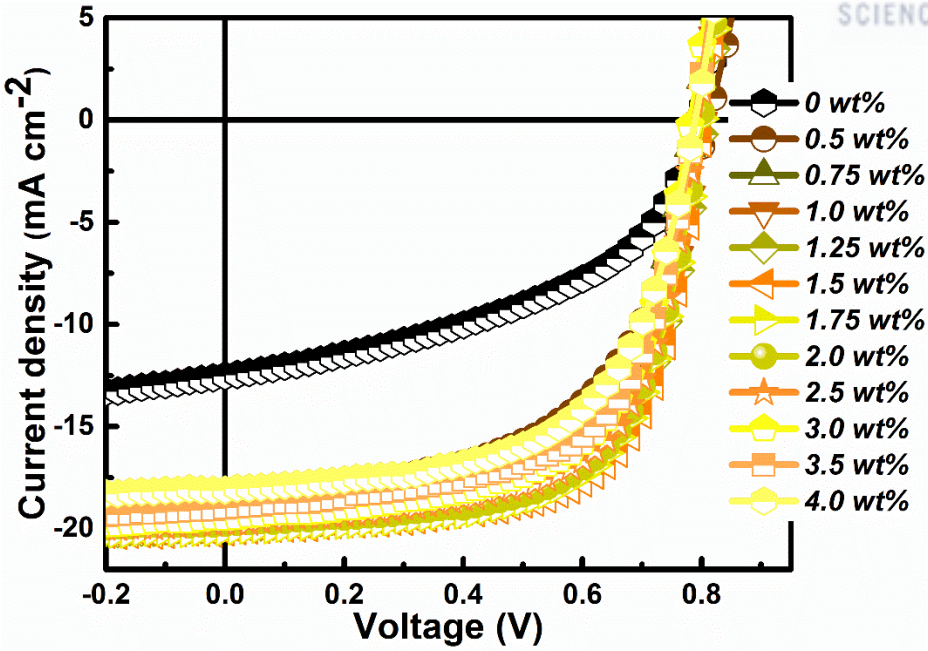

Figure 6.16. *J–V* characteristics of binary devices with different wt% of P4 as an additive under AM 1.5G irradiation at 100 mW cm^{-2}.

Table 6.3. Summary of device parameters of binary devices with different vol% of NMP only under AM 1.5G irradiation at 100 mW cm^{-2}.

Concentration	J_{SC} (mA cm^{-2})	V_{OC} (V)	FF (%)	PCE (%)
0 vol%	12.52	0.795	46.94	4.67
1.0 vol%	18.47	0.802	54.00	8.00
1.5 vol%	18.81	0.801	61.40	9.25
2.0 vol%	18.93	0.800	64.50	9.77
2.5 vol%	18.99	0.799	65.90	10.00
3.0 vol%	19.44	0.799	65.70	10.20
3.5 vol%	19.61	0.796	64.70	10.10
4.0 vol%	19.89	0.792	63.80	10.05
5.0 vol%	19.91	0.791	63.04	9.92
6.0 vol%	19.96	0.788	62.70	9.86
7.0 vol%	19.93	0.786	62.00	9.71
8.0 vol%	19.76	0.781	61.60	9.50

Table 6.4. Summary of device parameters of binary devices with different wt% of P1 as an additive under AM 1.5G irradiation at 100 mW cm^{-2}.

Concentration	J_{SC} (mA cm^{-2})	V_{OC} (V)	FF (%)	PCE (%)
0 wt%	12.52	0.795	46.94	4.67
0.5 wt%	18.51	0.815	53.06	8.01
0.75 wt%	18.67	0.807	57.40	8.65
1.0 wt%	19.07	0.805	61.24	9.40
1.25 wt%	19.61	0.805	61.83	9.76
1.5 wt%	20.19	0.804	62.20	10.10
1.75 wt%	19.84	0.802	61.60	9.80
2.0 wt%	19.83	0.790	60.90	9.54
2.5 wt%	19.38	0.788	60.30	9.21
3.0 wt%	18.86	0.785	58.70	8.69
3.5 wt%	17.91	0.784	57.90	8.13
4.0 wt%	17.47	0.781	57.10	7.79

Table 6.5. Summary of device parameters of binary devices with different wt% of P2 as an additive under AM 1.5G irradiation at 100 mW cm^{-2}.

Concentration	J_{SC} (mA cm^{-2})	V_{OC} (V)	FF (%)	PCE (%)
0 wt%	12.52	0.795	46.94	4.67
0.5 wt%	18.79	0.808	54.96	8.35
0.75 wt%	18.16	0.809	59.86	8.80
1.0 wt%	19.03	0.810	61.66	9.50
1.25 wt%	19.01	0.810	64.80	9.98
1.5 wt%	20.44	0.811	66.47	11.03
1.75 wt%	20.47	0.808	64.80	10.72
2.0 wt%	19.65	0.807	64.81	10.27
2.5 wt%	19.75	0.804	63.51	10.09
3.0 wt%	19.30	0.803	62.90	9.75

3.5 wt%	18.38	0.801	62.30	9.17
4.0 wt%	18.29	0.799	59.40	8.68

Table 6.6. Summary of device parameters of binary devices with different wt% of P3 as an additive under AM 1.5G irradiation at 100 mW cm^{-2}.

Concentration	J_{SC} **(mA** cm^{-2}**)**	V_{OC} **(V)**	**FF (%)**	**PCE (%)**
0 wt%	12.52	0.795	46.94	4.67
0.5 wt%	18.14	0.814	54.30	8.02
0.75 wt%	18.32	0.813	56.40	8.40
1.0 wt%	18.43	0.805	6.00	8.90
1.25 wt%	18.96	0.804	61.00	9.30
1.5 wt%	19.29	0.802	63.40	9.81
1.75 wt%	19.58	0.797	66.00	10.30
2.0 wt%	20.07	0.795	65.80	10.50
2.5 wt%	19.54	0.794	65.70	10.20
3.0 wt%	18.12	0.793	64.60	9.28
3.5 wt%	16.61	0.786	60.90	7.95
4.0 wt%	16.31	0.785	59.90	7.67

Table 6.7. Summary of device parameters of binary devices with different wt% of P4 as an additive under AM 1.5G irradiation at 100 mW cm^{-2}.

Concentration	J_{SC} **(mA** cm^{-2}**)**	V_{OC} **(V)**	**FF (%)**	**PCE (%)**
0 wt%	12.52	0.795	46.94	4.67
0.5 wt%	18.63	0.798	54.55	8.11
0.75 wt%	18.62	0.800	61.22	9.12
1.0 wt%	18.78	0.806	64.28	9.73
1.25 wt%	19.82	0.806	64.46	10.30
1.5 wt%	20.10	0.807	66.81	10.83

1.75 wt%	20.09	0.801	65.88	10.60
2.0 wt%	19.76	0.801	65.18	10.31
2.5 wt%	19.68	0.795	64.36	10.06
3.0 wt%	19.48	0.791	63.01	9.72
3.5 wt%	19.30	0.790	62.12	9.47
4.0 wt%	18.33	0.789	59.48	8.61

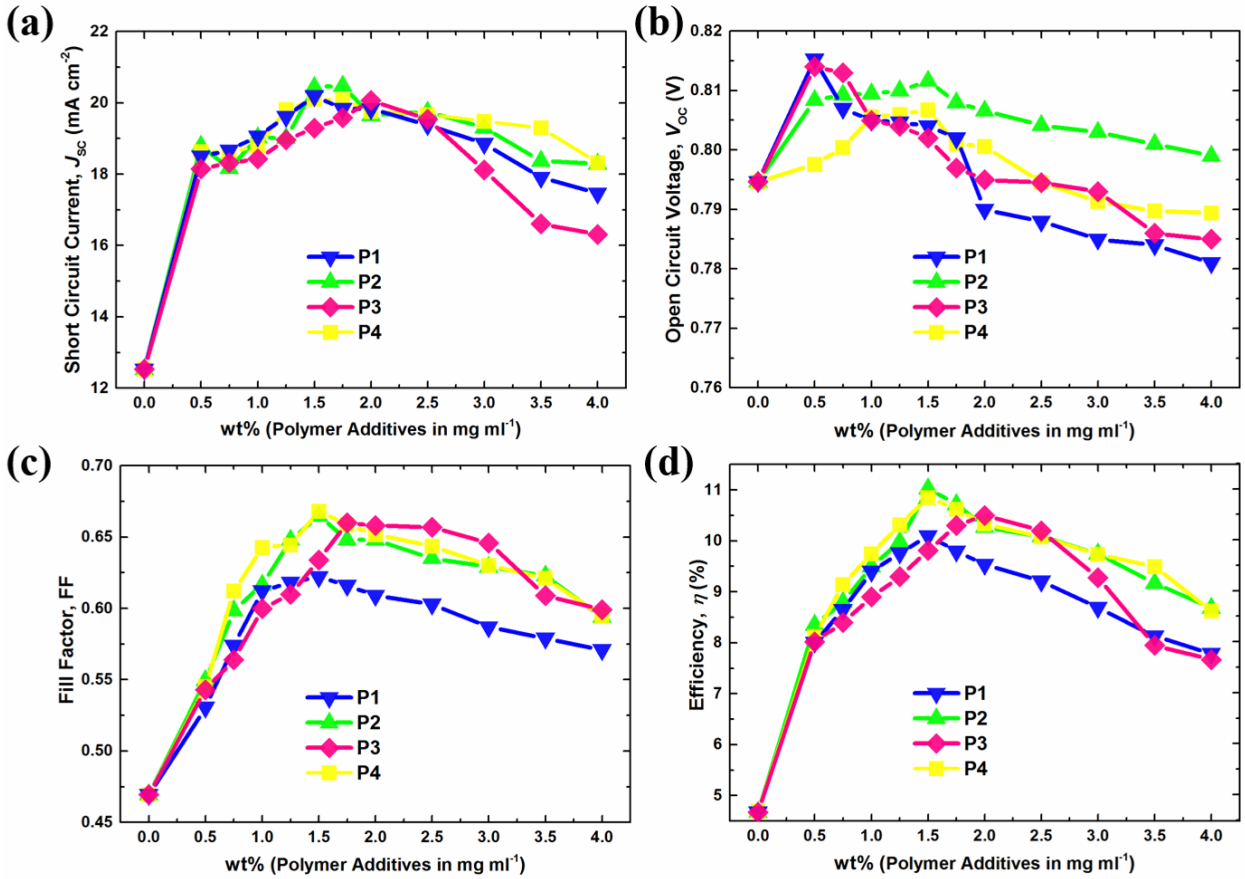

Figure 6.17. Comparison of device parameters in a nutshell. (a) Short circuit density, (b) open circuit voltage, (c) fill factor, and (d) efficiency of binary OSCs with PVDF-based ferroelectric polymers as different wt% of additives.

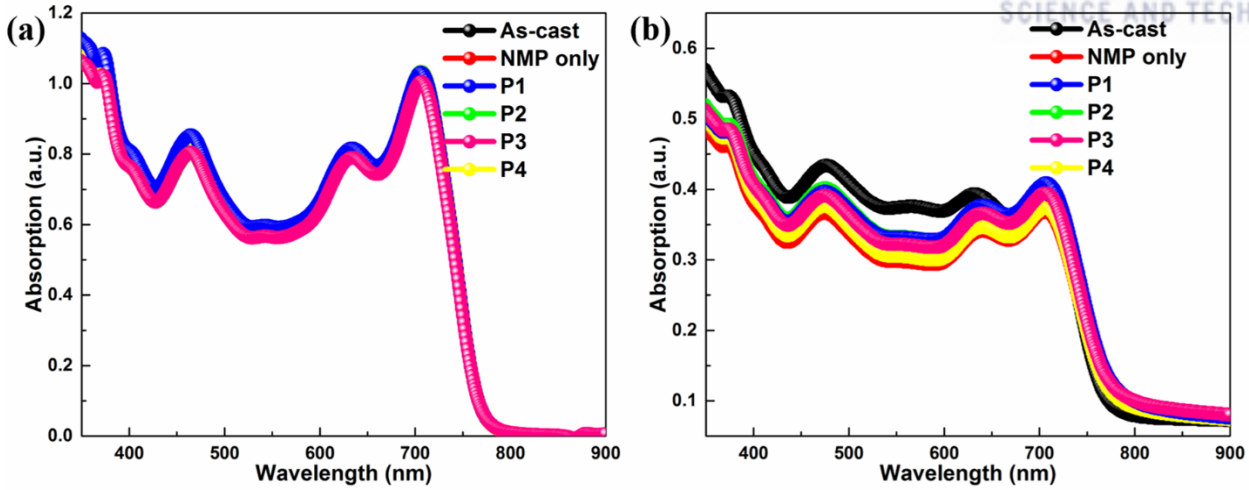

Figure 6.18. *U-V* Vis. absorption spectra of binary blends w/ and w/o PVDF-based ferroelectric polymers as additives in (a) solutions, and (b) thin films.

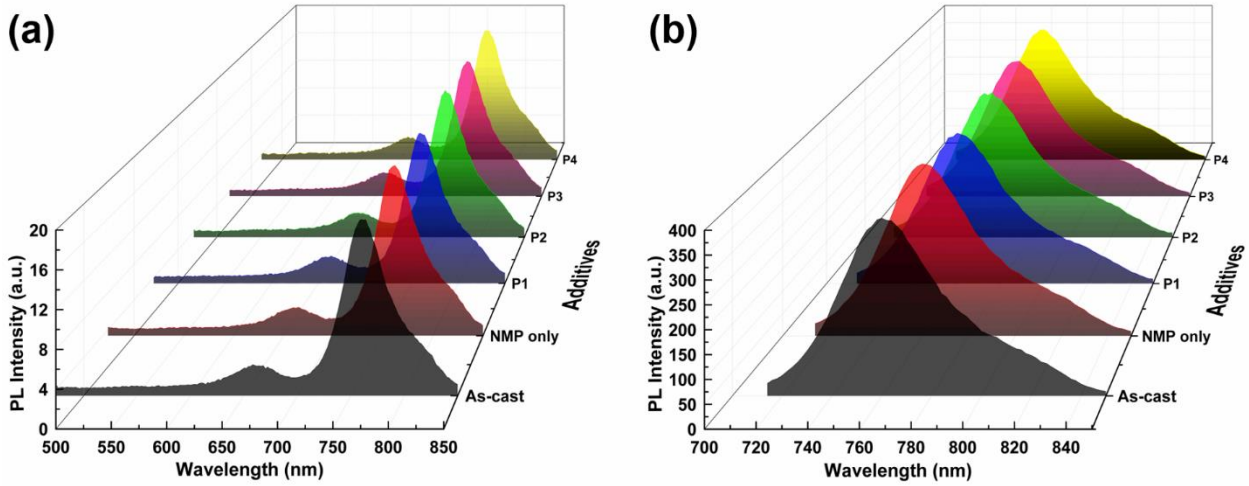

Figure 6.19. Photoluminescence spectra of binary blend solutions w/ and w/o PVDF-based ferroelectric polymers as additives after excitation at (a) 465 nm, and (b) 705 nm.

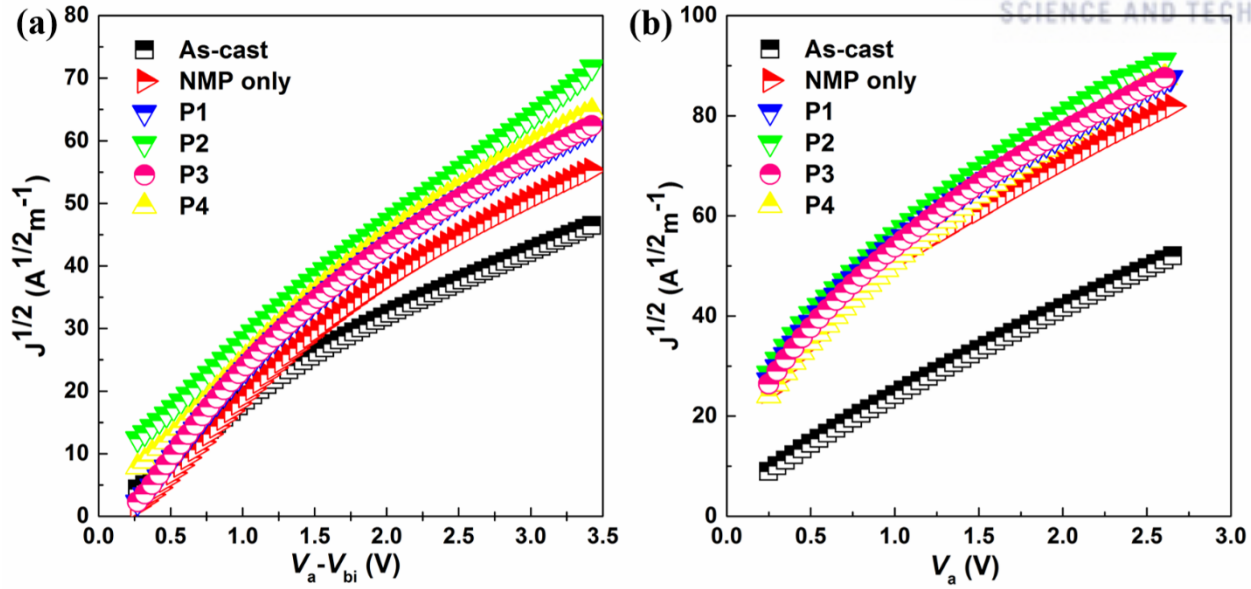

Figure 6.20. (a) Hole only. (b) Electron only mobility of binary blend active layer w/ and w/o PVDF-based ferroelectric polymers as additives.

Table 6.8. Summary of mobilities for hole only and electron only as well as charge dissociation probability of binary blend active layer w/ and w/o PVDF-based ferroelectric polymers as additives.

Additive	μh x 10^{-4} ($cm^2V^{-1}s^{-1}$)	μe x 10^{-4} ($cm^2V^{-1}s^{-1}$)	μh/ μe	*P(E,T)*
None	0.896	0.956	0.938	0.883
NMP	1.930	2.241	0.861	0.968
G18	2.939	3.931	0.747	0.976
G44	2.437	3.189	0.764	0.975
PVDF	2.074	2.587	0.801	0.968
P(VDF-TrFE)	2.144	2.780	0.771	0.977

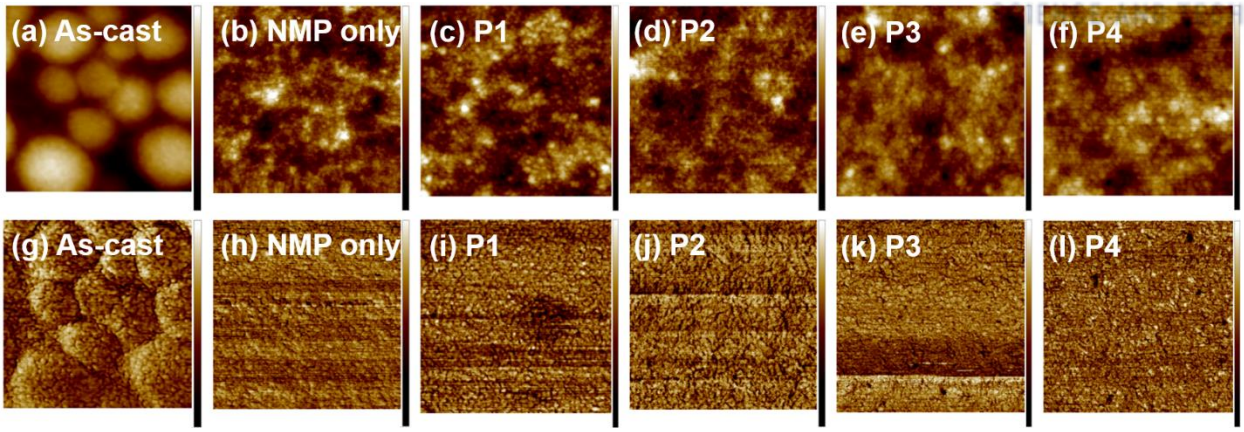

Figure 6.21. AFM topography height (a)~(f) and phase (g)~(l) images (scan size 1 × 1 μm) of binary blend films w/ and w/o PVDF-based ferroelectric polymers as additives. (a),(g) As-cast, (b),(h) NMP only, (c)(i) P1, (d)(j) P2, (e)(k) P3, and (f),(l) P4. Different color bars are used for the height and phase variance.

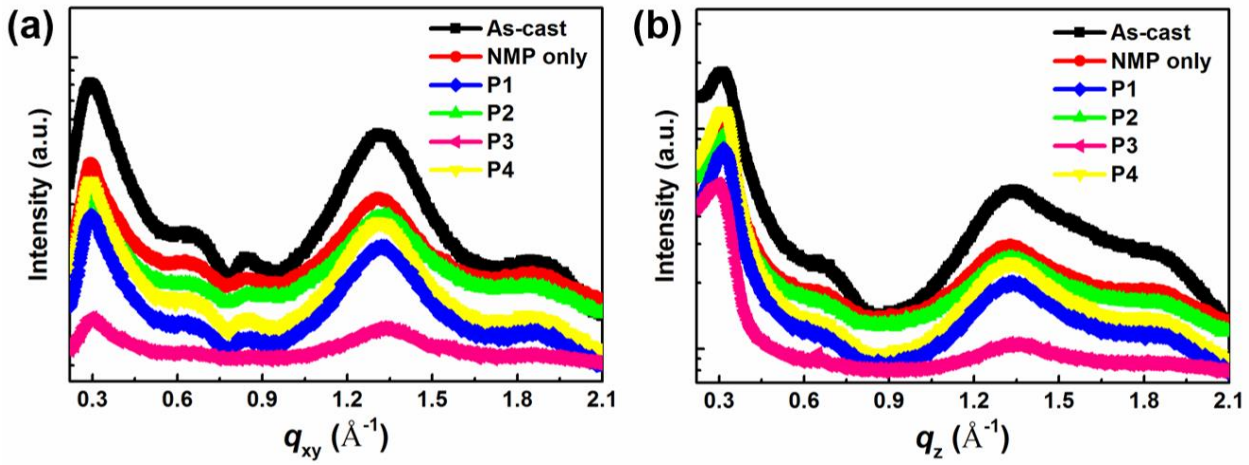

Figure 6.22. (a) In-plane and (b) out-of-plane line cut profiles obtained from GIWAXS data of binary blend films w/ and w/o various ferroelectric polymers as an additive.

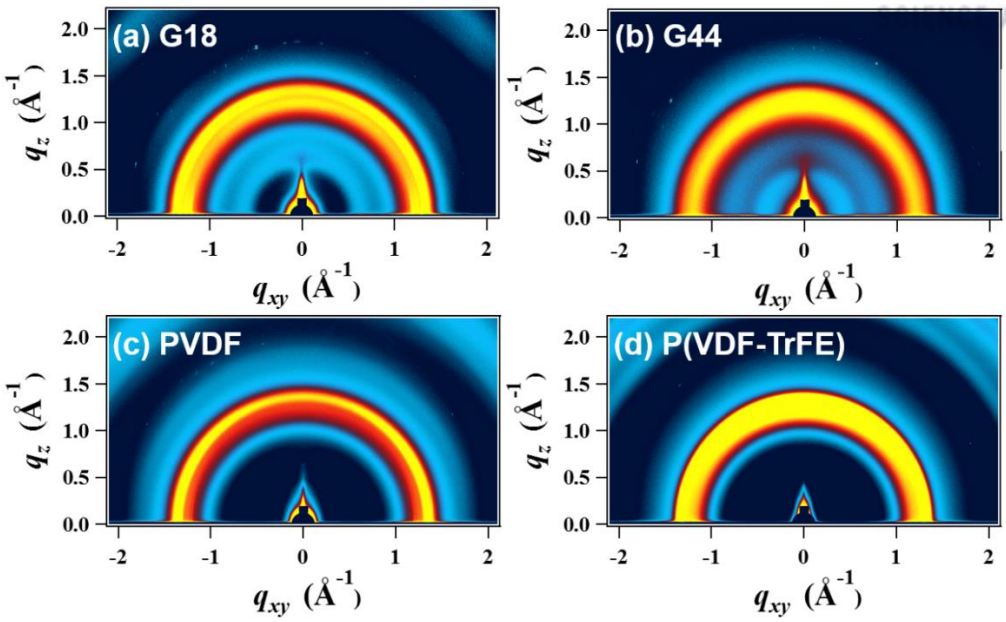

Figure 6.23. Grazing incidence wide angle X-ray scattering (GIWAXS) patterns of pure ferroelectric polymer films. (a) P1, (b) P2, (c) P3, and (d) P4. Different color bars are used for intensity variance.

Table 6.9. Lattice parameters in out-of-plane and direction of binary blend active layer films w and w/o PVDF-based ferroelectric polymers as additives.

Active layer	**Unit cell long axis**	**d_{100} (Å)**	**CCL (nm)**
None	0.316	19.89	20.74
NMP	0.322	19.50	26.01
G18	0.321	19.56	23.36
G44	0.320	19.64	23.42
PVDF	0.321	19.57	24.44
P(VDF-TrFE)	0.307	20.46	19.75
	π-π stacking cell axis	**d_{010} (Å)**	**CCL (nm)**
None	1.86	3.37	12.17
NMP	1.85	3.40	14.67
G18	1.85	3.39	13.83
G44	1.85	3.40	15.37
PVDF	1.86	3.38	15.91
P(VDF-TrFE)	1.86	3.37	13.07

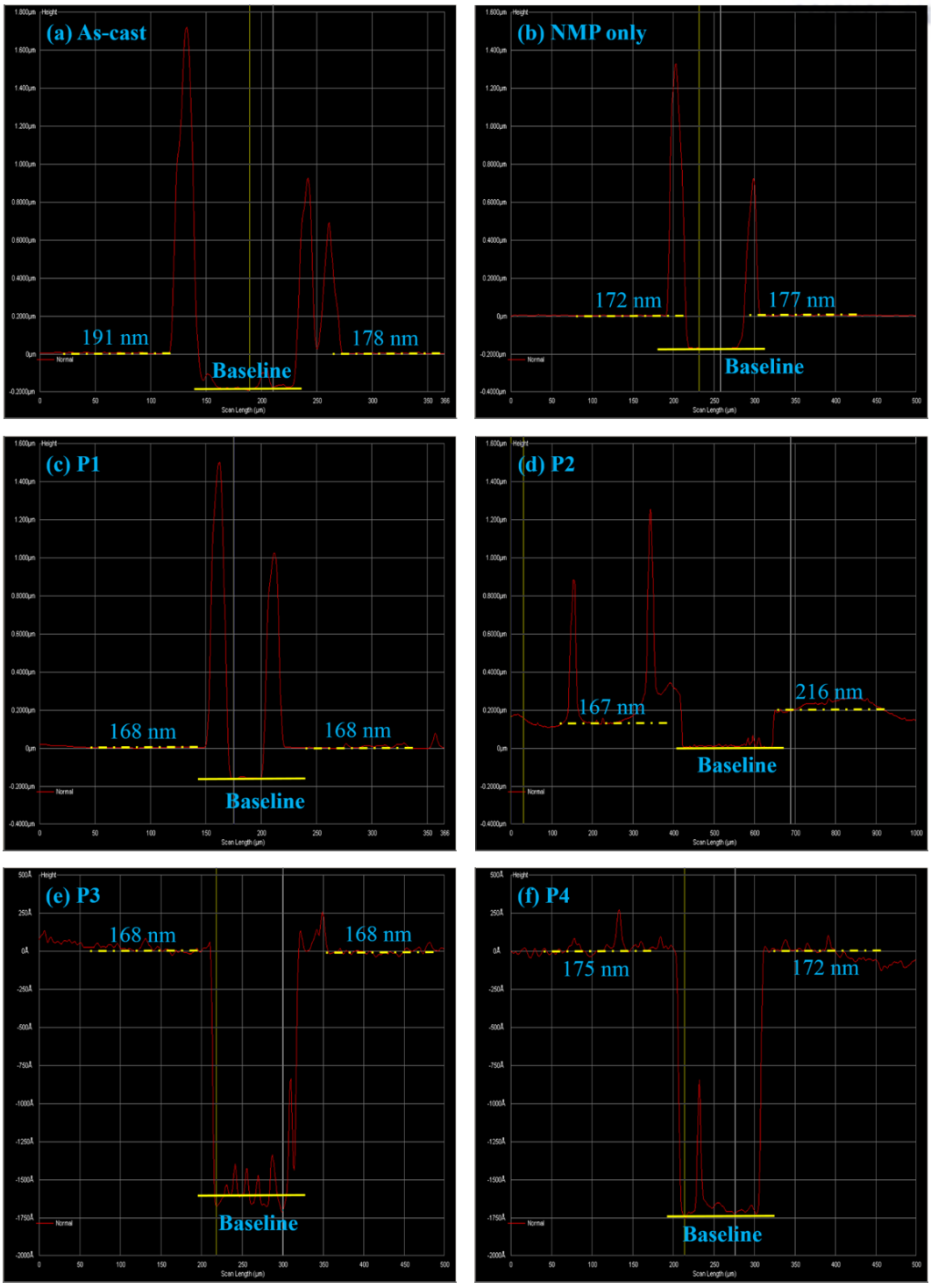

Figure 6.24. Thickness of binary blend films w/ and w/o PVDF-based ferroelectric polymers as an additive used for device measurement. (a) As-cast, (b) NMP only, (c) P1, (d) P2, (e) P3, and (f) P4.

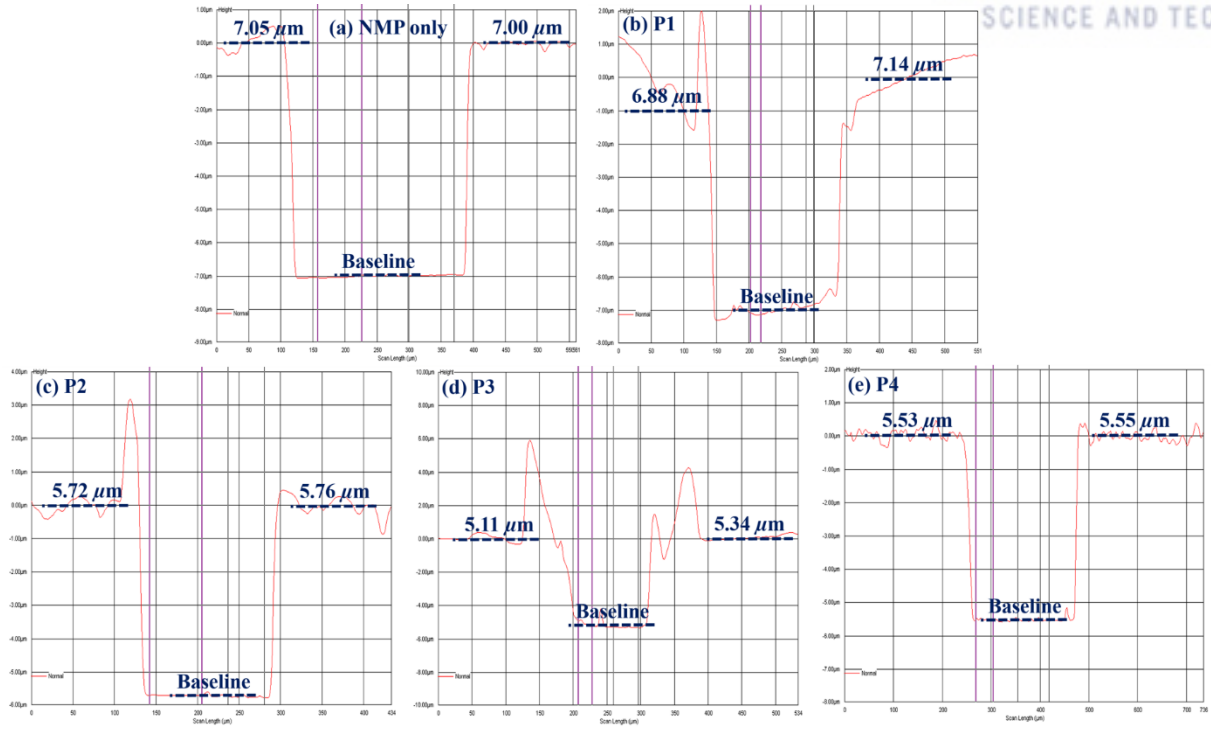

Figure 6.25. Thickness of binary blend films w/ and w/o PVDF-based ferroelectric polymers as an additive used for hysteresis measurement. (a) NMP only, (b) P1, (c) P2, (d) P3, and (e) P4.

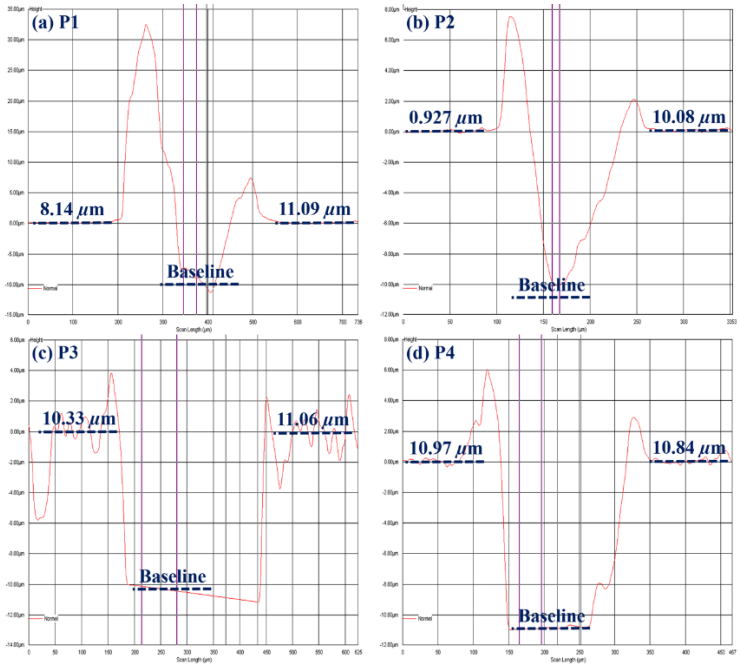

Figure 6.26. Thickness of PVDF-based pure ferroelectric polymers films used for hysteresis measurement. (a) P1, (b) P2, (c) P3, and (d) P4.

Chapter 7. Acknowledgements

I would like to express my heartiest thanks with a deep sense of gratitude to all those who provided me immense guidance and help for my study and stay in S. Korea during past four and half years.

First and foremost, I would like to express my deepest gratitude and respect to my supervisor Prof. Changduk Yang, for his enormous patience, excellent guidance and caring without whom I could not have come so far in the field of research. I am immensely grateful to him for stressing the need to develop the right attitude towards work throughout my Ph.D. study and at the same time provided his continuous support and persistent help during my stay in the lab.

Though the dissertation is mine, but I could never have reached the heights without the help, support, guidance, cooperation in research as well as pleasurable working atmosphere provided by my lab mates in ATOMS (Advanced Tech Optoelectronic Materials Synthesis Lab). I convey my sincere regards to Sangmyeon Lee, So-Huei Kang, Mijin Moon, Daehee Han, and Sungwoo Jung who not only provided excellent materials for OPV fabrication which helped in achieving good results but also provided continuous help and encouragement throughout my stay in Korea. Moreover, I would like to thank my respected seniors, Dr. Gyoungsik Kim, Dr. Junghoon Lee, and Dr. Satej Dharmapurikar for providing me their continuous guidance and support during initial stages of my Ph.D. course. Besides, I appreciatively thank Yongjoon Cho, Jiyeon Oh, Dr. Shanshsn Chen, Jungho Lee, Dr. Sujit Kumar, Byongkyu Lee, Minkyu Jeong, Hyojin Kang, Hyejin Cho, Yujin An, Dr. Yiho Kim, and Dr. Kyucheol Lee for sharing the happiness with me together during my stay in the lab. I would like to mention here that I am equally grateful to each and every one who name has not been mentioned here but were associated with my project at any stage during the Ph.D. period.

Additionally, I express my deep appreciation and thanks to all my friends outside the lab, who became pillars of my strength during past four and half years. Thank you for walking alongside me in every situation and making my life cheerful each and every day.

Last but not the least, I enormously thank my parents and my whole family whose continuous positivity and blessings helped me to get rid of all the frustrations and down times as well as brought confidence in me to overcome any obstacle. They continuously inspired me for bringing substantial effort to make my life meaningful and full of achievements.

Detailed Acknowledgements

Chapter 3.

This research work was supported by the National Research Foundation of Korea (NRF) grant funded by the Korea Government (MSIP) (2015R1A2A1A10053397 and 2014K1A3A1A19066591). GIWAXD experiment at PLS-II 6D UNIST-PAL beamline was sup- ported in part by MEST, POSTECH and UNIST-UCRF.

Chapter 4.

Section 4.1.

T.K. and C.Y. wrote the manuscript. T. K. carried out the experiments and performed the device fabrication, as well as analyzed the data. S. M. L. synthesized DR3TSBDT. This work was supported by the National Research Foundation of Korea (NRF) grant funded by the Korea government (MSIP) (2015R1A2A1A10053397). GIWAXD measurements at PLS-II 6D UNIST-PAL beamline and 9A beamline were supported in part by MEST, POSTECH, and UNIST UCRF.

Section 4.2.

T.K. and C.Y. wrote the manuscript. T.K. carried out the experiments and performed the device fabrication and other experiments, as well as analyzed the data. S.M.L. synthesized SMDs. This work was supported by the National Research Foundation of Korea (NRF) grant funded by the Korea government (MSIP) (2015R1A2A1A10053397). GIWAXD measurements at PLS-II 6D UNIST-PAL beamline and 9A beamline were supported in part by MEST, POSTECH, and UNIST UCRF.

Chapter 5.

T.K. and C.Y. wrote the manuscript. T.K. carried out the experiments and performed the device fabrication and other experiments, as well as analyzed the data. This work was supported by the National Research Foundation of Korea (NRF) grant funded by the Korea government (MSIP) (2015R1A2A1A10053397). GIWAXD measurements at PLS-II 6D UNIST-PAL beamline and 9A beamline were supported in part by MEST, POSTECH, and UNIST UCRF.

Chapter 6.

T.K. and C.Y. wrote the manuscript. T.K. carried out the experiments and performed the device fabrication and other experiments, as well as analyzed the data. H.-P. Kim carried out hysteresis measurement. S.J. performed synthesis of grafted polymer. GIWAXD measurements at PLS-II 6D UNIST-PAL beamline and 9A beamline were supported in part by MEST, POSTECH, and UNIST UCRF.

Appendix

List of Publications

- **Kumari, T.**; Moon, M.; Kang, S.-H.; Yang, C., Improved efficiency of DTGe(FBTTh$_2$)$_2$-based solar cells by using macromolecular additives: How macromolecular additives versus small additives influence nanoscale morphology and photovoltaic performance. *Nano Energy* **2016,** *24,* 56-62.

- **Kumari, T.**; Lee, S. M.; Kang, S.-H.; Chen, S.; Yang, C., Ternary solar cells with a mixed face-on and edge-on orientation enable an unprecedented efficiency of 12.1%. *Energy Environ. Sci.* **2017,** *10* (1), 258-265.

- Kang, S.-H.; **Kumari, T.**; Lee, S. M.; Jeong, M.; Yang, C., Densely Packed Random Quarterpolymers Containing Two Donor and Two Acceptor Units: Controlling Absorption Ability and Molecular Interaction to Enable Enhanced Polymer Photovoltaic Devices. *Adv. Energy Mater.* **2017,** *7* (15), 1700349.

- **Kumari, T.**; Lee, S. M.; Yang, C., Cubic-Like Bimolecular Crystal Evolution and over 12% Efficiency in Halogen-Free Ternary Solar Cells. *Adv. Funct. Mater.* **2018,** *28* (19), 1707278.

- Han, D.; **Kumari, T.**; Jung, S.; An, Y.; Yang, C., A Comparative Investigation of Cyclohexyl-End-Capped Versus Hexyl-End-Capped Small-Molecule Donors on Small Donor/Polymer Acceptor Junction Solar Cells. *Sol. RRL* **2018,** *2* (5), 1800009.

- **Kumari, T.**; Lee, S. M.; Lee, K. C.; Cho, Y.; Yang, C., Harmonious Compatibility Dominates Influence of Side-Chain Engineering on Morphology and Performance of Ternary Solar Cells. *Adv. Energy Mater.* **2018,** *8* (22), 1800616.

- Lee, J.; Lee, S. M.; Chen, S.; **Kumari, T.**; Kang, S.-H.; Cho, Y.; Yang, C., Organic Photovoltaics with Multiple Donor-Acceptor Pairs *Adv. Mater.* **2018,** 1804762.

- **Kumari, T.**; Jung, S.; Kim, H.-P.; Cho, Y.; Oh, J.; Lee, J. W.; Baik, J. M.; **Jo, W.;** Yang, C., Incorporation of Ferroelectric Additives enhances built-in electric field for better efficiency in BHJ Solar Cells, *under submission*.

Permission from all the Cited Journals used in this Dissertation

Chapter 3.

How macromolecular additives versus small additives influence nanoscale morphology and photovoltaic performance. *Nano Energy* **2016,** *24*, 56-62.

Copyright Clearance Center RightsLink®

Home | Account Info | Help

ELSEVIER

Title: Improved efficiency of DTGe(FBTTh2)2-based solar cells by using macromolecular additives: How macromolecular additives versus small additives influence nanoscale morphology and photovoltaic performance

Author: Tanya Kumari,Mijin Moon,So-Huei Kang,Changduk Yang

Publication: Nano Energy

Publisher: Elsevier

Date: June 2016

© 2016 Elsevier Ltd. All rights reserved.

Logged in as:
Tanya Kumari
Account #:
3001350897
LOGOUT

Please note that, as the author of this Elsevier article, you retain the right to include it in a thesis or dissertation, provided it is not published commercially. Permission is not required, but please ensure that you reference the journal as the original source. For more information on this and on your other retained rights, please visit: https://www.elsevier.com/about/our-business/policies/copyright#Author-rights

BACK | CLOSE WINDOW

Copyright © 2018 Copyright Clearance Center, Inc. All Rights Reserved. Privacy statement. Terms and Conditions.
Comments? We would like to hear from you. E-mail us at customercare@copyright.com

Chapter 4.

Section 4.1.

Ternary solar cells with a mixed face-on and edge-on orientation enable an unprecedented efficiency of 12.1%. Reproduced from *Energy Environ. Sci.* **2017,** *10* (1), 258-265 with permission from the Royal Society of Chemistry.

Author reusing their own work published by the Royal Society of Chemistry

You do not need to request permission to reuse your own figures, diagrams, etc, that were originally published in a Royal Society of Chemistry publication. However, permission should be requested for use of the whole article or chapter except if reusing it in a thesis. If you are including an article or book chapter published by us in your thesis please ensure that your co-authors are aware of this.

Reuse of material that was published originally by the Royal Society of Chemistry must be accompanied by the appropriate acknowledgement of the publication. The form of the acknowledgement is dependent on the journal in which it was published originally, as detailed in 'Acknowledgements'.

Material published by the Royal Society of Chemistry to be used in another of our publications

Authors contributing to our publications (journal articles, book or book chapters) do not need to formally request permission to reproduce material contained in another Royal Society of Chemistry publication. However, permission should be requested for use of a whole article or chapter. For all cases of reproduction the correct acknowledgement of the reproduced material should be given. The form of the acknowledgement is dependent on the journal in which it was published originally, as detailed in the 'Acknowledgements' section.

Acknowledgements —

The Royal Society of Chemistry publishes some journals in partnership with, or on behalf of, other organisations; these journals require a specific wording of the acknowledgement when work is reproduced from them. The text for the acknowledgement for these journals, and the standard wording to be used by all other journals are given below.

Standard acknowledgement

Reproduced from Ref. XX with permission from the Royal Society of Chemistry.

Non-standard acknowledgements

Reproduction of material from NJC (New Journal of Chemistry)
Reproduced from Ref. XX with permission from the Centre National de la Recherche Scientifique (CNRS) and the Royal Society of Chemistry.

Section 4.2.

Harmonious Compatibility Dominates Influence of Side-Chain Engineering on Morphology and Performance of Ternary Solar Cells. *Adv. Energy Mater.* **2018,** *8* (22), 1800616.

JOHN WILEY AND SONS LICENSE TERMS AND CONDITIONS

Oct 16, 2018

This Agreement between Miss. Tanya Kumari ("You") and John Wiley and Sons ("John Wiley and Sons") consists of your license details and the terms and conditions provided by John Wiley and Sons and Copyright Clearance Center.

License Number	4450631443246
License date	Oct 16, 2018
Licensed Content Publisher	John Wiley and Sons
Licensed Content Publication	Advanced Energy Materials
Licensed Content Title	Harmonious Compatibility Dominates Influence of Side-Chain Engineering on Morphology and Performance of Ternary Solar Cells
Licensed Content Author	Tanya Kumari, Sang Myeon Lee, Kyu Cheol Lee, et al
Licensed Content Date	May 28, 2018
Licensed Content Volume	8
Licensed Content Issue	22
Licensed Content Pages	8
Type of use	Dissertation/Thesis
Requestor type	Author of this Wiley article
Format	Print and electronic
Portion	Full article
Will you be translating?	No
Title of your thesis / dissertation	Investigation of Efficient Organic Solar cells through Optimized Morphology Control and Understanding of Mechanisms
Expected completion date	Feb 2019
Expected size (number of pages)	400
Requestor Location	Miss. Tanya Kumari Ulsan Nat. Inst. of Sci. & Tech. (UNIST) Ulju-gun, Eonyang-eup, Banyeon-ri, Ulsan, Republic of Korea (South Korea) 44919 Korea, Republic Of Attn: Miss. Tanya Kumari
Publisher Tax ID	EU826007151
Total	0.00 USD
Terms and Conditions	

TERMS AND CONDITIONS

This copyrighted material is owned by or exclusively licensed to John Wiley & Sons, Inc. or one of its group companies (each a"Wiley Company") or handled on behalf of a society with which a Wiley Company has exclusive publishing rights in relation to a particular work (collectively "WILEY"). By clicking "accept" in connection with completing this licensing transaction, you agree that the following terms and conditions apply to this transaction (along with the billing and payment terms and conditions established by the Copyright

Chapter 5.

Cubic-Like Bimolecular Crystal Evolution and over 12% Efficiency in Halogen-Free Ternary Solar Cells.

Adv. Funct. Mater. **2018,** *28* (19), 1707278.

JOHN WILEY AND SONS LICENSE TERMS AND CONDITIONS

Oct 16, 2018

This Agreement between Miss. Tanya Kumari ("You") and John Wiley and Sons ("John Wiley and Sons") consists of your license details and the terms and conditions provided by John Wiley and Sons and Copyright Clearance Center.

License Number	4450640345024
License date	Oct 16, 2018
Licensed Content Publisher	John Wiley and Sons
Licensed Content Publication	Advanced Functional Materials
Licensed Content Title	Cubic-Like Bimolecular Crystal Evolution and over 12% Efficiency in Halogen-Free Ternary Solar Cells
Licensed Content Author	Tanya Kumari, Sang Myeon Lee, Changduk Yang
Licensed Content Date	Mar 24, 2018
Licensed Content Volume	28
Licensed Content Issue	19
Licensed Content Pages	10
Type of use	Dissertation/Thesis
Requestor type	Author of this Wiley article
Format	Print and electronic
Portion	Full article
Will you be translating?	No
Title of your thesis / dissertation	Investigation of Efficient Organic Solar cells through Optimized Morphology Control and Understanding of Mechanisms
Expected completion date	Feb 2019
Expected size (number of pages)	400
Requestor Location	Miss. Tanya Kumari Ulsan Nat. Inst. of Sci. & Tech. (UNIST) Ulju-gun, Eonyang-eup, Banyeon-ri, Ulsan, Republic of Korea (South Korea) 44919 Korea, Republic Of Attn: Miss. Tanya Kumari
Publisher Tax ID	EU826007151
Total	0.00 USD
Terms and Conditions	

TERMS AND CONDITIONS

This copyrighted material is owned by or exclusively licensed to John Wiley & Sons, Inc. or one of its group companies (each a"Wiley Company") or handled on behalf of a society with which a Wiley Company has exclusive publishing rights in relation to a particular work (collectively "WILEY"). By clicking "accept" in connection with completing this licensing transaction, you agree that the following terms and conditions apply to this transaction (along with the billing and payment terms and conditions established by the Copyright